LA-7973-MS
Informal Report

The Reversed-Field Pinch Reactor (RFPR) Concept

University of California

LOS ALAMOS SCIENTIFIC LABORATORY
Post Office Box 1663 Los Alamos, New Mexico 87545

This work was supported by the US Department of Energy, Office of Fusion Energy.

LA-7973-MS
Informal Report

UC-20d
Issued: August 1979

The Reversed-Field Pinch Reactor (RFPR) Concept

R. L. Hagenson
R. A. Krakowski
G. E. Cort

MAJOR CONTRIBUTORS

Engineering:	W. E. Fox, R. W. Teasdale
Neutronics:	P. D. Soran
Tritium:	C. G. Bathke, H. Cullingford
Materials:	F. W. Clinard, Jr.
Plasma Engineering:	R. L. Miller
Physics:	D. A. Baker, J. N. DiMarco
Electrotechnology:	R. W. Moses

TABLE OF CONTENTS

THE REVERSED-FIELD PINCH REACTOR (RFPR) CONCEPT

by

R. L. Hagenson, R. A. Krakowski, and G. E. Cort

ABSTRACT

A conceptual engineering design of a fusion reactor based on plasma confinement in a Reversed-Field Pinch (RFP) configuration is presented. A 50% atomic mixture of deuterium and tritium (DT) is ohmically heated to ignition by currents flowing in the toroidal plasma; this plasma current also inherently produces the confining magnetic fields in a toroidal chamber having a major and minor radii of 12.7 and 1.5 m, respectively. The DT plasma ignites in 2-3 s and burns at 10-20 keV for ~ 20 s to give a fuel burnup of ~ 50%. A 5-s dwell period between burn pulses is allowed for plasma quench and refueling. Tritium breeding occurs in a granular Li_2O blanket which is packed around an array of radially oriented coolant tubes carrying a mixture of high-pressure steam and water. The slightly superheated steam emerging from this blanket would be used to drive a turbine directly. Low-pressure helium containing trace amounts of oxygen is circulated through the packed Li_2O bed to extract the tritium. A 20-mm-thick copper first wall serves as a neutron multiplier, acts as a tritium barrier, and supports image currents to provide plasma stabilization on a 0.1-s timescale; external windings provide stability for longer times. Approximately 38% of the total thermal energy is removed by this copper first wall. Thermal energy from the first wall and blanket is removed by separate coolant loops and is directly converted to electricity at an efficiency of 30% in a conventional thermal conversion cycle. All thermal systems outside the first wall operate steady state with the steam tubing inside the blanket experiencing less than a 5 K temperature variation between burn pulses; no auxiliary thermal energy storage is needed. A borated-water shield is located immediately outside the thermal blanket to protect the superconducting magnet coils, which are energized by homopolar motor/generators. Accounting for all major energy flows yields a system with a recirculating power fraction of 0.17, resulting in an overall plant efficiency of 25.0% for this 750 MWe(net) power reactor. A preliminary but comprehensive cost estimate indicates direct capital and power costs of $1100/kWe and 66.3 mills/kWeh, respectively.

I. INTRODUCTION

As part of its overall program for assessing the reactor potential of a number of alternative fusion concepts, the Office of Fusion Energy, Department of Energy, has funded systems studies according to a three tier structure. These studies are categorized in order of decreasing level of effort and detail as Level I, Level II, and Level III. The highest level of study (Level I) would include, in a multiman-year effort, considerable conceptual design and economics analysis, in addition to sophisticated, state-of-the-art physics and operating-point analyses. The lowest level of study (Level III) would characterize less understood and developed confinement schemes by means of relatively simple physics models and parametric analysis of potential reactor operating points. Generally, a Level III study would not provide a reactor embodiment *per se*, and, because of obvious gaps in the physics understanding of these relatively unexplored concepts, only a range of potential reactor operating points may be parametrically identified. The Reversed-Field Pinch Reactor (RFPR) study described herein lies somewhere between Levels I and II.

The primary motivation for this study is the investigation of the Reversed-Field Pinch Reactor for the production of electrical power. This reactor evaluation defines and quantifies the engineering systems required for the economic and reliable production of power from the RFPR; solutions to crucial technological problems, whenever the technology is sufficiently advanced, are proposed. Engineering research and development must be guided by a conceptual engineering design of a desirable power reactor. Analogously, the RFP experimental program must follow a course that ultimately leads to a workable reactor system and, therefore, must address pertinent problems at the earliest possible date if the engineering development is to proceed most effectively.

This study has focused on the development of a realistic reactor-plasma model, an extensive parameter study leading to a minimum cost system, and the development of a self-consistent engineering design. Two major priorities and/or constraints were imposed on this study. First, the engineering system would utilize only conventional technology when possible, and, secondly, the ease of maintenance would be emphasized. The first-wall/blanket structure consists of a water-cooled copper and stainless-steel structure, with tritium breeding occurring in a granular Li_2O bed. A direct-cycle, low-superheat

steam system is proposed for energy conversion to electricity, thereby eliminating an expensive secondary coolant loop. Ohmic heating of the DT plasma to ignition is inherent to the RFPR confinement scheme, and auxiliary heating is not necessary. A batch-burn (unrefueled) operation was also chosen to avoid the use of advanced ash/impurity-control (divertors) and fueling systems. The pulsed superconducting-magnet coils and energy storage system represent developmental items, although the magnet coils per se are near the state-of-the-art because of the modest system requirements (maximum field level ~ 2 T, maximum field rate-of-change ~ 40 T/s). Detailed designs exist for the proposed homopolar generators needed to energize the magnet systems; the homopolar generators could be replaced by ac machinery or fast-discharge dc alternators if these latter technologies prove to be economically attractive. Ease of maintenance is promised by designing the reactor core structure for removal without disturbing the magnet coils; the reactor core and remote maintenance unit is located within a common vacuum tunnel.

The scope of this study includes a first-order economic optimization of the total power plant. Preliminary engineering design of the systems needed to initiate and sustain the plasma burn cycle and to convert the resultant thermal energy into electricity is described. In Sec. II an executive summary provides a concise description of all major reactor components and explains the operation and maintenance of the RFPR. A summary assessment of the plasma physics understanding and technological requirements is included in the Executive Summary. The theoretical and experimental physics results upon which this design is based are reviewed in Sec. III. Beginning with a synopsis of previous RFP reactor calculations (Sec. IV.A), Sec. IV describes in detail all engineering/technology bases upon which this RFPR design rests. Specifically, Sec. IV describes the overall RFPR energy balance (Sec. IV.B), all aspects of the reactor plasma physics model (Sec. IV.C), and the costing methodology (Sec. IV.D) used in conjunction with the energy-balance and burn-physics models to develop an optimized point design (Sec. IV.E). Section IV culminates with a summary of the engineering and economic parameters (Sec. IV.F) that describe the RFPR operating point upon which more detailed systems designs are based. The quantitative development of the reactor embodiment, which was limited by the funding and scope of this study, is presented in Sec. V. An assessment of physics and technology needs for the RFPR in Sec. VI concludes this study.

II. EXECUTIVE SUMMARY

Both the physics fundamentals and the reactor embodiment of the Reversed-Field Pinch (RFP) are summarized in this section. The Executive Summary is intended to convey the essential elements of the Reversed-Field Pinch Reactor (RFPR) concept without recourse or reference to the bulk of this report.

A. Fundamental Physics Issues

Like the tokamak, the RFP is a toroidal, axisymmetric confinement device. Both systems use a combination of poloidal, B_θ, and toroidal, B_ϕ, magnetic fields to confine a plasma in a minimum energy state. For both systems the poloidal field, B_θ, is created by inducing through transformer action a large toroidal current, I_ϕ, within the plasma column; the B_ϕ field results from current flowing in external coils. Figure II-1 schematically depicts for both systems the field and pressure profiles across the plasma minor radius. Toroidal equilibrium in both the tokamak and the RFP can be achieved by either using a conducting shell near the plasma (Fig. II-1), an external vertical field, or a combination of both schemes. The RFP requires a conducting shell for plasma stabilization against unstable MHD modes with wavelengths in excess of the shell radius, r_w, whereas the tokamak is not necessarily subjected to this requirement. Localized MHD modes in the RFP are suppressed by the strongly sheared magnetic fields caused by a slight reversal of the B_ϕ field at the plasma edge (Fig. II-1). Although the tokamak does not require a conducting shell near the plasma column, avoidance of the kink instability establishes specific requirements on the relative magnitude of B_θ, B_ϕ, the plasma radius, r_p, and the major radius of the torus, R. Specifically, for the tokamak the parameter $q = (r_p/R)(B_\phi/B_\theta)$, called the safety factor, must be greater than unity. The criterion $q \geq 1$ essentially guarantees that MHD $m = 1$ kink modes with wavelengths in excess of the major circumference of the tokamak, $2\pi R$, will be stable. Experimental values of $q \sim 2\text{-}3$ are required for stable plasma operation. The RFP, on the other hand, operates with q less than unity (q actually falls through zero and becomes negative outside the plasma region, $r > r_p$). The presence of a passive conducting shell in the RFP replaces the $q > 1$ stability criterion with one that requires $(dq/dr) \neq 0$; that is, the variation of the plasma/field shear should not exhibit a minimum in the region enclosed by the conducting shell. The reactor disadvantages associated with (passive) wall stabilization or (active) coil stabilization

are countered by the advantages the RFP approach exhibits when not constrained by the $q > 1$ (i.e., Kruskal-Shafranov) criterion. Imposition of the $q = (r_p/R)(B_\phi/B_\theta) > 1$ constraint implies small values of R/r_p and B_θ/B_ϕ, which in turn creates the following problems:

- Since the plasma pressure is essentially held by the B_θ field, the ratio of plasma pressure to total field pressure (i.e., the β parameter) is small, implying a poor utilization of magnetic field energy per unit of fusion yield.
- Since B_θ/B_ϕ is limited and since practical coil design establishes physical limits on the toroidal field, B_ϕ, the plasma current I_ϕ is limited. This $q > 1$ imposed limit on I_ϕ generally precludes significant plasma heating by ohmic heating alone, thereby necessitating more complex and less efficient plasma heating schemes (i.e., neutral atom beams, radio-frequency heating).
- The constraint that $q > 1$ also enforces limits on the plasma aspect ratio R/r_p. In addition to obvious engineering and system design problems that accompany low-aspect-ratio tori, relatively large inhomogeneities result in the toroidal field, B_ϕ, that in turn leads to numerous trapped-particle instabilities and enhanced transport of particles and/or energy from the plasma.
- Generally the $q > 1$ constraint forces the utilization of the highest possible toroidal fields, B_ϕ, and, therefore, causes a difficult magnet design task and the storage of considerable quantities of magnetic energy per unit of contained plasma energy (related to the aforementioned β issue).

In a sense, therefore, the RFP approach "differentiates away" the $q > 1$ constraint imposed on tokamaks and in its place requires $(dq/dr) \neq 0$. The positive implications of this new stability criterion are:

- The aspect ratio R/r_p can be chosen solely on the basis of engineering considerations and convenience.
- The β limits predicted for the RFP are at least 10 to 50 times greater than $q > 1$ systems if ideal MHD theories are used. The use of resistive theories reduce this factor from 10-50 to 3-10, which still represents a significant improvement.

- The plasma may be brought to ignition by ohmic heating alone with the poloidal field system, which is also in place to confine the plasma pressure.
- The confinement of high-to-moderate β plasma is achieved primarily by poloidal fields, B_θ, which characteristically decrease with increased distance from the plasma, thereby considerably reducing fields and stresses at the magnets.
- The use of highly sheared fields near the plasma edge for the $dq/dr < 0$ RFP configuration makes possible a "vacuum" (low current) region to be established between the plasma and first wall.

Although implications of these improvements are significant from the reactor viewpoint, they are accompanied by the presently perceived need for a passively conducting first wall. Additionally, the energy that must be expended in establishing and maintaining the near minimum-energy RFP configuration is not known, but if this setup/sustenance energy is significant, operation as an ignition device may be precluded. This issue is addressed in more detail in Sec. II. Lastly, little or no consideration has been given by this study to the physics implications of fueling and ash-removal systems required for a steady-state operation; the RFPR design presented here is based on a long-pulsed (25-30 s) batch-burn operation. The favorable energy balance (recirculating power fraction is 0.17) computed for the batch-burn mode of operation reflects the efficient use of magnetic field energy by the RFP, although technological issues associated with pulsed superconducting magnets and energy transfer/storage systems will require further development and study.

The plasma issues of stability and field reversal, as they impact on the RFPR model are reviewed in Sec. III.A. Stable field profiles within the plasma, an example of which is illustrated in Fig. II-2, are modeled by Bessel functions. These profiles are integrated over the plasma radius to give the time-dependent, point model used in this study. Generally, ideal MHD stable profiles have been found using numerical methods if the following three constraints are imposed:

- net positive toroidal flux: $\int_o^{r_w} B_\phi 2\pi r dr > 0$ (II-1)
- poloidal β limit: $\beta_\theta < 0.5 + \beta_\theta(B_\phi = 0)$ (II-2)

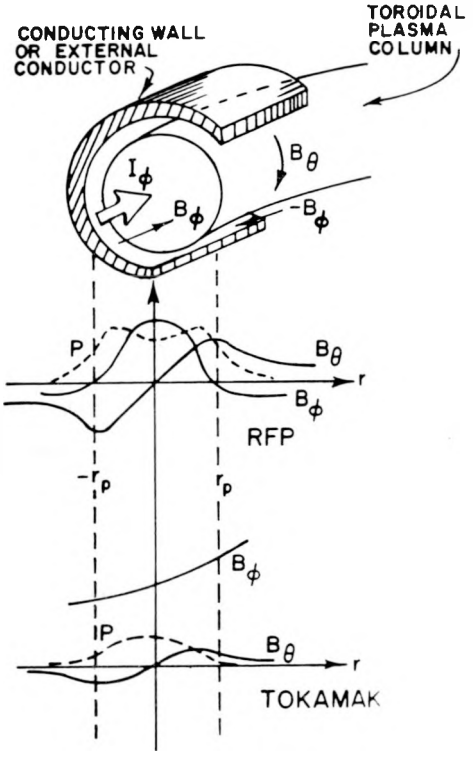

Fig. II-1. Comparison of magnetic and pressure profiles for a dq/dr ≠ 0 stabilized RFP and a q > 1 stabilized tokamak.

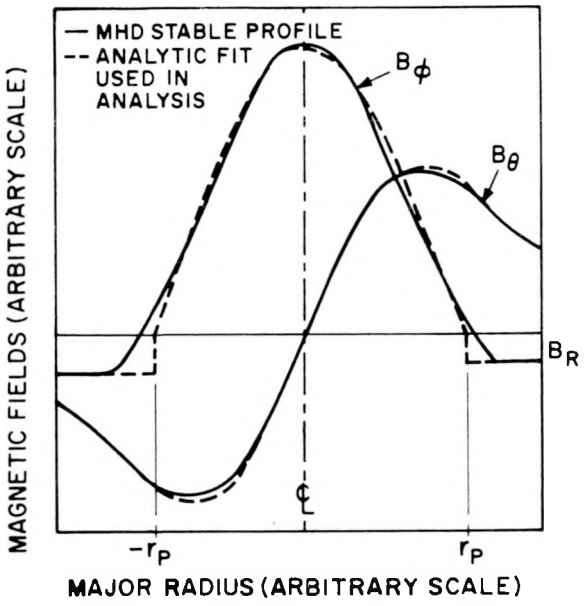

Fig. II-2. Comparison of stable RFP profiles computed numerically with the Bessel function profiles used to generate the point RFPR plasma model.

- Suydam criterion: $r\left[(d\ell n\nu/dr)\right]^2 + \left[dp/dr\right]8\mu_o/B_\phi^2 > 0$, (II-3)

where r_w is the radius of the conducting shell, $\beta_\theta(B_\phi = 0)$ is the local β at the zero point of the toroidal field, p is the plasma pressure, and $d\ell n\nu/dr$ is the magnetic field shear, $\bar{\theta}$, with $\nu = B_\theta/rB_\phi = 1/qR$. The first two conditions are imposed on all RFPR burn conditions, whereas the third condition cannot be imposed directly because of the point model used; the Bessel function profiles (Fig. II-2), however, are generally a very good approximation to profiles that satisfy the Suydam criterion.

The question of toroidal field reversal is also addressed in Sec. III.A, and probably represents the single greatest physics uncertainty for the reactor. The reactor computations assume field reversal occurs spontaneously and is maintained automatically throughout the burn period by an unspecified relaxation process or instability. Self-reversal of the toroidal field is an

experimental fact, but the associated energy loss is not known. The energy loss associated with this sustained self-reversal, therefore, was assumed equal to loss rates measured from large tokamak experiments (energy confinement times equal approximately to 200 Bohm diffusion times). That self-reversal occurs is not in question; the self-reversed pinch state has been observed in many RFP experiments over the last 25 years. A recent theory[1] of relaxed states has lead to a substantial increase in fundamental understanding of this minimum-energy, field-reversed state. Given any arbitrary dissipation mechanism, this theory predicts that a plasma surrounded by a flux conserving shell will relax to a minimum-energy, force-free zero-β state. This minimum-energy state is described by the Bessel function model given in Fig. II-2. Numerical methods have confirmed this behavior for high-β, reversed-field plasmas. The key descriptive parameters in the Taylor theory[1] are the pinch parameter, Θ, and the reversal parameter, F, where

$$\Theta = B_\theta(r_w)/\langle B_\phi \rangle \tag{II-4}$$

$$F = B_\phi(r_w)/\langle B_\phi \rangle \tag{II-5}$$

$$\langle B_\phi \rangle = (2/r_w^2) \int_o^{r_w} B_\phi \, r dr \quad . \tag{II-6}$$

Figure II-3 shows the locus of minimum energy states as described by the F - Θ plot; both the analytic ($\beta = 0$) Taylor state and the numerical high-β states are shown. The desired field-reversed state corresponds to $F < 0$ and $1.2 < \Theta < 1.6$. It is noted that high-β RFP states have been observed for higher Θ values, both experimentally and numerically, but the Taylor theory predicts an ultimate relaxation to the minimum energy states given on Fig. II-3; both the relaxation mechanism and associated time constants for this sustained, self-reversal of toroidal field are not well known at this time. It is noted the minimum-energy tokamak state is described by the Taylor theory as the point where $F = 1$ for which $\Theta \simeq r_p/R$. The penalties incurred for operation near this state, however, have been previously discussed.

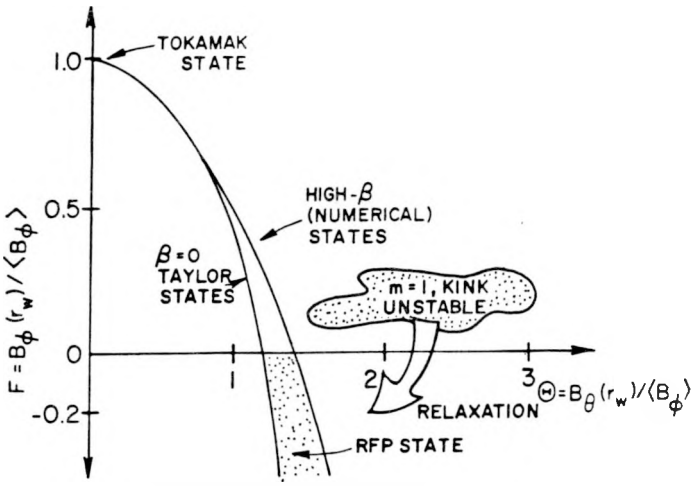

Fig. II-3. Region of stable, minimum-energy states displayed on F - Θ diagram for both low-β (Taylor) and high-β (numerical) RFP plasmas.

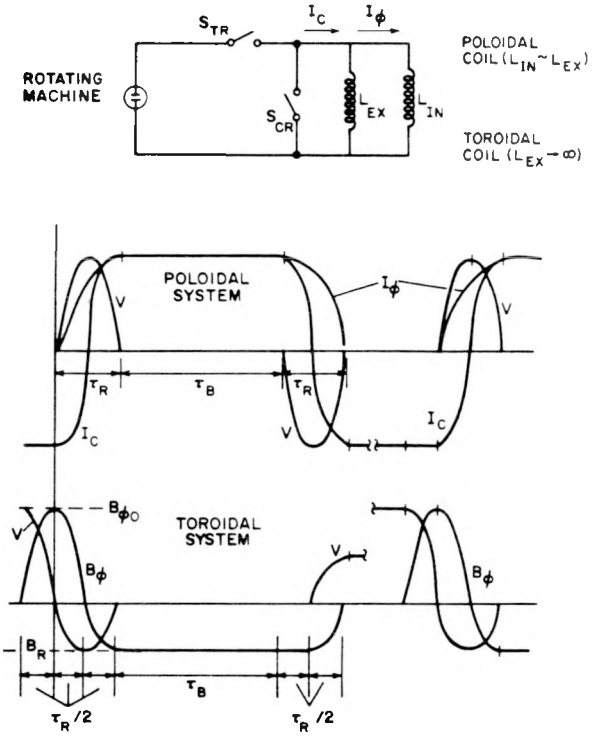

Fig. II-4. Schematic diagram of homopolar-generator driven circuit for TFC and PFC systems. The voltage is 5-6 kV, risetime τ_R = 100 ms, and τ_B ~ 21 s.

In modeling the RFPR, it has been assumed that minimization of energy loss incurred during the field reversal would occur if the burn trajectory followed closely the Taylor F - Θ curve or its high-β counterpart (Fig. II-3). All RFPR burn trajectories adopted for this study closely track this locus of minimum-energy states. As noted previously, however, the relaxation mechanism and energy loss associated with the assumed sustained self-reversal cannot be quantified at this time.

B. Reactor Description

To the casual observer a magnetically confined fusion reactor appears as an intertwined array of coolant ducts penetrating an almost inaccessible toroidal assembly of superconducting magnets. If, however, the toroidal aspect ratio can be made sufficiently large to approximate a linear geometry and allow the use of nearly cylindrical blanket modules, this problem of

accessibility can be considerably reduced. Furthermore, if the primary plasma confinement system can be combined with the major plasma heating scheme, large and complex appendages can be eliminated from the torus, and the reactor system becomes even less complicated. Finally, if the appreciable plasma pressures (30-60 MPa) can be supported primarily by poloidal magnetic fields, which characteristically decrease in strength as the minor radius increases, the low-field superconducting coils can be removed from the vicinity of the blanket/shield without a serious increase in stored magnetic energy; the accessibility problem is thereby further reduced. The RFP is unique in that it combines all three of these requirements; arbitrary aspect ratio, combined heating and confinement system, and low-field magnets. These features, additionally, exist for a scheme whose physics admits the potential for a regenerative, near minimum-energy, high-β plasma state. These physics characteristics directly and favorably impact the reactor design presented herein. Potential problem areas for the RFPR include the presently perceived need for a ~ 20-mm-thick copper first wall for short-time (~ 0.1 s) plasma stabilization and the need for long-pulse (~ 0.1-s risetime, 25-30 s dwell time) magnetic energy transfer and storage.

The time-dependent burn model, plasma and engineering energy balances, and the stability/equilibrium criteria upon which this RFPR design is based are described in Sec. IV. Table II-I gives a summary description of key reactor parameters. The RFPR operation is first described, and a general description of the plant layout follows.

1. Reactor Operation. The reactor startup time, τ_R, is taken as 10% of the energy containment time (~ 1 s for the reactor), which is consistent with diffusion scaling derived from past and present RFP experiments at LASL.[2] One of the goals of future experiments (e.g., ZT-40 at LASL)[2] is the demonstration of diffusive scaling during startup in terms of energy confinement times for increased plasma temperature and device sizes.

The time response of the toroidal and poloidal field system is shown in Fig. II-4. In the simplified electrical circuit L_{IN} specifies the time-varying inductance of the plasma chamber and L_{EX} represents a constant parasitic inductance. Closure of switch S_{TR} at time $-\tau_R/2$ connects the homopolar machine at full speed and voltage to the toroidal field coil. The current in the toroidal field coils rises to a maximum, producing the initial bias field $B_{\phi o}$. Preionization of the plasma occurs at this point in the

TABLE II-I

SUMMARY DESCRIPTION OF RFPR DESIGN PARAMETERS

PARAMETER	VALUE
First-wall radius, r_w(m)	1.5
Major radius, R(m)	12.7
Toroidal plasma current, I_ϕ(MA)	20.0
Toroidal field at the coil, $B_{\phi c}$(T)	2.0
Poloidal field at the coil, $B_{\theta c}$(T)	2.0
Toroidal coil energy, $W_{B\phi}$(GJ)	3.7
Poloidal coil energy, $W_{B\theta}$(GJ)	11.0
Field rise time, τ_R(s)	0.1
Burn time, τ_B(s)	21.6
Cycle time, τ_C(s)	26.6
Average fuel burnup, f_B	0.5
Average plasma density, n($1/m^3$)	$2.0(10)^{20}$
Average plasma temperature, $T_{i,e}$(keV)	15
14.1-MeV neutron current at first wall, I_w(MW/m^2)	2.7
Engineering Q-value, Q_E	5.8
Recirculating power fraction, $\varepsilon = 1/Q_E$	0.17
Average blanket power density, P_{BLK}(MW/m^3)	4.7
Average system power density, P_{SYS}(MW/m^3)	0.9
Total thermal power, P_{TH}(MWt)	3000
Net electrical power, P_E(MWe)	750
Net plant efficiency, $\eta_p = \eta_{TH}(1-\varepsilon)$	0.25

startup cycle, and a toroidal current, I_ϕ, is driven in the plasma. As seen from Fig. II-4, current normally flows in the poloidal field coils, with most of the field energy residing outside the coils when plasma is not present. Reversing this current in the presence of a low-temperature, conducting plasma induces the toroidal current and transfers the field energy inside the poloidal coils. The homopolar motor/generator serves as a transfer element, the poloidal field energy (~ 11 GJ) residing for the most part within the poloidal field coils. This transfer is accomplished by opening switch S_{CR}(crowbar) and using the homopolar motor/generator as a capacitive transfer element (S_{TR} closed). The current I_ϕ rises to a maximum as the B_ϕ field

continues to resonate inductively, ultimately yielding the desired reverse field $-B_{\phi R}$. At time τ_R switch S_{CR} is closed in both magnet coil systems, and the current I_ϕ and reverse field $-B_{\phi R}$ are maintained at a near constant value during the burn. As noted in Sec. II.A, self-reversal is assumed to occur with an appropriate energy-loss mechanism, and the mechanism of the ensuing sustained self-reversal cannot be specified at this time. This simplified discussion of the poloidal field system ignores the vertical field coils required for plasma equilibrium which are included in the final design (see Sec. V.F.).

Upon induction of the 20-MA (5.4 MA/m^2) toroidal current in ~ 0.1 s, the plasma ohmically heats to ignition in ~ 3 s, as shown by the results of the RFPR burn code in Fig. II-5. The plasma subsequently burns for 15 s at 20 keV

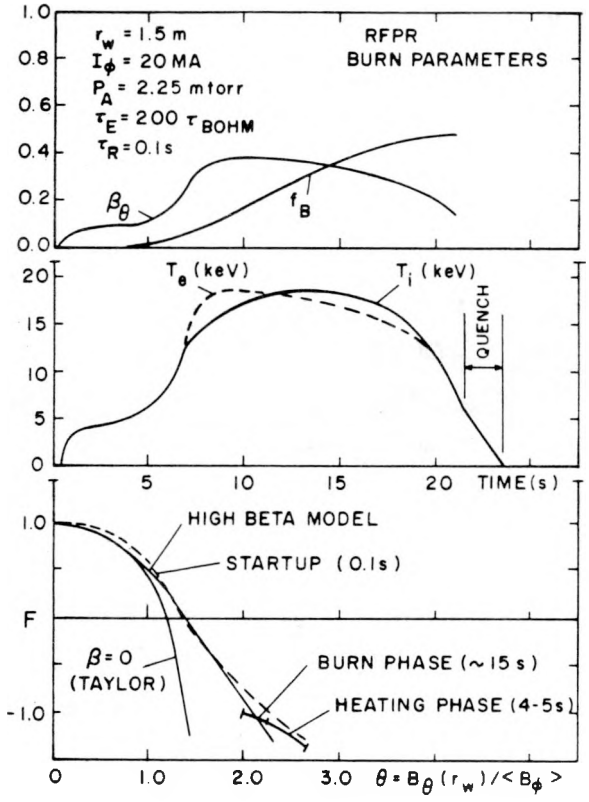

Fig. II-5. RFPR (superconducting coils, air-core system) burn parameters using an energy confinement time $\tau_E = 200\ \tau_{Bohm}$. The burn trajectory is in good agreement with that required by the high-β model for a minimum-energy configuration (Fig. II-3).

to yield a fuel burnup fraction f_B of 0.5. The end of the burn is determined by the ion temperature dropping below 8 keV, as the plasma losses begin to exceed the alpha-particle heating. At this point the plasma is expanded to the wall by opening switch S_{CR} in both poloidal and toroidal coil systems. The poloidal coil current is again reversed by using the homopolar as a transfer element, this action resulting in a negative poloidal coil current between burn pulses. The toroidal field energy left untrapped within the plasma is extracted from the reactor and stored in the homopolar between burn pulses. Magnetic field trapped in the plasma at the termination of the burn is assumed to be thermally dissipated and delivered as heat to the blanket through the first wall. Neutral DT gas is added at this point to promote a controlled plasma quench and dilution of the burn product ash. Continuous pumping by the vacuum system, (Roots blowers or cryopumps) readies the plasma

TABLE II-II

SUMMARY ENERGY BALANCE FOR A 21.6-s BURN AND A 26.6-s CYCLE TIME

PARAMETER	VALUE (MJ/m)
Initial plasma energy	0.05
Final plasma energy	2.5
Radiation energy[a]	28.1
Ohmic heating energy	7.1
Plasma energy loss (conduction)[b]	147.5
Plasma expansion energy	0.7
Eddy current losses in the blanket/shield	1.5
Magnetic-field energy lost at end of burn cycle[c]	21.5
Magnetic-field energy transfer losses[d]	8.1
Fusion neutron energy	792.
Auxiliary energy requirements[e]	14.3

[a] bremsstrahlung and line radiation
[b] based on an energy confinement time equal to 200 Bohm diffusion times
[c] assumed to be thermally dissipated
[d] based on a 95% efficient inductive/capacitive transfer from the homopolar motor/generator (capacitive) to the magnets (inductive) and back
[e] the cryogenic system required for the superconducting magnets consumes 21% of the auxiliary power.

chamber for the next burn pulse during the 5-s dwell period. Table II-II gives a summary energy balance for the burn cycle depicted in Fig. II-5.

Throughout the burn cycle, including the startup and approach to ignition, the energy confinement time was fixed at 200 times the instantaneous Bohm diffusion time, this scaling being deduced[3] from existing tokamak experimental data. Both in magnitude and functional scaling, this loss rate is sufficient to control the plasma β and leads to a stable burn trajectory. Simultaneously, the burn trajectory in F - Θ space, as seen from Fig. II-5, follows closely the predictions of the Taylor minimum-energy model. The physics operating point summarized in Fig. II-5 and Tables II-I and II-II represent the culmination of an extensive parameter search which used as an object function the plant capital and power cost (Sec. IV, Appendix E).

2. Reactor Plant Description. The RFPR is a toroidal system using the reaction products from the interaction of a 50% atomic mixture of deuterium and tritium to produce thermal energy that is converted to electricity by a conventional steam turbine/generator. Table II-I gives a summary description

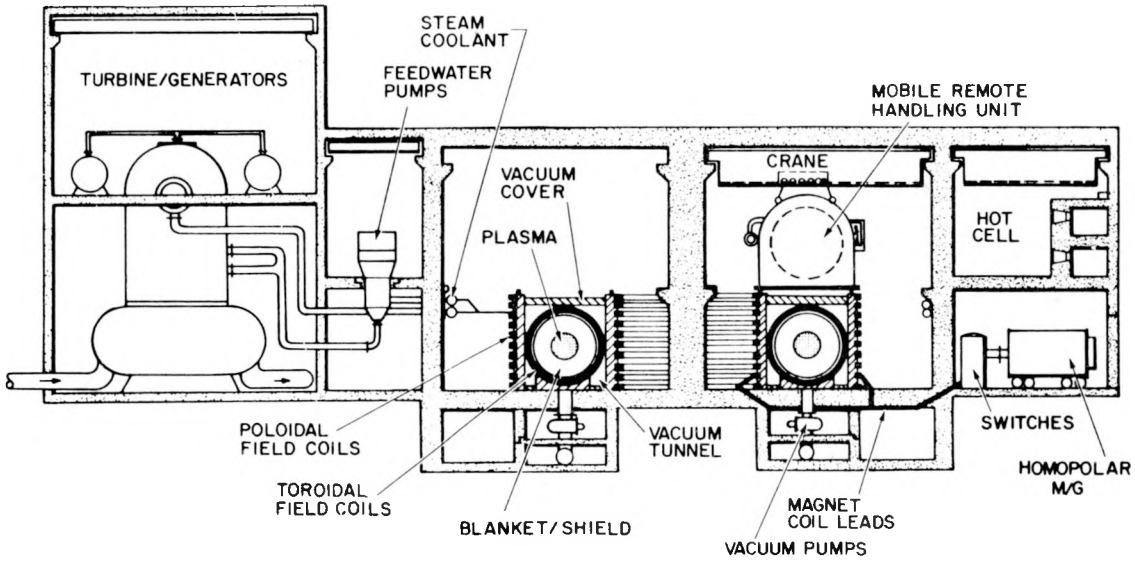

Fig. II-6. Elevation view of the 750 MWe(net) RFPR illustrating the locations of major system components. This drawing depicts one concept for vacuum entry based on a mobile remote handling unit. Other approaches based on vacuum interlocks are described in Sec. V.

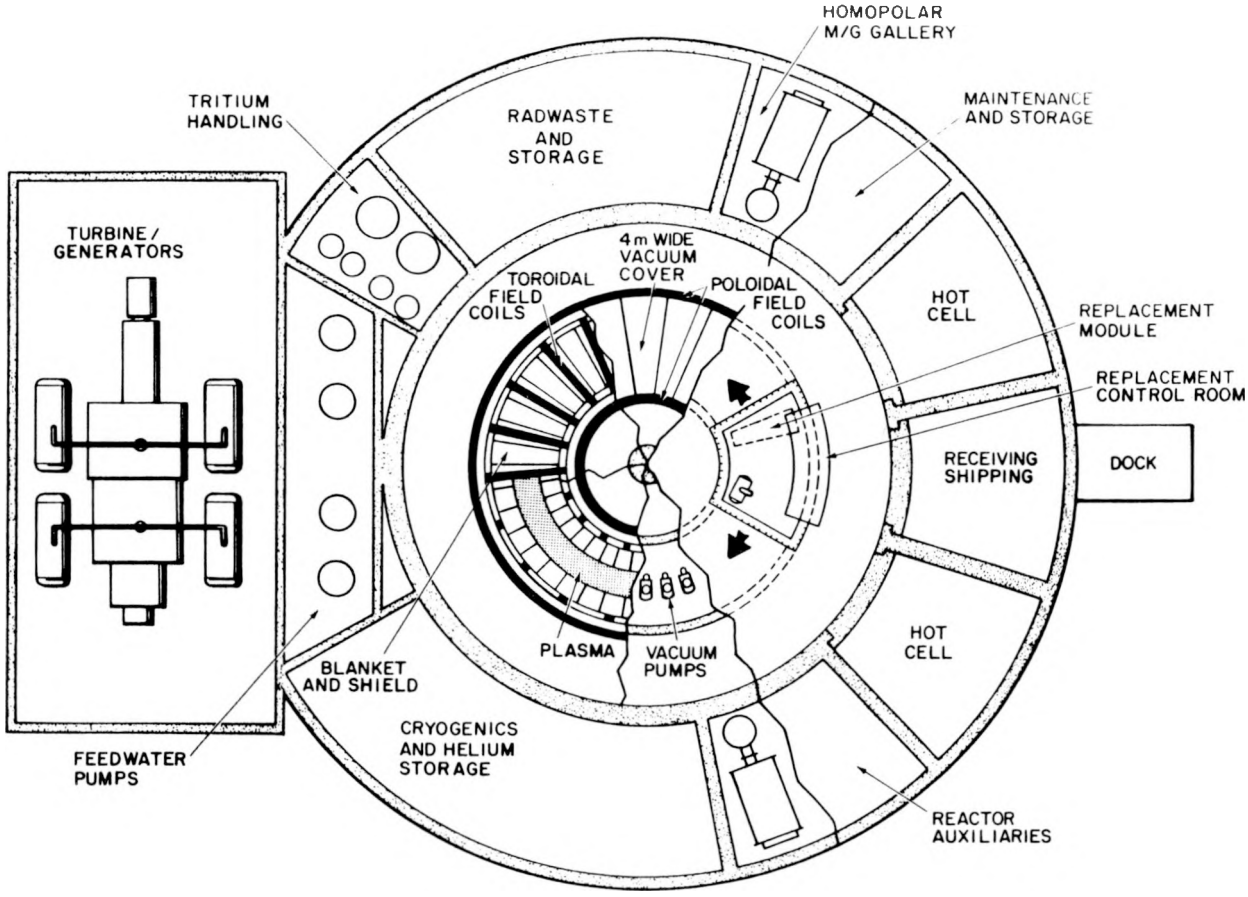

Fig. II-7. Plan view of the 750 MWe(net) RFPR illustrating the locations of major system components.

of the reactor parameters. Figures II-6 and II-7 give a highly schematic elevation and plan view, respectively, of the reactor plant. A more detailed engineering plant layout is given in Sec. V.A. The plasma is formed in a toroidal chamber consisting of 40 cylindrical 2-m-long modules resulting in a torus of 12.7-m major radius. The 2-m modules consist of a 20-mm-thick copper first wall providing plasma stabilization on ~ 0.1-s timescale, a blanket section for moderating neutrons and breeding tritium, feedback coils providing plasma stabilization for times $\gtrsim 0.1$ s, and a borated-water shield for protection of the superconducting magnet coils required for plasma containment. A cross-sectional view of a module shown in Fig. II-8 specifies the dimensions and locations of all major components. Figure II-9 depicts an isometric view of four 2-m-long modules. The 40-module torus rests within a

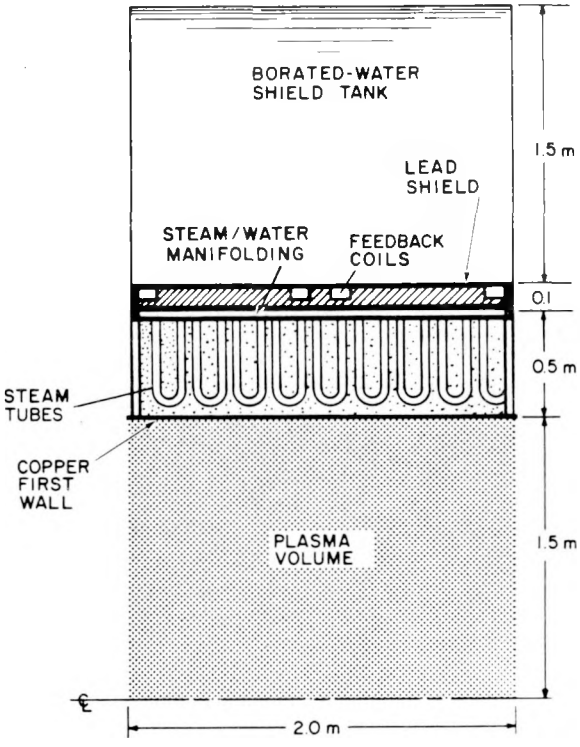

Fig. II-8. Cross section of a 2-m long reactor module for the RFPR including the copper first wall, Li_2O packed bed and associated high-pressure (5.5 Pa) steam tubes, feedback coils and a borated-water shield. The 20-mm-thick first wall would be cooled by a separate water circuit.

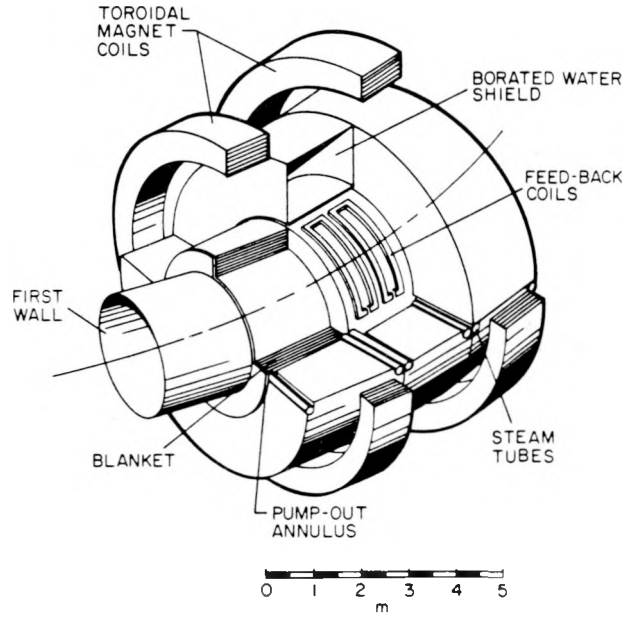

Fig. II-9. Isometric view of four 2-m-long RFPR reactor modules including the copper first wall, Li_2O packed bed and associated high-pressure steam tubes, feedback coils, water shield, and toroidal field coil.

vacuum tunnel (Figs. II-6 and II-7), and the spacing between each module is sufficient to provide the necessary vacuum conductance between the plasma chamber and the vacuum tunnel. The poloidal field coils are not integral with the reactor torus, but instead line the vertical walls of the vacuum tunnel (Figs. II-6 and II-7). The toroidal field coils shown in Fig. II-9 are sufficiently separated to permit removal of blanket modules without coil relocation.

Cost optimization studies (Sec. IV.E, Appendix E) predict a first-wall radius of 1.5 m. Tritium breeding occurs in granular Li_2O, which is packed around an array of steam tubes that remove the thermal energy from the blanket (Fig. II-8). Low-pressure helium (0.1 MPa), with trace amounts of oxygen and separate from the primary cooling system, is circulated through the Li_2O bed

to extract the tritium as an oxide. Superheated steam leaves the blanket and is converted directly to electricity by means of a steam turbine/generator with a computed net thermal efficiency of 28%. Modest changes in the blanket and steam-cycle design can easily increase this efficiency to 30%, which is the canonical value used throughout this study. This direct-cycle system is shown schematically in Fig. II-10. The blanket operates as the steam generator, and is analogous to a coal-fired plant where steam from the boiler tubes is used directly by the turbine. The large thermal capacity of the blanket negates the need for auxiliary thermal storage during the 5-s dwell time between the 21.6-s burn pulses. The thermal cycle experienced by the

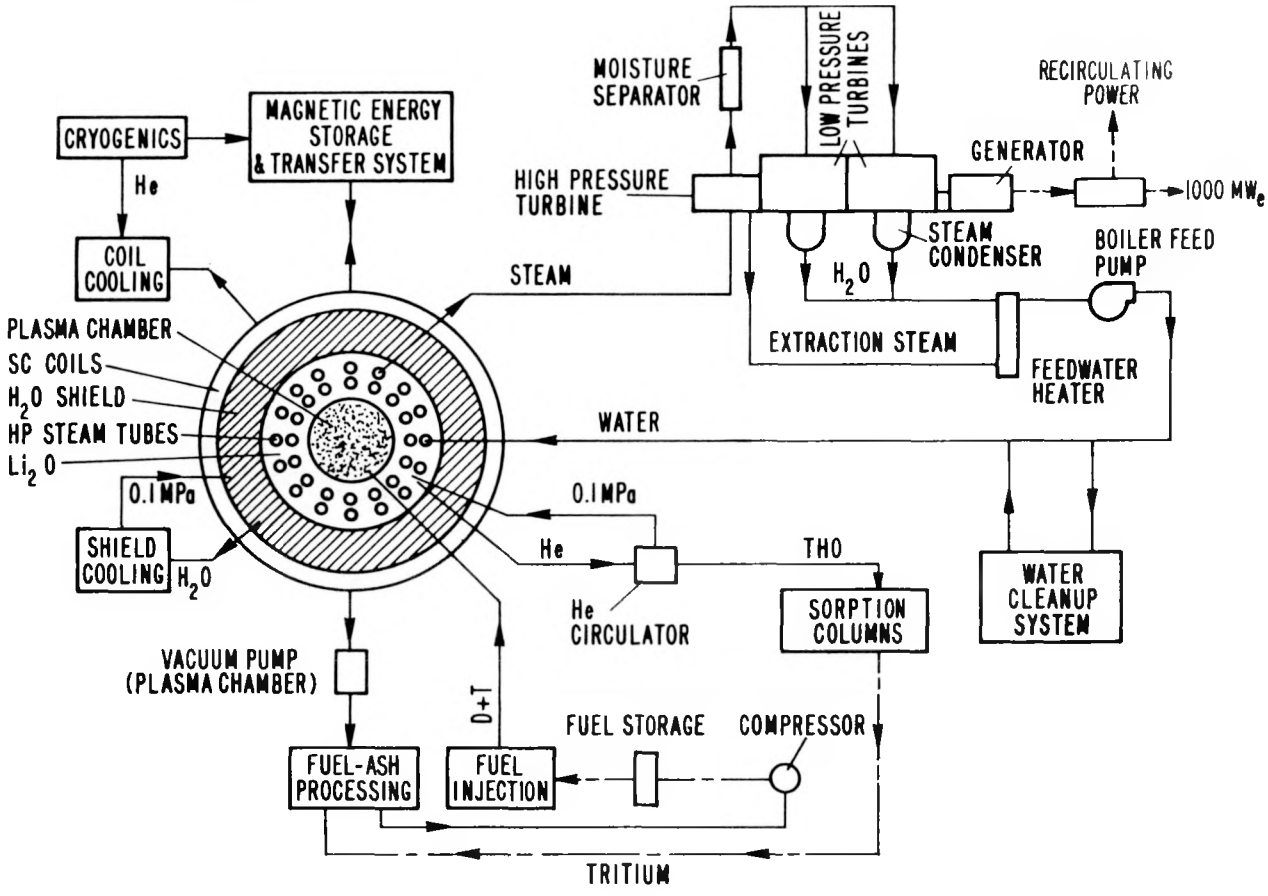

Fig. II-10. Line diagram for all major subsystems needed for the direct-steam-cycle RFPR. Not shown is the separate first-wall coolant loop that would serve primarily re-heat functions. Section V.C gives a more detailed cycle description.

direct-cycle steam system is calculated to be less than 5 K, whereas that for the first wall is 28 K (averaged-material temperature change). Table II-III summarizes key thermohydraulic parameters, including those for the separately-cooled first wall.

This water-cooled blanket was thought to be inherently more economic than previous designs using flowing liquid metals[3-5] or high-pressure helium[6] as coolant. Conservatively limiting the copper first-wall coolant temperature to 530 K, however, required a separate water-coolant loop which could only be used for feedwater heating (not shown in Fig. II-10). Since 38% of the total thermal power is removed by the first-wall coolant circuit, including the plasma/field energy dump and all alpha-particle energy, the overall thermal-conversion efficiency amounted only to 28%, compared to 30% for a typical light-water-cooled fission reactor. Parametric studies show (Sec. V.B.2) that operating the first wall at the blanket coolant temperatures would increase the overall cycle efficiency to 29%. Increasing the blanket/first-wall coolant temperature by 100 K above these reported in Table II-III would result in cycle efficiencies of 35%. Higher temperature

TABLE II-III

SUMMARY OF KEY NEUTRONIC AND THERMOHYDRAULIC PARAMETERS

PARAMETER	VALUE	
Tritium breeding ratio	1.11	
Nuclear heating in the blanket (MW/m)	23.3	
Nuclear heating in the shield (MW/m)	0.26	
Total energy deposited into first wall (MW/m)	14.3	
Total rated power (MWt/MWe)	3000/750	
System pressure (MPa)	5.5	
	First Wall	Blanket
Coolant flow rate (kg/s)[a]	39.6	19.7
Inlet temperature (K)	360	383
Outlet temperature (K)	530	551

[a]per module, 40 modules comprise the reactor.

operation, however, would require a reassessment of the conventional materials used.

3. Reactor Maintenance. An important objective of generating the preliminary plant layout depicted in Figs. II-6 and II-7 is to quantify the procedure by which the reactor can be maintained. Additionally, the preliminary plant layout is useful in determining preliminary estimates of plant capital and power costs, which are summarized in the following section.

As depicted in Figs. II-6 and II-7, the two major coil systems needed to drive the RFPR would be permanently fixed. The poloidal field coil (PFC) system would consist of large, superconducting hoops of NbTi/copper/stainless-steel structure that encircles the inner and outer major radii of the machine. The PFC system would be permanently fixed to structure associated with the walls of the toroidal vacuum tunnel and would not interfer with procedures needed to remove any of the 40, 2-m-long modules. The toroidal field coil (TFC) system consists of twenty low-field (2.0-T) solenoidal coils that encircle alternate reactor modules; each NbTi/Cu/stainless-steel structure would have a 3.6-m radius, be 1.2-m in length, and would have a thickness of 0.5 m. The current distribution in the PFC system would assure that the vertical field component is sufficient to maintain the RFP in toroidal equilibrium. Small, normal-conducting feedback coils would be placed between the blanket and shield (Figs. II-8 and II-9); these slow-pulsed coils (< 10-Hz) are considered part of the reactor module assembly.

A number of vacuum entry schemes have been considered. Figures II-6 and II-7 illustrates one scheme based upon the use of a mobile remote-handling unit and life-support system (i.e., a vacuum "leech") that would be placed over the reactor module(s) to be replaced. The mobile remote-handling unit would be sized to contain only one replacement module. The unit would move in the reactor hall above the vacuum tunnel, would make a local vacuum seal, and, after the unit was evacuated, would disconnect and remove a 4-m-wide by 8-m-long vacuum cover plate. Two toroidal field coils and approximately four reactor modules would be exposed and directly observable by maintenance personnel located in the mobile replacement control room (Fig. II-7). An alternative scheme would simply bring the entire vacuum tunnel to atmospheric pressure (inert gas) and use only a mobile replacement control room to remove modules first to the reactor hall and ultimately to a staging/repair hot cell area. In all likelihood both maintenance schemes might be used; the vacuum

leech would be employed only for spot or unscheduled maintenance, whereas the latter approach would be used during a major reactor overhaul. A third approach would operate both the vacuum tunnel and the reactor hall under vacuum; this vacuum building approach was not given detailed consideration.[7]

A schematic diagram depicting the method by which blanket and shield modules would be removed is given in Fig. II-11. The PFC system is not shown, since it would not interfer with the module replacement operation. As noted previously, the TFC system would be a fixed structure and sufficiently open to permit removal of blanket/shield modules by simple translational and vertical motions. Each 2-m-long by 3.5-m-radius module would be hydraulically and electrically independent of the others. As shown in Fig. II-11, a 50-tonne hemi-cylindrical shield tank would be lifted between the stationary toroidal field coils, after draining approximately 25 tonnes of borated water. Three first-wall/blanket modules, each weighing 60 tonnes, can then be removed

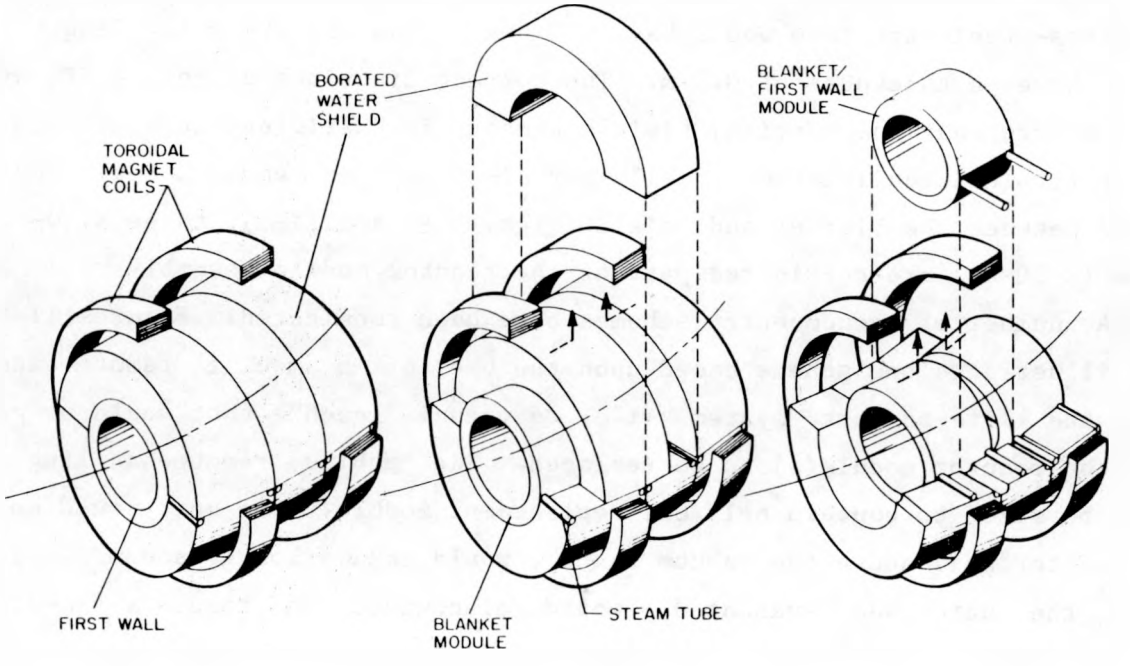

Fig. II-11. Sequence of maintenance operations anticipated for the removal of the RFPR reactor core. Lifting of the hemi-cylindrical, 2-m wide shield segments through the stationary toroidal field coils allows the first wall/blanket segments to be analogously removed. These module assemblies rest within a toroidal vacuum tunnel of 12.7-m major radius which is lined with the poloidal field coil system (not shown).

analogously. The superconducting magnet coils are considered to be highly reliable components that would rarely need maintenance. Provisions are made, however, for unexpected outages in these coils. Replacement of a TFC would require a number of blanket/shield modules to be removed, as described above. In addition a lower hemi-cylindrical shield segment would be extracted from the vacuum tunnel before the TFC (~ 70 tonne) could be lifted from the reactor assembly. All poloidal field coils in principle would be directly accessible in segments for maintenance without disturbing the reactor torus or the vacuum tunnel (Figs. II-6 and II-7).

The level of analysis of the remote handling task has not progressed beyond the level of the foregoing description. Given highly reliable PFC and TFC systems, each of the 40 reactor modules would require approximately 4-6 disconnections: two high pressure (5.5 MPa, ~ 150-mm diameter) steam lines, two high-pressure water lines (5.5-MPa, ~ 100-mm diameter) and electrical connections to the slow feedback coils. The power density in the borated-water shield would be very low (0.9% of the fusion energy, 10 kW/m^3) and probably could be removed by natural convection and conduction to the room-temperature support structure. Mechanical and reliability analyses of this joining/disconnection requirement remain to be performed.

4. Reactor Costing. Appendix C gives the costing procedure, data base and categorical breakdown. A cost summary is given in Table II-IV, and Fig. II-12 graphically displays the cost spectrum. The reactor plant costs comprise approximately 48% of the total direct costs, whereas the costs associated with the reactor *per se* amounts to 25% of the total direct cost. The costs given in Fig. II-12 and Table II-IV have been generated on the basis of a comprehensive system optimization that is described in Sec. IV and Appendix E. The sensitivity of RFPR capital cost to crucial variables, such as the maximum allowable β and the efficiency of magnetic-field energy transfer is also given in Sec. IV.

C. Reactor Assessment

An assessment of both physics and engineering aspects of the RFPR that is commensurate with the level of this study is given in Sec. VI. The observations made in Sec. VI are summarized here. Within the limits of the assumptions needed to develop the plasma model, the RFP configuration promises a high-aspect-ratio system that can operate in a long-pulsed or batch-burn mode while simultaneously maintaining a favorable energy balance, acceptable

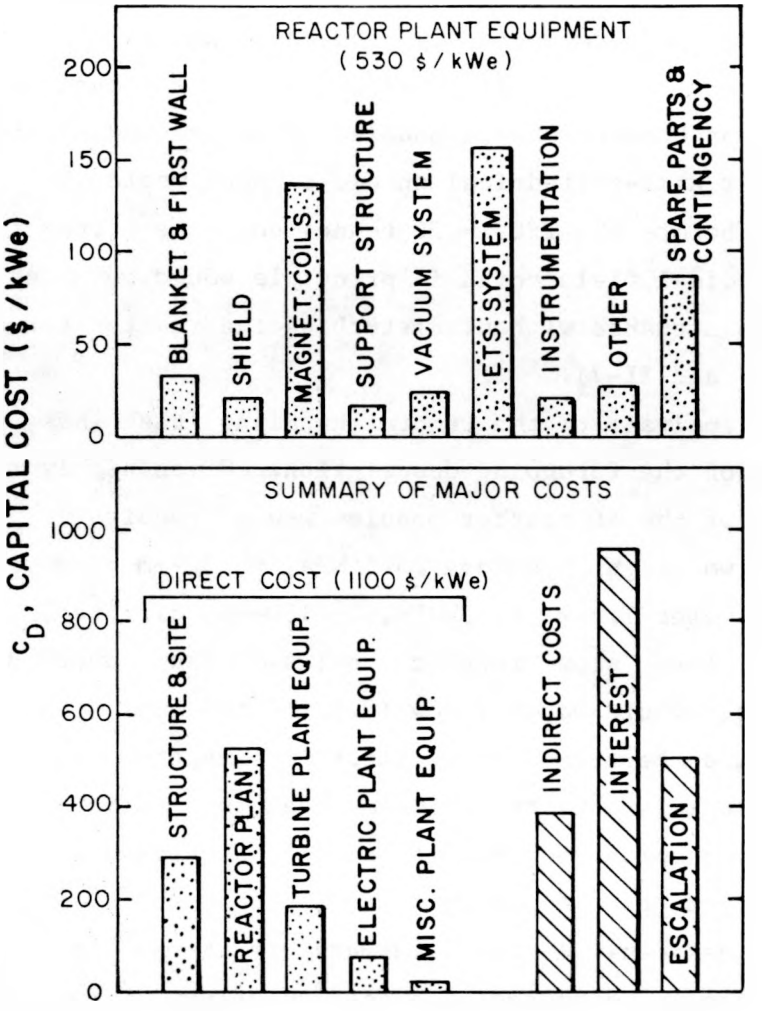

Fig. II-12. Summary of RFPR reactor plant equipment costs and major component costs.

plant costs, and a steady-state power output. Given that a means could be found to operate the RFP plasma in a truly steady state, if a steady state can be shown possible in an ignited high-to-moderate β system, all indicators of system performance would be improved by 10-20%, while the difficult problems of impurity control and refueling would have to be embraced. Adopting a "walk-before-run" philosophy and in view of marginal improvements expected if a steady-state RFP could be operated, it seems prudent to attack the technological problems inherent to long-pulsed operation (i.e., pulsed first wall, pulsed and reversible magnetic energy transfer/storage) rather than generate a series of new and unnecessary physics and technology

TABLE II-IV

SUMMARY OF RFPR CAPITAL COSTS

COST ACCOUNT NUMBER[a]	COST ACCOUNT TITLE	COST (M$)
20.	Land and land rights	2.5
21.	Structures and site facilities	216.5
22.	Reactor plant equipment	397.1
23.	Turbine plant equipment	138.5
24.	Electric plant equipment	56.7
25.	Miscellaneous plant equipment	15.4
26.	Special materials	1.3
90.	Total reactor direct capital costs	828.0
91.	Construction facilities, equipment and services (15%)	124.2
92.	Engineering and construction management services (15%)	124.2
93.	Other costs (taxes, insurance, staff training, plant startup, general/administrative)	41.4
94.	Interest during ten-year construction (10%/y = 64.4%)	719.8
95.	Escalation during ten-year construction (5%/y = 33.8%)	377.8
99.	Total reactor capital cost	2215.4
	Direct investment cost ($/kWe)	1104.0
	Total investment cost ($/kWe)	2953.9
	15% capital return (mills/kWeh)	59.8
	2% operating cost (mills/kWeh)	6.5
	Power cost (mills/kWeh)	66.3

[a]These numbers follow the cost accounting procedure described in Appendix B.

problems/uncertainties associated with a steady-state system. The favorable RFPR energy balance permits this more conservative posture.

1. Physics Assessment. The assessment of RFP physics that has served as a basis for this study is formed as a series of questions; generally, these questions cannot be answered by the present experimental/theoretical data base. In order of perceived importance, these physics questions are:

- What is the cost in terms of confinement time and plasma β of establishing the RFP configuration in a large, reactor-like plasma? Can this cost be minimized by a combination of self-reversal and programmed-reversal (i.e., assisted reversal)?
- What is the cost in terms of confinement time and plasma β of sustaining the minimum-energy RFP state? Is the sustained RFP state sufficiently quiescent to permit an ignited plasma?
- Given that gross MHD modes can be stabilized by a conducting shell and/or slow feedback, what are the β limits established by resistive processes such as tearing modes (magnetic island formation), rippling modes (induced by resistivity gradients), and the pressure-gradient-driven g-mode?
- Virtually no models exist for either the RFPR startup and rundown process. The crucial question for both processes revolves around the quantity and timescale of energy deposition to the first wall. This uncertainty, of course, is not unique to the RFP.
- What influence will alpha-particle heating exert on the stability and lifetime of the RFP field/plasma profiles?
- What is the relationship between the RFP "relaxation" versus "instability" mechanism(s), how is this relationship affected by the startup method, and is the RFP one example of any steady-state moderate-β system that must exhibit a capability for dynamic self-adjustment of plasma/field profiles?

2. Engineering/Technology Assessment. Many of the plant support systems, particularly the vacuum and remote maintenance systems, represent extensions of the state-of-the-art that probably can be made to operate satisfactorily given a sufficient development effort. The question of system reliability, as it impacts on the overall plant capacity factor, availability and cost, cannot be addressed until detailed systems designs have been made. Within the scope of this study and in a decreasing order of perceived importance, the crucial technologies for the RFPR appear to be associated with the design of the first-wall/blanket, pulsed superconducting magnets, and energy transfer/storage systems.

First-wall/blanket: A steam-generating packed-bed blanket appears feasible from the viewpoint of tritium containment, operations/maintenance, structural adequacy and overall steam-cycle requirements. The 20-mm-thick copper first wall, however, must intercept 38% of the total thermal energy, and, because of thermohydraulic and structural limits, the overall cycle

efficiency is conservatively limited to 30%. Radiation effects in the first wall, as measured by transmutation, gas-production, and displacement rates, may induce serious problems. Although the conducting first wall may not represent a structural member or vacuum barrier, the potential for increased electrical resistivity and loss of self-integrity may require frequent replacement and/or repair. Furthermore, the use of two separate coolant loops is not the most cost-effective approach, and future studies should focus on a first-wall/blanket coolant scheme that is more integrated than the one presented here.

Pulsed superconducting magnets: The maximum field for both the TFC and PFC is ~ 2.0 T and represents state-of-the-art for NbTi superconductor. The maximum flux change of 20-40 T/s represents state-of-the-art for small samples; detailed designs for a 20-T/s, 7-T coil has been made.[8] The coupling of the TFC and PFC circuits may represent a potential problem, although proper but more complex windings in the TFC can greatly reduce eddy-current losses when the PFC is energized on a ~ 0.1-s timescale.

Magnetic energy transfer and storage: Homopolar motor/generators have been proposed to energize and recover energy from the PFC and TFC systems. On the basis of energy residence time, the coils can be considered the storage system, and the homopolar motor/generators serve essentially as pulsed (0.1-s) transfer elements. A detailed conceptual engineering design has been made of a 1-GJ homopolar machine operating with a 0.03-s transfer time.[9] This machine has a 13-m active rotor length, 2-m diameter rotors, and rotates at 277 m/s. The 8-T magnetic fields for this machine would be produced by Nb_3Sn magnets. The desired 95% machine efficiency is beyond the state-of-the-art, particularly insofar as the surface speed and brush current density is concerned. A modest program should resolve most of these problems, particularly for the less stringent RFPR requirements; the RFPR requires 0.1-s transfer times and the transfer efficiency can fall below 90% without a serious cost penalty (Sec. IV.F.4).

Conventional switching is considered for use in the RFPR with each closing switch consisting of a parallel-connected ignitron and a mechanical bypass switch, and each opening switch constructed of a vacuum interrupter placed in parallel with a mechanical bypass switch.[10] The reliable operation of ~ 2700 switches, each carrying 25 kA, is of primary concern and provides an impetus to develop larger switching elements (> 100 kA) with high energy

transfer efficiency and reliability as design criteria. The technology needed for these switches appears straightforward, although a development effort is required. Solid-state switches offer a convenient and reliable solution to the RFPR switching needs, although economic considerations may point instead to the development of efficient mechanical breakers.

REFERENCES

1. J. B. Taylor, "Relaxation of Toroidal Discharges," Third Topical Conference on Pulsed High Beta Plasmas," Culham, United Kingdom, 1975, p. 59.

2. D. A. Baker and J. N. DiMarco, "The LASL Reversed-Field Pinch Program," Los Alamos Scientific Laboratory report LA-6177-MS (1975).

3. R. L. Hagenson and R. A. Krakowski, "A Cost-Constrained Design Point for the Reversed-Field Pinch Reactor," Am. Nuclear Soc. Third Topical Meeting on the Tech. of Cont. Nucl. Fusion, Santa Fe, NM, 1978, Vol. 1, pp. 90-100.

4. R. L. Hagenson, R. A. Krakowski, and K. I. Thomassen, "A Toroidal Fusion Reactor Based on the Reversed-Field Pinch (RFP)," in Fusion Reactor Design Concepts (IAEA Workshop on Fusion Reactor Design, Madison, Wisconsin, 1977), IAEA, Vienna (1978), pp. 337-355.

5. R. L. Hagenson, "A Toroidal Fusion Reactor Design Based on the Reversed-Field Pinch," Ph.D. Dissertation, Iowa State University, 1978, (also Los Alamos Scientific Laboratory report LA-7399-T (1978)).

6. R. Hancox and W. R. Spears, "Reversed Field Pinch Reactor Study, II. Choice of Parameters," UKAEA report CLM-R 172 (1977).

7. R. W. Werner, "The Cassette Blanket and Vacuum Building: Key Elements in Fusion Reactor Maintenance," Seventh Symposium on Engineering Problems of Fusion Research, Knoxville, Tennessee, 1977, pp. 1445-1452.

8. D. Weldon and J. Wollen, personal communication, Los Alamos Scientific Laboratory (1978).

9. K. I. Thomassen (ed.), "Conceptual Engineering Design of a One-GJ Fast-Discharging Homopolar Machine for the Theta-Pinch Reactor," Electric Power Research Institute report EPRI-ER-246, Project 469 (1976).

10. Staff of the CTR Division (Compiled by H. Dreicer), "The Reversed Field Pinch Concept and a Preliminary Conceptual Design for a Proof-of-Principle Experiment," Los Alamos Scientific Laboratory report LA-7527-MS (1978).

III. PHYSICS BACKGROUND

The relationship between the Reversed-Field Pinch (RFP) and its first cousin, the tokamak, has been qualitatively discussed in the Executive Summary, Sec. II.A. Both axisymmetric systems confine plasma with poloidal magnetic fields created with toroidal currents induced in the plasma, and both confinement schemes avoid the gross m = 1 (kink) instability by enforcing specific requirements on the safety parameter, $q(r) = (r/R)(B_\phi/B_\theta)$, where r is a (minor) radial point in the plasma, R is the major toroidal radius, B_ϕ is the local toroidal magnetic field, and B_θ is the local poloidal field. The tokamak requires that $q(r_p) > 1$-2 for most present day experiments. The RFP approach, on the other hand, attempts to "differentiate away" the $q(r_p) > 1$ Kruskal-Shafranov limit by requiring instead that $dq/dr < 0$ (more specifically, $dq/dr \neq 0$). The reactor implications of these two different constraints have been addressed in Sec. II.A. This section first quantifies these differences by means of a simple analytic argument. The theoretical and experimental basis used for projecting the RFP into a reactor embodiment is then reviewed.

A. RFP/Tokamak Comparison

Figure III-1 depicts idealized toroidal, B_ϕ, and poloidal, B_θ, field profiles for the RFP and the tokamak. Shown also is the local shear $\bar{\theta} = -d\ell nq/dr$, where q is the safety factor. Defining β_θ as the ratio of plasma pressure, 2nkT, to poloidal field pressure at the plasma radius, $B_\theta^2(r_p)/2\mu_o$, the total plasma beta is given by

$$\beta = \beta_\theta/(1 + q^2(R/r_p)^2) \quad . \tag{III-1}$$

Since the Kruskal-Shafranov limit imposes $q > 1$ for tokamaks, and since aspect ratios, R/r_p, much below 3-4 become impractical, $\beta << \beta_\theta$ for the tokamak. The RFP, on the other hand, is limited by $dq/dr < 0$, and the safety factor can be very small or even negative, thereby decoupling the total beta from direct considerations of q or R/r_p; typically $\beta \simeq \beta_\theta$ for the RFP. In order to examine explicitly the dependence of β_θ on RFP parameters vis a vis the $dq/dr < 0$ constraint, a specific field profile must be used. The Bessel function model described in Appendix A is employed here to give the following expression for β_θ.

$$\beta_\theta = 1 - (\alpha r_p/2x^2)^2 \left[B_{\phi_o}/B_\theta(r_p)\right]^2 \quad , \tag{III-2}$$

where $\alpha r_p = 2.405$ is the zero of the modified Bessel function of the first kind, x is the ratio of plasma radius, r_p, to conducting shell radius, r_w, and B_{ϕ_o} is the initial toroidal bias field. Since $x \sim 0.8 - 0.9$, and B_{ϕ_o} generally is considerably less than the poloidal field at the plasma surface, $B_\theta(r_p)$, total betas for the RFP can exceed appreciably those for tokamaks.

The potential for higher toroidal current densities, j_ϕ, in the RFP also exists. Expressing the safety factor in terms of j_ϕ results in

$$j_\phi = (2/\mu_o)(B_\phi/qR) \quad . \tag{III-3}$$

For $q > 1$ and reasonable values of B_ϕ and R, the toroidal current density in a tokamak generally is insufficient to provide ohmic-heating power densities that are sufficient to induce ignition. Since the RFP has no such restriction on q, ohmic heating to ignition is possible. The ohmic heating in an RFP can be typically 10-100 times greater than in a tokamak. Pressure balance for both an RFP and a tokamak requires $\beta_\theta B_\theta^2 = 2\mu_o(2nkT) \simeq 3\ T^2$ for plasma densities yielding reasonable 14.1-MeV neutron wall loadings (2-3 MW/m^2) and plasma temperatures of 10-20 keV. For the q-stabilized tokamak $B_\theta = (r_p/R)\ (B_\phi/q)$; requiring $q \gtrsim 1$ gives $B_\theta = 1.2$ T for a typical B_ϕ at the plasma surface of 5 T and an aspect ratio $R/r_p \sim 4$. Only by increasing the toroidal field, B_ϕ, or decreasing the aspect ratio, both presenting engineering and technological problems, can B_θ and, hence, I_ϕ, be raised. From pressure balance $\beta_\theta \simeq 2$ is needed, which is typical of present experiments. The RFP, on the other hand, operates with $\beta_\theta \sim 0.3$, increasing B_θ, I_ϕ and j_ϕ by a factor of ~ 3. In this case no limit is placed on B_θ, as was necessary for the tokamak. The poloidal current density, j_θ, in the RFP is comparable to j_ϕ, and the total ohmic-heating power density can easily be 20 times that allowed in the tokamak. The RFP approach, however, does not admit the significant benefits of high-to-moderate beta, arbitrary aspect ratio, and access to the full potential offered by efficient and high

ohmic-heating power densities without imposing problems and uncertainties. This latter aspect is addressed in the following sections.

B. RFP Theory

The Reversed-Field Pinch[1-3] is a toroidal axisymmetric device in which the primary containment field B_θ is generated by the toroidal current I_ϕ flowing in the plasma. Figure III-2 compares the field profiles for the RFP with those for other toroidal axisymmetric systems. The RFP can support a toroidal current density that is of sufficient strength to heat ohmically a DT plasma to ignition. Grossly unstable magnetohydrodynamic modes with wavelengths longer than the minor radius r_w are eliminated by a conducting shell and/or external conductors. Localized modes are suppressed by the

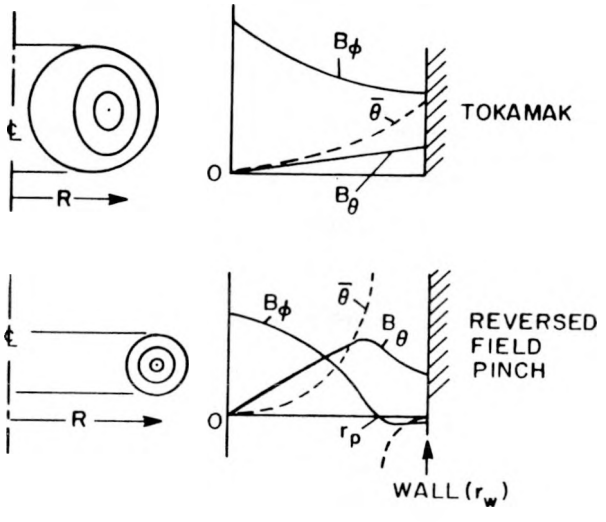

Fig. III-1. Field profiles for a tokamak and Reversed-Field Pinch (RFP) showing the variation of toroidal B_ϕ and poloidal B_θ fields. The shear of the magnetic fields, θ, is considerably larger in the RFP.

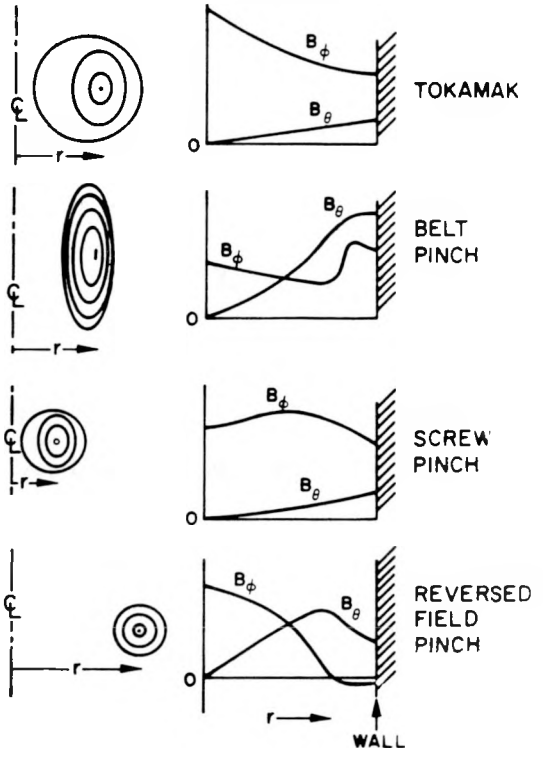

Fig. III-2. A comparison of field profiles for various toroidal axisymmetric fusion concepts.

strongly sheared magnetic fields in the outer plasma region which satisfy the Mercier criteria[4] (toroidal analog of the Suydam criteria[5]), allowing poloidal betas up to 0.58 as predicted by ideal MHD theory.[1]

Many toroidal pinch systems confine the plasma using an azimuthal or poloidal field B_θ and a toroidal field B_ϕ, as is shown in Fig. III-2, with most approaches achieving MHD stability by operating below the Kruskal-Shafranov current limit.[6,7] This current limit implies unstable modes would require magnetic field wavelengths longer than the major circumference, $2\pi R$, of the torus. Maintaining $q = (r_p/R)(B_\phi/B_\theta) > 1$ requires small values of B_θ/B_ϕ, leading to a low total beta (B_θ confines the plasma pressure) and geometrically "tight" toroidal systems (small R/r_w). Low aspect ratios in turn lead to inhomogeneous toroidal fields which produce many trapped particle instabilities and enhances the particle and energy diffusion rates.[8-11] Tokamak designs for increasing the total plasma beta are based upon noncircular plasma concepts[10,11] and the flux conserving schemes,[11] which may allow $\beta = 0.03$-0.10. Belt pinches[12,13] (Fig. III-2) and high-beta tokamaks[13,14] also seek to increase β values. The screw pinch[13-15] (Fig. III-2) is theoretically stable for q values as low as 0.7-1.5 with a total beta as high as 0.25 possible; stability for the screw pinch is provided by pressureless plasma currents (i.e., current flowing parallel to magnetic flux lines) near the wall. Unlike these q-stabilized devices the RFP can operate with an aspect ratio that is independent of MHD stability limits and, therefore, can be chosen solely for engineering and economic reasons. The Kruskal-Shafranov limit does not apply to the RFP, and large ohmic-heating currents are possible. The restrictions of small aspect ratio and small values of B_θ/B_ϕ, therefore, are removed. Theoretical values of total β equal to ~ 0.40 are predicted.[1] A considerable volume of theoretical analyses has been generated for the RFP over the last decade, which indicate that this beta limit may be overly optimistic. This section summarizes this literature, which generally point to beta limits in the range 0.1-0.3. It is noted that since most RFP experiments to date have been conducted on very small devices, much of the reactor prognosis must rest on this theoretical base.

1. Plasma Stability. The pinch discharge is one of the earliest fusion concepts to be investigated[16-23] and initially consisted of a resistively heated current-carrying conductor radially compressed by the azimuthal field generated by the axial current. The simple pinch, however, is unstable to

both sausage- and kink-type instabilities. In 1954 Kruskal and Schwarzschild[18] analyzed the stability of a cylindrical sharp-boundary plasma carrying a toroidal current, I_ϕ, in an infinitely thin surface layer and found the system to be unstable for the m = 0 (sausage instability) and m = 1 (kink instability) MHD modes. Tayler[19] showed in 1957 that all mode numbers were in fact unstable for this simple pinch, and the growth rates for all instabilities were of the same magnitude as the sound speed in the plasma.

The sharp-boundary model was then extended to include an axial field, B_ϕ, both inside and outside of the plasma, and a conducting shell encircling the pinch.[20-23] The m = 0 and m = 2 modes were stabilized using only an axial field, whereas a conducting shell was needed to stabilize the m = 1 mode. The sharp-boundary stability criteria is given approximately by

$$x > \frac{1}{5(1-\beta_\theta)} \quad , \quad \beta_\theta < 0.5 \quad , \tag{III-4}$$

where β_θ is the plasma pressure inside the pinch divided by the poloidal field pressure at the surface of the pinch, and x is the plasma radius r_p divided by the stabilizing first-wall radius r_w.

Sharp-boundary pinches are not encountered experimentally, and a model that allowed the current to permeate the plasma region was needed. A necessary, although not sufficient, condition for a diffuse linear pinch was developed in 1958 and is referred to as the Suydam criterion.[5]

$$r\left(d\ell n\nu/dr\right)^2 + (dp/dr)8\mu_o/B_\phi^2 > 0 \quad , \tag{III-5}$$

where $\nu = B_\theta/rB_\phi = 1/Rq(r)$ represents the number of rotations of a field line per unit length along the toroidal coordinate. The local plasma pressure is p and $\mu_o = 4\pi(10)^{-7}$ h/m. The quantity $d\ell n\nu/dr$ is the rate of change in pitch angle with radial distance and is called the "shear" of the field. As seen in Eq. (III-5), high shear is desirable for stability. Sample pressure and field profiles which satisfy this criteria must be determined numerically and are shown in Fig. III-3. The field shear near the plasma center vanishes, and Eq. (III-5) is satisfied by a positive or nearly zero pressure gradient dp/dr.

The pressure gradient is negative near the outer edge of the discharge, as the pressure is reduced to near zero at the wall, and this destabilizing effect must be cancelled by highly sheared fields in the outer regions; the region of high shear is generated by the reversed toroidal field (Fig. III-3).

Using ideal MHD theory, necessary and sufficient conditions for stability were found by Newcomb[24] in 1960 for a linear diffuse pinch. This theory predicts stability for all m and k values if and only if the pinch is stable for $m = 0$, $k \to 0$ and $m = 1$, $-\infty < k < \infty$. The application of the Newcomb criteria requires the solution of the Euler-Lagrange equation[17] in which the displacement $\xi(r)$ is found which minimizes the system potential energy. The stability criteria predicts that any displacement from the equilibrium configuration must yield an increase in potential energy. This numerical calculation, as well as other methods developed in 1960 by Furth and Suydam[25-26] for investigating stability, generally require computer solutions. More recent (1971-1974) calculations [27-29] yield the stable RFP profiles shown in Fig. III-3. The important conditions for stability are positive total axial flux, $\beta_\theta \leq 0.5 + \beta(B_\phi = 0)$ and a profile that satisfies the Suydam criterion [(Eq. (III-5)]. The first two conditions are directly applicable to reactor calculations and are monitored in this study by the zero-dimensional models. Application of the Suydam condition would require a one-dimensional MHD code, however, and the precise shape of a stable plasma profile must be included when a reactor energy balance is being considered. The RFPR point plasma model is based on an assumed stable profile, and the Suydam criterion is satisfied *de facto*.

Robinson[29] noted in 1971 that a stable configuration also requires that no minimum in the pitch $1/\nu = rB_\phi/B_\theta$ *versus* radius be present[29] (i.e., $dq/dr \neq 0$). The pitch $1/\nu = Rq$ must fall monotonically from $r = 0$ to the conducting wall. In the vacuum region B_ϕ is a constant, B_θ is proportional to $1/r$ and the resultant pitch varies as r^2. If both B_ϕ and B_θ are positive, the pitch would increase in the vacuum region, and a pitch minimum will occur. Reversing the direction of the B_ϕ field in the vacuum region allows the pitch to decrease continually outside the plasma. A current-free vacuum region, therefore, is allowed and required between the plasma and the wall for the RFP.

The calculation of MHD stable equilibria has been extended to toroidal coordinates[30,31] in 1972 using numerical techniques, where the stability of localized modes is determined by the Mercier[4] criterion (toroidal analog of the Suydam criterion). These numerical studies showed that the toroidal RFP configuration produces enhanced stability for aspect ratios in the range 1-5 when compared to a linear device. For aspect ratios approaching unity, however, extreme toroidal effects induce instabilities. Stable equilibria where found to exist when $\beta_\theta \lesssim 0.6$ for aspect ratios greater than ~ 2. Aspect ratios greater than ~ 5 allow the use of linear pinch stability theory (i.e., Suydam criterion) with substantially the same results.

A large body of additional information has been added to the theory of pinches since 1970. The predictions of microinstability and nonideal (resistive) MHD theory has been summarized.[1-3] The beta limit in the RFPR may depend on resistive instabilities that allow the plasma to attain a state of lower magnetic energy by changing the topology of the flux surfaces. The resistive tearing mode, rippling mode, and g-mode (interchange mode) have been theoretically identified.[3] The resistive tearing mode can form magnetic islands and is considered the most dangerous. The rippling mode is driven by the resistivity gradient, and the g-mode is driven by a pressure gradient; both modes are localized on a flux surface and may cause enhanced transport. Numerical simulations of these modes depend on the magnetic Reynolds number, S, (also called the Lundquist number), which is the resistive diffusion time divided by the sound transit time in the plasma. As S increases these modes become more localized, and the grid spacing in the numerical code is forced to decrease until the number of mesh points and computer time becomes prohibitive. For these localized or high-S modes, important stabilizing effects, such as finite-Larmor-radius stabilization, have not been included in these numerical computations. Present day computers are limited to $S \lesssim 10^5$, while reactor plasmas are expected to have $S \sim 10^{10}$; reactor-relevant resistive calculations, therefore are not possible, although some insight may be gained from calculations[3] performed for experimental ($S \sim 10^5$) conditions.

Field and pressure profiles have been found numerically that are stable to resistive tearing modes for poloidal betas in the range 0.25-0.30. The resistive rippling mode is stabilized by thermal conduction above 40-eV temperatures and is not considered a problem for RFP reactors. The resistive g-mode is found to be unstable by all numerical simulations. This mode,

however, becomes more localized as S is increased, and its effect on transport should correspondingly decrease. These results are encouraging and suggestive of an operating poloidal beta of ~ 0.3, although based on present knowledge, this conclusion must be considered speculative. This limiting value of poloidal beta is approximately that used for the RFPR calculations. Because of these uncertainties in the RFP beta limits, the dependence of reactor cost on β_θ has been investigated parametrically in Sec. IV.F.4.

2. Self-Reversal Processes. The self-reversal of the outer toroidal field observed in RFP experiments (Sec. III.C) has been predicted theoretically.[32-35] For a slight energy dissipation, the pinch will naturally relax to a state of minimum energy. Since the reactor plasma must be controlled for ~ 10^8 MHD times, it is reassuring that the RFP, like the tokamak, operates near a minimum-energy state. In describing the "coordinates" of this minimum-energy state, the pinch parameter, Θ, and the reversal parameter, F, are defined

$$\Theta = B_\theta(r_w)/\langle B_\phi \rangle \tag{III-6}$$

$$F = B_\phi(r_w)/\langle B_\phi \rangle \tag{III-7}$$

$$\langle B_\phi \rangle = (2/r_w^2) \int_o^{r_w} B_\phi r dr \quad . \tag{III-8}$$

Figure III-4 gives the locus of points in F - Θ space where the low-beta, minimum-energy states would be found. For the tokamak the minimum-energy Taylor state occurs at $\Theta \simeq 0$ and F = 1.0. For $\Theta \gtrsim 1.2$ the minimum-energy Taylor state for the RFP inside a perfectly conducting wall of radius r_w has a force-free region with a reversed field. It is noted that by fast programming of the toroidal currents, the pinch parameter, Θ, can be pushed into the unstable F > 0 region and through gross or local instabilities the system should reverse to a minimum-energy RFP state. The magnetic fields B_θ and B_ϕ for the RFP Taylor state are described by the Bessel functions $J_1(\alpha r)$ and $J_0(\alpha r)$, respectively, for this $\beta_\theta = 0$ theory. The reactor magnetic field profiles are also modeled by Bessel functions which allow for $\beta_\theta > 0$ as described in Sec. IV.C.1 and Appendix A. Using classical diffusion

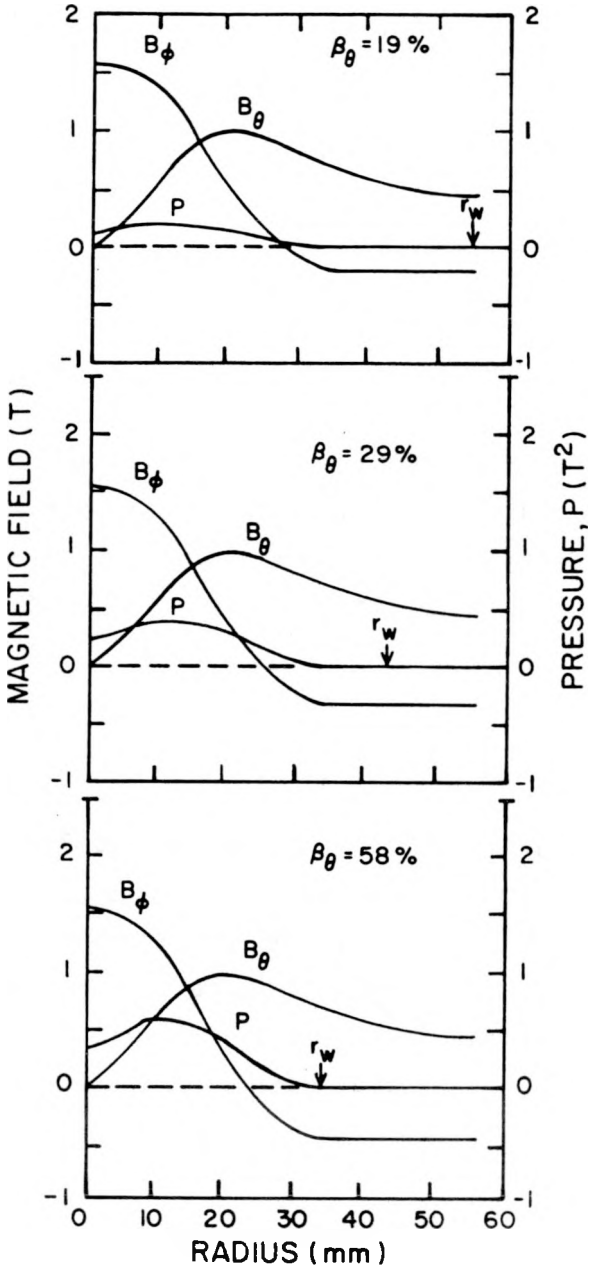

Fig. III-3 Sample MHD stable pressure and field profiles for a a linear pinch showing the effect of increasing the pressure on the location of the conducting wall for stability.[1]

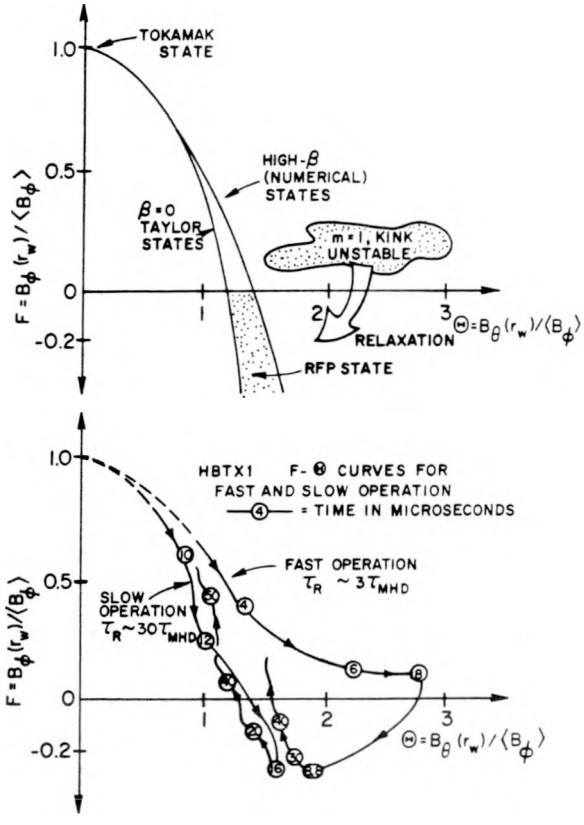

Fig. III-4. Trajectories of stable, minimum-energy RFP states displayed on the F - Θ Taylor diagram for both theoretical[32-34] and experimental [36] configurations.

coefficients, numerical calculations[37] have shown the existence of high-beta, Suydam-stable states (β_θ = 0.3-0.4) at Θ = 1.5-2.0 and F = -0.5 to -1.0. These conditions are designated as the High-Beta Model[36] on Fig. III-4 and are

used to specify the magnetic field and pressure profiles during the reactor burn (Appendix A).

From experimental, theoretical, and reactor viewpoints perhaps the least understood aspect of the RFP is the formation, relaxation, and sustenance of the reversed-field state. Although the theoretical understanding given to the RFP by Taylor's universal explanation[32-34] has been significant, the unresolved relaxation mechanism(s) and associated energy loss and stability presents the single largest uncertainty for this RFPR design. It has been known experimentally for twenty years[38] that a toroidal pinch located inside a flux-conserving shell can spontaneously produce reversed toroidal field in the region between the plasma and the conducting wall. Numerous, relatively small RFP experiments have since shown that field reversal can occur either spontaneously or artificially (i.e., field programming). Ideal MHD theories, which conserve the integral $\oint(\vec{V}\times\vec{B})\cdot\vec{B}d\vec{V}$ on every flux tube,[39] of course, cannot predict the dissipative process required to describe the field reversal. The difficult and developing nature of resistive MHD theories is one reason for the poor theoretical understanding of the RFP, although much progress has been made in the past few years. By assuming a small amount of plasma resistivity and nonconservation of the flux integral, Taylor was able to demonstrate[32-34] that a force-free, Bessel-function configuration describes a minimum-energy RFP state. This theory also shows that for $\Theta \gtrsim 1.6$ the lowest energy state is helical, whereas in a spherical geometry the minimum-energy state becomes the Spheromak configuration.[40] The precise mechanism by which the RFP state is attained depends strongly on the initial setup and specific experimental conditions, but the final RFP state generally appears to be independent of these initial conditions.[41] This behavior is demonstrated by the HBTXI results shown in Fig. III-4. Driving the RFP rapidly pushes the pinch into the kink-unstable region of F - Θ space, and the plasma rapidly relaxes to the RFP state. Slower startup procedures avoids this energy-intensive method of field reversal.

Relaxation to the RFP state may occur by a large amplitude m = 1 (kink) MHD instability,[42] which produces modes that are paramagnetic and can lead to field reversal within a flux-conserving shell; this process has been observed in many small experiments. Field-reversal by such gross instabilities, however, can be quite violent. Mechanisms that rely on the accumulation of many successively-growing, small-amplitude kink instabilities[43] would

represent a more gentle, energy-conserving reversal mechanism that in many ways would be similar to the m = 1 "saw-tooth" activity that has become part of the tokamak lore. Fully turbulent and resistive models are being developed as explanations for the field reversal.[36] One candidate for a relaxation mechanism is the resistive tearing mode, which can lead to the formation of magnetic islands[44] and a subsequent "braiding" and reconnection of flux lines; nonlinear calculations support the contention that the m = 1 resistive tearing mode could produce the self-reversed state. The potential role of the pressure-gradient g-mode (interchange mode) and other related resistive instabilities in driving relaxation mechanisms has yet to be resolved.

In addition to the unknown energy losses and beta constraints that accompany field reversal, the reactor embodiment depends sensitively on an ability to sustain the RFP configuration. Three-dimensional MHD simulations of the self-reversal process demonstrate that the interaction between two modes can lead to a nearly axisymmetric field configuration,[45] and the field-reversed configuration can be sustained as long as the toroidal current is maintained constant. A dual cascade theory of turbulence has also been shown theoretically to lead to an RFP structure.[46] These theories remain too developmental and unsubstantiated by large experiments to be incorporated into this reactor study. Nevertheless, a number of reversal mechanisms that may be postulated to sustain and maintain a "universal" relaxed state can be identified. The dependence of beta and energy confinement time on the turbulence level and associated enhanced transport, however, remain crucial and unresolved issues for the reactor. The importance of these issues on the method of setup and sustenance (self-reversal versus assisted-reversal versus programmed reversal) of a reactor-grade RFP, therefore, remains the major uncertainty for this study.

3. Toroidal Equilibrium. Most theoretical studies of the RFP have focused on the ideal and resistive MHD stability of this toroidal configuration. As noted previously, application of resistive theories to understand the field-reversal process and turbulent transport has occurred only recently. The issue of toroidal equilibrium, per se, has always been integral with studies of ideal MHD stability. Toroidal equilibrium of the axisymmetric RFP is well established by both analytic and numerical computation.[1] Questions remain, however, on the effects of departure from axisymmetry caused by field errors that will inevitably occur in actual

engineering systems. For the purpcses of this study, toroidal equilibrium is assumed readily attainable by moderate variations in the poloidal coil current distributions, and the focus has been placed, instead, on adequately including constraints that are related to the gross and microstability.

C. RFP Experiments

A large number[16,17,47] of linear pinch devices, in which the electrodes were inserted directly into the plasma at the ends of the tube, were constructed during the period 1957-1958. Current rise rates of 10^{10} to 10^{11} A/s and initial gas pressures of 2 to 10^3 mtorr were readily obtainable in devices with lengths ranging from a few centimeters to nearly a meter and diameters up to 0.6 m. Because of the short confinement times, measurements performed away from the ends of these linear pinches do not appear to be dominated by end effects associated with impurity influx and electrode cooling. These early experiments generally exhibited the expected instabilities discussed in Sec. III.A. Many of these experiments[16,17,47] also incorporated a bias field, which suppressed the sausage (m = 0) mode. According to sharp-boundary stability theory (Sec. III.A), a bias field and a conducting shell around the plasma may provide a stable plasma configuration. This theory, however, is insufficient in predicting the experimentally observed behavior of a diffuse plasma, and the kink (m = 1) mode persisted. The Suydam criterion for a diffuse-current layer demonstrated the possibility of improved stability by imposing a reversed axial field outside the plasma column or by using self-reversal during the current initiation. The toroidal RFP experiments that ensued are listed in Table III-I.

One of the first experiments to impose a reversed field[48] was designated as RFP1. By using an initial bias field $B_{\phi_o} \simeq 0.1$ T and by programming the magnetic and electric fields to reverse outside of the pinch during the current rise, the plasma was maintained for 10-15 μs at ion temperatures up to 130 eV. Plasma compression increased the density by approximately a factor of 5, which resulted in peak ion densities of 3×10^{22} m^{-3}. Without field programming MHD instabilities forced the plasma to the wall within 3 μs.

The relatively slow current risetime (~ 1 ms) for the ZETA device,[49-53] initially operated in 1958, induced toroidal electric fields of only ~ 100 V/m and, therefore, allowed the use of a metallic vacuum vessel. Plasma currents, sustained for 1-3 ms through a low pressure gas in the presence of a stabilizing bias field B_{ϕ_o} (0.02 - 0.1 T), produced plasma temperatures of

TABLE III-1

SUMMARY OF EXISTING AND PROPOSED RFP EXPERIMENTS

DEVICE	FIRST-WALL RADIUS(m)	MAJOR RADIUS(m)	PLASMA CURRENT (kA)	RISE TIME (ms)	DECAY TIME (ms)	PLANNED COMPLETION DATE
RFP1 (USA)	0.035	0.25	20	0.002	0.015	--
ZETA (UK)	0.50	1.50	100-900	1.0	3.0	--
HBTX (UK)	0.065	1.00	40-110	0.015	0.03	--
ETA/BETA (ITALY)	0.05	0.40	30-150	0.001-0.006	0.1	--
ETL/TPE-1 (JAPAN)	0.05	0.40	80-120	0.002-0.005	0.03	--
TPE-1R	0.11	0.50	250	0.005	0.10	--
STP (JAPAN)	0.04	0.12	50	0.004	0.025	--
ZT-1 (USA)	0.05	0.37	30-200	0.0001-0.006	0.01-0.03	--
ZT-S (USA)	0.077	0.40	30-140	0.0025	0.04	--
ETA/BETA-II (ITALY)	0.125	0.65	200-300	0.004-0.120	0.05-1.0	9/78
HBTXIA (UK)	0.26	0.80	400	0.10-0.50	1.0-5.0	79-80
ZT40(US)	0.20	1.14	150-600	0.0025-1.0	1.0-5.0	9/79
RFXI (UK)	0.60	1.80	700-1000	2.0-10	10-20	?
RFXII (UK)	0.60	1.80	1000-1500	20.0-50.0	50.0-100.0	?
RFP/POP	0.60	2.40	6000	10.0	100.0	?

10-50 eV and energy confinement times of approximately 100 μs. Values of pinch parameter [Eq. (III-6)], Θ, were in the range 2-5 with β_θ up to 0.10. A reversed toroidal field was not imposed on the outside of the plasma. Continuing experimental studies[51] made during the period 1965-1968 exhibited a regime of improved stability for times up to 3 ms at electron temperatures of 100-200 eV. The improved stability was accompanied by a "quiescent period," wherein normally high field fluctuations decreased by an order of magnitude. This quiescence occurred only when both the magnetic and electric fields were reversed in the outer plasma regions with $\Theta > 1.8$. Recent analysis of ZETA experimental data[53] has produced substantially the same conclusions; energy containment times were estimated to be 3-10 ms during the quiescent state and $\beta_\theta \simeq 0.10$. In this experiment no reverse field was imposed on the plasma; self-reversal occurred when the plasma relaxed to a state of minimum potential energy (Sec. III.A.2).

As indicated on Table III-I, ZETA was a significant experiment for its time; no other toroidal experiment exceeded the ZETA dimensions until the PLT and T-10 tokamak experiments were built. ZETA was unique in another sense; although field reversal has been demonstrated on many RFP experiments, only

ZETA has shown the quiescent period of enhanced confinement and reduced transport. The conditions for quiescence were:[41] I_ϕ = 300-900 kA, P_A = 1-2 mtorr, B_ϕ and E_ϕ < 0 at the wall, T = 150-200 eV, n = $5(10)^{19}$ m^{-3}, $\beta \simeq 0.1$, and τ_E = 3-10 ms. These results could be significant, particularly in view of the limited energy store on ZETA and the potential for additional plasma heating if a supplemental, slow B_ϕ field control could have been used to prolong the plasma lifetime.

In the HBTX experiment[54,55] reversed-field configurations were produced by fast programming. Operation with the pinch parameter $\Theta \sim 2$ suppressed the kink (m = 1) instability for all experimental conditions. Energy confinement times of $\tau_E \sim 15$ μs were predicted during the 20 μs stable configuration. The peak temperature increased as the square of the toroidal current up to 110 eV with β_θ = 0.4-0.6.

Experimentally stable RFP configurations were found in ETA-BETA[56,57] for toroidal currents up to 60 kA, whereas instabilities occurred at higher currents. Stable discharges were obtained for 10 μs containment times and plasma compressions ($x = r_p/r_w$) of ~ 0.6. The plasma was characterized by an average temperature of 10 eV and β_θ = 0.2-0.3. Self-reversal has also been observed for x = 0.4-0.5, yielding plasma decay times of 25-30 μs.

The ETL-TPE-1[58,59] device has been operated as a screw pinch and a RFP. Electron temperatures of ~ 10 eV were maintained for ~ 20 μs, whereupon β_θ rises above 0.6, the plasma column develops an m = 1 helical motion and touches the wall. Preliminary RFP operation of the STP (operated primarily as a high-beta tokamak) experiment has also showed improved stability using reversed-field programming.[60]

The ZT-I experiment[28,61] was initially designed to operate with a rapid current risetime, ($\dot{I}_\phi \simeq 1.4 \times 10^{12}$ A/s) using inductive energy storage with fused interrupters. Ion temperatures of ~ 1 keV and electron temperatures of ~ 40 eV were obtained. Operated in this fast mode, the ZT-I produced hot, but very unstable plasma. Reversed-field programming of ZT-I occurred on a slower time scale than the pinch time, and completely stable MHD profiles were not obtained. Derating the device to toroidal currents of 40-70 kA and reducing the current rise to 10^{11} A/s allowed a more effective field programming. The ion temperatures were decreased an order of magnitude and favorable stability was obtained. Confinement times of 10-15 μs resulted when reversed-field programming was successfully implemented; these times compare to 3-4 μs with

no reversed field. Loss of containment appeared to result when β_θ increased above the stability limit (~ 0.5).

The major purpose of the ZT-S experiment was to examine the scaling of confinement time with minor radius; the bore was increased from 0.10 for ZT-I to 0.15 for ZT-S. The confinement time is expected to scale as the field diffusion time, which is proportional to the square of the plasma radius. The confinement time increased from 10-15 μs in ZT-I to 25-30 μs in ZT-S, which scales approximately as the square of the minor radius.

These promising results have led to the proposal of many new experiments, which include a 0.24-m bore experiment (ETA BETA II, University of Padua, Italy) and a 0.40-m bore device (ZT-40, Los Alamos Scientific Laboratory), both using field programming techniques. A 1.20-m bore, self-reversal experiment (RFX, Culham Laboratory, United Kingdom) is also planned. Most recently, an ambitious RFP experiment with the same bore as RFX but with considerably more toroidal current, has been proposed.[62] It is hoped that the above experiments will produce favorable scaling with plasma dimensions, confinement time, beta, toroidal current, and magnetic Reynolds number.

REFERENCES

1. D. A. Baker and J. N. DiMarco, "The LASL Reversed-Field Pinch Program Plan," Los Alamos Scientific Laboratory report LA-6177-MS (1975).

2. H. A. B. Bodin, "Reversed Field Pinches," Third Topical Conference on Pulsed High Beta Plasmas, Culham, United Kingdom, 1975, pp. 39-57.

3. Sergio Ortolani (Scientific Secretary), Proceedings of the Workshop on the Reversed Field Pinch (RFP), Universita Di Padova, Padova, Italy (1978).

4. C. Mercier, "A Necessary Criteria of Hydromagnetic Stability for a Plasma with Symmetry of Revolution," Nuclear Fusion 1, 47-53 (1960).

5. R. B. Suydam, "Stability of a Linear Pinch," Proceedings of the Second United Nations International Conference on the Peaceful Uses of Atomic Energy, Geneva, Switzerland, 1958, Vol. 31, pp. 157-159.

6. M. D. Kruskal, "Large-Scale Instability in the Stellarator," USAEC Rept. NYO-6045 (1954).

7. V. D. Shafranov,, "The Stability of a Cylindrical Gaseous Conductor in a Magnetic Field," Atomnaiia Energiia (English Translation) 1, 709-713 (1956).

8. L. A. Artsimovich, "Tokamak Devices," Nuclear Fusion 12, 215-252 (1972).

9. S. O. Dean, "Status and Objectives of Tokamak Systems for Fusion Research," USAEC Rept. WASH-1295 (1973).

10. H. Toyama, S. Inoue, K. Itoh, A. Iwahashi, H. Kaneko, and K. Makishima, "Experiments on Noncircular Tokamak and Related Topics," Sixth International Conference on Plasma Physics and Controlled Nuclear Fusion Research, Berchtesgaden,, West Germany, 1976, (Nuclear Fusion, Supplement 1977), Vol. I, pp. 323-334.

11. J. D. Callen, J. F. Clarke, R. A. Dory, J. A. Holmes, F. B. Marcus, and D. G. McAlees, "Tokamak Plasma Magnetics," Sixth International Conference on Plasma Physics and Controlled Nuclear Fusion Research, Berchtesgaden, West Germany, 1976, (Nuclear Fusion, Supplement 1977), Vol. II, pp. 369-384.

12. C. K. Chu, H. C. Lui, M. F. Reusch, and R. T. Taussig, "Initial Dynamics, Equilibrium, and Heating of Toroidal Belt Pinches," Third Topical Conference on Pulsed High Beta Plasmas, Culham, United Kingdom, 1975, pp. 553-556.

13. J. A. Hoekzema, "Toroidal Equilibrium of Non-Circular Sharp Boundary Plasmas Surrounded by Force-Free Fields," Third Topical Conference on Pulsed High Beta Plasmas, Culham, United Kingdom, 1975, pp. 535-539.

14. Kei-ichi Hirano, "Screw Pinches and High Beta Tokamak with Circular Cross-Section," Third Topical Conference on Pulsed High Beta Plasmas, Culham, United Kingdom, 1975, pp. 87-91.

15. C. Bobeldijk, "Results of SPICA," Third Topical Conference on Pulsed High Beta Plasmas, Culham, United Kingdom, 1975, pp. 493-496.

16. S. Glasstone and R. H. Lovberg, Controlled Thermonuclear Reactions (Van Nostrand Reinhold Company, New York, N.Y., 1960), pp. 523.

17. D. J. Rose and M. Clark, Jr. Plasmas and Controlled Fusion, 2nd ed. (The M.I.T. Press, Massachusetts Institute of Technology, Cambridge, Massachusetts, 1965), pp. 493.

18. M. D. Kruskal and M. Schwarzschild, "Some Instabilities of a Completely Ionized Plasma," Proceedings of the Royal Society of London, A223, 348-360 (1954).

19. R. J. Tayler, "Hydromagnetic Instabilities of an Ideally Conducting Fluid," Physical Society, B70, 31-48 (1957).

20. M. N. Rosenbluth, "Stability of the Pinch," Los Alamos Scientific Laboratory report LA-2030 (1956).

21. V. D. Shafranov, "On the Stability of a Cylindrical Gaseous Conductor in a Magnetic Field," J. Nucl. Energy 5, 86-91 (1957).

22. R. J. Tayler, "The Stability of a Constricted Gas Discharge," Proceedings of the Second United Nations International Conference on the Peaceful Uses of Atomic Energy, Geneva, Switzerland, 1958, Vol. 31, pp. 160-170.

23. M. Kruskal and J. L. Tuck, "The Instability of a Pinched Fluid with a Longitudinal Magnetic Field," Proceedings of the Royal Society of London, A245, 222-237 (1958).

24. W. A. Newcomb, "Hydromagnetic Stability of a Diffuse Linear Pinch," Annals of Physics 10, 232-267 (1960).

25. H. P. Furth, "Sufficient Conditions for Hydromagnetic Stability of a Diffuse Linear Pinch," Physics of Fluids 3, 977-981 (1960).

26. B. R. Suydam, "Stability of a Linear Pinch, Part II," Los Alamos Scientific Laboratory report LAMS-2381 (1960).

27. D. A. Baker and L. W. Mann, "Progress Report of the LASL Controlled Thermonuclear Research Program," Los Alamos Scientific Laboratory report LA-5656-PR (1974).

28. D. A. Baker, L. C. Burkhardt, J. N. DiMarco, P. R. Forman, A. Haberstich, and H. J. Karr, "Z-Pinch Experiments with Shock Heating," Proceedings of the Fourth IAEA Conference on Plasma Physics and Controlled Nuclear Fusion Research, Madison, Wisconsin, 1971, Vol. 1, pp. 203-216.

29. D. C. Robinson, "High-β Diffuse Pinch Configurations," Plasma Physics 13, 439-462 (1971).

30. D. A. Baker and L. W. Mann, "MHD Studies of Numerically Obtained Toroidal Equilibria," Proceedings of the Second Topical Conference on Pulsed High Beta Plasmas, Munich, West Germany, 1972, pp. 69-72.

31. A. Haberstich, D. A. Baker, J. N. DiMarco, L. W. Mann, and S. Ortolani, Stability and Diffusion of the ZT-I Reversed-Field Pinch," Third Topical Conference on Pulsed High Beta Plasmas, Culham, United Kingdom, 1975, pp. 249-253.

32. J. B. Taylor, "Relaxation of Toroidal Plasma and Generation of Reverse Magnetic Fields," Phys. Rev. Lett. 33, 1139-1141 (1974).

33. J. B. Taylor, "Relaxation of Toroidal Discharges to Stable States and the Generation of Reverse Magnetic Fields," Fifth IAEA Conf. on Plasma Physics and Controlled Fusion, Tokyo, Japan, 1974, Vol. 1, pp. 161-167.

34. J. B. Taylor, "Relaxation of Toroidal Discharges," Third Topical Conf. on Pulsed High Beta Plasmas, Culham, United Kingdom, 1975, p. 59.

35. S. Ortolani and G. Rostagni, "Reverse Field Configurations with Minimum Potential Energy," Third Topical Conference on Pulsed High Beta Plasmas, Culham, United Kingdom, 1975, pp. 335-339.

36. H. A. B. Bodin, personal communication, Culham, United Kingdom, (1979).

37. A. A. Newton, Li Yin-An, J. W. Long, and B. C. Yeung, "Numerical Investigation of Reversed Field Pinches," Third Topical Conf. on Pulsed High Beta Plasmas, Culham, United Kingdom, 1975, pp. 323-328.

38. S. A. Colgate, J. P. Ferguson, and H. P. Furth, "A Toroidal Stabilized Pinch," Proc. 2nd UN Conf. on Peaceful Uses of Atomic Energy 32, 129-139 (1958).

39. L. Woltjer, "A Theorem on Force Free Magnetic Fields," Proc. Nat. Acad. Sci. 44, 489-491 (1958).

40. M. N. Bussac, H. P. Furth, M. Okabayashi, M. N. Rosenbluth, and A. M. M. Todd, "Low Aspect-Ratio Limit of the Toroidal Reactor: The Spheromak," presented at the Seventh International Conference on Plasma Physics and Controlled Nuclear Fusion Research, Innsbruck, Austria, 1978, paper IAEA-CN-37-X-1.

41. H. A. B. Bodin and B. E. Keen, "Experimental Studies of Plasma Confinement in Toroidal Systems," Reports on Progress in Physics 40, 1415-1565 (1977).

42. A. Sykes and J. A. Wesson, "Field Reversal in Pinches," Phys. Rev. Letts. 37, 140 (1976).

43. D. C. Robinson, "Tearing-Mode-Stable Diffuse-Pinch Configurations", Nucl. Fusion 18, 939-953 (1978).

44. H. P. Furth, J. Killeen, and M. N. Rosenbluth, "Finite-Resistivity Instabilities of a Sheet Pinch," Phys. Fluids 6, 459-484 (1963).

45. C. W. Gowers, D. C. Robinson, A. Sykes, A. J. L. Verhage, J. A. Wesson, M. R. C. Watts, and H. A. B. Bodin, "An Experimental, 3-D Numerical and Analytical Study of Reversed-Field Pinches (RFP)," Sixth International Conference on Plasma Physics and Controlled Nuclear Fusion Research, 1976, (Nuclear Fusion, Supplement 1977), Vol. I, pp. 429-445.

46. D. Montgomery, L. Turner, and G. Vahala, "Three-Dimensional Magnetohydrodynamic Turbulence in Cylindrical Geometry," Phys. Fluids 21, 757-764 (1978).

47. L. C. Burkhardt, "Partial Chronology of Z-Pinch Studies at Los Alamos Scientific Laboratory," Los Alamos Scientific Laboratory report LA-5922-H (1975).

48. T. Ohkawa, H. K. Forsen, A. A. Schupp, Jr., and D. W. Kerst, "Toroidal Discharge Experiments with Rapid Programming," Phys. Fluids 6, 846-857 (1963).

49. E. P. Butt, R. Carruthers, J. T. D. Mitchell, R. S. Pease, P. C. Thonemann, and M. A. Bird, "The Design and Performance of ZETA," Proceedings of the Second United Nations International Conference on the Peaceful Uses of Atomic Energy, Geneva, Switzerland, 1958, Vol. 32, pp. 42-64.

50. W. M. Burton, E. P. Butt, H. C. Cole, A. Gibson, D. W. Mason, and R. S. Pease, "Plasma Loss in Zeta," Nuclear Fusion, Supplement 3, 903-919 (1962).

51. E. P. Butt, H. C. Cole, A. N. Dellis, A. Gibson, M. Rusbridge, and D. Wort, "Conditions for Improved Stability in ZETA," Proc. of the Conf. on Plasma Physics and Controlled Nuclear Fusion Research, Culham, United Kingdom, 1965, pp. 751-764.

52. D. C. Robinson and R. E. King, "Factors Influencing the Improved Stability of ZETA," Proc. of the Third International Conf. on Plasma Physics and Controlled Nucl. Fusion Research, Novasibirsk, USSR, 1968, Vol. 1, pp. 263-276.

53. E. P. Butt and A. A. Newton, "New Results from ZETA," Third Topical Conf. on Pulsed High-Beta Plasmas, Culham, United Kingdom, 1975, pp. 425-429.

54. A. J. L. Verhage and D. C. Robinson, "Stability of Pinches with a Reversed Field in HBTX I," Third Topical Conf. on Pulsed High Beta Plasmas, Culham, United Kingdom, 1975, pp. 267-271.

55. C. A. Bunting, A. A. Newton, and M. R. C. Watts, "Studies of Ion Temperature and Total Radiated Energy from Pinches in HBTXI," Third Topical Conf. on Pulsed High Beta Plasmas, Culham, United Kingdom, 1975, pp. 437-441.

56. A. Buffa, S. Costa, G. F. Nalesso, and G. Malesani, "Experiments on Programmed and Naturally Relaxing RFP Configurations," Third Topical Conf. on Pulsed High Beta Plasmas, Culham, United Kingdom, 1975, pp. 261-265.

57. A. Buffa, S. Costa, R. Giannella, G. Malesani, G. F. Nalesso, and S. Ortolani, "Heating, Diffusion, and Stability of Reverse Field Pinch Configurations," Sixth International Conference on Plasma Physics and Controlled Nuclear Fusion Research, Berchtesgaden, West Germany, 1976, (Nuclear Fusion, Supplement 1977), Vol. I, pp. 447-461.

58. K. Ogawa, T. Shimada, S. Kiyama, Y. Hirano, Y. Maejima, and I. Hirota, "High Beta Plasma Confinement in Reversed Field Pinch (ETL TPE-1)," Third Topical Conference on Pulsed High Beta Plasmas, Culham, United Kingdom, 1975, pp. 255-259.

59. T. Shimada, Y. Hirano, Y. Maejima, and K. Ogawa, "Toroidal Pinch Experiments in ETL," Sixth International Conference on Plasma Physics and Controlled Nuclear Fusion Research, Berchtesgaden, West Germany, 1976, (Nuclear Fusion, Supplement 1977), Vol. I, pp. 463-469.

60. K. Hirano, S. Kitagawa, M. Wakatani, Y. Kita, S. Yamada, and S. Yamaguchi, "Plasma Confinement of Nagoya High Beta Toroidal Pinch Experiments," Sixth International Conference on Plasma Physics and Controlled Nuclear Fusion Research, Berchtesgaden, West Germany, 1976, (Nuclear Fusion, Supplement 1977), Vol. I, pp. 503-510.

61. L. C. Burkhardt, J. N. DiMarco, P. R. Forman, A. Haberstich, H. J. Karr, and J. A. Phillips, "Recent Results from the Shock Heated Toroidal Z-Pinch Experiment ZT-I," Proceedings of the Second Topical Conference on Pulsed High Beta Plasmas, Munich, West Germany, 1972, pp. 33-36.

62. Staff of the CTR Division (Compiled by H. Dreicer), "The Reversed-Field Pinch Concept and a Preliminary Conceptual Design for a Proof-of-Principle Experiment," Los Alamos Scientific Laboratory report LA-7527-MS (1978).

IV. REACTOR DESIGN BASIS

In presenting a conceptual engineering design of a power source that is as developmental as fusion, the importance of clearly describing the physics and engineering models that form the design basis cannot be overstated; more often than not the assumptions upon which the conceptual design is based and the sensitivity of results to these assumptions is equally if not more important than the many tables and graphs generated by such a study. Like other fusion schemes, fundamental understanding of the RFP is growing and evolving. This reactor study represents a projection into the future of a concept with numerous scientific and technological uncertainties and unknowns. A well-planned research and development program will ultimately resolve many of these issues, and studies such as this one hopefully would influence the direction of that program. For this reason a detailed understanding of the design basis and the ways in which it might be influenced by future developments becomes equal in importance to the interim results presented herein.

After a brief review of past RFP reactor studies (Sec. IV.A), the RFP energy balance (Sec. IV.B) and reactor model (Sec. IV.C, Appendix A) are described. The costing model used to generate the major object function is summarized (Sec. IV.D), and the development of the interim point design is quantified (Sec. IV.E). The point design that has evolved (Sec. IV.F) is used as a basis to examine key technology issues (Sec. V).

A. Previous RFP Engineering Designs

Early reactor studies of the RFPR were performed at the Los Alamos Scientific Laboratory in 1975[1] and independently at the Culham Laboratory from 1969-1975.[2-4] The Culham effort developed into a sizable, comprehensive study that was recently concluded.[5-9] Without exception these early design studies were based on a steady-state point plasma model (plasma temperature and density assumed constant throughout the burn) and attempted to resolve only those plasma parameters necessary to assure an acceptable reactor energy balance; minimal consideration was given to associated engineering requirements. The recently concluded Culham study[5-9] will ultimately lead to a consistent engineering design and represents an independent counterpart to the study reported herein.

Early reactor calculations[1] assumed the plasma could be held at constant temperature (15 keV), poloidal beta ($\beta_\theta = 0.5$), and plasma compression ($x = r_p/r_w = 0.4$) for a specified time. The blanket power multiplication was assumed, and plasma current limits were estimated on the basis of the total allowabl neutrons incident on the first wall and a specified first-wall lifetime.

The early Culham studies[2-4] used tokamak plasma codes with appropriate RFP resistivities and classical losses. In these studies MHD stability is determined by a limiting poloidal beta,[10] $\beta_{\Theta L} = 0.075\Theta^3$, where Θ is the pinch parameter (Eq. III-6). This beta constraint results from an increase in the field shear as the plasma current is increased and cannot be used above $\Theta \sim 2$. The supporting of more plasma pressure as the pinch moves away from the stabilizing wall is in opposition to the results obtained for configurations with the field shear already established. (Sec. III.B)

When the limiting-beta model is used, plasma transport is assumed to be classical if $\beta_\theta < \beta_{\theta L}$; when $\beta_\theta > \beta_{\theta L}$, however, instabilities are assumed to grow, supposedly saturate and appear as enhanced energy loss that is proportional to $e^{[(\beta_\theta - \beta_{\theta L})k]}$. The constant k is chosen sufficiently large for $\beta_{\theta L}$ not to be exceeded by more than a few percent. For a device where $r_p = 1.5$ m, $I_\phi = 25$ MA, $\Theta = 1.75$, and $n = 4(10)^{19}$ m^{-3}, the plasma heats ohmically to ignition in 1.0 s. Cold particles are then injected to maintain the plasma temperature at 20 keV for the 20-s burn period. This steady-state system would operate at $\beta_\theta = 0.46$ by means of the assumed turbulent loss mechanism. The stability of the configuration during this process is difficult to assess. Energy-balance calculations are not performed, although a thermal output of 2000 MW is calculated for an aspect ratio of 5.

The reactor study recently completed at Culham[5-9] invokes the same plasma loss mechanisms described above, where an enhanced thermal conduction would maintain a steady-state burn at a constant beta. For a device with $r_p = 1.75$ m the parameters of the ohmically heated plasma (4.5 s heating phase for $I_\phi = 19$ MA) are T = 10 keV, $n = 2.5(10)^{20}$ m^{-3} and $\beta_\theta = 0.35$ during the 27.5-s burn phase; a 30% fuel burnup results. Using a full burn cycle of 40 s and normal conducting coils requires a 0.42 recirculating electric power fraction, resulting in a net output power of 600 MWe from a reactor of 16-m major radius at an estimated capital cost of $2000/kWe. Using superconducting magnet coils[9] the recirculating power fraction is reduced from 0.42 to 0.21.

The plasma characteristics and performance predicted by the Culham team are surprisingly close to those reported by the LASL group.

No comprehensive RFP reactor studies could be identified in 1979. Parametric studies of reactor plasma performance continue, however, both at LASL and the University of Illinois.[11]

B. Energy Balance

Evaluation of potential operating cycles requires a model that is sufficiently detailed to allow a realistic reactor energy balance. Figure IV-1 schematically depicts the RFPR energy balance. The plasma initially has an energy W^{o}_{INT}. The total stored magnetic energy W_{BO} is then transferred to the magnets, and the energy $W_{BO}(1-\eta_{ETS}) = W_{ETS}$ is lost during this energy transfer/storage process. The remaining magnetic energy $W_{BO}\eta_{ETS}$ is partitioned between vacuum field energy, transport losses W_{TR}, eddy current losses in the blanket W_{EB} and magnet coil W_{EC}, plasma ohmic-heating energy W_{OHM}, and field energy trapped inside the plasma W^{IN}_{B}. The high-beta plasma expansion restores some of the field energy by direct-conversion work W_{DC}, although for the nearly constant-radius RFP burn, W_{DC} is negligible. The plasma produces neutron W_{N}, radiation W_{RAD}, conduction W_{COND}, internal plasma W_{INT}, and field W^{IN}_{B} energies which eventually appears as thermal energy in the blanket. It is emphasized that all of the field trapped in the plasma at the end of the burn, W^{IN}_{B}, is assumed to be thermally dissipated and transferred through the first wall. All thermal energy delivered to the first-wall and blanket coolant is converted with a thermal efficiency η_{TH} to produce a gross electric energy W_{ET}. Auxiliary energy requirements W_{A} (pumps, cryogenics, plant operation, etc.), given as a fraction f_{A} of W_{ET}, complete the energy balance. A fraction ε of the total electrical energy W_{ET} must be recirculated as makeup energy $W_{C} = \varepsilon W_{ET}$, the net electric energy is then $W_{E} = (1-\varepsilon)W_{ET}$, and the over-all plant efficiency is $\eta_{p} = (1 - \varepsilon)\eta_{TH}$.

An engineering Q-value, Q_{E}, is defined as

$$Q_{E} = \frac{W_{ET}}{W_{C}} = \frac{1}{\varepsilon} = \frac{\eta_{TH}\left[W_{N}+W_{INT}+W_{RAD}+W_{COND}+W^{IN}_{B}+W_{EB}\right]}{W^{o}_{INT}+W_{OHM}+W^{IN}_{B}+W_{TR}+W_{EB}+W_{EC} - W_{DC}+W_{ETS}+W_{A}} , \qquad \text{(IV-1)}$$

and is used as a major performance indicator for the RFPR. An economic evaluation (Sec. IV.D), however, ultimately provides the final evaluation of a

given RFPR operating point, although the value of Q_E directly impacts the final plant and power costs.

It is noted that a considerably more detailed design would be required to elevate the assessment of auxiliary plant energy requirements (i.e., Fig. IV-1) from the parametric level. A similar statement could be made with respect to the costing of the balance of plant (Sec. IV.D). An ongoing study[12] of balance-of-plant (BOP) costing and energy requirements is addressing this issue for a number of magnetic fusion concepts, including the RFPR. For the purposes of this study, BOP items are treated either parametrically or in terms of lumped unit variables. The energy balance given by Eq. (IV-1) is evaluated as a function of time by the point RFP plasma model (Appendix A).

C. Reactor Physics

This section gives a summary description of the physics models used to describe the reactor startup, thermonuclear burn, and postburn quench or rundown. A detailed development of the burn model can be found in Appendix A. Application of the plasma stability/equilibrium issues described in Sec. III.B is also addressed in this section.

1. Plasma Model. The poloidal and toroidal magnetic-field profiles within the plasma are modeled, respectively, by the Bessel functions $A_\theta J_1(\alpha r)$ and $A_\phi J_o(\alpha r)$, which according to Fig. IV-2 show good agreement with calculated MHD stable profiles. The constants A_θ and A_ϕ are determined by the conservation of total current and flux in the plasma (Appendix A). Enforcing pressure balance and integrating over the isothermal plasma cross-section allows the use of spatially-averaged parameters for the calculation of burn dynamics. A consistent calculation of the multi-species plasma (ions, electrons, and alpha particles) follows the plasma radius with time in conjunction with the voltages and currents in the plasma and associated electrical circuitry. Alpha-particle thermalization using a Fokker-Planck formalism, ohmic heating using classical resistivity, radiation (bremsstrahlung, cyclotron, and line) losses, and anomalous (radial) thermal conduction and particle diffusion are included in this time-dependent model. A detailed presentation of the magnetic field models, plasma energy balance, and the numerical methods used is given in Appendix A.

a. Startup. The startup time is taken as 10% of the energy containment time, which is ~ 1 s for a reactor using classical diffusive scaling from the ZT-I and ZT-S experimental results and, therefore, is consistent with diffusion scaling from past and present RFP experiments.[1] A conducting copper first wall, with an electrical skin depth equal to the startup time, is present to stabilize the plasma and promote field reversal during the 0.1-s initiation phase. The initial, uniform toroidal field, $B_{\phi o}$, superposed onto an increasing toroidal plasma current, results in a field configuration that initially is similar to that in a tokamak. This initially q-stabilized system must then be transformed into a RFP by proper programming of the fields, self-reversal of the magnetic fields or a combination thereof (i.e., assisted self-reversal). The achieving of stability during this setup phase seems unlikely, and turbulence similar to that exhibited in tokamaks may result. Energy losses during this startup phase have not been explicitly included in

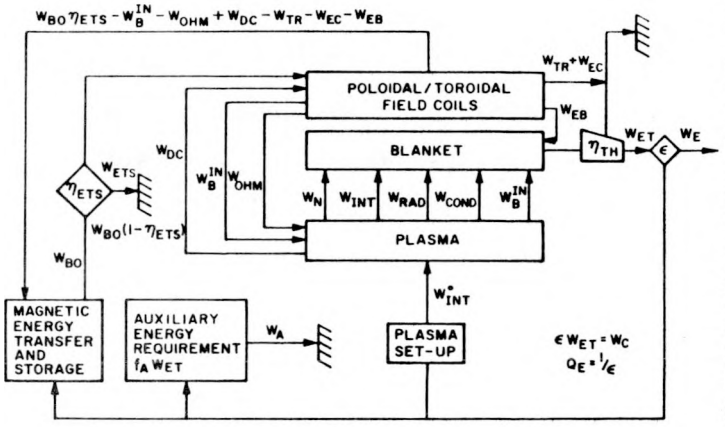

Fig. IV-1. Complete RFPR energy balance used in conjunction with a time-dependent RFP plasma model to evaluate a range of reactor operating points. Refer to text for notation.

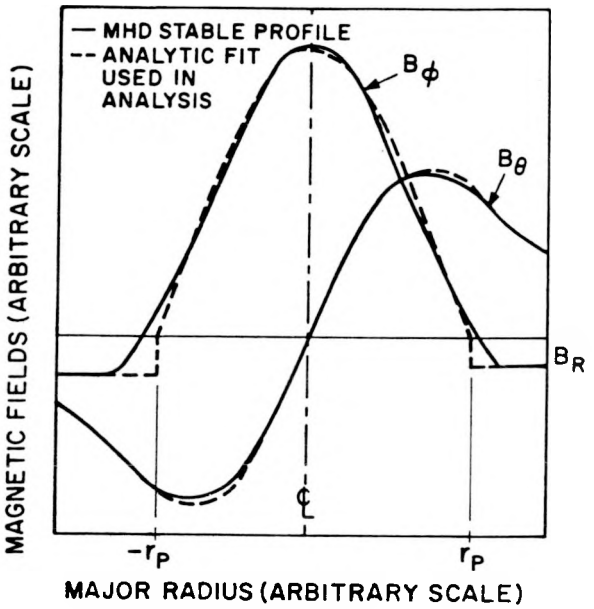

Fig. IV-2. Comparison of assumed Bessel-function poloidal, B_θ, and toroidal, B_ϕ, fields with numerically computed MHD-stable field profiles.

the RFPR plasma model. Pressure balance is assumed during startup using the Bessel function model (Appendix A).

Preionization is assumed to be achieved uniformly to an electron density of n_e equal to 10^{-6} of the neutral density, n_o, for the computer simulations.[13] The toroidal electric field, E_ϕ, applied[13] to the plasma by the homopolar machine energizing the poloidal coil system must be sufficient to sustain breakdown at this level of preionization. This electric field is taken as $I_\phi R_p/(2\pi R)$ where R_p is the resistance of the plasma. This approximation ignores the inductive spike which occurs for ~ 1 μsec at the time of current initiation when the plasma current is near zero. The minimum electric field for breakdown is ~ 5 V/m-mtorr for pressures above ~ 0.5 mtorr when the reactor minor radius is on the order of a meter.[13]

Electron runaway is observed[14-16] above electric fields corresponding to 20 V/mtorr and is taken as a maximum allowable field.[13] When a significant fraction (~ 0.1) of the neutral population is ionized, electron-ion collisions will dominate and determine the conditions for electron runaway. The critical electric field,[17] $E_c = 1.6 \times 10^{-11} n_e \eta_\parallel T_e^{1/2}$, when divided by the electric field imposed on the plasma, $E = \eta_\parallel I_z/\pi r_p^2$, gives $E_c/E = 2 \times 10^{-7}(N_e \beta_\theta)^{1/2}$, where the electron line density N_e(1/m) and pressure balance is used. In this expression $\eta_\parallel$(ohm m) is the parallel plasma resistivity and T_e(keV) is the electron temperature. Setting $E_c/E > 50$ results in an insignificant energy loss associated with runaway electrons.[17] Very low β_θ values occur at startup when the plasma temperature is low, however, and the initial 20 V/m-mtorr becomes the limiting constraint. Electron runaway at higher temperatures does not appear as a problem. Taking typical values of $N_e \sim 10^{21}$ m^{-1} and $\beta_\theta \sim 0.01$ (during startup) gives $E_c/E \sim 630$.

Assuming the aforementioned preionization model, plasma breakdown is then modeled with a tokamak startup code until the plasma temperature reaches ~ 0.1 keV. The discharges typically are started at relatively low filling pressures (~ 0.5-1 mtorr) in order to minimize the power loss associated with line radiation at low temperatures (~ 0.01 keV). The line-radiation power is proportional to $n_e n_{im}$, where n_{im} is the impurity number density, and may be difficult to overcome if the initial density is too high. The final density is then achieved by gas injection after the resonance line radiation from low-Z impurity ions has diminished. The peak resonance for oxygen occurs at

~ 0.01 keV; neutral DT gas is allowed to flow into the system for T > 0.02 keV until the required density is achieved.

A sample startup calculated for typical RFPR dimensions (r_w = 1.5 m) is shown in Fig. IV-3. A sinusoidal voltage of 10 kV/turn with a quarter period of 0.1 s appears virtually constant during the initial 0.012 s (or until T_e reaches 0.1 keV) modeled by the tokamak startup code. The initially rapid decrease in electric field to 6 V/mtorr is a result of the transition from the avalanche distribution ($n_e < 0.01\ n_o$, with $T_e \sim 0.01$ keV) to a Maxwellian electron distribution of lower temperature (T_e = 0.003 keV), where the high-energy (> 0.015 keV) tail of the distribution ionizes the DT neutrals. The toroidal electric field imposed on the plasma at this point varies between 6-14 V/m-mtorr as the bulk of the neutrals are ionized.

The major power components incurred during startup are also shown in Fig. IV-3. The difference between the ohmic-heating power, P_{OHM}, and ion-neutral charge exchange power, P_{CX}, equals the power required to ionize the DT neutrals. The large line-radiation power, P_{LINE}, at 0.01 keV is apparent; a 1% oxygen fraction is assumed. After the oxygen resonance line is overcome (T_e > 0.02 keV), the initial filling pressure (1 mtorr) is increased to 2 mtorr in 0.005 s for this sample case, while holding the impurity fraction constant. The bremsstrahlung power during this early phase increases to a maximum of only 0.3 MW/m at 0.012 s, and the cyclotron radiation is insignificant. The ion and electron diffusive energy losses are less than 0.01 MW/m during this tokamak-like startup phase.

The 1% oxygen impurity fraction was used above only for illustrative purposes to model the startup; the impurity fraction was taken to be zero during the burn in order to reduce the number of parameters that must be studied. The initial starting density may be reduced until electron runaway becomes serious. The initial inductive spike begins at toroidal electric fields of ~ 75 V/m-mtorr and drops to 20 V/m-mtorr after 15 μs for a filling pressure of 1 mtorr. As the density is decreased the initial large electric field is maintained for longer times. For ionization levels below 0.10 the electric field continues to increase until large numbers of electrons experience runaway, and the discharge fails to develop. An experimentally determined filling pressure of 0.1-0.2 mtorr[18] for a plasma radius of ~ 0.5 m gives an estimate of the minimum filling pressure. The startup code predicts the electric field to be greater than 20 V/m-mtorr during the period when

$n_e/n_o < 0.1$ at these minimum densities. Changing the applied voltage on the system proportionally varies the time scale. The magnitude of all quantities plotted in Fig. IV-3, however, remains virtually unchanged; doubling the voltage would decrease the timescale by a factor of two.

These calculations are used only to gain an understanding of the startup process. Estimates of the tolerable impurity level, allowable applied voltages and necessary starting densities indicate that the reactor (r_w = 1.5 m, ~ 10 kV/turn applied to plasma, 2.25-mtorr filling pressure) should successfully undergo startup in accordance to transients shown in Fig. IV-3. The energy dissipated during this phase would be insignificant. Consequently, the reactor burn can be modeled by simply starting the burn calculation at a plasma temperature in the range of 0.1 keV. This procedure ignores MHD activity during startup which will enhance the transport losses. As addressed in Sec. III.B.2, the issue of turbulent loss during field reversal and the procedure by which these losses can be minimized remain as an important but unresolved issue for the RFP.

b. Thermonuclear Burn. An optimal burn cycle is one in which the plasma ohmically heats the plasma to ignition (5-6 keV), alpha-particle heating raises the plasma temperature to 10-20 keV, and transport losses subsequently maintain a thermally stable burn until either a significant fuel burnup occurs, or the maintenance of a steady-state burn in a fueled system is permitted. All burn cycles investigated in this study are batch burn in which the initial charge of fuel is partially burned, quenched and flushed from the system in preparation for a subsequent burn cycle. This procedure avoids the potential difficulties associated with refueled operation, which includes divertors for impurity and ash removal and the injection of fuel during the burn. Reduced or eliminated pulsed-power requirements, leading to a higher engineering Q-value Q_E (and lower costs) and reduced thermal cycling of the first wall, make the steady-state option attractive, however, and warrants further study. Consideration of steady-state operation, is beyond the scope of this study, and, furthermore, the attainment of an acceptable energy balance in a long-pulsed mode of operation points out the unique near-term attractions of the RFP physics (Sec. III.A)

Burn dynamics have been investigated previously for purely classical transport losses.[19-21] In this case the plasma would ignite and subsequently continue to heat throughout the burn period until overheating forces a

premature plasma quench in order to maintain a realistic (upper) beta constraint. The dependence of β_θ on the normalized plasma radius, $x = r_p/r_w$, is approximated by

$$\beta_\theta = 1 - (x_m/x)^2, \qquad \text{(IV-2)}$$

where a constant current I_ϕ and negligible plasma pressure at $x = x_m$, (the minimum compression) is assumed. Ideal-MHD stability criteria were used in this case, allowing $x_m = 0.4$ to be achieved immediately after the full plasma current is established and before significant plasma heating has occurred. Using only classical losses (bremsstrahlung and cyclotron radiation and ion thermal conduction), the temperature would rise uncontrollably, causing the plasma to expand continuously to the wall with β_θ rising to a maximum of 0.84 at $x = 1$. According to ideal MHD theory, stable profiles are known to exist[1] for $\beta_\theta \lesssim 0.58$, requiring premature quench of the plasma in order to meet this limit. In order to satisfy the beta limit for the case of classical plasma losses, the plasma was expanded to the wall when β_θ reached 0.3 by sinusoidally decreasing the plasma current I_ϕ with a quarter-period of 0.1 s. The time-dependence of x and β_θ is shown in Fig. IV-4, along with the ion (T_i), electron (T_e) and alpha (T_α) temperatures, and the ohmic (W_{OHM}), radiation (W_{RAD}), alpha (W_α), direct-conversion (W_{DC}) and the resultant plasma internal (W_{INT}) energies. The direct-conversion of thermonuclear energy into electrical energy (W_{DC}) would result from the high-β plasma expanding against a nearly-constant magnetic field. For this case an empirical fit of results yielded an engineering Q-value $Q_E \simeq 1.6 I_\phi^{0.25}$ for $20 \lesssim I_\phi \lesssim 70$ MA, giving $3.4 \lesssim Q_E \simeq 4.6$. Satisfying physics and thermo-mechanical constraints led to a reactor design[19,20] with a 2-m minor radius, $I_\phi = 40$ MA and $Q_E \simeq 4.0$. The resultant burn dynamics are shown in Fig. IV-4 and uses an initial filling pressure of 2 mtorr to give a 2 MW/m^2 14.1-MeV neutron wall loading. All magnetic field energy trapped in the plasma at the termination of the burn was assumed to be resistively dissipated and to appear as thermal energy at the first wall. This dominant loss makes up ~ 50% of the total electrical loss in the system; the remaining losses were associated with the transfer losses, W_{ETS}, and joule losses incurred in the room-temperature magnets, W_{TR}. This situation suggests that increases in Q_E could be achieved if the fusion yield

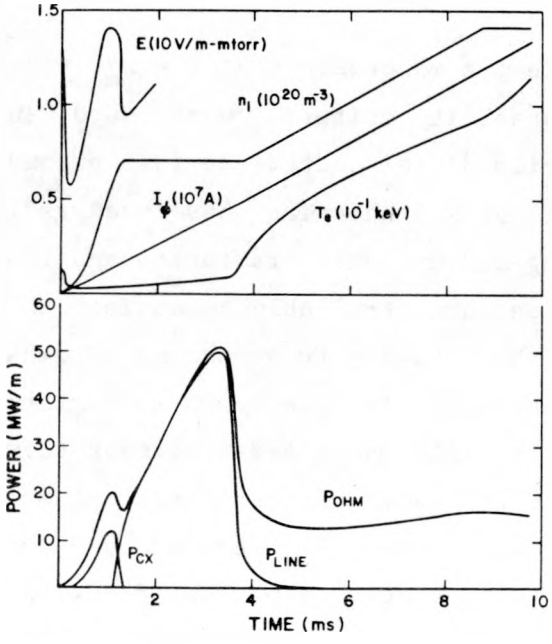

Fig. IV-3. Time-dependence of various plasma parameters and dominant powers for a tokamak-like RFPR startup.

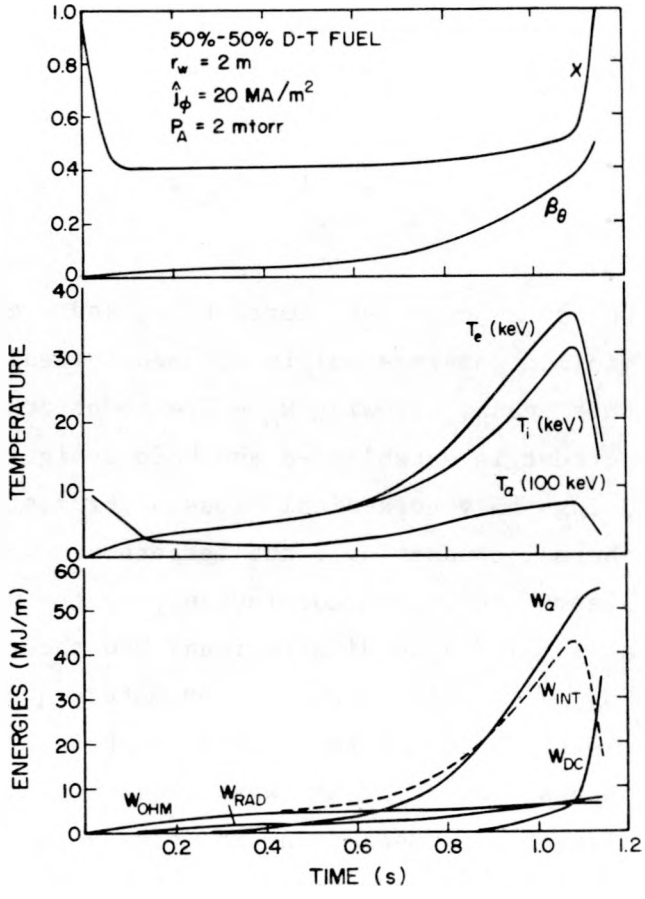

Fig. IV-4. Time-dependence of plasma parameters and energies for the 50/50 DT operating point.

for a given amount of trapped field energy at quench can be increased. In a general sense, the field energy required to give a specified neutron wall loading must be minimized. Higher fuel burnups achievable with thermally stable burns were needed to increase Q_E.

One method of temperature control examined in a previous study[19-21] lowered the initial tritium ratio below 0.50. The plasma then provides automatic temperature control by tritium burnup, resulting in decreased alpha-particle heating and natural radiative losses. An extensive parameter search[20] determined an optimum tritium fraction of 0.1 and allowed the plasma temperature to reach 50-60 keV and subsequently to decrease as a result of fuel burnup. The burn dynamics for this tritium-burnout control mode is depicted in Fig. IV-5. The longer burn times at high ion temperatures

resulted in greater joule losses in the normal conducting coils and a decreasing thermonuclear output, respectively. Consequently, a saturation and eventual decrease occurred in Q_E as the tritium fraction increased. Lower tritium fractions produce an insufficient yield. Using the optimal tritium fraction of 0.1, higher values of Q_E were found in the range 5-7 primarily as a result of the higher fuel burnup achieved (~ 10% for the 50-50% DT case compared to ~ 19% for the 90-10% DT case) at lower magnetic field levels. These improvements in Q_E were encouraging, although the burn time had increased by more than a factor of five because of the lower plasma reactivity (i.e. lower density, higher temperature).

In order to establish a more realistic plasma model that is consistent with longer plasma operation, burns cycles that operate near the minimum energy plasma state, as defined by Taylor[22-24] (Sec. III.B.2 and IV.C.2), and enforced beta limits, guided by resistive MHD calculations, were adopted. As detailed in Sec. IV. C.2, operating near the RFP minimum-energy state requires[10] $\Theta = B_\theta(r_w)/\langle B_\phi\rangle \simeq 1.5\text{-}2.0$ and $F = B_\phi(r_w)/\langle B_\phi\rangle \simeq -1.0$, where $\langle B_\phi\rangle$ is an integral average over the plasma cross section. Maximum poloidal betas of 0.25-0.40 are inferred by resistive-MHD stability calculations, although reactor-relevant, resistive numerical calculations are impossible because of present-day computer limitations. The plasma transport is also unknown, although use of accepted tokamak scaling[25-27] gives an anomalous electron thermal conduction with an energy confinement time $\tau_E \sim 200\ \tau_{Bohm}$.[21] The Bohm time is given by $\tau_{Bohm} = r_w^2\ B_\theta/63\ T_e$, where MKS units are used with T_e in keV Anomalous transport would be caused by local instabilities and may be the result of pressure-driven modes such as the resistive g-mode (Sec. III. B.1). As β_θ is increased transport would be enhanced, and a poloidal-beta limit at which the burn temperature would saturate results, yielding thermal stability. The use of an enhanced loss given by $\tau_E = 200\ \tau_{Bohm}$, or a loss mechanism that is driven explicitly by a limiting beta, $\tau_E \sim c/\exp[k(\beta_\theta - \beta_{\theta L})]$, where c and k are constants chosen to prevent $\beta_{\theta L}$ from being exceeded by more than a few percent,[3,4] give similar results for reactor sizes of economic interest (r_w = 1-2 m). In essence, therefore, Bohm-like scaling appears to be desirable for ignited systems which operate in a long-pulsed, constant radius, high-β mode.

A typical burn trajectory is shown in Fig. IV-6 using $\tau_E = 200\tau_{Bohm}$ as the anomalous energy loss time. A thermally stable burn results at a near optimal temperature of 10-20 keV, achieving a fuel burnup $f_B \sim 0.5$. A poloidal beta of ~ 0.4 is reached during the burn, which is ultimately terminated as burnup effects cause the ion temperature to fall below 8 keV. A similar trajectory is produced using an anomalous loss rate dictated by a limiting beta. Figure IV-6 is essentially reproduced using $\beta_{\theta L} = 0.3$ with a maximum poloidal β_θ of 0.32 being reached during the burn. In either case the burn trajectory is in good agreement with that suggested by the high-β model[10] for a minimum-energy configuration satisfying the Mercier criteria.

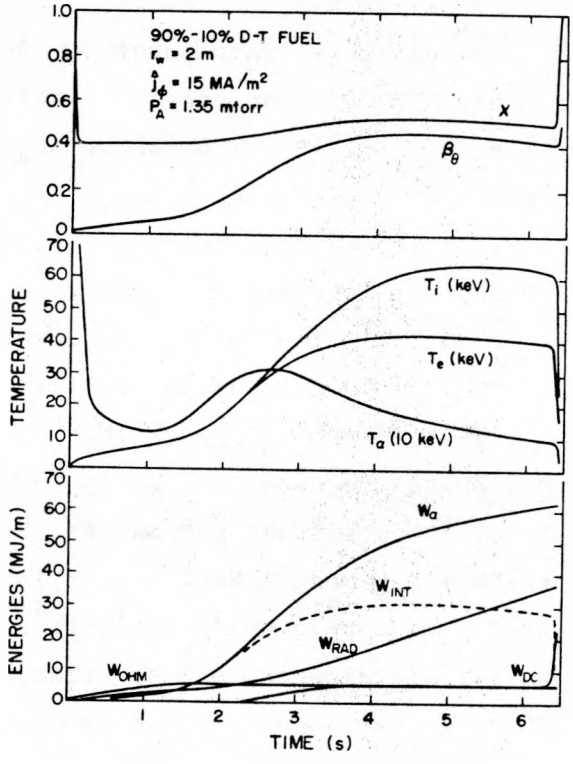

Fig. IV-5. Time-dependence of plasma parameters and energies for the 90/10 DT operating point.

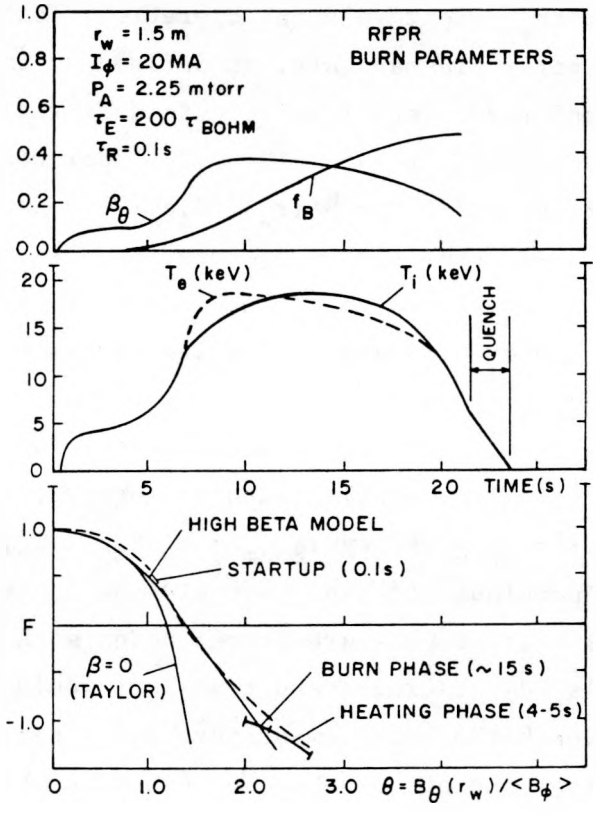

Fig. IV-6. RFPR (superconducting coils, air-core system) burn parameters using an energy confinement time $\tau_E = 200\ \tau_{Bohm}$. The burn trajectory is in good agreement with that required by the high-β model for a minimum-energy configuration.[10]

The burn trajectory shown in Fig. IV-6 is used as the reference case for evaluation of reactor performance in this study. This thermally stable burn achieves ignition in ~ 3 s. The ~ 15-s batch burn is followed by a 2-3 s quench period (Sec. IV.C.1.c) during which time the trapped magnetic field and post-burn plasma would be thermally dissipated at the first wall. Flushing the system with neutral gas, while continuously pumping out the ash, readies the chamber for the next pulse. The total burn cycle lasts for 21.6 s, 5-s is allowed for pumpout and refueling, and the total cycle would be 26.6 s long for a duty factor of 81.2%.

c. Rundown (Quench). Termination of the burn occurs as the toroidal current, I_ϕ, is decreased sinusoidally, allowing the plasma to relax to the wall. The plasma is then assumed to be wall confined, where heat loss is controlled by radiative processes and thermal conduction across magnetic field trapped inside the plasma. Taking bremsstrahlung radiation to be dominant and a thermal conduction time equal to 200 Bohm times, the characteristic loss times would be

$$\tau_{BR} = 0.36\ T_e^{3/2}/(\beta_\theta B_\theta^2\ Z_{eff}) \qquad \text{(IV-3)}$$

$$\tau_{COND} = 3.2\ r_w^2\ B_\theta/T_e, \qquad \text{(IV-4)}$$

where the Bessel function profiles (Appendix A) have been used. For typical plasma parameters at quench (T_e = 4 keV, β_θ = 0.1, B_θ = 2 T, Z_{eff} = 3, and r_w = 1.5) the loss times are τ_{BR} = 2.4 s and τ_{COND} = 3.6 s, implying the plasma energy would be extracted in approximately 2 s. On the basis of classical transport, thermal conduction losses are a factor of ~ 25 times less than predicted by Eq. (IV-4) and would be insignificant compared to the radiation loss. The plasma kinetic energy represents only 10% (β_θ = 0.1) of the total energy (plasma plus trapped field energy) remaining at quench, which implies that the plasma energy could be replaced several times by the ohmic dissipation of the field. A highly conservative assumption has been used throughout this model in that all of the field trapped inside the plasma at quench is postulated to be thermally dissipated at the first wall. Using classical resistivity, the timescale for energy addition to the plasma by ohmic heating is given by

$$\tau_{OHM} = 4.3\ r_w^2\ T_e^{3/2}\ \beta_\theta / Z_{eff}, \qquad \text{(IV-5)}$$

where the Coulomb logarithm has been taken as 15 and the Bessel function profiles again have been used. Equating the ohmic heating rate incurred during the resistive decay to the radiative and Bohm-like conduction losses, $1/\tau_{OHM} = 1/\tau_{COND} + 1/\tau_{BR}$, a plasma temperature of ~ 3 keV at $\beta_\theta \sim 0.075$ would be sustained until the magnetic field (B_θ = 2 T) has significantly decreased. Dividing Eq. (IV-5) by β_θ, this field decay time is estimated to be ~ 20 s. An enhanced loss mechanism, therefore, must be introduced to extract the total energy in the desired ~ 2 s. The introduction of neutral gas[28] during the quench period should permit efficient energy removal in the desired time.

The problem of energy extraction during quench must ultimately be subjected to a comprehensive and self-consistent study. Both the transient and quasisteady-state interactions of a neutral-gas blanket has been modeled for other concepts[28] by a one-dimensional MHD code that accounts for all ionized and neutral species interactions. Neutral-gas densities of ~ $3(10)^{19}/m^3$ were required to extract the plasma energy in 2-3 s with insignificant wall effects. Although large surface currents were present in this high-β plasma,[28] the increase in plasma energy resulting from ohmic heating amounted to only ~ 25%. Similar effects are expected for the RFPR postburn plasma. These encouraging calculational results imply that the plasma energy can be extracted efficiently and that the dissipation of trapped field may not be as severe as the RFP plasma model has assumed. In fact, employing a controlled shutdown in which the plasma current is decreased as the plasma edge cools may allow a large fraction of the trapped field to be released and recovered. Since ~ 40% of the total recirculating electric power is required to replace this dissipated field energy, significant increases in the engineering Q-value will occur if a portion of this quench field is recovered.

It is noted that the qualitative description given in this section of the plasma rundown or quench process has been based on classical or anomalous transport. Even state-of-the-art numerical models[28] cannot describe or assess the importance of collective processes. This problem is sufficiently complex to predict that a clear resolution will not be available until devices can

generate and quench reactor-grade, thermonuclear plasmas. The question of a controllable rundown has only recently been seriously considered for the larger tokamak experiments presently being designed. This issue is important for the long-pulsed RFPR because of the narrow 1-5 s "window" available to restart the device; quench times that fall short of this desirable range may led to undesirable pulsed thermal loading of the wall, whereas quench times that are in excess of this range will lead to a lower duty cycle and undesirable blanket/coolant temperature oscillations, requiring perhaps the addition of heretofore unneeded thermal capacity to the engineering cooling systems.

2. Stability and Equilibrium. Analytic work by Taylor[22-24] predicts that the lowest energy state for negligible plasma beta inside a perfectly conducting shell is the reversed-field force-free configuration for $\Theta > 1.2$, where $\Theta = B_\Theta(r_w)/\langle B_z \rangle$ and $\langle\rangle$ denote an integral average inside the conducting shell. Using classical diffusion coefficients, numerical calculations[10] have shown the existence of high-β, stable states ($\beta_\theta = 0.3$-0.4) at $\Theta = 1.5$-2.0 and $F = -0.5$ to -1.0, where $F = B_\phi(r_w)/\langle B_\phi \rangle$. These conditions are denoted as the high-β model,[10] which is shown as a plot of F versus θ in Fig. IV-6 along with the Taylor condition. The actual trajectory in $F - \Theta$ space followed during the burn is also shown. In obtaining this F-Θ trajectory the poloidal field, B_θ, is increased sinusoidally (0.1-s quarter period) on the same timescale that the external B_ϕ field is completely reversed. Both fields are then held constant during the burn. The resultant F-Θ profile is in good agreement with the high-β model and could be improved if external field programming is used. Operation in this mode, of course, will require a conducting first wall that can electrically respond to plasma changes on the timescale of the risetime (0.1 s). The required thickness of copper at a useful blanket temperature (550-650 K) corresponds to 20 mm. Copper has been selected for the conducting first wall and, as will be seen, has both positive and negative impact on the blanket design and overall thermal cycle (Sec. V).

For times longer than 0.1 s external feedback conductors must provide the image currents required for stability. These conductors would be room-temperature copper coils approximately 0.1-m thick and located immediately outside the high-temperature blanket. The feedback system must sense instabilities and respond on a 0.1-s timescale, and the conducting first-wall shell provides wall stabilization on a shorter timescale. Gross plasma

equilibrium is provided by the poloidal field system, which produces both a pure poloidal field and a vertical field necessary to maintain the plasma position near the center of the plasma chamber. An analysis of the slow (~ 1 - 10 Hz) feedback requirements for this mode of RFPR operation could not be made within the scope of this study, although a simple analysis of the equilibrium field configuration is given (Sec. V.F).

D. Costing Model

Economic guidelines recommended for national use by fusion systems studies[29,30] are used for the costing framework, in spite of the fact that these procedures and guidelines are still under development. The difficulties in comparing various cost models have led to the development of this common costing procedure and eventually should provide the needed uniformity in assessing different concepts. The costing guidelines describe uniform accounting categories and procedures, although a uniform cost data base is yet to be nationally adopted. A cost data base, therefore, has been generated by this study to provide an interim optimization tool and to facilitate comparisons. It is emphasized that absolute cost values are intended only for the intercomparison of reactor designs and are not intended for absolute comparisons with existing energy technologies on the basis of present costs.[30]

The total capital cost of the plant is comprised of direct, indirect, and time-related (escalation and interest) costs. Direct costs are quoted on the basis of 1978 prices, result from the purchase of materials, equipment and labor, and take into account allowances for spare parts and contingencies. Indirect costs, taken as a percentage of the direct costs, result from support activities necessary to complete the project and are divided into three major accounts: 15% for construction facilities, equipment, and services; 15% for engineering and construction management services; and 5% for taxes, insurance, staff training, and plant startup. Escalation and interest are computed as a percentage of the direct plus indirect costs, assuming a 10-year construction period. Aggregrate percentages of 33.8% and 64.4%,[30] respectively, result for an escalation rate of 5% and interest rate of 10%. Having determined the total capital cost c_D($/kWe), the power cost c_p (mills/kWeh) is computed on the basis of a 15% return on capital investment, an added 2% of the total capital cost for operating expenses and a power factor of 0.85.

Like most conceptual designs of fusion reactors, the depth of analysis is not sufficient to allow cost estimates to be made on an item-by-item basis. Consequently, a strong reliance had to be made on the use of grossly integrated unit costs. This costing procedure, detailed cost breakdown, and unit cost data base are summarized in Appendix B. A recent balance-of-plant (BOP) study[12] of a number of alternative fusion concepts, including the RFPR, gives a more detailed breakdown of BOP costs and power requirements; this EPRI-sponsored study,[12] however, is based completely on the design information contained herein, although the ad hoc addition of a helium coolant system to the latter BOP design study will cause serious inconsistencies.

E. Development of Point Design

1. Physics Operating Point. The burn trajectory shown in Fig. IV-6 results from the thermally-stable batch-burn fuel cycle discussed in Sec. IV.C.1.b. An initial DT filling pressure of 2.25 mtorr yields a 14.1-MeV wall loading of 2.75 MW/m^2 for the 21.6-s startup/burn/quench phases and a 5-s downtime (81% cycle duty factor). The thermal and mechanical response of the first wall is computed simultaneously with the plasma response (Sec. IV.C.1.b) and system energy balance (Sec. IV.B); both the thermal and mechanical response of the first wall appear acceptable, these aspects of the blanket design being addressed in more detail in Sec. V.

Previous studies[31] have investigated the economic trade-offs associated with high wall loading and increased power rating versus a lower plant availability because of the shortening of wall replacement intervals. An optimal first-wall loading of 2.0-3.0 MW/m^2 for 316 stainless steel at 800 K was reported.[31] Using copper as the first-wall material may change these conclusions, although the aforementioned wall loading is considered reasonable.[32] Fulfilling the stability criteria established for this study (Sec. IV.C.2) and requiring $\beta_\theta \lesssim 0.3\text{-}0.4$ during the burn inherently requires a 20-MA plasma current that ohmically heats the plasma to ignition in ~ 3 s. A first-wall radius of 1.5 m results in the desirable burn trajectory shown in Fig. IV-6 and allows a manageable gross plant output (< 1000 MWe) with a large aspect ratio torus ($A = R/r_w \simeq 8 - 10$) for enhanced accessibility and maintainability.

It is emphasized that the physics design point adopted for this study represents the result of examining a number of approaches to the RFPR, some of which were described in Sec. IV.C. This evolution of the present physics

design point is not described in detail here, but has been quantified in Ref. 21 and Appendix E. More often than not this evolution and development has been induced by a continual interaction between fundamental physics constraints, the projected response and performance of a reactor-like plasma, the resulting system energy balance, the feasibility of reactor component design (particularly blanket/first-wall, magnets, and energy storage/transfer systems), and final costs. The final physics design point (Fig. IV-6, Sec. IV.F) presented here is a culmination of this complex interactive process, the logic for which can be made comprehensible only through hindsight.

2. Reactor System Components. The creation of a reactor embodiment based on the physics design point described in the previous section was guided by the desire to:

- Arrive at an economic power system
- Use more-or-less conventional engineering materials and technologies
- Use a direct-cycle steam system
- Develop a reliable and readily maintainable system based on the RFP potential for a relatively open magnet structure.

The result of a synthesis of these essential elements is depicted schematically in Fig. IV-7. The basic features of this system that have been subjected to engineering scrutiny in Sec. V are:

- A copper first wall of 20-mm thickness that is cooled by a separate, pressurized-water coolant circuit.
- A stainless-steel blanket that is packed with granular Li_2O breeding and heat-recovery material. Thermal energy is recovered from this packed-bed blanket by water/steam U-tubes that penetrate the blanket radially and are manifolded in the annular region formed by the blanket and radiation shield.
- Use of a borated-water shield contained in hemi-cylinder stainless steel tanks.
- Modularization of the reactor torus into ~ 40 units of ~ 2-m length and composed of the above mentioned three elements (first-wall/blanket/shield).
- Use of permanently fixed toroidal field coils that are sufficiently spaced to permit reactor modules to be extracted through intervening regions.

- Elimination of vacuum seals between reactor modules by supporting the RFPR torus within an all-encompassing vacuum tunnel.
- Placement of the fixed poloidal/vertical field coils in an accessible area without unacceptable increases in stored magnetic energy.

In addition to providing the electrically conducting medium required for short-term plasma stability, the high-strength copper first wall contributes to neutron multiplication for enhanced tritium breeding in a relatively thin Li_2O blanket (0.5 m), while conservatively withstanding a moderate thermal cycle imposed by the RFPR batch-burn operation. Because of the large thermal capacity of the blanket, all systems outside of the first-wall operate in a thermodynamic steady state, providing continuous and constant thermal power to the steam turbines.

The pulsed superconducting magnets are energized by homopolar motor generators which provide a low-cost source of ~ 10 GJ of energy deliverable in ~ 0.1 s. Early conceptual designs[19-21] were based on normal-conducting coils and an iron-core poloidal-field transformer. A simplified circuit, shown in Fig. IV-8, for the poloidal field system would take the form of a parallel connection of a capacitor (homopolar motor/generator) and the inductors L_i and L_e associated with the regions (or magnetic fluxes) internal and external to the poloidal field coil, respectively. An iron core ($L_{EX} \to \infty$) ideally couples the current in the poloidal coil, I_c, to the plasma current, I_ϕ, giving $I_c \simeq I_\phi$, and requires a total stored energy in the homopolar generator of $0.5\ L_i I_p^2$. For an air-core system the current swing in the poloidal-field coil is $L_e \Delta I_c = (L_e + L_i) I_\phi$, and, taking $L_e \sim L_i$, the maximum coil current is also $I_c \simeq I_\phi$ when using bipolar-current operation ($-I_c$ to $I_c \to \Delta I_c = 2I_c$). In this case the energy is initially stored in the magnetic flux external to the poloidal coil. Upon initiation of the plasma current, the homopolar generator is used as a transfer capacitor and need have only one-half the energy (assuming an ideal case of $L_e \sim L_i$) required for the iron-core system. Omission of the massive and costly iron core (1000 MWe RFPR requires ~ 700 Wb of flux or ~ 10^8 kg of iron for typical reactor dimensions) is the primary motivation for using an air core. Through the use of bipolar-current operation and an air-core system little or no increase results in coil requirements, and a decrease occurs in the size of the energy storage system (used as a transfer capacitor) when compared to the iron-core system.[21] Maintaining toroidal plasma equilibrium, however, requires the addition of a

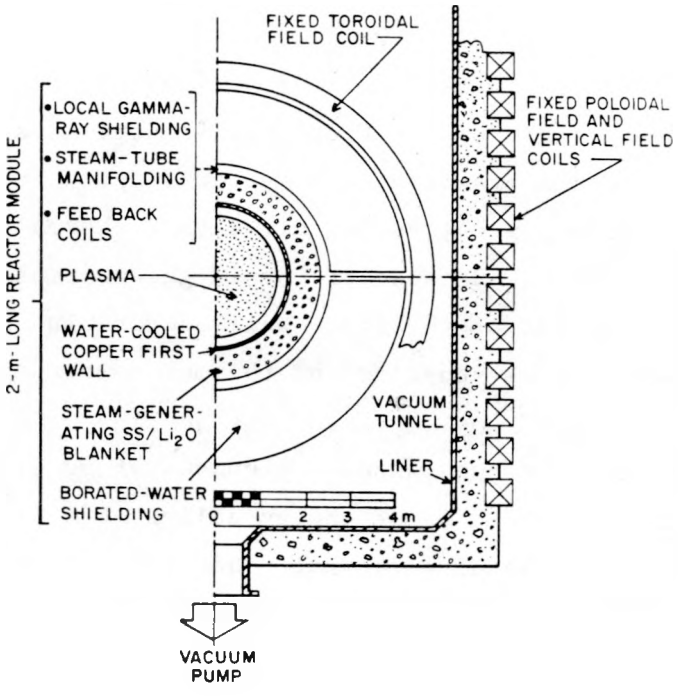

Fig. IV-7. Schematic cross-sectional view of RFPR module, vacuum tunnel, and magnet systems showing relative positions and sizes of major core component.

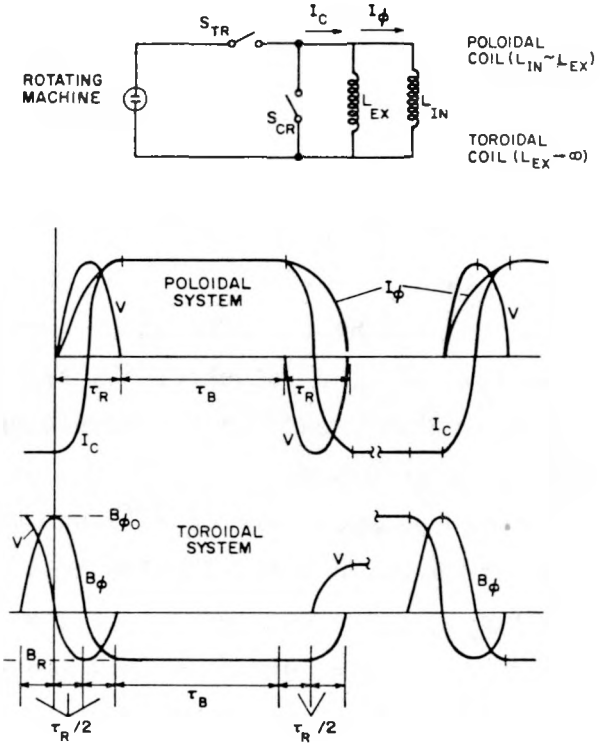

Fig. IV-8. Schematic diagram of homopolar-generator driven circuit for TFC and PFC systems. The voltage is 5-6 kV, risetime τ_R = 100 ms, and τ_B ~ 21 s.

vertical field by the poloidal field circuit, which complicates the above argument, although the basic conclusions remain unchanged. A detailed discussion of the air-core poloidal system used in the final design is given in Sec. V.F.

The decision to use superconducting coils was based entirely upon economic considerations. Normal-conducting coil thicknesses of 1.0-1.4 m (poloidal plus toroidal coil) were found to give a minimum cost system; thinner coils enhance the resistive losses while thicker coils are simply to costly. These coils can be replaced by smaller superconducting coils for approximately the same cost; furthermore, the resistive dissipation is now eliminated resulting in a higher Q_E and even lower total cost. Superconducting coils used in the final design are also described in Sec. V.F.

F. Point-Design Parameters

1. Physics Parameters. The time response of the physics design point selected for engineering analysis is given in Fig. IV-6. Time-averaged values of important physics parameters are summarized in Table IV-I.

TABLE IV-I

AVERAGE PLASMA PARAMETERS DURING THE RFPR BURN PHASE

PARAMETER	VALUE
Plasma minor radius, r_p(m)	1.5
Plasma major radius, R(m)	12.7
Plasma aspect ratio, $A = R/r_p$	8.47
Toroidal current, I_ϕ(MA)	20.0
Average toroidal current density, j_ϕ(MA/m^2)	2.8
Initial toroidal bias field at coil, B_{ϕ_o}(T)	2.0
Reversed toroidal field at plasma surface, B_R(T)	-1.3
Poloidal field at plasma surface, B_θ(T)	3.0
Poloidal field at coil, $B_{\theta c}$(T)	2.0
Pinch parameter during burn, $\Theta = B_\theta(r_w)/\langle B_\phi \rangle$	2.0
Reversal parameter during burn, $F = B_\phi(r_w)/\langle B_\phi \rangle$	-1.0
Filling pressure, P_A(mtorr)	2.25
Average poloidal beta, β_θ	0.3
Ion temperature, T_i(keV)	15-20
Electron temperature, T_e(keV)	15-20
Electron density, n_e(m^{-3})	$2.0(10)^{20}$
Electron-electron collision frequency, ν_{ee}(1/s)	10,000
Ion-ion collision frequency, ν_{ii}(1/s)	170.
Ion or electron mean-free-path, $\lambda_{ii} = \lambda_{ee}$(m)	5900
Ion Larmor radius, r_L(mm)	8
Electron collisionality, ν_{ee}/ω_{ce}	$2.2(10)^{-8}$
Ion collisionality, ν_{ii}/ω_{ci}	$1.3(10)^{-6}$
$\lambda_{ii}/r_p = \lambda_{ee}/r_p$	3900
Average energy confinement time, $\langle \tau_E \rangle$(s)	1.0
Lawson parameter, $\langle n\tau_E \rangle$(s)	$2.0(10)^{20}$
Time-integrated Lawson parameter, $\langle n\tau \rangle$(s/m^3)	$3.7(10)^{21}$

TABLE IV-II

RFPR DESIGN SUMMARY: AIR-CORE POLOIDAL TRANSFORMER, SUPERCONDUCTING COILS

PARAMETER	VALUE
First-wall radius, r_w(m)	1.5
Major radius, R(m)	12.7
Poloidal coil current, $I_{\phi c}$(MA)	45.5
Plasma current, I_ϕ(MA)	20.0
Toroidal current density, j_ϕ(MA/m^2)	5.4
Filling pressure, P_A(mtorr)	2.25
Burnup, f_B	0.54
Lawson parameter during burn, $\langle n\tau_E \rangle$(10^{20} s/m^3)	2.0
Required toroidal coil energy, W_{TOR}(GJ)	3.7
Required poloidal coil energy, W_{POL}(GJ)	11.0
Burn time, τ_B(s)	21.6
Cycle time, τ_C(s)	26.6
Average 14.1-MeV wall loading, I_w(MW/m^2)	2.7
Engineering Q-value, Q_E	5.8
Recirculating power fraction, $\varepsilon = 1/Q_E$	0.17
Plant efficiency, $\eta_p = \eta_{TH}(1-1/Q_E)$	0.25
Total thermal power, P_{TH}(MWt)	3000
Thermal power density, p_{TH}(MWt/m^3)[a]	0.50
Gross electric power, P_{ET}(MWe)	903.
Net electric, P_E(MWe)	750.

[a]Based on volume enclosed by and including superconducting coils.

2. Engineering Parameters. Key engineering parameters for the interim design point are presented in Table IV-II. The reactor energy flow is listed in Table IV-III, from which the recirculating power, as described in Section IV.B, is computed. Appendix C contains a detailed table of major reactor nuclear island and balance-of-plant parameters. Cost optimization[21] (Appendix E) has lead to an air-core poloidal transformer with bipolar current operation; this approach minimizes the amount of external energy storage (homopolar generator) and the coil current. A cost advantage also results

TABLE IV-III

REACTORS ENERGIES REQUIRED FOR CALCULATION OF THE ENGINEERING Q-VALUE $Q_E(\eta_{TH} = 0.30)$

PARAMETER	VALUE (MJ/m)
Initial plasma, W^o_{INT}	0.05
Final plasma, W_{INT}	2.5
Radiation, W_{RAD}	28.1
Ohmic heating, W_{OHM}	7.1
Thermal conduction, W_{COND}	147.5
Direct conversion, W_{DC}	0.7
Eddy-current losses in blanket, W_{EB}	1.5
Field in plasma at end of burn, W_B^{IN}	21.5
ETS transfer loss, W_{ETS}	8.1
Neutron energy (16.3 MeV/n), W_N	792.
Auxiliary requirements[a], W_A	14.3
Recirculating power, W_C	51.0

[a]Refrigeration requirements for the cryogenic systems account for ~ 21% of the auxiliary requirements.

when superconducting versus normal coils are used because of the elimination of transport losses during the extended burn period.

3. Economic Parameters. Table IV-IV contains a summary of the RFPR plant costs using the economic guidelines[29,30] described in Sec. IV.D. Appendix D gives the cost data base, resultant plant costs for each accounting category, and the cost reference list. Reactor plant equipment costs comprise 48% of the total reactor direct capital costs. Figure IV-9 gives a graphical display of the major component cost.

4. Design-Point Sensitivities. Although the engineering analysis (Sec. V) has focused on the design point given in Fig. IV-6 and Tables IV-I through IV-IV, important uncertainties associated with assumptions made in developing the design basis (Sec. IV.A-D.) exist. The assumed maximum allowable beta and the energy transfer/storage (ETS) efficiency, η_{ETS}, were identified as two particularly important variables. Figure IV-10 illustrates the dependence of reactor cost, c_D(\$/kWe) and efficiency, Q_E, on the maximum allowable β for the fixed parameters indicated. This parameter search essentially varied filling density and toroidal current to maintain a constant

TABLE IV-IV

RFPR ECONOMIC SUMMARY

ACCOUNT TITLE		MILLION DOLLARS
Land and land rights		2.5
Structures and site facilities		216.5
Reactor plant equipment		397.1
Blanket and first wall	25.4	
Breeding material	3.3	
First wall and structural material	22.1	
Shield	16.6	
Magnets	66.9	
Toroidal	38.8	
Poloidal	28.0	
Reactor structure and support	12.8	
Reactor vacuum (Roots blowers)	18.7	
Power supply and switching	117.6	
Auxiliary cooling	38.0	
Radwaste treatment and disposal	6.9	
Fuel handling and storage	1.1	
Other reactor plant equipment	10.9	
Instrumentation and control	16.0	
Spare parts allowance	16.5	
Contingency allowance	49.6	
Turbine plant equipment		138.5
Electric plant equipment		56.7
Miscellaneous plant equipment		15.4
Special materials		1.3
Total reactor direct capital cost		828.0
Construction facilities, equipment and services (15%)		124.2
Engineering and construction management services (15%)		124.2
Other costs (5%)		41.4
Interest during 10-year construction (64.4%)		719.8
Escalation during 10-year construction (33.8%)		377.8
Total reactor capital cost		2215.4
Plant factor		0.85
Direct investment cost ($/kWe)		1104
Total investment cost ($/kWe)		2954
Capital return 15% (mills/kWeh)		59.8
Operating 2% (mills/kWeh)		6.5
Power cost (mills/kWeh)		66.3

burn time, τ_B, cycle time, τ_C, and net electrical power, P_E, while maintaining the reactor dimensions, r_w and R, fixed. Serious degradation in reactor performance is expected if the maximum-allowable β_θ falls below ~ 0.15. Below this beta limit, longer refueled burns would be required in order to recover and/or improve the performance of the design point selected. Figure IV-11 gives the dependence of c_D ($/kWe) and Q_E on the ETS efficiency. The value η_{ETS} = 0.95 appears feasible with considerable development, but η_{ETS} values appreciably below the design value can be tolerated without serious degradation in reactor performance.

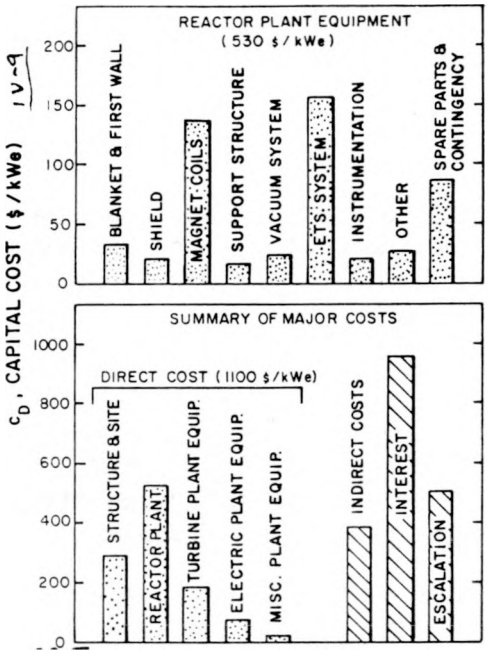

Fig. IV-9 Summary of plant reactor costs and major cost components.

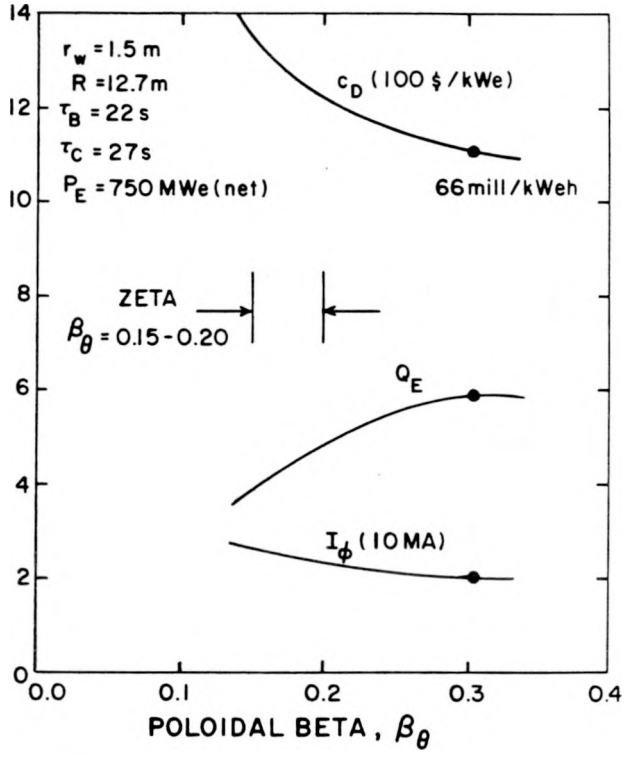

Fig. IV-10 Sensitivity of RFPR direct capital cost, c_D, engineering Q-value, Q_E, and toroidal current, I_ϕ, on the maximum allowable β_θ for the fixed parameters shown.

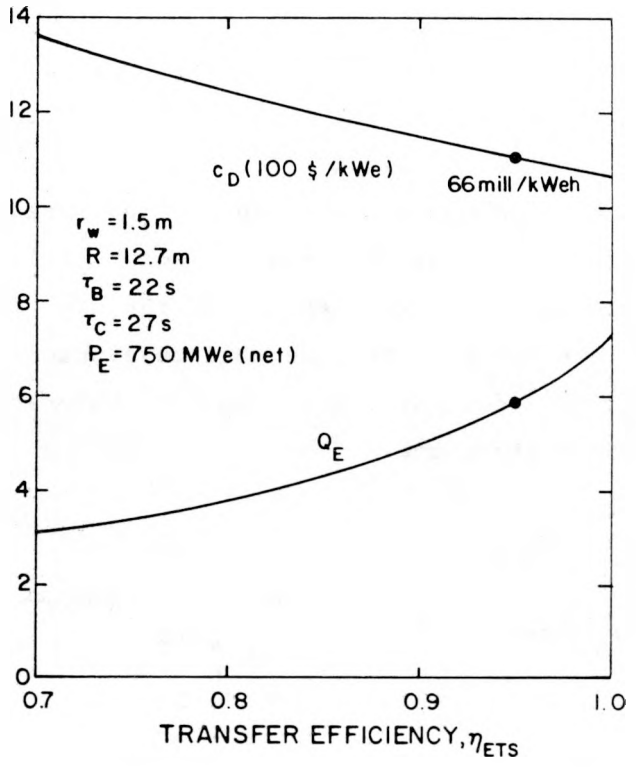

Fig. IV-11. Sensitivity of RFPR direct capital cost, c_D, and engineering Q-value, Q_E, on the intrinsic efficiency of (homopolar) transfer/storage efficiency.

REFERENCES

1. D. A. Baker and J. N. DiMarco, "The LASL Reversed-Field Pinch Program Plan," Los Alamos Scientific Laboratory Rept. LA-6177-MS (1975).

2. H. A. B. Bodin, T. E. James, and A. A. Newton, "A Pulsed Fusion Reactor Based on the Toroidal Pinch." Proc. of the BNES Nucl. Fus. Reac. Conf., Culham, United Kingdom, 1969, pp. 255-266.

3. H. A. B. Bodin, E. P. Butt, R. Carruthers, T. E. James, A. A. Newton, and G. Rostagni, "The Pulsed Reverse Field Pinch Reactor", Plasma Phys. and Cont. Nucl. Fus. Res., (Fifth International Conf., Tokyo, 1974), Vol. 3, p. 631.

4. B. C. Yeung, J. W. Long and A. A. Newton, "Reactor Burning Calculations for a Model Reversed Field Pinch," Third Topical Conf. on Pulsed High Beta Plasmas, Culham, United Kingdom, 1975, pp. 575-579.

5. J. D. Lawson, "Reversed Field Pinch Reactor Study, I. Physical Principles," UKAEA, Culham Laboratory report CLM-R171 (1977).

6. R. Hancox and W. R. Spears, "Reversed Field Pinch Reactor Study, II. Choice of Parameters," UKAEA, Culham Laboratory report CLM-R172 (1977).

7. A. A. Hollis and J. T. D. Mitchell, "Reversed Field Pinch Reactor Study, III. Preliminary Engineering Design," UKAEA, Culham Laboratory report CLM-R173 (1977).

8. R. Hancox, M. Bagatin, L. J. Baker, S. Bobbio, H. J. Crawley, and P. A. Davenport, "A 600 MW(e) Reversed Field Pinch Reactor Study," in Fusion Reactor Design Concepts (IAEA Workshop on Fusion Reactor Design, Madison, Wisconsin, 1977), IAEA, Vienna (1978), p. 319 (Also Culham Laboratory report CLM-P 501).

9. R. Hancox and C. R. Walters, "A Reversed Field Pinch with Superconducting Windings," Seventh International Conference on Plasma Physics and Controlled Nuclear Fusion Research, Innsbruck, Austria, 1978, paper IAEA/CN/37 I-1.

10. A. A. Newton, Li Yin-An, J. W. Long, and B. C. Yeung, "Numerical Investigation of Reversed Field Pinches," Third Topical Conf. on Pulsed High-β Plasma, Culham, United Kingdom, 1975,pp. 323-328.

11. R. W. Moses, Los Alamos Scientific Laboratory, and R. Nebel, University of Illinois, unpublished Reversed-Field Pinch Code Development (1979).

12. N. Amherd (ed.), "Balance-of-Plant Study of Alternative Fusion Reactor Concepts," Electric Power Research Institute report to be published (1979).

13. R. Papoular, "The Genesis of Toroidal Discharges," Nucl. Fus. 16, 37-45 (1976).

14. W. Bernstein, F. F. Chen, M. A. Heald, and A. Z. Kranz, "Runaway Electrons and Cooperative Phenomena in B-1 Stellarator Discharges," Phys. Fluids 1, 430-437 (1958).

15. T. Coor, S. P. Cunningham, R. A. Ellis, M. A. Heald, and A. Z. Kranz, "Experiments on the Ohmic Heating and Confinement of Plasma in a Stellarator," Phys. Fluids 1, 411-420 (1958).

16. J. M. Berger, I. B. Bernstein, E. A. Frieman, and R. M. Kulsrud, "On the Ionization and Ohmic Heating of a Helium Plasma," Phys. Fluids 1, 297-300 (1958).

17. A. V. Gurevich, "On the Theory of Runaway Electrons," Soviet Physics JETP 12, 904-912 (1961)

18. W. M. Burton, E. P. Butt, H. C. Cole, A. Gibson, D. W. Mason, and R. S. Pease, "Plasma Loss in ZETA," Nucl. Fus., Supplement 3, 903-919 (1962).

19. R. L. Hagenson, R. A. Krakowski, and K. I. Thomassen, "A Toroidal Fusion Reactor Based on the Reversed-Field Pinch (RFP)," in Fusion Reactor

Design Concepts (IAEA Workshop on Fuson Reactor Design, Madison, Wisconsin, 1977), IAEA, Vienna (1978), pp. 337-355.

20. R. L. Hagenson, "A Toroidal Fusion Reactor Design Based on the Reversed-Field Pinch," Ph.D. Dissertation, Iowa State University, 1978, (also Los Alamos Scientific Laboratory report LA-7399-T (1978)).

21. R. L. Hagenson and R. A. Krakowski, "A Cost-Constrained Design Point for the Reversed-Field Pinch Reactor," American Nucl. Soc. Third Topical Mtg. on the Technology of Cont. Nucl. Fus., Santa Fe, New Mexico, 1978, Vol. 1, pp. 90-100.

22. J. B. Taylor, "Relaxation of Toroidal Plasma and Generation of Reverse Magnetic Fields," Phys. Rev. Lett. 33, 1139-1141 (1974).

23. J. B. Taylor, "Relaxation of Toroidal Discharges to Stable States and the Generation of Reverse Magnetic Fields," Fifth IAEA Conf. on Plasma Physics and Controlled Fusion, Tokyo, Japan, 1974, Vol. 1, pp. 161-167.

24. J. B. Taylor, "Relaxation of Toroidal Discharges," Third Topical Conf. on Pulsed High β Plasmas, Culham, United Kingdom, 1975, p. 59.

25. A. Hirose and H. M. Skarsgard, "On the Energy Confinement Times of Tokamaks," Nucl. Fusion 18, 1737-1742 (1978).

26. A. B. Berlizov, G. A. Bobrovskij, A. A. Bagdasarov, N. L. Vasin, A. N. Vertiporokh, and V. P. Vinogradov, "First Results from the T-10 Tokamak," Sixth Conf. on Plasma Physics and Controlled Nucl. Fus. Res., Berchtesgaden, 1976, Vol. 1, pp. 3-18.

27. E. Apgar, B. Coppi, A. Gondhalekar, H. Helava, D. Komm, and F. Martin, "High-Density and Collisional Plasma Regimes in the Alcator Programme," Sixth Conf. on Plasma Phys. and Controlled Nucl. Fus. Res., Berchtesgaden, 1976, Vol. 1, pp. 247-266.

28. T. A. Oliphant, G. E. Gryczkowski, and T. Kammash, "Transient Charge-Exchange Effects in a Neutral-Gas Layer," Nucl. Fus. 16, 263-268 (1976).

29. S. C. Schulte, T. L. Willke, and J. R. Young, "Fusion Reactor Design Studies-Economic Evaluation Guidelines," Battelle (Pacific Northwest Laboratories) report PNL-SA-2648 (1978).

30. S. C. Schulte, personal communication, Battelle, Pacific Northwest Laboratories (1978).

31. G. M. Fuller, "Fusion Reactor First Wall/Blanket Systems Analysis," EPRI Contract No. RP 472-1, McDonnell Douglas Astronautics Company, St. Louis, Missouri, (September 1977).

32. D. L. Kummer (Principal Investigator), "Alloys for the Fusion Reactor Environment," Prepared for Division of Magnetic Fusion Engineering of the Department of Energy by McDonnell Douglas Astronautics Company, St. Louis, Missouri (April 1977).

V. REACTOR ENGINEERING AND TECHNOLOGY

Using the design bases given in Secs. IV.B-D, following the development procedure outlined in Sec. IV.E, and referring to the design point summarized in Sec. IV.F, performance requirements of important engineering systems have been estimated. This section presents the results of this engineering analysis, after a brief description of the RFPR operation is given. Because of temporal and fiscal limits imposed on this study, only first-wall/blanket and power conversion subsystems have been examined in detail. Treatment of magnets, energy transfer/storage, vacuum, tritium, control and maintenance systems should be considered preliminary.

A. Reactor Plant Operation and Description

The RFPR would operate as an unrefueled (batch-burn) system in which preionization, field reversal, and ignition by ohmic heating would occur in a run-up period $\tau_R \simeq 0.1$ s. The transient burn would occur for $\tau_B = 21.6$ s in a 12.7-m major radius torus with first-wall radius equal to 1.5-m. Approximately 50% of the 2.25-mtorr DT would fuse, yielding a total thermal energy each pulse of 79.8 GJ (3000 MWt average thermal power) and an average fusion neutron wall current of 2.7 MW/m^2. The recirculating power fraction for the 750 MWe(net) plant would be $\varepsilon = 1/Q_E = 0.17$.

The long-pulsed operation is depicted by Fig. V-1 in terms of the poloidal field coil (PFC) current, $I_{\phi c}$, the toroidal plasma current, I_ϕ, and the toroidal fields, $B_{\phi o}$(initial) and $-B_R$(reversed). Current is first driven in the toroidal field coil (TFC) to produce a uniform toroidal bias field $B_{\phi o} = 1.6$ T. At this time (t = 0) the plasma is preionized, and a constant current, $I_{\phi c} = 32$ MA, is flowing in the PFC. The PFC current is reversed in the presence of the low-temperature but electrically conducting plasma by switching the PFC energy temporarily to a homopolar motor/generator (a capacitive element) and then back to the PFC in the time $\tau_R \simeq 0.1$ s. It is noted that the homopolar motor/generator serves only as a transfer element, in that the PFC energy (11.0 GJ) resides primarily within the superconducting coil system. Upon reversal of the PFC current, $I_{\phi c}$, a current I_ϕ is induced in the plasma during the time when the toroidal field, B_ϕ, continues to resonate inductively. The main energy store for the TFC system is also a homopolar motor/generator (3.7 GJ). The toroidal field ultimately becomes negative in the vacuum/blanket/shield region between the TFC and the plasma edge, the B_ϕ field within the plasma being trapped and remaining positive. At

the time when B_ϕ is fully reversed outside the plasma at a value $-B_R$ and the plasma current has reached a maximum, both PFC and TFC systems are "crowbarred" (i.e., the homopolars are short-circuited from the coils). Both I_ϕ and $-B_R$ are maintained constant throughout the burn period, τ_B, by a self-reversal mechanism that is characterized by an energy confinement time equal to 200 Bohm diffusion times. Figure V-2 depicts the time dependence of ion and electron temperature, poloidal beta, and fractional burnup during the ~ 15-s ignited stage. It is noted that nearly ~ 3-s are required to achieve ignition. The burn phase is terminated when the ion temperature rapidly decreases through 8 keV because of fuel burn-up and alpha-particle accumulation. At this point the crowbar switches in both the TFC and PFC electrical circuits are opened. Using the homopolar motor generator as a transfer element, the PFC current is again reversed, and the associated energy is stored in the superconducting poloidal coils. The toroidal field energy not trapped in the plasma is also transferred to the homopolar motor/generator used for the TFC system energy storage. All field energy trapped within the plasma is assumed to be thermally dissipated during the plasma quench, and the coil/homopolar transfers occur with an intrinsic machine efficiency of 95%.

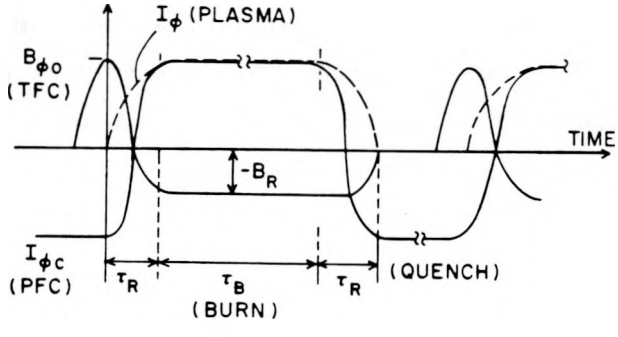

Fig. V-1. Typical RFPR burn cycle depicted in terms of plasma current poloidal coil current, and toroidal field.

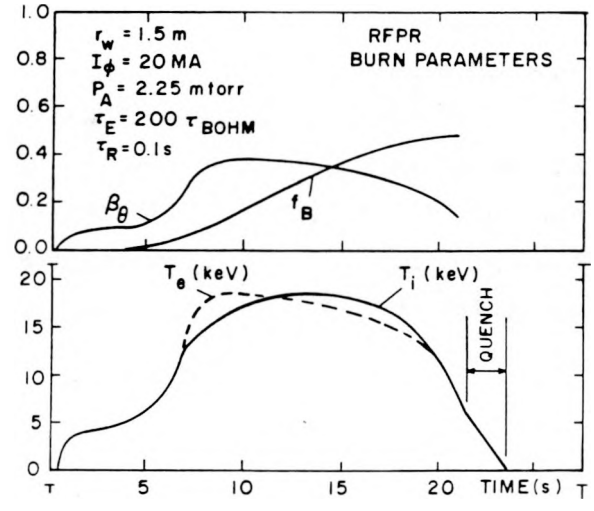

Fig. V-2. Time dependence of plasma temperature, beta, and burnup for a typical burn cycle.

The cooling or quenching the expanded but still reactive plasma now occurs. This process is poorly characterized both in terms of timescale and uniformity of energy deposition (Sec. IV.C.1.c). A quench process that occurs by classical thermal conduction and resistive field decay would be prohibitively long. Generally, it is supposed that neutral gas would be added to the plasma and instabilities would occur to aid in a timely and controllable plasma quench. For these computations the 2.5 MJ/m of postburn plasma energy and the associated 21.5 MJ/m of trapped field energy, amounting to a total of 2.53 MJ/m^2, would be uniformly deposited to the first wall on a ~ 4-s timescale. For ~ 5 s after initiating the plasma quench the continuously operating vacuum system would purge the 568 m^3 plasma chamber, while fresh DT gas would be added. Typically, the baseline, steady-state helium concentration would be maintained by this continuous purge at or below ~ 1 atom %. The physics parameters associated with this operating point have been summarized in Table IV-I. Figure V-3 gives the time-dependence of important plasma powers for this design.

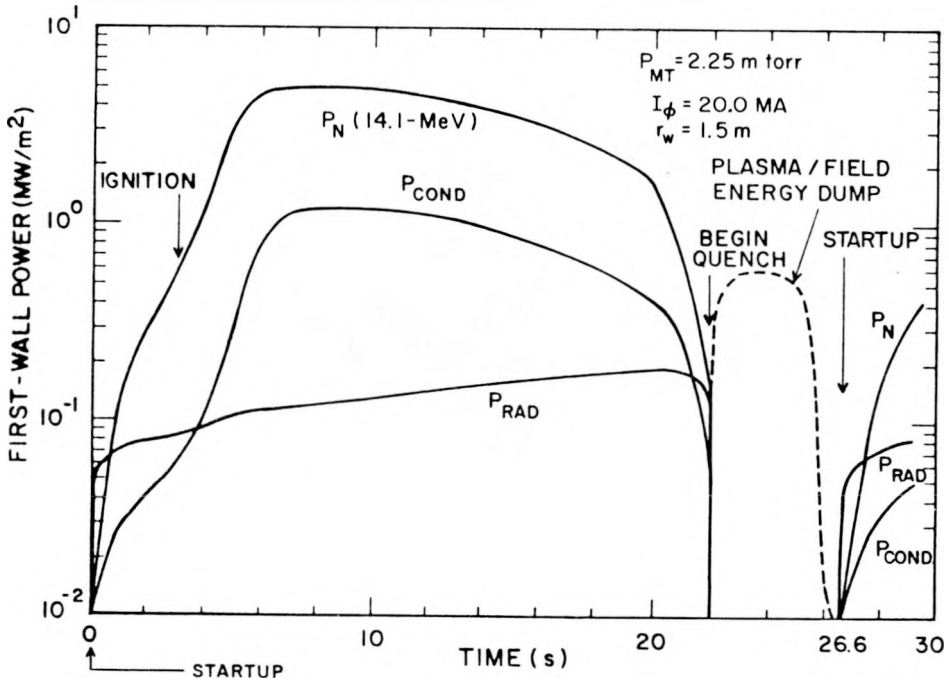

Fig. V-3. Time dependence of neutron, P_N, conduction, P_{COND}, and radiation, P_{RAD}, power flux at RFPR first wall. The power flux associated with the plasma/field dump, assuming a more-or-less uniform deposition, is also shown.

The power-plant embodiment that has been developed on the basis of the reactor operations described above is depicted in Figs V-4 to V-7. The 1.5-m-radius plasma chamber is formed by 40, 2-m-long first-wall/blanket/shield modules, four of which are depicted in Fig. V-4. Figure V-5 gives an isometric view of the RFPR, plan and elevation views are presented in Fig. V-6, and Fig. V-7 summarizes the major coolant flow for this system. The 12.7-m major-radius torus rests within a vacuum tunnel and is completely detached from the PFC system. A separate water-cooled copper first wall (20-mm thick) provides an electrically conducting shell and operates near the blanket temperature (530 K). The 0.5-m-thick stainless-steel blanket contains a 40 v/o Li_2O packed bed into which penetrates radially

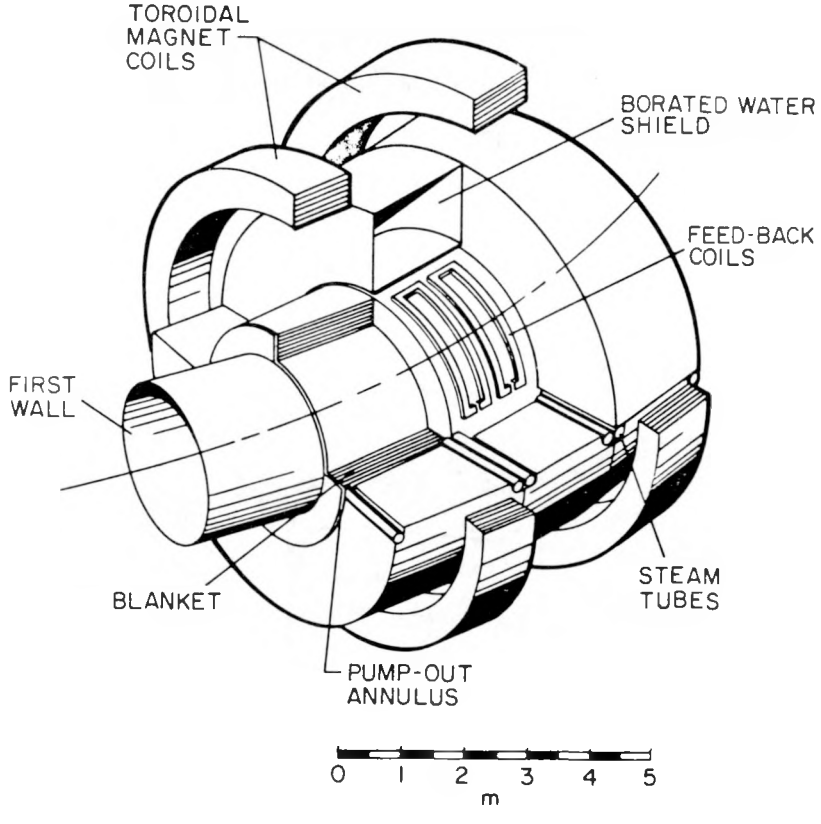

Fig. V-4. Isometric view of four 2-m-long RFPR reactor modules including the copper first wall, Li_2O packed bed and associated high-pressure steam tubes, feedback coils, water shield, and toroidal field coil. The 12.7-m radius torus would rest in a vacuum tunnel, 40 modules would be required to complete the torus, and the poloidal field coils (not shown) would line the walls of the vacuum tunnel.

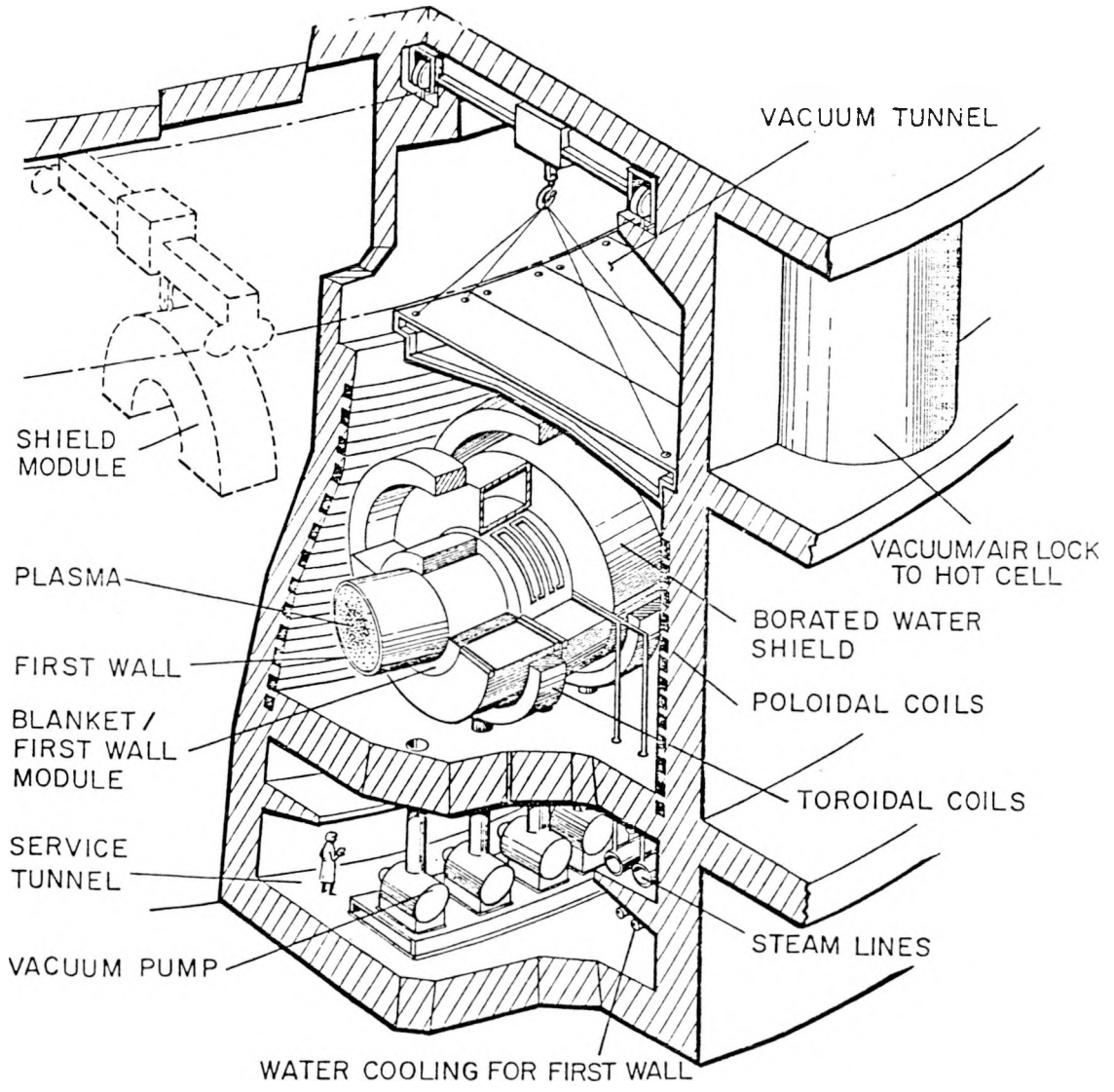

Fig. V-5. Isometric view of RFPR power plant.

water/steam-cooled U-tubes. A low-pressure (0.1 MPa) helium purge gas is drifted through the granular Li_2O bed to extract tritium. The slightly superheated (5 K) steam emerging from this blanket is used to drive directly a turbogenerator, the first-wall water coolant being used only for feedwater and reheat functions (Fig. V-7). Despite the 81% duty factor for the burn cycle depicted in Figs. V-1 to V-3, the large thermal capacity of this blanket configuration results in less than a 5-K temperature cycle within the blanket structure, although the averaged first-wall temperature undergoes a 28-K excursion.

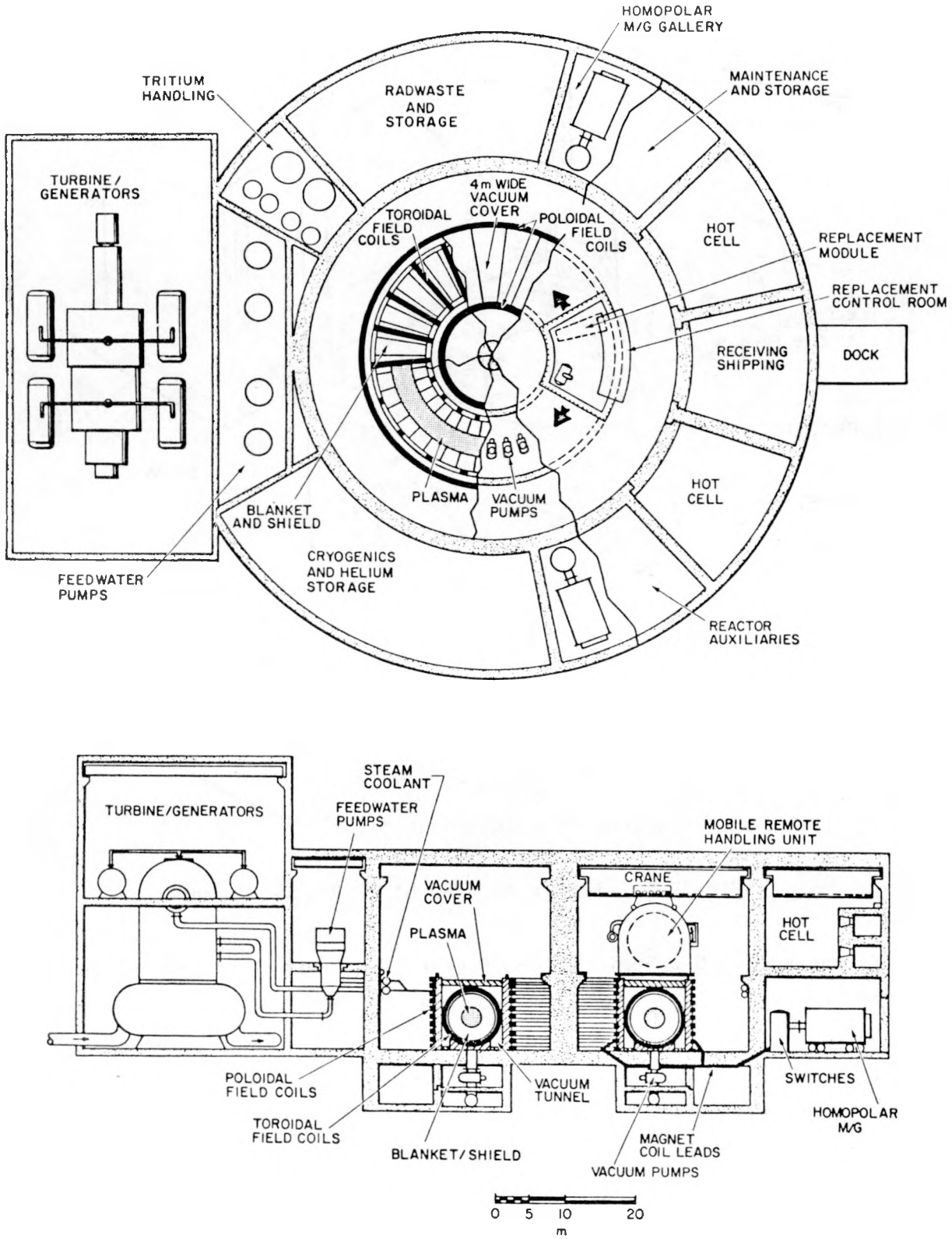

Fig. V-6. Plan and elevation view of the RFPR power plant.

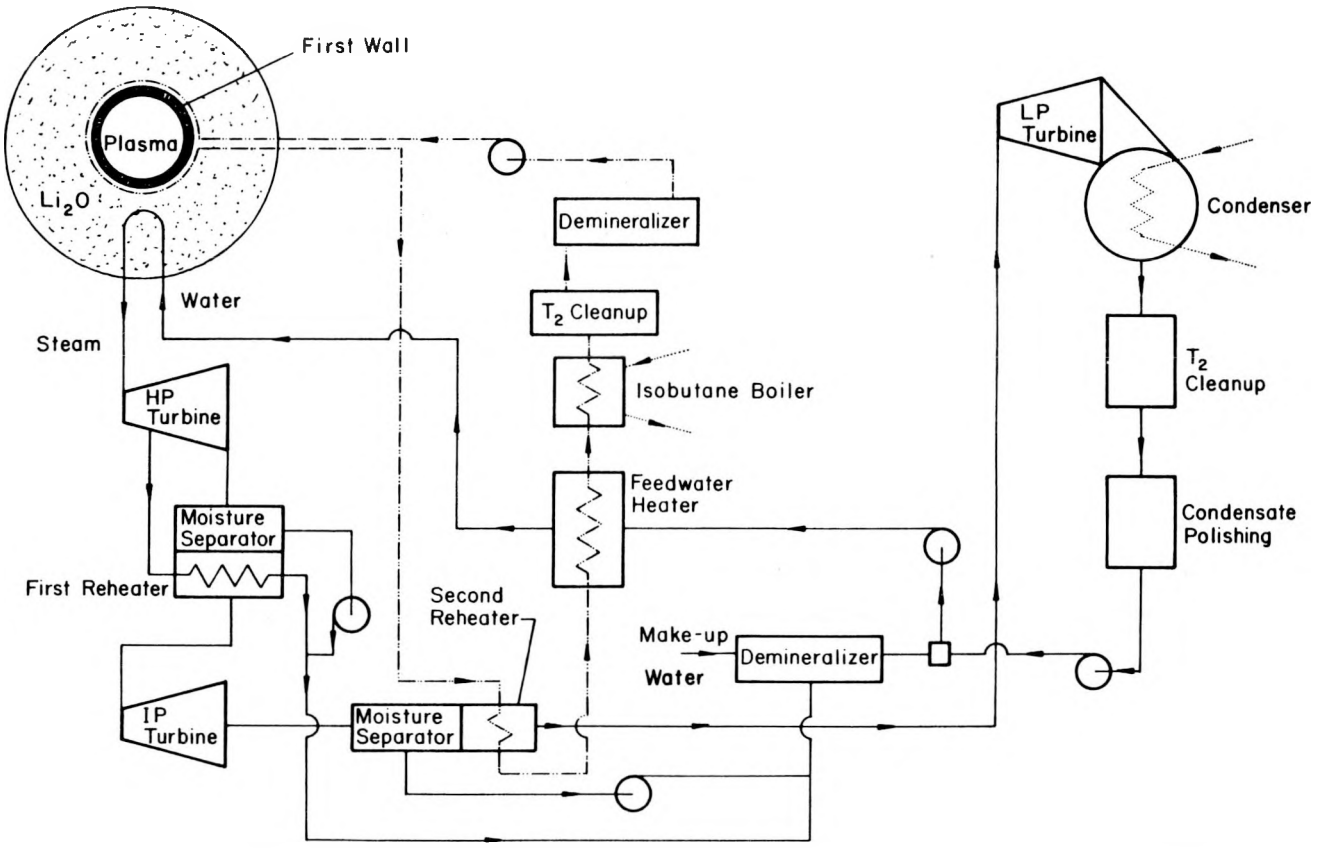

Fig. V-7. Flow diagram illustrating RFPR thermodynamic cycle.

Each of the 40 RFPR modules are electrically and thermohydraulically independent. Both the TFC and PFC systems are fixed structures, with the PFC system far removed from the reactor core (Figs. V-5 and V-6). The TFC spacing is adequate for removal of reactor modules without disturbing these coils.

The following sections address the preliminary engineering designs associated with the first-wall/blanket (Sec. V.B), the steam power cycle (Sec. V.C), tritium handling (Sec. V.D), vacuum (Sec. V.E), magnet coils and power supplies (Sec. V.F), and the maintenance of the plant (Sec. V.G). Table IV-II gives a summary description of key engineering parameters, a more detailed listing being given in Appendix C.

B. First Wall and Blanket

The RFP physics characteristics outlined in Sec. III.B directly affect the preliminary blanket design presented herein. This design invokes a "conventional", steam-generating technology embodied in the water/steam cooling of a packed Li_2O bed, stainless steel structure, and stagnant

borated-water shield. This direct-cycle steam system is not uniquely applicable to the RFPR, but adaptation of this scheme to the RFPR was made to investigate the technological and economic advantages associated with the elimination of a secondary heat-transfer loop. This section addresses only neutronic, thermohydraulic and mechanical/structural aspects of the blanket; steam cycle, tritium handling and operations/maintenance are discussed in Secs. V.C, V.D, and V.G, respectively.

1. Neutronics Analysis. To minimize costs and to reduce technological risks, a blanket and shield have been designed using existing materials and technology. The nucleonic analysis determined energy deposition rates, tritium breeding rates, displacement rates, and helium and hydrogen production rates for several materials and dimensional variation in the RFPR model. Only the results of the final design iteration are reported.

a. Neutronics Model. Two sub-modules constitute the RFPR core: the first-wall/blanket module and the shield module. Figure V-8 depicts the neutronics model. The first-wall/blanket module consists of a plasma-vacuum region followed by a copper first wall. Use of a copper first wall represents a net benefit for tritium breeding in providing some neutron multiplication. Beyond the first wall is the blanket, which is a water/steam-cooled packed Li_2O bed and stainless-steel structure. For the purpose of the neutronics analysis all materials in the blanket were homogenized. The shield module consists of a Cu feedback coil, a thin lead region for gamma-ray attenuation, and a stagnant, borated-water shield for neutron shielding. Beyond the shielding are located the Cu/NbTi magnets. Several transport calculations were performed using the first-wall/blanket/shield/coil model depicted in Fig. V-8.

A one-dimensional 18-zone radial-transport computation[1] was performed in the P_3S_8 approximation on the first-wall/blanket/shield/coil geometry using coupled neutron/gamma-ray cross sections. The 30 neutron groups and 12 gamma-ray groups in the cross-section library were derived from ENDF/B-IV data. Displacement kermas were obtained from Ref. 2. Each calculation determined the gamma-ray/neutron heating and tritium production in the first-wall/blanket submodule. Furthermore, the displacements per atom (dpa) and the hydrogen and helium production rates were calculated for both sub-modules. The effectiveness of the blanket was determined by the tritium

production and heat removal characteristics, whereas, the shielding effectiveness was measured by the dpa and heating rate in the magnet coils.

b. Neutronics Results. Although several nucleonic calculations were performed, only the result of the final design is reported. Dimensions and compositions are given in Table V-I and schematically illustrated in Fig. V-8. Table V-I also summarizes all primary neutronics results and response functions. For a 14.1-MeV neutron wall loading of 2.5 MW/m^2 the total heating in the first-wall/blanket module is 26.1 MW/m, with an average energy density in the blanket of 4.75 MW/m^3. The first-wall/blanket system captures 99.1% of the fusion neutron energy and illustrates the effectiveness of this relatively thin blanket for heat removal. Figure V-9 displays the radial distribution of both neutron and gamma-ray heating (zones 3-10, Table V-I). All neutronic results are given for a 2.5 MW/m^2 neutron wall loading, which was subsequently scaled to the 2.7 MW/m^2 wall loading adopted for the final design.

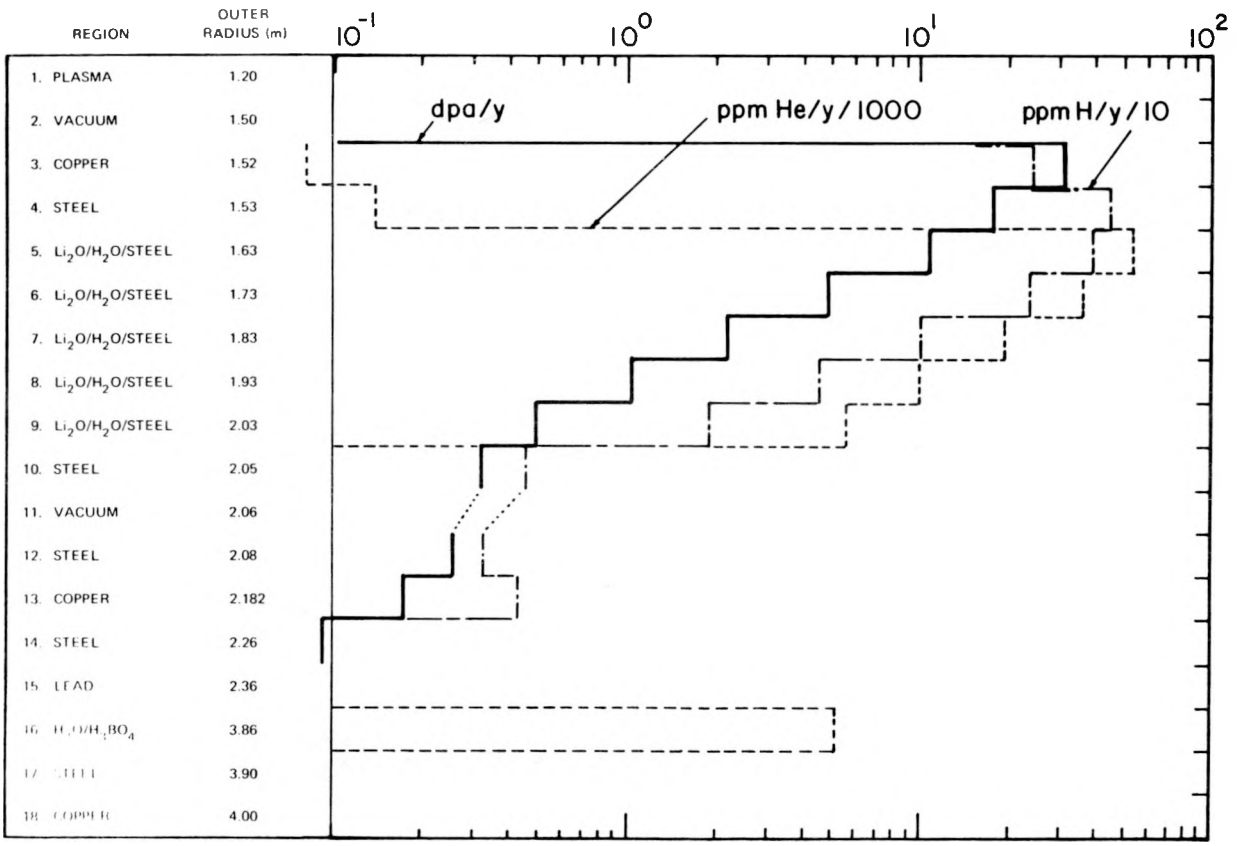

Fig. V-8. Schematic representation of neutronics model.

TABLE V - I

SUMMARY OF NEUTRONICS RESULTS FOR A WALL LOADING I_ω = 2.5 MW/m^2

ZONE	OUTER RADIUS(m)	CONTENT	VOLUME (m^3/m)	HEATING (W/m)[a] NEUTRON	GAMMA	TOTAL	HYDROGEN (ppm/yr)	HELIUM (ppm/yr)	DISPLACEMENT (dpa/y)	TRITIUM BREEDING (tritons/neutron) ^{6}Li	^{7}Li	TOTAL
1	1.20	PLASMA	4.52				0	0	0			
2	1.50	VACUUM	2.54				0	0	0			
3	1.52	Cu FIRST WALL	1.90(-1)	7.805(+5)	4.439(+6)	5.219(+6)	2.47(+2)	8.33(+1)	3.05(+1)			
4	1.53	SS	9.58(-2)	1.652(+5)	5.665(+5)	7.317(+5)	4.51(+2)	1.35(+2)	1.76(+1)			
5	1.63	Li_2O+H_2O+SS[b]	9.93(-1)	6.938(+6)	2.419(+6)	9.356(+6)	3.88(+2)(2.74(+2))[d]	5.48(+4)(7.94(+1))[d]	1.09(+1)	3.953(-1)	7.615(-2)	4.715(-1)
6	1.73	"	1.06	3.999(+6)	1.428(+6)	5.427(+6)	2.37(+2)(1.17(+2))	3.60(+4)(3.25(+1))	4.88	2.789(-1)	3.663(-2)	3.157(-1)
7	1.83	"	1.12	2.113(+6)	8.121(+5)	2.925(+6)	1.02(+2)(5.09(+1))	1.94(+4)(1.38(+1))	2.23	1.587(-1)	1.744(-2)	1.761(-1)
8	1.93	"	1.18	1.090(+6)	4.538(+5)	1.544(+6)	4.43(+1)(2.97(+1))	9.93(+3)(7.88)	1.03	8.571(-2)	8.247(-3)	9.395(-2)
9	2.03	"	1.24	6.105(+5)	2.568(+5)	8.673(+5)	1.92(+1)(9.71)	5.67(+3)(2.53)	4.92(-1)	5.136(-2)	3.831(-3)	5.519(-2)
10	2.05	SS	2.56(-1)	4.649(+3)	5.420(+4)	5.885(+4)	4.60	1.20	3.19(-1)	(9.699(-1))[e]	(1.423(-1))[e]	(1.1124)[e]
11	2.06	VACUUM	1.29(-1)									
12	2.08	SS	2.60(-1)	3.480(+3)	3.912(+4)	4.260(+4)	3.21	0.84	2.59(-1)			
13	2.18	Cu	1.37	1.103(+4)	1.335(+5)	1.445(+5)	4.15	1.02	1.74(-1)			
14	2.26	SS	1.09	3.672(+3)	3.351(+4)	3.719(+4)	0.14	0.53	9.39(-2)			
15	2.36	Pb	1.45									
16	3.86	H_2O+H_3BO_3[c]	2.93(+1)	1.171 (+4)	8.162(+3)	1.987(+4)	1.16(-2)	5.18(+3)	0			
17	3.90	SS	9.75(-1)	5.185(-5)	1.098(-1)	1.098(-1)			8.80(-10)			
18	4.00	Cu	2.48	1.047(-4)	9.123(-1)	9.125(-1)			5.79(-10)			

[a] Total Heating (16.3 MeV/neutron), (MW/m)

Region	Neutron	Gamma	Total	Percent
1-10	1.570(+1)	1.043(+1)	2.613(+1)	99.07
11-18	2.989(-2)	2.143(-1)	2.442(-1)	0.93
Total	1.573(+1)	1.064(+1)	2.637(+1)	

[b] 40 v/o Li_2O, 10 v/o H_2O, 15 v/o Steel, 35 v/o void

[c] 18.8 a/o ^{10}B

[d] production in structure

[e] totals

With a 20-mm-thick copper first wall the tritium breeding ratio is 1.11. The ability to breed without a neutron multiplier results from the 14.5% neutron multiplication from the (n,2n) reaction in the copper first wall. A regional breakdown of tritium production and the contribution from ^{6}Li and ^{7}Li is also given in Table V-I. Zone 9 adds very little to the tritium breeding but is necessary for reasons of energy distribution and removal.

Although the 20-mm-thick copper first wall aids in tritium production, adverse materials effects are expected. Table V-I summarizes the hydrogen and helium production rate (ppm/y) and the displacement rate (dpa/y) for a 100% plant factor. The hydrogen and helium production within the first wall is 247 and 83 ppm/y, respectively, for a 2.5 MW/m^2 wall loading, and when coupled with the 30.5 dpa/y and 3015 ppm/y reactions from (n,2n) interactions represents a potential materials problem for the first wall. On the other hand, the dpa/y in the superconducting coils appears tolerable from the viewpoint of radiation effects, and the thermal loading in this region should have little impact on the cryogenic refrigeration requirements.

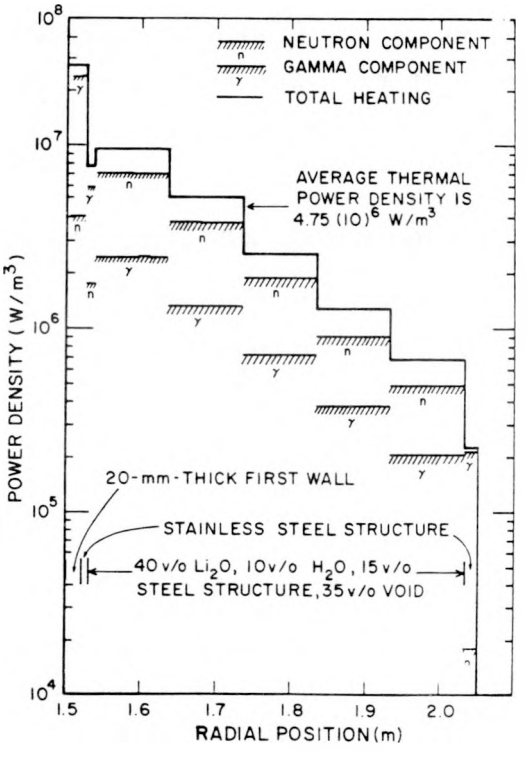

Fig. V-9. Power density in first-wall and blanket regions (Zone 3-10).

The data presented in parentheses for zones 5-9 in Table V-I represent the hydrogen and helium production rate in the structural material alone. The increase in H and He production from zone 4 to 5 results from a net cross section and homogenization effect; a slight increase in the (n,p) and (n,α) cross section occurs from 14 to 10 MeV. More important is the material self-shielding caused by homogenization in the blanket, and the numbers in parentheses, consequently, represent upper limits.

2. First-Wall and Blanket Thermohydraulics.

a. First Wall. The 20-mm-thick copper first wall receives 38% of the total thermal energy produced by the RFPR. This first-wall thermal loading is much greater for the RFPR than for an equivalent tokamak because of the assumed batch-burn, divertorless operation. In addition, the higher bremsstrahlung flux, greater wall thickness, and higher (n,2n) reaction rate account for the greater first-wall thermal fluxes and power densities. Table V-II summarizes the various thermal inputs to the first wall. One manifestation of the (n,2n) reaction in copper can be observed by comparing the volumetric heating rate with that in the stainless steel structure. The first-wall energy flux resulting from the shorter-time deposition of plasma/field energy during the quench period is close to the bremsstrahlung

TABLE V-II

FIRST WALL ENERGY FLUXES AND POWER DENSITIES

PARAMETER	VALUE
Average 14.1-MeV neutron wall loading (MW/m^2)	2.7
Thermal conduction energy per burn cycle (MJ/m^2)	15.7
Bremsstrahlung energy per burn cycle (MJ/m^2)	3.0
Postburn plasma internal energy deposited at first wall (MJ/m^2)	0.27
Postburn field energy deposited at first wall (MJ/m^2)	2.3
Burn time (s)	21.6
Cycle time (s)	26.6
Volumetric nuclear heating rate in copper averaged over burn time (MW/m^3)	33.8
First-wall bremsstrahlung flux averaged over burn time (MW/m^2)	0.86
First-wall heat flux averaged over 4-s quench period (MW/m^2)	0.64

and thermal conduction fluxes encountered during the burn period. Consequently, for the assumed 4-s quench period (Sec. IV.C.1.c), the first-wall thermal flux remains relatively constant over the entire power cycle.

The first-wall configuration is described in Sec. V.B.3, and the coolant channel configuration is depicted in Fig. V-10. The coolant flow within the first wall could be in the toroidal direction or in the azimuthal direction. The circumferential or azimuthal flow direction was chosen only for illustrative purposes. Table V-III summarizes the thermohydraulic results for a first wall cooled by water, using the physical data given in Table V-IV.

TABLE V-III

SUMMARY OF FIRST-WALL THERMOHYDRAULICS

PARAMETER	VALUE
Water flow rate, (kg/s)	1584
Inlet pressure (MPa)	5.52
Inlet temperature (K)	360
Outlet temperature (K)	530
Number of coolant channels/module	100
Coolant channel cross section (mm)	15 × 15
Length (m)	9.4
Equivalent hydraulic diameter (mm)	15
Flow rate per channel (kg/s)	0.40
Flow velocity (m/s)	2.07
Reynolds number	176,000
Pressure drop (kPa)	21
Local peak heat flux at channel wall (MW/m^2)	1.79
Averaged peak heat flux at channel wall (MW/m^2)	1.12
Critical heat flux for subcooled-flow boiling (MW/m^2)	
Gambill correlation	1.11
Tong correlation	2.2
Average peak wall temperature at coolant channel (K)	552
Maximum copper temperature (K)	613
Maximum steel temperature (K)	584

TABLE V-IV

MATERIAL PROPERTIES USED IN FIRST-WALL HEAT-CONDUCTION ANALYSIS

Material	Density kg/m^3	Specific Heat J/kg K	Thermal Conductivity W/m K
Copper	8880.	394.	335
Steel	7800.	546.[a]	16.9[a]
Water	879.	4406.	0.6725

[a]At 540 K, all other properties were assumed constant with temperature.

The 21-kPa (3-psi) pressure drop is relatively low, and includes an allowance for form losses at the manifolds. This estimate gives reasonable assurance that the heat transfer could be improved, if necessary, by altering the flow passage geometry without a serious pumping penalty to the overall steam cycle.

Two of the available[3] correlations for the critical heat flux in subcooled forced-convection systems were used to evaluate the margin needed to prevent the well-known unstable transition to film boiling and burnout. It should be recognized that forced-convection critical heat-flux correlations have not been developed that apply universally to all fluids and all geometries. Both correlations used to obtain the results in Table V-III were derived from data covering the range of applicable parameters. The Gambill correlation is reported[3] to predict low values of the critical heat flux when compared with low pressure small-tube data for water. The Tong correlation is reported[3] to correlate 95% of the data to an accuracy of ± 20% for various geometries with uniform circumferential heat flux. Neither correlation accounts for possible effects of body forces on the critical heat flux caused by centrifugal acceleration as the flow traverses the 1.5-m-radius circular path. Revising the flow passage geometry to a longitudinal configuration obviously would eliminate this consideration. The local peak heat flux listed in Table V-III is conservative because it is a momentary maximum located only at a small area of the coolant channel wall. It appears that a minimum for the departure from nucleate boiling (DNB) ratio is at least 1.2, but experimental verification of this safety margin should be made in a more comprehensive design study. A major uncertainty in determining the adequacy

of the DNB margin is the effect of the non-uniformity in space and time of the first-wall heat flux on the critical heat flux correlation.

The maximum copper temperature (613 K) is less than the temperature (673 K) at which the allowable stress was determined (Sec. V.B.3), based on a creep criterion for high strength copper.[4] The first-wall temperatures were calculated by a finite-element heat-conduction computer model[5] which is based on the coolant temperature and flow velocity at the channel exit, the power inputs listed in Fig. V-3 and Table V-II, and material properties listed in Table V-IV. The typical symmetry element used in the computer model is illustrated in Fig. V-11, and the resulting temperature distributions at various times during the burn phase are depicted in Fig. V-12. The transient temperature variation in the copper and steel during a burn cycle is shown in Fig. V-13. The maximum change in the averaged first-wall temperature is 28 K at the plasma/first-wall interface the temperature change amounts to 68.5 K. The maximum temperature change in the steel structure during a given burn cycle is 21 K. Because of the moderate temperature change during a cycle, thermal fatigue should not be serious (Sec. V.B.3) for the proposed high-strength copper alloy.[4] The issue of radiation effects and the unresolved

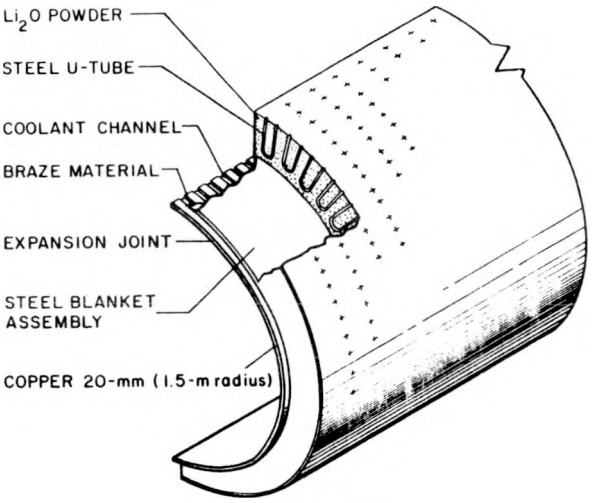

Fig. V-10. Detailed view of copper first wall. The dimensions of first-wall are exaggerated for illustrative purposes.

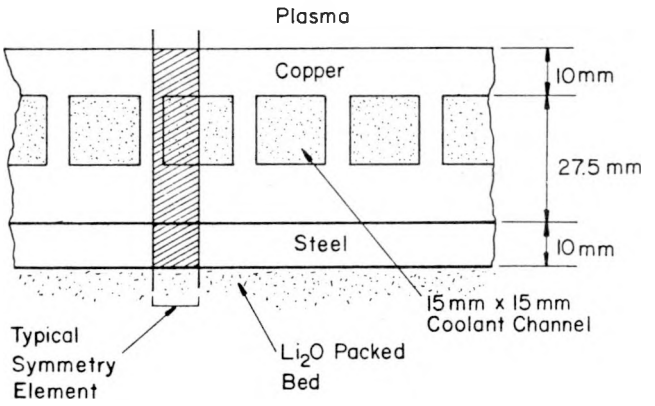

Fig. V-11. First-wall detail showing symmetry element used for first-wall heat-transfer calculation.

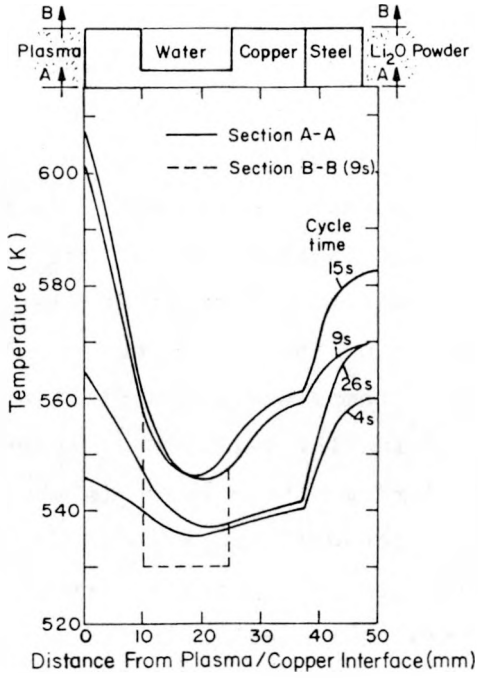

Fig. V-12. Radial temperature distributions in copper first wall at a position between coolant channels.

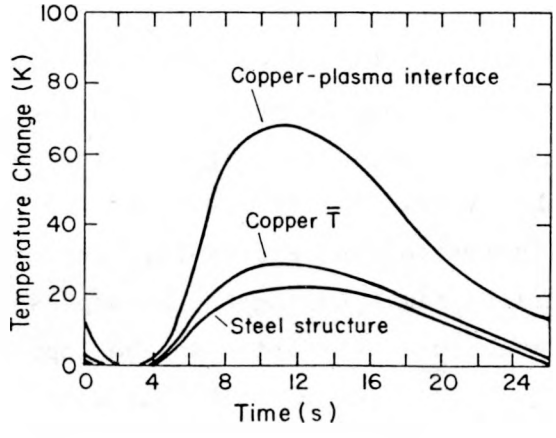

Fig. V-13. Time dependence of peak temperatures in copper first wall and steel structure.

synergism associated with this thermal cycling, however, may present problems. It is emphasized that the copper first wall does not serve a structural or vacuum-barrier function other than the requirement to preserve its self-integrity and to maintain an acceptable electrical resistivity. The materials issue is briefly addressed in Sec. V.B.4.

b. Blanket. In order to analyze the 0.5-m-thick Li_2O blanket, the packed bed was subdivided into five 0.1-m-thick annular regions for both the neutronic (Sec. V.B.1) and heat-transfer calculations. The volumetric power density within each annular region was taken to be constant; the actual heating rate decreases exponentially and continuously across the blanket. The step-wise varying power density assumed for this blanket thermal calculation is illustrated in the lower part of Fig. V-14. The heating rates vary by a factor of 9 from the first-wall region to the outer blanket region, and the average power density is 4.75 MW/m^3. The radial coolant U-tubes, also shown in Figs. V-10 and V-14, are spaced on a uniform rectangular grid, projecting radially inward from the outboard manifolds (Sec. V.B.3). Because of the axial or toroidal uniformity, the nominal heat input to all the U-tubes is the

same at a given radial position, and the spatial variation in heat flux at the coolant channel wall can be determined from symmetry considerations based on the uniform grid. Since the nominal flow rate in all U-tubes is also specified to be the same, the coolant enthalpy rise, temperature, and steam quality can be determined by integration. Following this procedure, the locations of boiling transitions, peak wall temperatures, and DNB ratios can be determined. The upper sketch in Fig. V-14 illustrates the locations where single-phase convection, nucleate boiling, bulk boiling, dryout, and postdryout heat-transfer occur in the U-tube. Table V-V lists important design parameters for the U-tubes and packed bed. Because of the cylindrical geometry, the spacing between adjacent U-tubes increases with radius from 40 mm near the first-wall region to 50 mm in the outer blanket region. The legs of each U-tube are parallel with a center-to-center spacing of 40 mm. Nominally, 5890 U-tubes are required for each 2-m-long module. The tubes are made of Croloy 2-1/4 steel alloy with an outside diameter of 12.5 mm and a 1-mm wall thickness. The tubes support external fins arranged longitudinally to enhance heat transfer from the packed Li_2O bed. The fin design was not optimized in this study. The temperature isotherms that characterize a unit cell located within the packed bed near the first wall are shown in Fig. V-15. Table V-V and Fig. V-15 present the dimensions and configuration of the fins. The results of the blanket thermohydraulic calculations are summarized in Table V-VI, whereas Table V-VII gives a comparison with light-water fission reactors. The remainder of this section addresses three important issues associated with this steam-generating blanket: flow distribution, boiling stability, and packed-bed temperature distribution.

Flow distribution. The design of boiling water systems must always consider the possibility of steady-state flow maldistribution and transient instabilities. This potential problem may be exacerbated for the toroidal geometry in that the U-tubes are aligned at many different angles with respect to the gravity vector. This problem should be ameliorated somewhat by the relatively short U-tube length and lower fluid flow rates in comparison with conventional steam generators (Table V-VII). Consequently, the pressure loss in a U-tube is expected to be extremely low. For instance, by application of the Martinelli-Nelson[6] two-phase friction multiplier, the pressure drop is estimated to be less than 1.4-kPa (0.2 psi). Appropriate inlet orificing to increase the single-phase pressure loss to each U-tube, therefore, can meter

TABLE V-V

DESIGN PARAMETERS FOR U-TUBE AND Li_2O PACKED BED

PARAMETER	VALUE
U-TUBES:	
Material:	Croloy 2-1/4 (2 1/4% Cr-1% Mo) (ASME Specification SA-213, Grade T22)
Overall length (m)	0.5
Length of flow path (m)	1.06
Outside diameter (mm)	12.5
Wall thickness (mm)	1.0
Number per module	5890
Spacing between legs (mm)	40
Spacing between adjacent U-tubes (mm)	40-50
Number of longitudinal fins	8
Fin thickness (mm)	1.25
Fin length (mm)	4 and 10 (4 each)
Blanket volume occupied by U-tubes and fins (Fig. V-14)	4.1% (region 1) 7.1% (region 5) 5.6% (average)
Properties:	
Allowable Stress (MPa), (1 MPa = 145 psi)	
811 K	53.8
867 K	29.0
844 K (design temperature)	34.5[a]
Thermal conductivity, 540 K (W/m K)	16.9
Specific heat, 540 K (J/kg K)	546
Density (W/m K)	7800
Li_2O PACKED BED:	
Volume fraction of Li_2O plus void per module	0.75
Void fraction in packed bed	0.47
Properties used in analysis[b]	
Thermal conductivity of He-filled packed bed (W/m K)	1.2
Specific heat (J/kg K)	3165
Density of packed bed (kg/m^3)	1208

[a] by linear interpolation

[b] properties will vary depending on many variables, actual data on Li_2O packed beds are nonexistent.

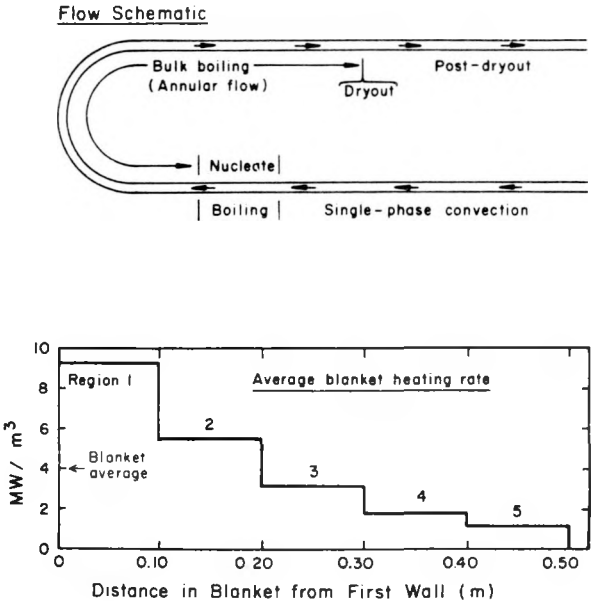

Fig. V-14. Schematic of flow regimes in water/steam coolant U-tubes illustrating radial dependence of the blanket power density.

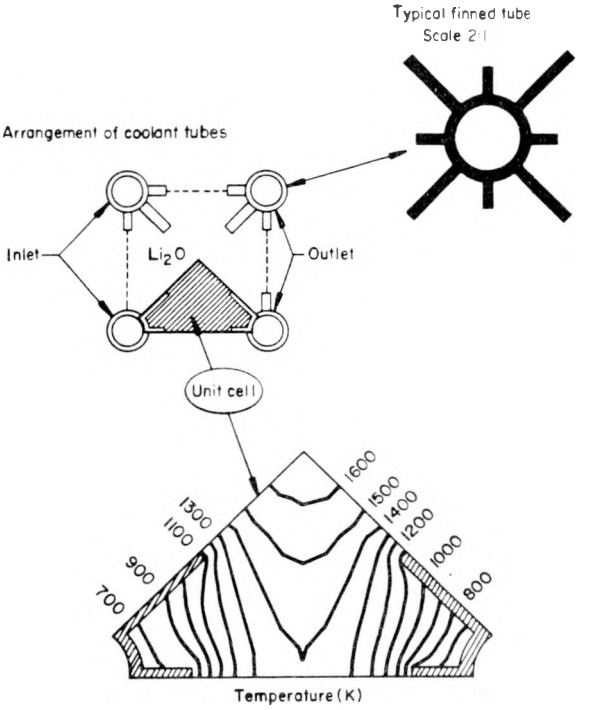

Fig. V-15. Lattice arrangement of blanket coolant U-tubes showing unit cell selected to compute two-dimensional temperature distribution.

the flow and damp out instabilities.[6] With a relatively-high, uniform inlet pressure loss (~ 7 kPa) that is independent of orientation and boiling phenomena downstream, the flow in the U-tubes should be maintained uniform with little pumping pressure loss.

Boiling heat transfer and stability. Single-phase forced convection near the inlet to the U-tube gradually transforms to nucleate boiling (Fig. V-14). In this region the well-known Jens and Lottes correlation[3] for subcooled and low-quality forced convection was used to predict tube-wall temperatures. The transition to high-quality forced convection takes place at 5 to 10% steam quality and has been predicted with good accuracy by the Chen equation.[3,6] This correlation was used in the region labeled "bulk boiling (annular flow)" in Fig. V-14. The flow in this region is annular with a liquid layer attached to the wall and a central high-velocity vapor core. As the quality increases with distance downstream, the annular liquid layer disappears from the wall, and the remaining liquid is carried along with the high-speed vapor in the

TABLE V-VI

RESULTS FROM BLANKET THERMOHYDRAULICS CALCULATIONS

PARAMETER	VALUE
Coolant flow rate (kg/s)	788.4
Coolant flow rate per U-tube (kg/s)	$3.37(10)^{-3}$
Inlet temperature (K)	383
Outlet temperature (K)	551
Nominal coolant pressure (MPa)	5.5
Heat flux at U-tube inside diameter[a] (MW/m^2)	0.43 - 0.066
Volumetric heating rate in packed bed[a] (MW/m^3)	9.42 - 0.7
Coolant mass velocity ($kg/s\ m^2$)	38.9
Coolant Reynolds number	
Water inlet	$4.74(10)^6$
Steam outlet	22,000
U-tube pressure loss (kPa)	< 1.4
U-tube wall temperature (K)	475 - 781
Peak Li_2O temperature (K)	1678

[a]Averaged over reactor duty cycle

form of droplets or mist. The location of the point where the annular layer disappears (dryout) is predicted by the Macbeth correlation[3,6] and depends on the pressure, tube diameter, mass velocity, and quality. The steam quality that characterizes the dryout conditions becomes higher as the mass velocity and pressure is lowered. The Macbeth correlation predicts dryout for the U-tubes at a quality equal to 0.97. More recent correlations,[7] that are specifically tailored for low mass velocities, predict a higher steam quality at dryout. For the postdryout heat transfer, the "frozen droplet model" was adapted.[3,5] This model ignores the presence of liquid drops in the vapor flow, resulting in conservatively low heat transfer and high vapor temperatures.

The fouling resistance applied to the U-tube walls was taken[8] as $1.76(10)^{-4}$ m^2K/W for treated boiler feedwater. The maximum tube wall temperature for each leg of the U-tube in each of the five radial blanket regions (Fig. V-14) was calculated as follows.

TABLE V-VII

SUMMARY OF STEAM CYCLE CONDITIONS

PARAMETER	RFPR	BWR/6	PWR
Rated output (MWt/MWe)	3000/828	3293/1000	2568/886
System pressure (MPa)	5.5	5.9	15.1 (primary) 6.3 (secondary)
Steam generator temperatures (K)			
inlet	383	558	508
outlet	551	---	572
Superheat (K)	7.8	0.0	19.4
Total coolant flow rate (kg/s)	1584(first wall)	1777	8273 (primary)
	788 (blanket)		702 (secondary)
Total heat transfer area (m^2)	2262 (first wall)	---	4620 (core)
	12,000 (blanket)	---	28,000 (steam generators)
Steam generator tubes			
number	$2.76(10)^5$	---	31,060
length (m)	1	---	18
temperature (K)	844	---	589
pressure (MPa)	6.2	---	7.2
Overall thermal-to-electric conversion effficiency	0.28	> 0.3	> 0.3

- Starting at the inlet manifold, the fluid enthalpy, temperature and quality were calculated along the tube length based on the known flow rate and heat input.
- At the exit region of each radial blanket region, where fluid temperatures and wall heat fluxes are the highest, the appropriate boiling correlation was applied to determine the temperature difference between the tube-wall temperature and the fluid bulk temperature.
- The calculated tube-wall temperature was then adjusted upward to account for the fouling factor.

These calculated tube-wall, coolant and Li_2O packed-bed temperatures are shown as a function of blanket thickness in Fig. V-16. The maximum tube wall temperature is 781 K in the postdryout region. If this temperature could be

reduced, for example by internal fins in the U-tube at that hot spot, a corresponding increase in the steam exit temperature would be possible. The cycle efficiency, as indicated in Sec. V.C, would correspondingly be increased. The tube-wall temperatures as computed in Fig. V-16, were used as a boundary condition to estimate temperatures in the Li_2O packed bed.

Temperatures in packed bed. The spacing between the adjacent coolant tubes was made small in order to minimize the temperature extremes in the packed bed. The temperatures were calculated for the typical unit cell model shown in Fig. V-15. For convenience in modeling, the unit cell in all regions was taken as a right equilateral triangle with a hypotenuse equal to the spacing between adjacent U-tubes (40-50 mm). The heat-conduction model[5] used the tube wall temperature as a boundary condition. With the exception of the U-tube inner diameter, all external boundaries were taken as adiabatic because of symmetry. The volumetric heating rates in the Li_2O and steel structure were specified by the neutronics calculations (Table V-I, Fig. V-9).

The physical properties of the packed bed and steel used in the analysis are listed in Table V-V. The thermal conductivity of dense Li_2O solid has been reported as 1.73 W/m K at room temperature. Data at higher temperatures could not be found, but ZrO_2 and fused SiO_2 have similar room temperature conductivities and show an increase in conductivity with temperature. Other oxides, such as BeO, MgO and Al_2O_3, show a decreasing thermal conductivity with increased temperature. The room-temperature thermal conductivities of the latter materials, however, are much higher (> 26 W/m K), and in the temperature range of interest become still higher than that of SiO_2 or ZrO_2. Consequently, the high-temperature properties of ZrO_2 were used to model the Li_2O packed bed.

Powdered materials are generally used as thermal insulators, but a high thermal conductivity is desirable for the application under consideration. A variety of empirical and theoretical relationships are available for estimating the thermal properties of phase mixtures when the corresponding values for the constituents are known. For the present case, however, experimental values for ZrO_2 powder in dry air[9] at 1120 K were used as a basis for extrapolation. The reported conductivity (0.7 W/m K)[9] was adjusted upward to 1.2 W/m K in order to account properly for the effects of helium instead of air in the voids. If this value should prove to be too optimistic, ample

design margin exists to increase conduction out of the packed bed by extending the external fins on the U-tube (Fig. V-15).

The temperature distribution calculated for the region of the highest heat generation is shown in Fig. V-16. The peak temperature occurs at the center of the square array, as illustrated in Fig. V-15. A range of Li_2O melting temperatures have been reported, but the minimum value appears to be near 1700 K. Localized melting is not expected to be seriously detrimental. The corresponding tube-wall and coolant temperatures in both U-tube legs are also given in Fig. V-16.

The temperature response of the packed bed and U-tube to power pulses in the most strongly heated radial region (Fig. V-14) is shown in Fig. V-17. The maximum temperature change for a U-tube during a power pulse amounts to only

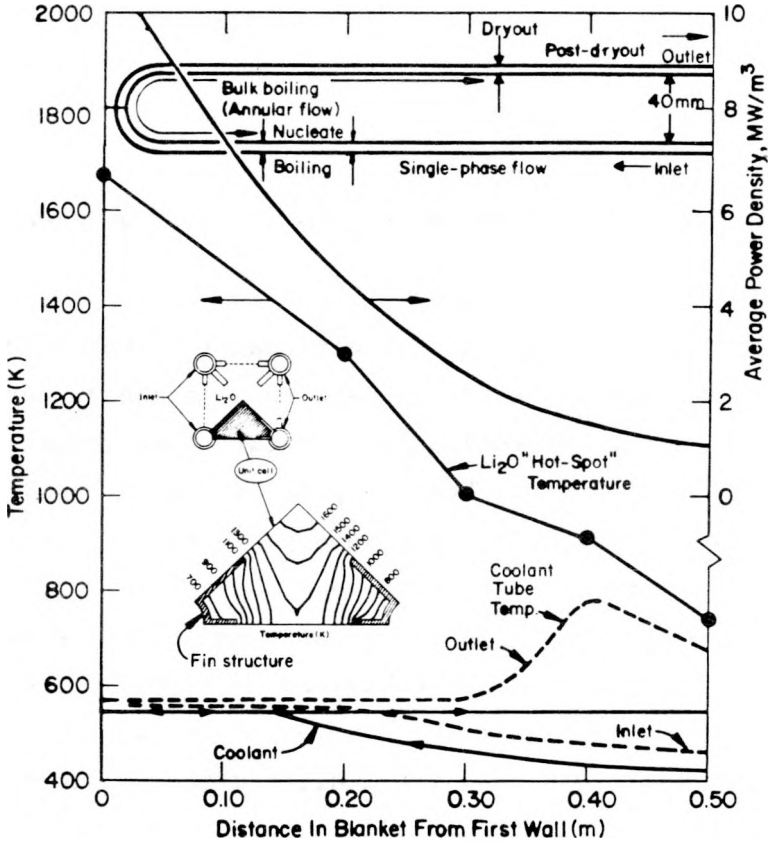

Fig. V-16. Radial temperature distribution in Li_2O pack-bed blanket and steam/water coolant tube.

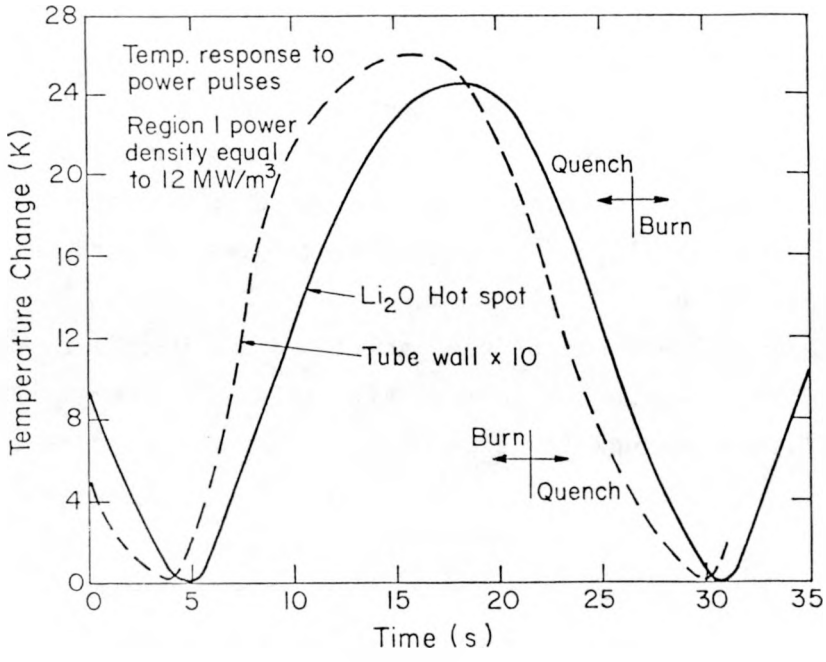

Fig. V-17. Time-response of blanket and coolant U-tube at the position of maximum temperature.

2.4 K. Because of the large thermal capacity and low thermal diffusivity of the Li_2O powder, any auxiliary thermal storage to accommodate burn pulses and to maintain a constant outlet coolant temperature appears unnecessary. The Li_2O temperature distributions have been coupled with the local distribution of tritium generation (Table V-I) to determine the space and temporal evolution of tritium inventory and release rate (Sec. V.D).

3. Mechanical Design. The RFPR torus has a major radius of 12.7 m and a 1.5 m minor radius. To facilitate assembly and maintenance the torus is made up of 40 modules, as shown in Fig. V-18, and each is 2 m in length. The blanket module design is based on electrical, neutronics, thermal, chemical, and structural considerations and ideally should be inexpensive, easily replaceable, and operate with a high margin of safety. In order of increasing radius, the module consists of a 20-mm-thick water-cooled copper first wall and a 0.5-m thick granular bed of Li_2O in a stainless steel annular container. A low-pressure helium gas flows through the Li_2O packed bed to remove tritium.

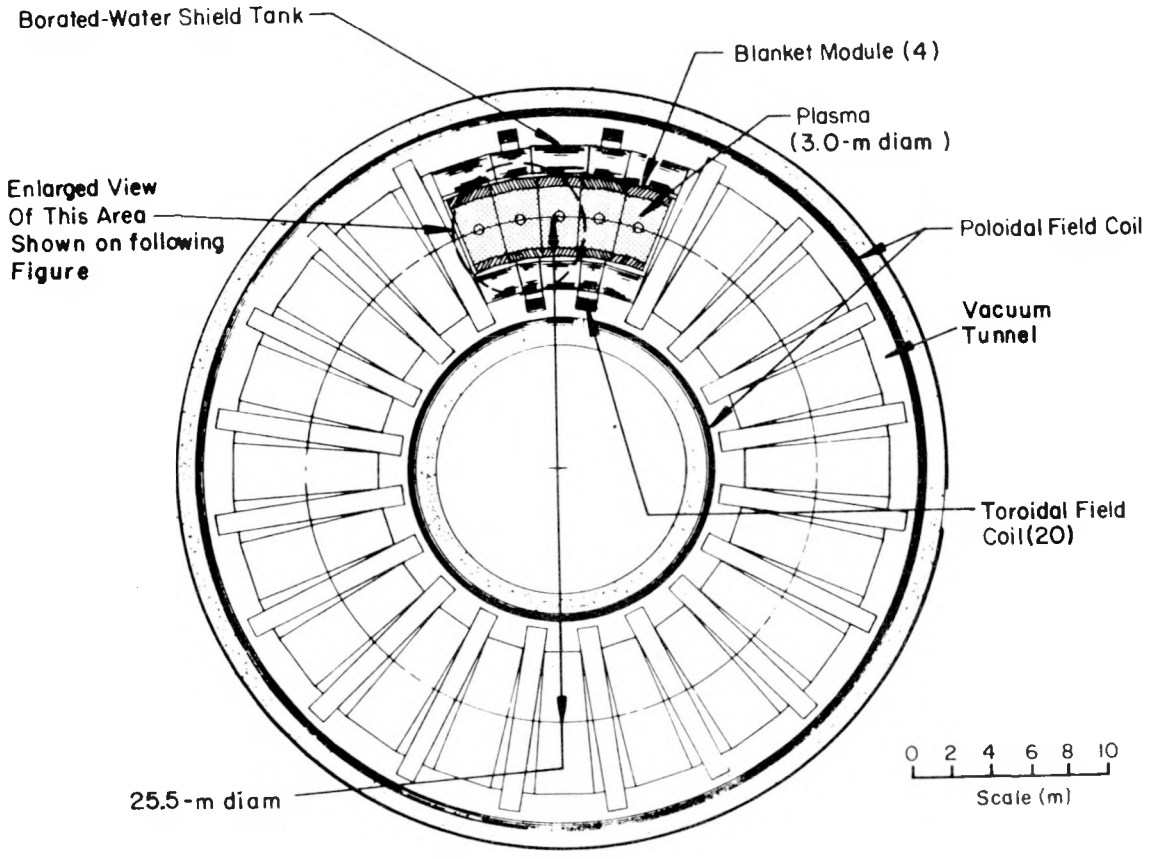

Fig. V-18. Top view of RFPR torus showing relative size of module.

The packed-bed is cooled by circulating water/steam in radial U-tubes that are joined to a common manifold at the outer diameter of each module. Surrounding the modules are hemi-cylindrical steel tanks of borated-water shielding, which are also modular but are separately removable from the blanket/first-wall module. The poloidal and toroidal magnets are fixed structures through which the blanket/first-wall and shielding modules can be removed. The entire torus rests within a toroidal vacuum tunnel. Figure V-19 shows a more detailed view of the torus, whereas an isometric view of the blanket/first-wall module is depicted in Fig. V-20.

a. Materials Selection and Design Concept. A typical lateral cross section of the blanket module is shown in Fig. V-21. The basic module structure is made of stainless steel. Lateral and circumferential stiffeners within the structure will be required, as is shown in Fig. V-21. To the inner wall of the module is brazed a 20-mm-thick, high strength, oxygen-free copper[4]

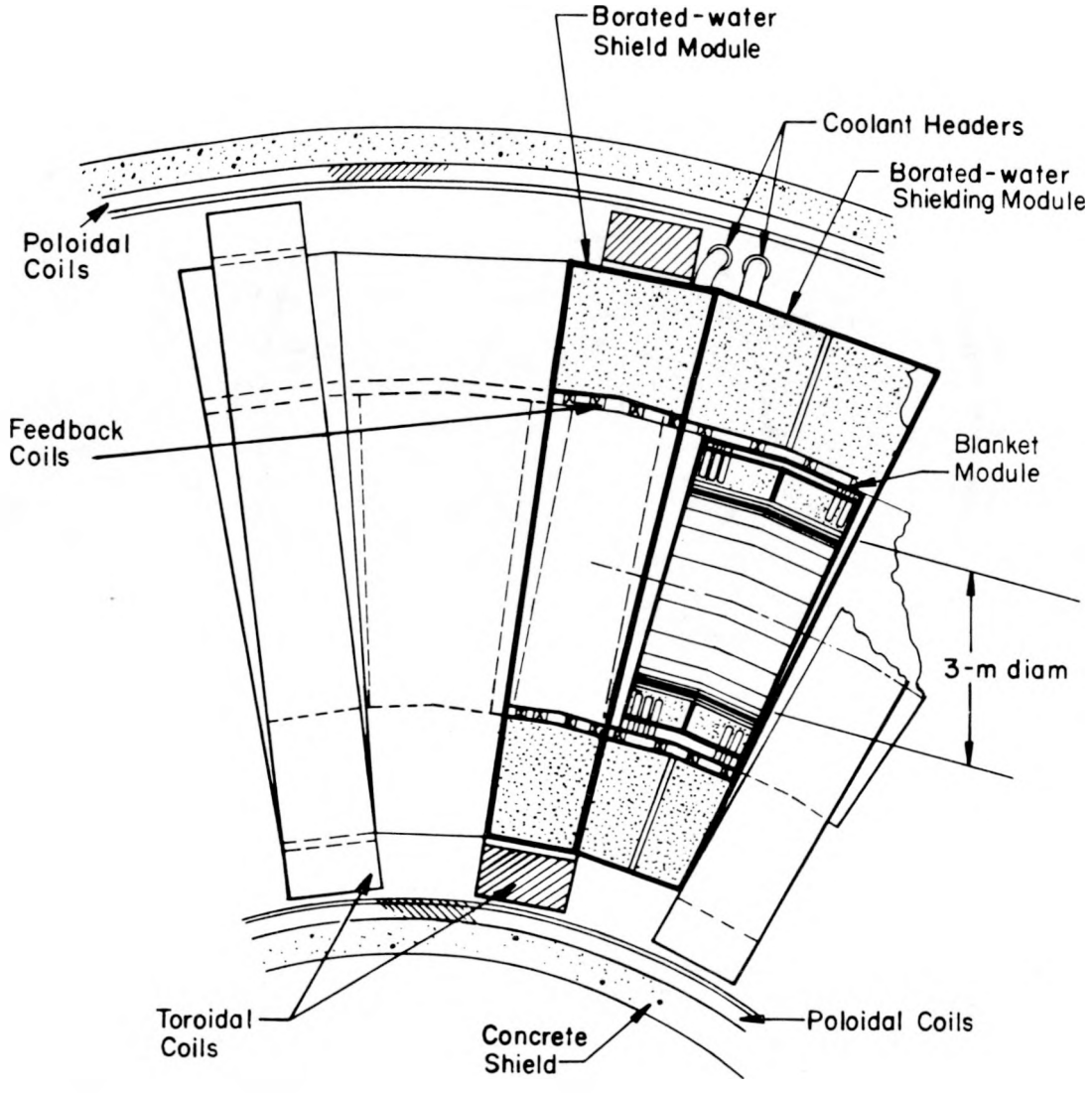

Fig. V-19. Detailed view of RFPR modules positioned in vacuum tunnel.

cylinder with 10-mm thick coolant flow passages. A mechanical interlock is provided between modules at the first wall for structural stability. The interlock can be seen more clearly in Fig. V-20, which also illustrates the method by which the blanket modules would be vertically removed and inserted. Not shown are the vacuum gaps that must exist between each 2-m-long blanket

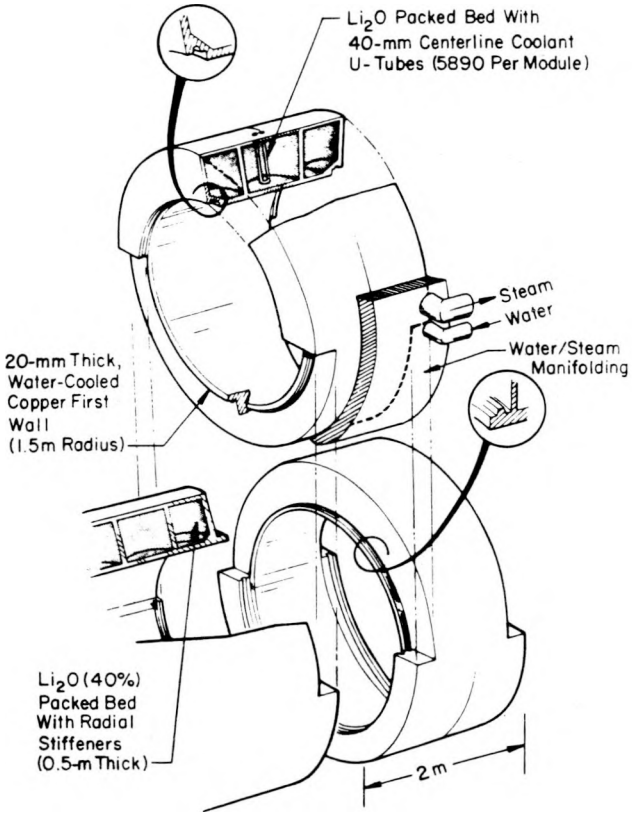

Fig. V-20. Isometric view of reactor module illustrating replacement scheme.

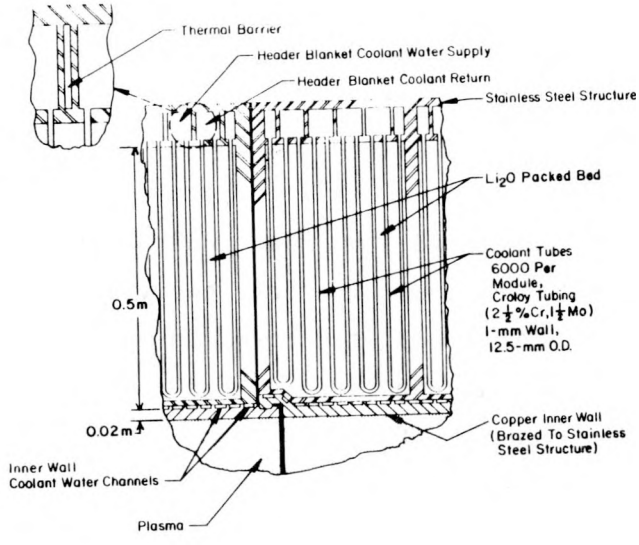

Fig. V-21. Sectional view of steam-generating, packed bed blanket and and first-wall assembly.

module (Sec V.E); the structural interlock between each module would support these vacuum conductances to the vacuum tunnel.

The heat generated in the Li_2O powder is removed from the blanket by boiling water circulating in radially oriented U-tubes shown in Figs. V-20 and V-21. The U-tubes are connected at the outer diameter of the blanket module to circumferential inlet and outlet coolant manifolds. A thermal barrier insulates the inlet water manifold from the adjacent outlet steam manifold. The U-tubes are fabricated from Croloy (2-1/4% Cr, 1% Mo), a seamless tubing alloy that is in widespread use for commercial steam generators and superheaters. This material was selected over austenitic stainless steel partly because of improved resistance to stress-corrosion cracking (Sec V.B.4). The coolant tubes are spaced on approximately 40-mm centers and would support external fins to enhance and control heat transfer from the Li_2O

packed bed. The U-tubes may have to be bent, as illustrated in Fig. V-22, to reduce neutron steaming.

b. Fabrication and Maintenance. The stainless-steel module would be of all-welded construction, except for the furnace braze required to attach the copper first wall. The fabrication sequence has not been determined, but a final step would be the filling of the steel annulus with Li_2O particles, followed by vibration compaction to achieve a uniform particle distribution. The completed blanket modules are assembled into a torus within a vacuum tunnel, after which they are surrounded by borated-water shielding tanks, as shown in Fig. V-23. Magnetic feedback coils and a thin gamma-ray shield would be attached to the inner surface of these hemicylindrical shielding tanks prior to insertion into the vacuum tunnel and around the blanket module.

The completed torus in the vacuum tunnel is illustrated in Fig. V-24. Also illustrated is the location of the poloidal field coils, which are permanently fixed to the concrete walls of the vacuum tunnel (Sec. V.F). A toroidal service tunnel is located directly below the reactor torus to contain vacuum pumping systems, coolant lines, and electrical leads. This arrangement provides close proximity to the blanket for service connections while

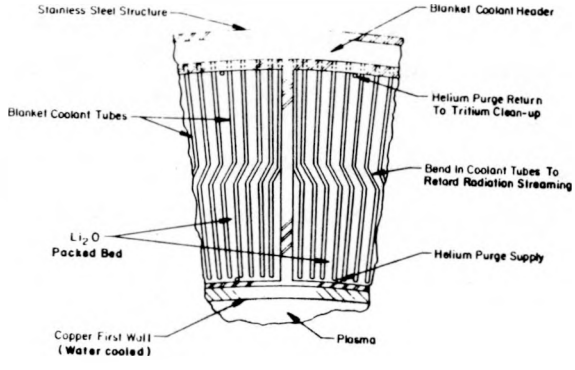

Fig. V-22. Section view of blanket with coolant U-tubes.

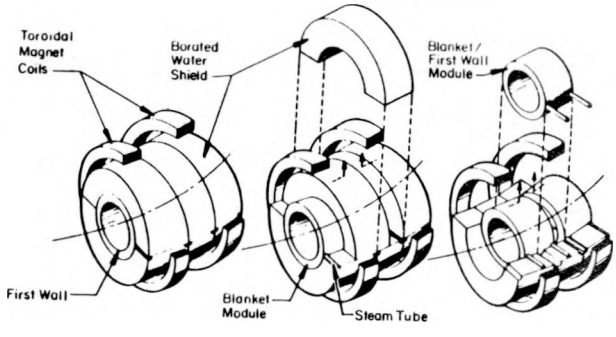

Fig. V-23. Schematic drawing of RFPR modules, illustrating removal sequence of shield and first-wall/ shield modules.

minimizing the vacuum volume and providing clear overhead access for maintenance of the torus.

All service connections to the blanket, magnet coils, and shielding tanks must be remotely operated. Insertion and removal of coils, shielding tanks, and blanket modules is carried out by the high-capacity (100 tonne) overhead crane shown in Fig. V-24. The weights of a complete blanket module and a shield module are both 60 tonnes. The bridge shown beneath the crane supports a trolly that can shuttle torus components between the vacuum tunnel and nearby hot cells. An air lock positioned between the vacuum tunnel and the hot cells reduces the vacuum pumping requirements caused by maintenance operations. Specialized hot cells for service operations on each of the major components could be located some distance from the reactor torus by use of the trolly and crane system. It is possible that more than one trolly and bridge may prove to be optimum.

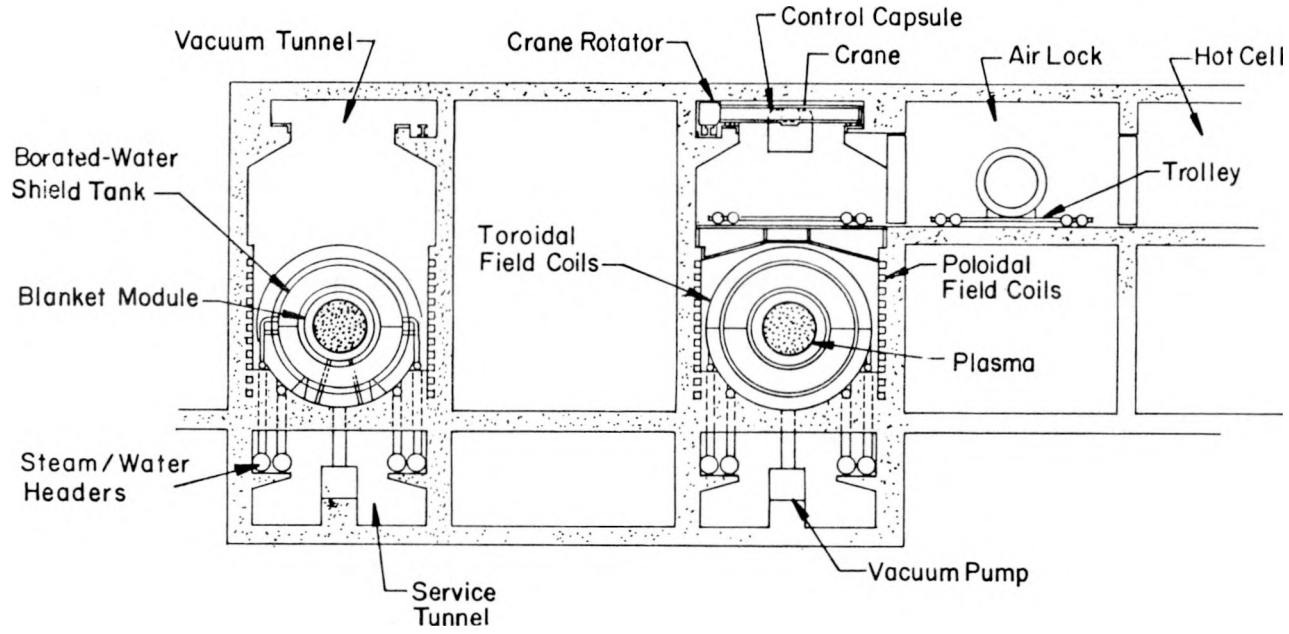

Fig. V-24. Cross-sectional view of RFPR torus located in vacuum tunnel.

c. Structural Adequacy. A detailed analysis of all the structural loads that may be applied to the torus was not possible within the scope of this study. The concept can be shown to be mechanically and operationally sound. A design analysis, based on procedures recommended by the ASME boiler and pressure vessel code, Sec. III,[10] must be carried out by a more comprehensive design study. Because of the emphasis placed in this study on existing technologies and conventional materials and because no new and unusual loading on the module could be identified, an analysis based on procedures that would be recommended by design codes was performed where possible.

The module mechanical design is based on an allowable stress of 103 MPa (15,000 psi) in the stainless-steel structure and coolant headers. The allowable stress in the Croloy U-tubes was 34 MPa (5000 psi). This stress coincides with the 1% per 100,000 hr creep stress limit at 800 K for this alloy.[11] The high-strength copper first wall[4] is designed to an allowable stress of 138 MPa (20,000 psi at 673 K). The allowable stresses include a safety factor of 4 against the ultimate strength.[4]

The loads applied to the blanket module are expected to be varied. The coolant pressure in the U-tubes, headers, and first-wall cooling passages is 5.5 MPa (800 psia). The primary load on the copper first wall is caused by the pulsed magnetic field and consists of a quasi-sinusoid with a positive duration of about 0.1 s at 3.4 MPa (500 psi) and a negative duration of about 0.1 s at -3.4 MPa. Gravity loading is expected to be small in comparison to other loads on the structure. Thermally induced loads are more difficult to evaluate; no thick sections with large temperature gradients exist in the design, and the average thermal transients appear acceptable ($\leq$ 28 K). The ASME boiler and pressure vessel code[10] (Sec. NC-3219.2), among other criteria, states that no thermal fatigue analysis is required where temperature differences are less than 50 K. Temperatures are longitudinally uniform in the blanket module, and the U-tubes are free to expand in the radial direction. The radial temperature difference across the stainless steel structure from the first wall to the coolant manifolds amounts only to approximately 45 K. The mean coefficient of linear expansion for the copper first wall will be closely matched to the steel to which it is brazed. Any residual differential expansion will be accommodated by the braze material. Large temperature differences exist in the Li_2O packed bed and in the external fins attached to the U-tubes, but the resultant stresses do not appear to be

structurally significant. Impulse loading and fatigue loading were assumed to be covered by the 4 to 1 safety factor.

The interlocking joints and associated vacuum gaps between each module (Fig. V-20) can be designed to accommodate thermal expansion. The module supports likewise must provide for thermal expansion while achieving the rigidity required for structural stability of the torus.

The copper first wall, if self-supporting, is not structurally stable because of its thin cross section and large diameter. This copper shell can be brazed to the stainless-steel module structure, thereby providing an integrated and structurally sound module. Because of the radial and longitudinal bracing panels required within the blanket module (Fig. V-21), the loads transmitted from the first wall are easily supported. These bracing panels will also support the U-tubes and provide additional heat conduction paths through the Li_2O packed bed.

Because of the low-pressure helium used to purge tritium from the packed bed, failure of the steel module vessel would result in tritium and vacuum leakage, but no large release of energy is expected. Failure of a main coolant line or manifold would release energy to the vacuum tunnel and could damage the module, but the balance of the torus and magnets should be unaffected. Failure of one of the U-tubes within a module would cause a rapid pressure increase within the packed bed. Ample time should exist to vent the pressure through a relief valve in order to prevent rupture of the blanket structure.

4. Material Considerations. The scope of this study does not permit a detailed assessment of materials problems and needs. Two concerns seem evident however: the integrity of the pressurized steam tubes and the range of effects expected to occur within the copper first wall. These two issues are briefly addressed. The major concern associated with the steam tubes, aside from obvious radiation hardening and possible helium embrittlement, is stress corrosion cracking. The increase in electrical resistivity and the loss of structural integrity appear as major material problems for the copper first wall.

a. Steam Tubes. One of the problems that was overcome in the development of integral nuclear-superheat fission reactors was the prevention of oxygen-chloride stress corrosion cracking.[12] The significant variables for reactor application are stress level, oxygen and chloride concentrations,

chemical additives, coolant pH, temperature, and alloy composition. Alternate wetting, drying and boiling heat transfer appear as significant variables, presumably because of the concentrating of chlorides. The austenitic stainless steels are particularly susceptable to stress corrosion cracking under conditions of alternate wetting and drying of the tube wall. The Croloy steel, which is a complex chromium and molybdenum alloy, was selected for the blanket U-tubes. This alloy is magnetic and may be considered "ferritic" in that its microstructure in the annealed state is composed mainly of ferrite (alpha-iron) and carbides. The ferritic stainless steels are immune to stress corrosion cracking.[13] Recent literature[14] on stress corrosion cracking of steam generator tubing alloys deals exclusively with the 18-8 austenitic stainless steels and the high nickel alloys (Inconel-600, Incoloy-800). Nevertheless, control of the water chemistry will be vital in order to minimize corrosion and scaling in the U-tubes. For example, in Universal Pressure boilers, which are high-capacity high-temperature boilers of the "once-through" type (i.e., without a steam drum), water chemistry is controlled to the specifications listed on Table V-VIII.[15] These boilers use tubes of Croloy, have been commercially available since 1957, and account for many of the large utility installations presently in existence.

TABLE V-VIII

RECOMMENDED LIMITS OF SOLIDS IN FEEDWATER FOR UNIVERSAL PRESSURE BOILERS (PPM)[15]

	MAXIMUM LIMIT	TYPICAL CONCENTRATIONS
Total solids	0.050	0.020
Silica	0.020	0.002
Iron	0.010	0.003
Copper	0.002	0.001
Oxygen	0.007	0.002
Hardness	0.0	0.0
Carbon dioxide	0.0	not measured
Organic	0.0	0.002
pH	9.2 - 9.5	9.45

b. Copper First Wall. Table V-IX summarized the results of the neutronics analysis (Sec. V.B.1) that has direct applicability to radiation damage in the 20-mm-thick copper first wall. A brief survey of changes in electrical resistivity, thermal conductivity, hydrogen embrittlement, swelling, and strength is given.

Increases in the electrical resistivity of copper may result from the introduction of point lattice defects (i.e., vacancies and interstitials), dislocations, voids, transmutation-induced impurities, and magnetoresistivity effects. The point defect contribution is expected to saturate at ~ 0.0034 $\mu\Omega$-m at 300 K.[16] This contribution to the increased resistivity will saturate at a considerably lower value at elevated temperatures because of the reduction in point defect content. Since the starting resistivity is ~ 0.04 $\mu\Omega$-m,[17] the effect of point defects should be quite small.

A high dislocation density may result from plastic deformation or from the formation of radiation-induced dislocation loops. However, even a density of 10^{16} dislocations/m^2, which is unlikely to be sustained at 600 K, increases

TABLE V-IX

SUMMARY OF RADIATION EFFECTS IN COPPER FIRST WALL (20-mm-THICK, 2-m-LONG MODULE, 1.5-m RADIUS)

PARAMETER	VALUE
Fusion neutron wall loading (MW/m^2)	2.7
14.1 MeV neutron current (n/m^2 s)	$1.1(10)^{18}$
Temperatures	
peak temperature (K)	613
average temperature (K)	550
temperature gradient (K/mm)	2.5
temperature change (K)	28
Displacement rate[a] (dpa/y)	30
Helium production[a] (ppm/y)	83
Hydrogen production[a] (ppm/y)	250
(n,2n) reaction rate[a,b]	3015

[a] these values represent averages over the thickness of the copper shell.
[b] forms primarily Ni and Zn.

resistivity by only a few percent.[18] The resistivity contribution from this source, therefore, is expected to be insignificant.

Voids or large defect aggregates should not have an important effect on resistivity. Similarly, the contribution from magnetoresistivity at 2 T and 600 K is estimated to be a few percent at most and more likely will be less than one percent.[19]

The high flux of 14-MeV neutrons will generate a significant concentration of metallic impurities through (n,2n) reactions (Table V-IX). Both Ni and Zn impurities will be formed with Ni predominating. Assuming the formation of only the former element, which will have the greater effect on the electrical resistivity, the resistivity increase predicted will be slightly exaggerated. Allowing one Ni atom per (n,2n) reaction, the rate of impurity formation would be ~ 3000 ppm/y. Using two sets of data for Cu-Ni alloys,[20] the corresponding resistivity increase is estimated to be 9 to 11%/y. This resistivity increase translates into a decrease in the electrical time-constant of the copper shell by ~ 10%/y, which can be accommodated by incorporating a design flexibility in the active feedback circuit. These changes should have little influence on the wall lifetime from the viewpoint of plasma stability.

Thermal conductivity. Since thermal conduction in copper takes place primarily by the motion of electrons, an increase in electrical resistivity will result in a decrease in thermal conductivity. To a first approximation the changes in electrical and thermal resistivities may be assumed to be proportional[17] (Wiedemann-Franz law). Consequently, changes in the thermal properties are not expected to be serious over the expect ~ 5-y lifetime.

Hydrogen embrittlement. Electrolytic tough-pitch copper (standard electrical wire grade) contains Cu_2O. Heating of this metal in hydrogen above ~ 775 K results in internal formation of H_2O (steam) which causes embrittlement.[21] A maximum shell temperature of 613 K should, therefore, be sufficiently low to avoid this problem in the presence of molecular hydrogen. The presence of atomic hydrogen isotopes at the inner shell surface and the presence of transmutation-induced hydrogen within the lattice, however, may result in embrittlement at this operating temperature. It may be desirable to specify oxygen-free high-conductivity (OFHC) copper for this application, although this would preclude the use of a solution-hardened, high-strength alloy.[4] This problem may be serious and should be examined in more depth.

Irradiation-induced swelling of copper occurs between ~ 500 and 825 K, depending on bombarding particle, damage rate, damage level, and gas content of the metal.[22] For "gassy" copper subjected to neutron irradiation at damage rates of 6×10^{-7} dpa/s, the swelling range is shifted to ~ 500 to 775 K, with a maximum occurring at ~ 625 K. The initial swelling rate at 775 K corresponds to ~ 0.4 v/o/dpa.[22] The copper first wall will have a high gas content because of transmutation-induced H and He and is expected to suffer a damage rate similar to the above value (~ 10^{-6} dpa/s). An initial swelling rate of ~ 11 v/o/y at 590 K, therefore, is indicated, but saturation effects may set in before a damage level of 30 dpa is reached. Possible constraint by the stainless steel structure backing the copper first wall must also be considered. The temperature difference of ~ 50 K between inner and outer surfaces may result in a variation of swelling rate through the thickness. A rough estimate[22] indicates a 10% swelling gradient (e.g., from 11 vol% to 10 vol%). Some variation may also result from different displacement and gas generation rates at inner and outer surfaces. It is noted that the copper shell must only support eddy currents and its own weight; a structural or vacuum-barrier function is not required. Nevertheless, if these predictions prove to be correct, the copper shell must be designed to accommodate swelling to an extent where the blanket structure per se is not subjected to an undesirable stress.

Irradiation damage often results in strengthening and embrittlement of metals as a consequence of microstructural changes, particularly when heated at relatively low temperatures and/or subjected to high strain rates. At least up to 400 K,[21] copper is strengthened by irradiation, and, although experimental results showing embrittlement or decreased stress-rupture lifetime for this metal could not be found, these effects are likely consequences of the formation of a damage microstructure.

At temperatures below approximately half the melting point and in fast neutron fluxes greater than 10^{17} n/m^{2}s, metals typically show an enhanced creep rate compared to that observed for the unirradiated material.[23] This enhanced creep results from the generation of point defects during irradiation. Since the copper shell will operate from 0.40 to 0.45 times the melting temperature in a fast neutron flux of ~ 5×10^{18} n/m^{2}s, accelerated creep can be expected.

In summary, the following radiation/electrical/mechanical effects are expected for the copper conducting shell:

- Electrical resistivity will be increased ~ 10%/y primarily as a result of the transmutation-induced formation of nickel.
- Thermal conductivity will be decreased roughly in proportion to increases in electrical resistivity.
- Hydrogen embrittlement is a possibility, suggesting the use of OFHC copper.
- A large amount of swelling and appreciable swelling gradients are anticipated, although some reduction of these effects might be achieved by prior adjustment of microstructure.
- The copper first wall is likely to suffer decreased ductility and stress-rupture lifetime and an increase in creep rate.

Consequently, the major concern appears to be related to mechanical rather than electrical degradation of performance. The relatively passive role anticipated for the copper shell and the possibility to operate at a reduced shell lifetime, however, may permit a greater degree of design flexibility in dealing with these potential problems. Most importantly, however, is the need to quantify these somewhat preliminary projections and to fold results from more detailed study into a more comprehensive design of the copper shell.

C. Steam Power Cycle

The blanket module is cooled by two independent 5.5-MPa (800 psia) cooling-water loops. The first coolant loop circulates through the U-tubes in the Li_2O packed bed and exits as slightly superheated steam. The steam drives directly a high-pressure (HP) turbine without using a secondary coolant loop and steam generator. For this Rankine direct-cycle system, shown in Fig. V-25, the blanket acts as the steam generator and superheater. The thermodynamic power cycle summarized in Table V-X is a relatively conventional wet-steam cycle that is similar to a commercial fission reactor plant.[6,15] The second loop cools the first wall, removing approximately 38% of the total thermal power. Because the temperature capability of the copper first wall is less than for the stainless steel blanket and because the heat flux to the first-wall coolant channels is higher than in the tritium-breeding/neutron-moderating packed bed, coolant temperatures are maintained lower in the first-wall coolant loop, and net flow boiling is prevented.

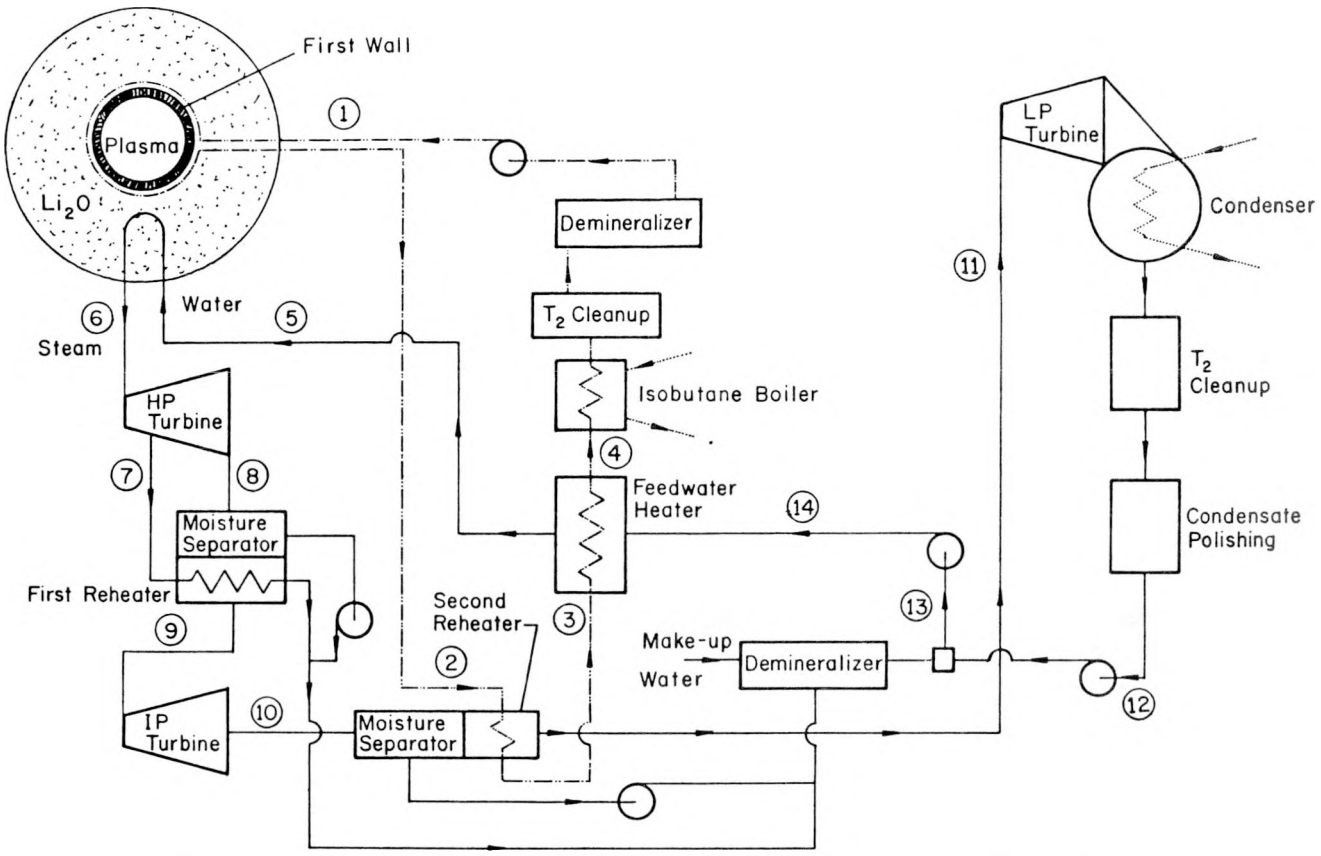

Fig. V-25. Flow diagram illustrating RFPR thermodynamic cycle. The flow conditions in each stream are indicated on Table V-X.

1. Cycle Description.

a. Cycle Flows and Efficiency. The flow diagram given in Fig. V-25 shows the two separate coolant loops as solid and bar-dot lines, respectively. The circled numbers on Fig. V-25 correspond to the flow and state point conditions listed in Table V-X. Referring to Fig. V-25, the first-wall coolant (1585 kg/s) enters point [1] at 360 K and exits at point [2] at 530 K. This coolant is then directed to the second reheater where a portion of its energy is used to reheat the primary steam between the intermediate pressure (IP) and low-pressure (LP) turbines. The first-wall coolant is then sent to a liquid-liquid heat exchanger, [3-4] where additional energy is extracted to heat the feedwater flowing to the blanket U-tubes. Finally, a low temperature organic fluid bottoming cycle is used to extract the remaining useful energy [4-1] from the first-wall coolant. The tritium cleanup operations in each of the two coolant loops have not been defined and are illustrated only to indicate where in the loop they would be placed. Demineralizing and

TABLE V-X

STEAM CYCLE AND FLOW CONDITIONS FOR THE SYSTEM DEPICTED IN FIG. V-25.

STREAM NUMBER	FLOW RATE (kg/s)	T(K)	P(KPa)	h(MJ/kg)	MOISTURE CONTENT (%)	REMARKS
1	1584	360	5516	----	100	First-wall coolant inlet
2	1584	530	5495	----	100	First-wall coolant outlet
3	1584	515	5488	----	100	Second reheater outlet
4	1584	497	5481	----	100	Feedwater heater outlet
5	788.4	383	5516	0.631	100	Li_2O blanket coolant inlet
6	788.4	551	5512	2.818	0	HP turbine inlet
7	15.8	503	2758	2703	5.5	Bleed steam for first reheat
8	716.1	487	2069	2.659	7.5	HP turbine exhaust
9	716.1	500	2065	2.836	0	IP turbine inlet
10	716.1	421	552	2.624	6.1	IP turbine exhaust
11	680.3	450	548	2.801	0	LP turbine inlet
12	680.3	300	3.4	0.112	100	Condenser exit
13	788.4	322	2065	0.204	100	Feedwater pump inlet
14	788.4	323	5516	0.207	100	Feedwater heater inlet

condensate polishing are conventional steps in a nuclear steam cycle and are illustrated here for completeness.

The blanket coolant enters the packed bed at 5.52 MPa and 383 K [5] and exits as slightly superheated steam at 551 K [6]. The flow rate is 788.4 kg/s, which is about half that in the first-wall coolant loop. Approximately 15.8 kg/s of the steam is extracted from the high-pressure turbine at 503 K for use in the first reheater. Typically, several stages of feedwater heating are used, with bleed steam being extracted at more than one turbine stage. Because of the available energy in the low-temperature water that cools the first wall, the additional steam extraction for feedwater heating is unnecessary. The net turbine work produced in the HP expansion is 126.2 MW, assuming 85% efficiency. After moisture separation the remaining 716 kg/s of steam exits the reheater [9] at 500 K and 2.07 MPa, where it enters the IP turbine. The net rate of work in this expansion is 151.1 MW. The fluid conditions at position [10] are 0.55 MPa and 429 K before entering the second moisture separator and reheater. After this step 680.3 kg/s of

steam at 0.55 MPa and 450 K remains for expansion in the LP turbine. This expansion again is assumed to occur with an 85% efficiency and results in 419.5 MW of useful work. The net power delivered in the organic fluid bottoming cycle is 152 MW, which results in a total useful power for the cycle of 848 MW. From this power must be subtracted the work required to operate the first-wall coolant circulating pump, [4-1] the primary coolant condensate pump, [12-13] the primary coolant feed pump, [13-14] and other auxiliaries. The net useful work produced in the cycle is 828 MW, which yields an overall cycle efficiency (i.e., not including circulating power to maintain the plasma) of 28%.

b. Moisture Removal. Pressure and temperature limitations in the blanket force the cycle expansion lines to be located in the wet-steam region of the Mollier chart. Steam is delivered to the high-pressure turbine inlet at a temperature that is only 8 K above saturation. Although this amount of superheat does improve cycle efficiency, it does not eliminate the problem, which is encountered with all saturated steam cycles, of managing large quantities of condensed moisture in the turbine. High moisture in the steam not only reduces expansion efficiency but also causes erosion of the turbine blades. Increasing the superheat of the inlet steam will increase cycle efficiency and alleviate problems caused by excessive moisture. Saturated steam cycles are in widespread use for commercial nuclear power plants, however, and are being further developed for production of electricity from fluids heated from geothermal sources.

Two methods of moisture removal are normally used. After exiting the U-tubes and expanding in the HP turbine (Fig. V-25), the steam passes through a moisture separator, which is a low pressure-drop separator located externally to the turbine. After passing through this separator, the steam is reheated by bleed steam before entering the IP turbine. A second external moisture separator and reheater is located between the IP turbine and the LP turbine. The energy for the second reheater is supplied by the first-wall coolant. In the LP turbine the second method of moisture removal is used, which employs grooves in the back of the turbine blades to drain the moisture from certain stages. The separated moisture is carried off with the bleed steam and recycled back with the feedwater. The moisture level in the high and intermediate pressure turbines reaches a maximum of 7.5%, which is consistent with present practice. The moisture level in the LP turbine

reaches a maximum of 14%, which is also consistent with present practice. The expansion portion of the power cycle is shown on a Mollier chart in Fig. V-26. The increase in the enthalpy and entropy of the working fluid at each of the moisture separation and reheat steps is indicated on Fig. V-26.

2. Cycle Efficiency and Alternatives. Alternatives to the direct steam cycle described above include both the Boiling Water Reactor (BWR) cycle, wherein approximately 10 to 15% of the circulating water is converted to steam, and the Pressurized Water Reactor (PWR) cycle, where no net steam generation occurs in the primary coolant loop. A large steam separator discharges saturated steam to the turbine in the BWR cycle, and the majority of the coolant flow is recirculated back to the reactor. The PWR cycle typically operates at much higher pressures than is desirable for this RFPR blanket design, and lower pressure steam is generated in a secondary loop in a large heat exchanger (steam generator). The typical net efficiency for these nuclear reactor plants is 30%. Minor revision would be required in the RFPR blanket design to substitute one of these cycles, but the ~ 30% cycle efficiency could not be achieved. The reason for the somewhat lower RFPR cycle efficiency is that the copper first wall was not allowed to operate at the U-tube temperature, while 38% of the thermal energy is delivered to the first wall. Consequently, it is necessary to cool preferentially the first-wall region at a sacrifice to the overall cycle thermal efficiency. The operating conditions for one of these alternative cycles would be essentially identical to that listed in Table V-VII.

It is possible to upgrade the thermal efficiency of the present cycle by increasing the steam outlet temperature emerging from the U-tubes, while simultaneously operating within the range of current practice for utility power plants. This increase in steam temperature could be accomplished, for example, through the use of a more heat resistant alloy for the U-tubes or by increasing the heat-transfer surface area by the use of internal fins in those regions where tube-wall temperatures are maximum (Sec V.B.2.b). Figure V-27 shows the effect of increasing the steam exit temperature on cycle efficiency. The solid curve indicates the enhanced efficiency if the temperature limitation imposed on the copper first wall is maintained, whereas the dotted curve shows the increased efficiency if the first-wall exit temperature is increased to that of the steam exiting from the blanket U-tubes.

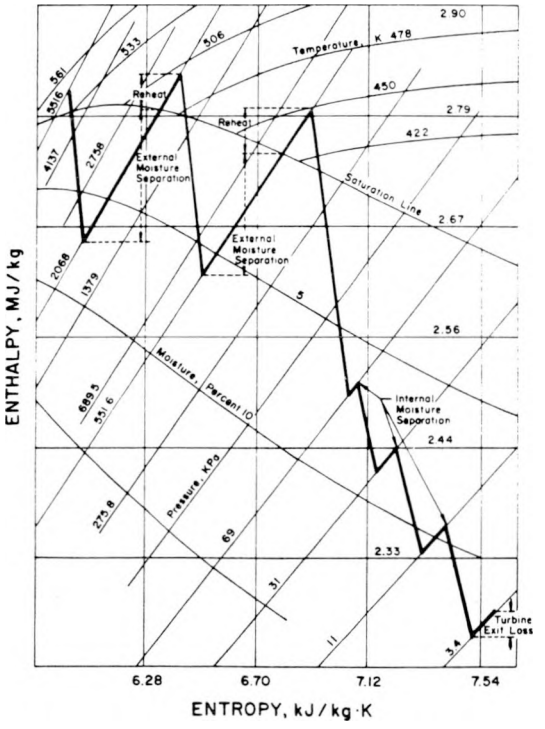

Fig. V-26. Mollier diagram illustrating RFPR steam cycle.

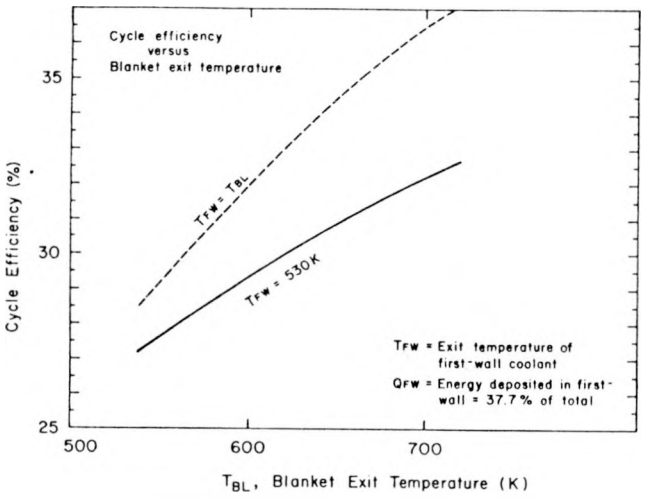

Fig. V-27. Effect of first-wall and exit steam temperature on steam cycle efficiency.

In addition to the ability to maintain different flow rates and temperature levels as described, one of the additional advantages of the two parallel coolant loops is the flexibility in controlling water chemistry and tritium. The impurity concentrations that are compatible with Croloy tubing[6] under boiling conditions are likely to be more stringent than those required for copper at a much lower temperature than adopted for the U-tubes. Additionally, the tritium containment/isolation task for the coolant streams will probably be different. Each demineralizer and tritium removal system, therefore, can be optimized for the concentration requirement and water flow rate of the respective loop.

Additional cooling alternatives for this blanket design concept are flowing liquid metals and high-pressure helium.[24] The potential use of helium as a coolant was investigated and found to be impractical because of relatively low heat transfer rates and high pressure drop required for acceptable flow passage geometry. It is interesting to note that several other blanket designs[25-30] consider the use of water and steam as a primary

coolant. A few of these concepts predict higher thermal efficiencies for the steam cycle than that presented herein. The increased efficiency is generally a result of much higher steam temperatures than adopted by this study. These other water/steam-cooled concepts, however, may not give sufficient consideration to important design problems that may restrict the maximum temperatures and efficiencies that are achievable in practice. For example, some concepts either do not require tritium breeding or do not deal with tritium handling and containment. Other designs do not consider practical aspects of a steam cycle, such as moisture limits in a turbine, corrosion and scaling, or maximum heat fluxes in a boiling system without burnout. Still other designs do not discuss structural requirements needed to contain a high-pressure fluid at high temperatures.

The use of topping and bottoming or dual-fluid cycles is finding increasing favor as fuel costs rise to make increased conversion efficiency more desirable.[30] A working fluid other than water for use in one of the cycles is common. Organic refrigerants have been considered[31] as the secondary fluid for geothermal applications because of favorable thermodynamic properties in the lower temperature ranges of interest. A dual cycle, utilizing steam and isobutane, has been considered[32,33] by the Los Alamos Scientific Laboratory for a demonstration system with a pressurized geothermal water source at 553 K.

For the cycle shown in Fig. V-25 reject heat from the first-wall coolant is used to boil a secondary working fluid (isobutane) for the low-temperature bottoming cycle. Assuming that this heat can be converted to mechanical work with an efficiency[31] of 17%, the useful output of the bottoming cycle would be 152 MW. This added conversion results in an increase in the overall cycle efficiency from 23% without the bottoming cycle to 28%. The latter number represents 61% of the available work from a reversible Carnot cycle operating between a source at 551 K and a sink at 300 K. This represents a respectable performance compared with modern fossile fuel and nuclear plants that typically achieve 65% of the ideal Carnot efficiency.

D. Tritium

As seen from Sec. V.B, tritium would be bred in the Li_2O solid breeder, which was chosen because of its refractory nature and the desire for a high-temperature receptacle for the fusion neutron energy. Bred tritium would either be trapped within the packed-bed Li_2O particles or would be released

diffusively, depending on the local thermal conditions. Released tritium would be rapidly oxidized by ppm-levels of oxygen in the helium (0.1 MPa) purge gas and either continuously or periodically be removed from the Li_2O blanket; the rapid formation of T_2O is crucial to this blanket concept in order to prevent serious tritium loss and primary coolant contamination. Tritium oxide removed by the helium purge stream would be processed by the usual methods:[34-36] water (T_2O) absorption on molecular sieve. Again, because of the limited scope of this study only two important issues have been addressed: the physical properties of Li_2O as a tritium breeder and refractory heat receptacle, and the kinetics of tritium release from the packed bed. Both issues are clearly coupled.

Tritium isolation from both the first-wall and blanket coolant loops has been assumed on the basis of present understanding. Low-levels of oxygen in the packed-bed, presumably present in reactor-grade helium or released by the destruction of Li_2O that occurs during the breeding process, should rapidly oxidize gaseous T_2. Diffusion of T_2O through steel at the temperatures envisaged should be negligible. Isolation of tritium gas in the plasma chamber from the first-wall coolant water also appears feasible in that diffusion at the 613 K peak temperatures would in principle lead to negligible transport through the 20-mm-thick copper that separates the plasma chamber from the first-wall coolant channel. The tritium containment and isolation question, however, remains far from resolved for an actual engineering system (i.e., systems with joints, weldments, three-dimensional shapes, etc.). The maintenance of a tritium-free first-wall coolant loop is probably more uncertain than for the blanket coolant system. The separation of coolant loops, however, may permit operation of a slightly contaminated first-wall loop, if necessary, although the impact of this operational mode on the overall fuel balance remains to be quantified.

1. Physical Properties of Li_2O. Lithium is required in the blanket for tritium breeding purposes, but its chemical and physical form is a matter of blanket design. Past blanket studies have included liquid lithium or solid lithium components. The RFPR design is based on a Li_2O packed-bed approach because of a desire to use existing technologies such as a direct-cycle steam conversion system and a stainless steel blanket structure. Lithium oxide has the advantages of a solid, a high lithium content (46.45% Li by weight) and a high melting point (~ 1700 K).

Other blanket designs have also used Li_2O as a solid breeder. In one design[37] Li_2O pellets flow by gravity to serve as both a tritium-breeding material and a heat-transport medium. Results have been published[38] of a conceptual blanket design with helium-cooled Li_2O pebbles. The present design differs from these concepts because the tritium-rich flow stream is decoupled from the blanket primary coolant stream; a low pressure (0.1 MPa) helium purge is used to extract tritium as an oxide, and the high-temperature Li_2O bed is cooled by radial water/steam tubes. The Li_2O bed, therefore, is not actively cooled, thereby minimizing problems associated with particle erosion and dust formation. The blanket composition is: Li_2O (40 v/o), H_2O (10 v/o), steel (15 v/o) and voidage (35 v/o).

The proposed method of tritium scavenging is supported by the existing experimental data.[39] Low-pressure helium gas (0.1 MPa) was selected for purging because of its chemical inertness, helium production[40] by nuclear reactions in the blanket, and the available experimental tritium-release data.[41] Lithium oxide is commercially available in white crystalline or powder form. Presently no industrial uses can be identified that consume large quantities of Li_2O. The oxide can be prepared by several methods.[42] A commercial powder product has a specific surface area of about 180 m^2/kg. Some investigators[40,43] have already reported successful methods for commercial Li_2O production.

Table V-XI summarizes the Li_2O temperature distribution in the RFPR

TABLE V-XI

DISTRIBUTIONS OF BLANKET (Li_2O) TEMPERATURE, POWER DENSITY, AND TRITIUM BREEDING RATE USED TO DETERMINE TRITIUM INVENTORY AND RELEASE RATES

RADIAL POSITION (m)	AVERAGE CELL TEMP. (K)	VOLUME (m^3/module)	MIN. TEMP. (K)	MAX. TEMP. (K)	POWER DENSITY MW/m	POWER DENSITY MW/m^3	TRITIUM BREEDING RATE Tritium/Neut.	TRITIUM BREEDING RATE kg/m^3 s
1.63	1242	0.0099	600	1671	9.36	9.43	0.47	$2.48(10)^{-8}$
1.73	1013	0.0106	590	1287	5.43	5.14	0.32	$1.56(10)^{-8}$
1.83	820	0.0112	570	1002	2.93	2.63	0.18	$8.12(10)^{-9}$
1.93	782	0.0118	540	905	1.54	1.30	0.09	$4.16(10)^{-9}$
2.03	658	0.0124	500	735	0.87	0.70	0.06	$2.32(10)^{-9}$

blanket. The results of tritium production from the neutronics studies (Sec. V.B.1) are also summarized in Table V-XI; these results are in general agreement with other similar designs.[38] It is estimated that at the design temperatures the tritium release rates will be marginal-to-adequate (Sec. V.D.2), and the Li_2O consumption will be consistent with the lifetime objective of the blanket modules. Furthermore, the blanket design may be optimized for enhanced tritium release by tailoring the blanket coolant design for a more optimal and nearly-uniform temperature profile. Although a Li_2O temperature greater than 873 K may be expected to maximize the tritium release rates[44] this conclusion appears to depend sensitively on particle morphology and diffusion kinetics (Sec. V.D.2.).

Reliable and precise thermodynamic data are needed for prediction and understanding of Li_2O systems. A literature survey was carried out to obtain the Li_2O properties listed in Table V-XII. In addition, Li_2O is known to be chemically reactive with H_2O, CO_2 and refractory compounds.[38] For this reason introduction of appreciable quantities of moisture, carbon and refractories were avoided in this blanket design.

Under neutron irradiation, Li_2O pellets go through the following nuclear reactions:

$$Li_2O + n \xrightarrow{^6Li} LiOT + {}^4He \qquad (V\text{-}1)$$
$$Li_2O + n \xrightarrow{^7Li} LiOT + {}^4He + n'$$

The LiOT formation is followed by T_2O formation by the reaction

$$2\ LiOT \rightarrow Li_2O + T_2O\ . \qquad (V\text{-}2)$$

Hence, the rate of T_2O formation is equivalent to the rate of Li_2O consumption in the absence of other possible reactions such as:

$$Li_2O \rightarrow Li + O_2 \qquad (V\text{-}3A)$$

$$T_2O \rightarrow T_2 + 1/2\ O_2 \qquad (V\text{-}3B)$$

TABLE V-XII

PHYSICAL PROPERTIES OF Li_2O

PROPERTY			VALUE	REFERENCE
Molecular weight			29.88	45
Dens ty (kg/m^3)			2013	45
Crystalline form			cubic	45
Lattice constant (Å)			4.619	46
Index of refraction			1.644	45
Atomic distance (Å)		Li-O	2.00 (1.82)	39(46)
		Li-Li	2.32 (2.90)	39(46)
		O-O	3.27	39
Molar volume (m^3/kg-mol)			0.0148	47
Melting point (K)			1840	47
			> 1700	45
Boiling point (K)			2830	47
			2873	39
Viscosity (Pa s)			1.690	48
Vapor pressure (Pa)	1200 K		$5.56(10)^{-5}$	49
	1500 K		$2.01(10)^{-1}$	49
	1773 K		27.86	49
	2000 K		558.52	49
Heat capacity (kJ/kg-mol K)	298.89 K		54.30	50
			54.16	51
Thermal conductivity (W/m K)	298.89 K		1.73	39
Heat of formation (kJ/kg-mol)	298.15 K		$-5.98(10)^5$	52
Free energy of formation (kJ/kg-mol)	298 K		$-5.45(10)^5$	39
	873 K		$-4.59(10)^5$	53
Heat of hydration (kJ/kg-mol)			$1.30(10)^5$	39
Latent heat of fusion (kJ/kg-mol)			$5.86(10)^4$	39
Latent heat of vaporization (kJ/kg-mol)			$2.34(10)^5$	39

$$Li + T_2O \rightarrow LiOT + 1/2\ T_2 \qquad (V\text{-}3C)$$

$$Li_2O + T_2O \rightarrow 2\ LiOT \qquad (V\text{-}3D)$$

$$Li_2O + 1/2\ O_2 \rightarrow Li_2O_2\ . \qquad (V\text{-}3E)$$

The existing data,[54] suggest that tritium production occurs primarily through T_2O generation as evidenced by the condensation of 95.1 - 98% of the gaseous products at 201 K.

Experimental data[39,41,55] on tritium release from Li_2O are sparse and poorly defined. Generally, Li_2O powders were subjected to neutron irradiation, and the time evolution of tritium release was monitored upon subsequent heating. The shape of tritium release curves reflects a range of particle sizes and pellet morphology, and a derivation of a diffusion coefficient from such data at best is risky. For instance, the "activation energy" obtained for tritium release from Li_2O by one experiment[41] was computed to equal 28.6 kJ/mol, which is almost an order of magnitude below that expected for bulk diffusion processes. Nevertheless, diffusion coefficients were estimated from these tritium-release data and are compared on Table V-XIII. Although agreement between the two experiments that were analyzed is reasonably good, it is doubtful that the effective diffusivities describe purely bulk processes. This fact, when coupled with the narrow temperature range investigated by these experiments, has lead to the use of these Li_2O data only for purposes of comparison and calibration with diffusivity data from other ceramics.

TABLE V-XIII

COMPARISON OF MEASURED TRITIUM DIFFUSIVITIES IN Li_2O

TEMPERATURE (K)	DIFFUSIVITY (m^2/s)[55]	DIFFUSIVITY (m^2/s)[41]
873	2×10^{-13}	4×10^{-13}
923	5×10^{-13}	5×10^{-13}
923	1×10^{-13}	5×10^{-13}

For the purposes of estimating the diffusive release and tritium inventory (Sec. V.D.2), available data for hydrogen-isotope diffusion in a range of ceramic materials was compiled. This compilation is displayed graphically in Fig. V-28 in the form of an Arrhenius plot. The few data points available for Li_2O are also included.[41,55] Adopting the usual functional form $D(T) = D_o e^{-E_D/kT}$, the pre-exponential factor D_o is taken as $7(10)^{-6}$ m^2/s, and the diffusion energy was taken as 204 kJ/mol; these parameters correspond to sintered BeO (Curve D, Fig V-28). This approach is arbitrary but conservative. For instance, if the tritium-release data from Ref. 41 were used, E_D would be 28.6 kJ/mol, $D_o \simeq r_p^2/\pi^2\tau \simeq 3.38(10)^{-13}$ m^2/s, and $D(m^2/s) \simeq D_o e^{-3460/T} + 2.48 = 4.0(10)^{-12}\ e^{-3460/T}$, where the pellet radius $r_p \simeq 10^{-4}$ m and the release time $\tau \simeq 3000$ s. This "diffusivity" prediction is also shown in Fig. V-28, and would predict considerably higher release rates, for the temperature distributions used.

A tritium flow diagram was conceptualized on the basis of known data.[39,41,55] Figure V-29 shows a schematic view of the tritium recovery process. Oxidation of the tritium stream is completed in a converter bed, followed by helium separation at liquid-nitrogen temperatures. Although no design effort could be devoted to developing a better understanding of the scheme suggested by Fig. V-29, the approach appears to be relatively conventional,[36] given that the kinetics of tritium release from the Li_2O blanket can be resolved. The following section addresses this latter issue.

2. Tritium Transport in Blanket. Several issues concerning tritium may influence the design and operation of the blanket. One such issue considered here is related to the development of a blanket design that can attain tritium self-sufficiency within a reasonable time. The release of tritium from the Li_2O particles to the helium purge gas is an essential element of this issue. A related concern is the spatial and total tritium inventory within the blanket.

In order to address these issues a one-dimensional, time-dependent tritium transport model has been developed. This model is described in Appendix D. The unit cell used to compute the Li_2O radial "macrodistribution" of temperature (Fig. V-15, V-16) was applied to the kinetics of tritium buildup and release. Each radial position in the blanket is occupied by Li_2O particles of nominal radius r_p. The local Li_2O pellet temperature and power density allows an estimate of the "microdistribution" of temperature

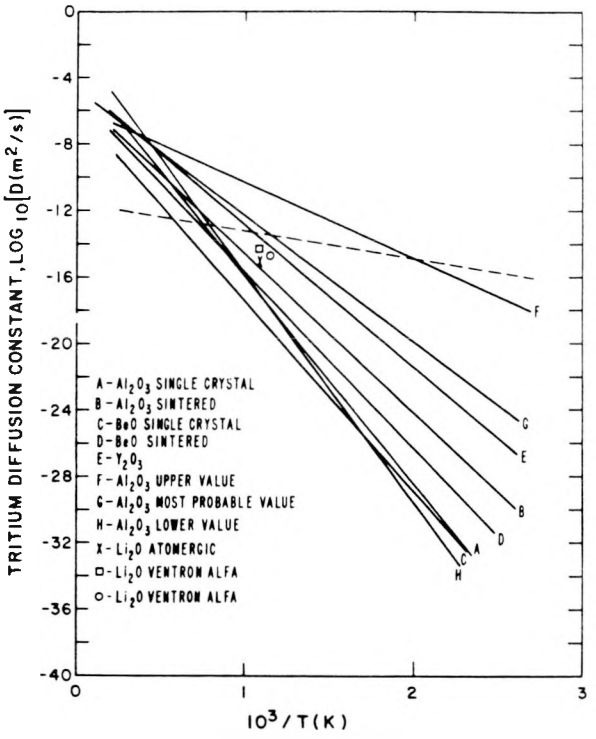

Fig. V-28. Summary of hydrogen diffusion data for a number of ceramic materials. Curves A-E are from Ref. 56, curves F-H are from Ref. 57. The dashed curve is interpreted from data given in Ref. 41, and the data points are from Ref. 55.

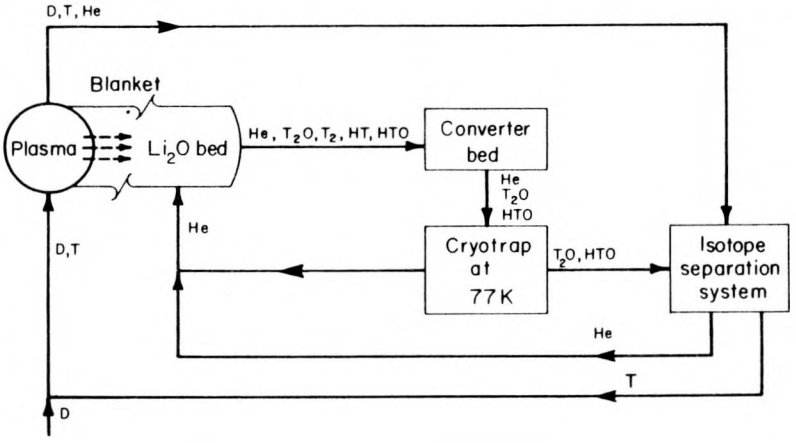

Fig. V-29. Schematic deuterium-tritium flow cycle.

throughout the pellet. If the pellet of radius r_p is assumed to be composed of individual grains of radius, r_g, the time-dependent diffusion equation can be applied to that grain at a temperature given by the microdistribution. The tritium partial pressure at each grain boundary was assumed equal to that surrounding the Li_2O pellet (i.e., rapid grain boundary diffusion), and the tritium diffusivity for a given grain was evaluated according to the microdistribution of temperature within the pellet. Tritium release and inventory at any time is summed over all grains within a pellet. This summing procedure is continued over all pellets situated along the macrodistribution of temperature, as given by the thermohydraulic calculations (Fig. V-16). Following this numerical procedure allows the time and space evolution of the tritium concentration and release to be determined within a given unit cell at a given radial position as a function of assumed diffusion coefficient, grain

radius, r_g, and pellet radius, r_p. Finally, the tritium distributions are integrated over the entire blanket to yield the total tritium inventory I(kg/m), release rate L(kg/s m), and production rate R(kg/s m). Figures V-30 and V-31 show the dependence of I/Rt and L/R on time t for a range of realistic r_p and r_g values. For the tritium diffusivity assumed (i.e., for BeO[56], Fig. V-28), the Li_2O macrodistribution of temperature given in Fig. V-16 indicated only ~ 80% equilibrium (tritium production equals release) after a number of years (Fig. V-30). The results presented in Fig. V-31 corresponds to a macrodistribution of temperature in which the thermal unit cell closest to the first wall was repeated radially outward through the blanket. Generally, the system will become self-sufficient in tritium when the value of L/R exceeds the inverse of the tritium breeding ratio, BR. Packed beds with the largest pellet radius (enhanced temperature peaking

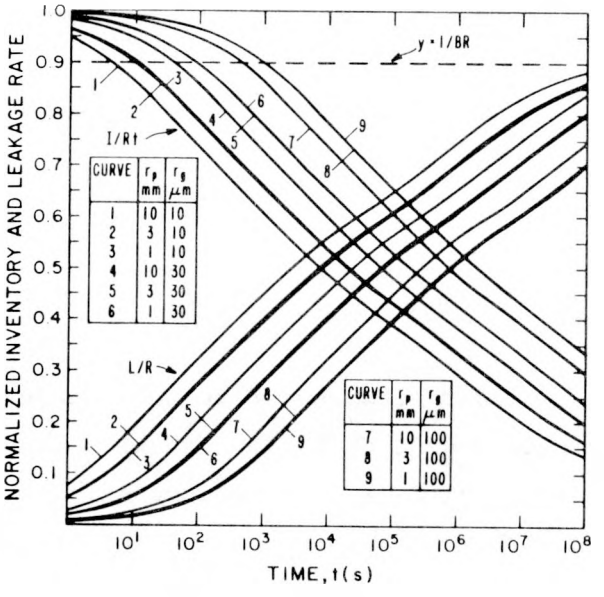

Fig. V-30. Time dependence of normalized tritium blanket inventory I(kg/m) and release rate L (kg/s m) for a Li_2O (40 v/o) packed bed of 0.5-m thickness as a function of Li_2O pellet radius r_p and grain radius r_g, using BeO tritium diffusivity.[56] The Li_2O temperature distribution given in Figs. V-15 and V-16 were used.

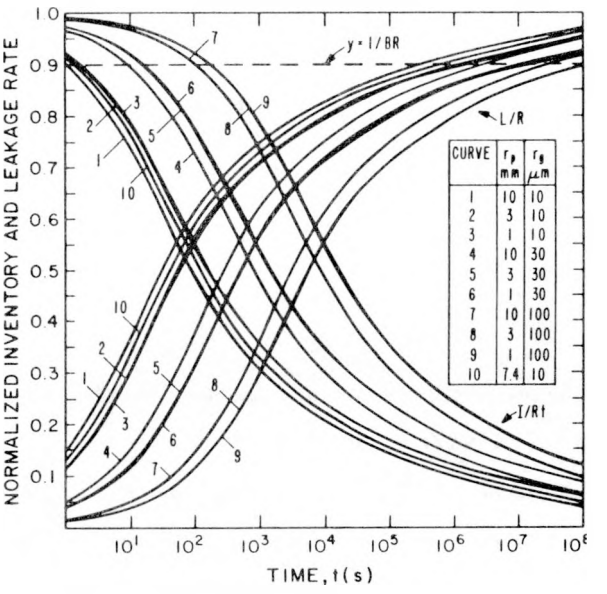

Fig. V-31. Time dependence of normalized tritium blanket inventory I(kg/m) and release rate L (kg/s m) for a Li_2O (40 v/o) packed bed of 0.5-m thickness as a function of Li_2O pellet radius r_p and grain radius r_g, using BeO tritium diffusivity.[56] The inner blanket Li_2O temperature distribution given in Fig. V-15 was repeated throughout the blanket.

within a pellet) and smallest grain size (enhanced diffusive loss) give a breakeven time of $7(10)^5$ s that increases to $1(10)^8$ s for the smaller pellets and larger grain sizes. None of these cases achieve an equilibrium blanket inventory within a projected 5-y lifetime, but after five years the tritium retained in the blanket typically lies in the range 0.3-1.0 kg/m (8.2-27.3 kg/GWt). The value of tritium diffusivity used for Li_2O, as well as radiation effects on both tritium transport and changing pellet morphology, represent important uncertainties. Generally, the specific tritium inventories in the blanket reported above are considered conservatively high. For instance, use of the Ref. 55 "diffusivity" data (dashed curve, Fig. V-28) would bring the specific blanket inventory below the 0.01-1.0 kg/GWt range predicted for a typical fusion reactor.[58]

The radial profiles of the tritium inventory as a function of time for the conditions depicted on Fig. V-31 are given in Fig. V-32. These profiles are shown also in Fig. V-33, normalized to the total amount of tritium bred. The detailed time evolution of iso-concentration lines within a blanket unit cell is given in Appendix D.

In designing a fusion blanket it is important that the blanket be capable of tritium self-sufficiency within an acceptable time period. By self-sufficiency is meant obtaining tritium through leakage from the Li_2O pellets at a rate equal to or greater than the rate at which it is consumed by the plasma and external losses. This condition can be written as,

$$L \geq R/BR \quad , \tag{V-4}$$

where R(kg/s) is the tritium production rate and BR is the breeding ratio. The time needed to attain self-sufficiency, τ^*, is obtained by the equality expressed by Eq. (V-4) and is displayed graphically in Figs. V-30 and V-31 for a given Li_2O condition by the line $y = 1/BR$. The time required to achieve self-sufficiency, as defined by τ^*, can be tailored somewhat by varying r_p, r_g or the temperature distribution, the control over which is depicted by the results in Figs. V-30 and V-31. Generally, the time for tritium self-sufficiency required for a blanket with the temperature distribution given in Fig. V-16 is unrealistically large (Fig. V-30), and a more uniform and elevated temperature distribution (Fig. V-31) would be more desirable.

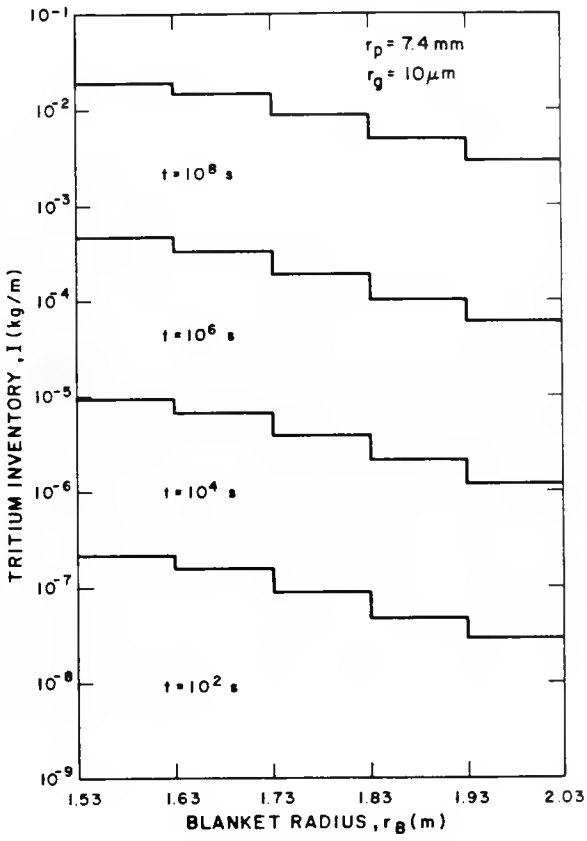

Fig. V-32. Radial distribution of the tritium inventory as a function of time for the case where the temperature distribution at the first wall region (Fig. V-15) was repeated throughout the blanket (Fig. V-31).

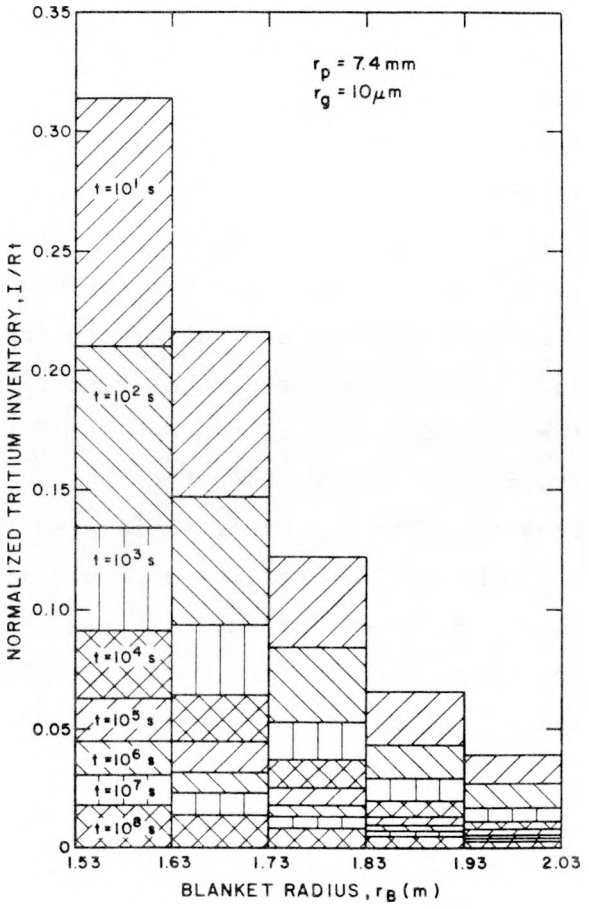

Fig. V-33. Normalized tritium inventory as a function of blanket radius and time for the case given in Figs. V-31 and V-32.

These results, again, depend sensitively on the assumed tritium "diffusivity" and the release model used (Appendix D).

Another quantity of interest is the amount of tritium, I^*(kg/m), needed to sustain the reactor at full power until tritium self-sufficiency is attained. It is shown in Appendix D that I^* is given by

$$I^* = R\tau^*(1/BR-1) + I(t = \tau^*) \quad . \tag{V-5}$$

Table V-XIV summarizes the numerical values of τ^* and I^* for the temperature distribution and pellet characteristics depicted in Fig. V-31. It is

TABLE V-XIV

SUMMARY OF TRITIUM INVENTORIES AS A FUNCTION OF TIME, PELLET RADIUS, AND GRAIN SIZE[a]

RADII (m) OF PELLET x10^{-3}	GRAIN x10^{-5}	τ^* s	I^* kg/m	$I(t=\tau^*)$ kg/m	I(t=1y) kg/m	I(t=3y) kg/m	I(t=5y) kg/m	I(t=10y) kg/m
1	1	1.71(+6)	1.23(-3)	1.12(-2)	1.40(-1)	3.37(-1)	5.02(-1)	8.60(-1)
1	3	1.52(+7)	1.11(-2)	1.00(-1)	1.91(-1)	4.98(-1)	7.69(-1)	1.37
1	10	(b)	(b)	(b)	2.62(-1)	6.73(-1)	1.06	1.93
3	1	1.50(+6)	1.06(-3)	9.80(-3)	1.36(-1)	3.25(-1)	4.84(-1)	8.28(-1)
3	3	1.31(+7)	9.90(-3)	8.67(-2)	1.88(-1)	4.87(-1)	7.51(-1)	1.33
3	10	(b)	(b)	(b)	2.58(-1)	6.63(-1)	1.03	1.90
10	1	3.21(+5)	2.87(-4)	2.17(-3)	9.42(-2)	2.22(-1)	3.32(-1)	5.81(-1)
10	3	2.93(+6)	2.57(-3)	1.97(-2)	1.48(-1)	3.59(-1)	5.37(-1)	9.20(-1)
10	10	3.21(+7)	2.87(-2)	2.17(-1)	2.15(-1)	5.48(-1)	8.44(-1)	1.51
7.38	1	6.75(+5)	5.34(-4)	4.49(-3)	1.13(-1)	2.65(-1)	3.94(-1)	6.83(-1)

[a] numbers in parentheses indicate exponents raised to the base 10.

[b] not determined because the pertinent times exceed $1.0(10)^8$ s

emphasized that these results are only indicative, in that the tritium diffusivity is a very sensitive but poorly resolved parameter. The sensitivity of the tritium release kinetics and blanket inventory to the assumed tritium diffusivity constant is depicted in Fig. V-34, which gives the time dependence of the normalized release rate, L/R for the Ref. 56 (BeO) and Ref. 42 (Li_2O release data) diffusivities. Both the calculated temperature profiles (normal) (Fig. V-16) and a profile where the hottest first-wall cell was repeated (uniform) throughout the blanket are shown. For curves 2 and 4 on Fig. V-34 tritium self-sufficiency (L/R = 1/BR) is achieved within 97 and 232 s, respectively, and the respective steady-state tritium inventories within the Li_2O amounts only to $2.68(10)^{-6}$ and $5.83(10)^{-6}$ kg/m. Clearly, the influence of the tritium diffusivity coefficient can be dramatic.

3. First-Wall Tritium Permeation. The permeation of hydrogen from the plasma chamber through the first wall is a complex phenomenon that involves electrical, physical, chemical, and nuclear interactions. Only the first wall permeability, excluding the hydrogen effects such as first-wall embrittlement

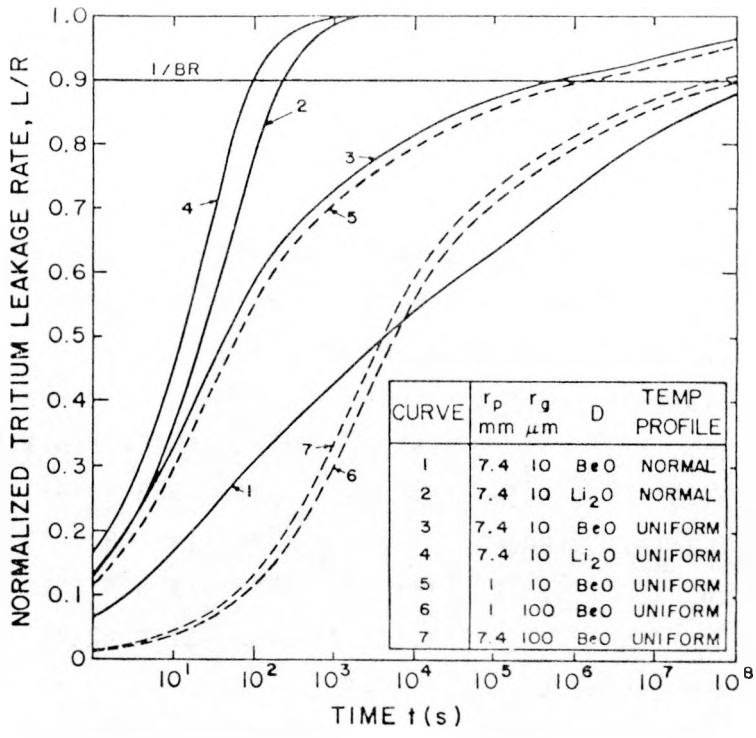

Fig. V-34. Comparison of tritium release kinetics for two diffusivities: BeO[56] and Li_2O (release data)[41].

and bulk chemical reaction (Sec. V.B.4), is discussed here. The effects on tritium permeation of nuclear processes, including radiation effects and electromagnetic interactions, have not been examined.

Plasma hydrogen isotopes are expected to undergo the following consecutive interactions with the 20-mm-thick copper first wall:

- Van der Waals adsorption
- Chemisorption
- Dissolution of hydrogen isotopes in the metal
- Lattice diffusion
- Transfer of atoms from the solid solution
- Recombination to form hydrogen molecules
- Desorption

The overall direction and magnitude of the permeation process is determined by the temperature, T, pressure, P, and concentration, C, gradients across the solid membrane of thickness, ℓ, and surface area A. Only a steady-state permeation process is considered for calculations of hydrogen fluxes, J, through the first wall. The following assumptions are made, where subscript 1 refers to the vacuum/first-wall interface, and subscript 2 refers to the outboard edge of the first wall:

- $P_1 > P_2$, $T_1 > T_2$ and $C_1 > C_2$.
- Permeation rate is diffusion limited.
- Fick's law for planar diffusion is valid, $J = -D(\partial C/\partial r)$, where D is the diffusion coefficient
- Sieverts' law for hydrogen solution holds, $C = S\sqrt{P}$, where S is the solubility constant
- Hydrogen chemical activity in the metal is proportional to its concentration.

On the basis of these assumptions it follows[59] that

$$J = (A/\ell)\phi(\sqrt{P_1} - \sqrt{P_2}), \qquad \text{(V-6)}$$

where ϕ is the permeability, $\phi = \phi_o e^{-Q/kT}$, which is related to the diffusivity by $\phi = DS$. The quantities ϕ_o and Q are the pre-exponential permeability constant and the activation energy according to an Arrhenius-type temperature dependence.

The most appropriate permeability data[60-62] for the copper first wall temperature and pressure ranges apply to the temperature range 473 K < T < 713 K and the pressure range 1 Pa < P < 150 Pa, and can be represented by

$$\phi(m^3/s\ m\ Pa) = 6.00(10)^{-12} e^{-77.3/kT} \quad . \qquad \text{(V-7)}$$

Equation (V-7) was applied to Eq. (V-6) with $A = 750\ m^2$ (total first-wall area), $\ell = 0.02$ m, $P_1 = 0.13$ Pa (1 mtorr) and $P_2 = 0$. The kinetic theory of diffusion[63] was used for the tritium isotope correction (i.e., $(D_H/D_T = \sqrt{3} = 1.73)$ to the hydrogen data, which was within experimental error with the measured[64] value of 1.85. The calculated tritium fluxes corresponded to 0.14 Ci/day at 500 K and 3.2 Ci/day at 600 K. Webb[59] and Jost[63] have discussed permeability measurements made at low pressures. A linear dependence on pressure, instead of a square root dependence given in Eq. (V-6), was observed. This behavior would imply lower permeation rates for pressures below 1 mtorr than those calculated here.

E. Vacuum

Detailed consideration could not be devoted to the design of the RFPR vacuum system. The function of this system is to maintain a relatively pure, helium-free DT level at ~ 2 mtorr pressure. Each 2-m-long, 1.5-m-radius (first-wall) module would be suspended in a toroidal vacuum trough or tunnel of 12.7-m major radius (Fig. V-5). The vacuum within the tunnel would be sufficiently low to pull exhaust gases through the conductances created by engineered gaps between each reactor module (Fig. V-20). It is expected that the tunnel vacuum would not differ appreciably from the desired, preionization pressure of a few millitorr. After a given burn cycle, DT gas would be injected into the vacuum chamber by means of a number of small (few millimeter diameter) tubes placed around the torus. The quantity of gas so injected would be sufficient to increase the pressure in the vacuum chamber to perhaps an order of magnitude above the desired operating vacuum. This gas would be extracted through the torus and intermodule conductances into the vacuum tunnel and, ultimately, through the vacuum pumps. This periodic backfilling and purging technique is expected to maintain the helium background to a few percent of the operating DT pressure. The effects and influence of surface/gas recycle, impurities other than helium, and outgassing will undoubtedly be important, but these issues have not been addressed. The operational DT inventory in the plasma chamber is 0.37 g (1270 ℓ-torr). Given that an amount of gas equal to an order of magnitude greater than this value would be required to operate the suggested purge process, the DT handling rate would amount to 12.0 kg/d; the total pumping speed required of the tunnel vacuum system would at a minimum be 200,000 ℓ/s. Accounting for outgassing and wall recycle would increase this figure to $\sim 10^6$ ℓ/s. Although a comprehensive vacuum design is not within the study scope, estimates have been made of the plasma-chamber/tunnel vacuum time constant and the vacuum pump required to maintain the tunnel vacuum.

1. Vacuum Time Constants. It is noted that the postulate has been made that moderate (10^{-6} torr) to high (> 10^{-8} torr) vacuums would not be required for the RFPR. The simple conductance arguments made here, therefore, must contend with the possibility of both molecular and viscous flow. An important issue for the intermodule evacuation scheme represented in Fig. V-20 is the module separation required to assure vacuum time constants on the order of a few seconds. The resolution of this issue will depend upon whether molecular

versus viscous flow occurs, the latter giving more favorable results. Using MKS units, the collision mean-free-path is given by[65]

$$\lambda(m) = kT/(\sqrt{2}\pi\ Pd^2) \qquad (V\text{-}8)$$

$$= 4.11(10)^{-5}\ T/P \quad ,$$

where the molecular diameter d(m) for hydrogen isotopes is taken[65] as $2.75(10)^{-10}$ m, and the pressure is P(Pa) = P(mtorr)/7.6. Figure V-35 depicts a stylized version of the reactor module assembly, where $\ell \simeq 2$ m, $\Delta b \simeq 2.0$ m and $r_w = 1.5$ m. For T = 600 K and P = 2 mtorr, λ equals 0.09 m, which is less than most of the system dimensions considered, except the intermodule spacing, δ (Fig. V-35). Consequently, the flow encountered in the geometry depicted in Fig. V-35 will occur partly in the transition regime between molecular and viscous flow.

On Fig. V-35 are indicated three positions: position 0, midplane in plasma chamber; position 1, in the plasma chamber at the radial duct formed by two adjacent modules; position 2, in the vacuum tunnel. Pressures P_i (i = 0,1,2) exist at each position, and V_{ij} is the volume encompassed between any two positions. The vacuum conductances associated with volumes V_{01} and V_{12} are given by[65]

$$F_{01}(m^3/s) = F_{01V} + ZF_{01T} \qquad (V\text{-}9A)$$

$$F_{01V} \equiv (\pi r_w^4/16\eta\ell)(P_0 + P_1) \qquad (V\text{-}9B)$$

$$F_{01T} \equiv (2\pi/3)(r_w^3\ v_A/\ell) \qquad (V\text{-}9C)$$

$$Z = \frac{1 + (8/\pi)^{1/2}(r_w/\eta v_A)(P_0 + P_1)}{1 + 1.23\ (r_w/\eta\ v_A)(P_0 + P_1)} \qquad (V\text{-}9D)$$

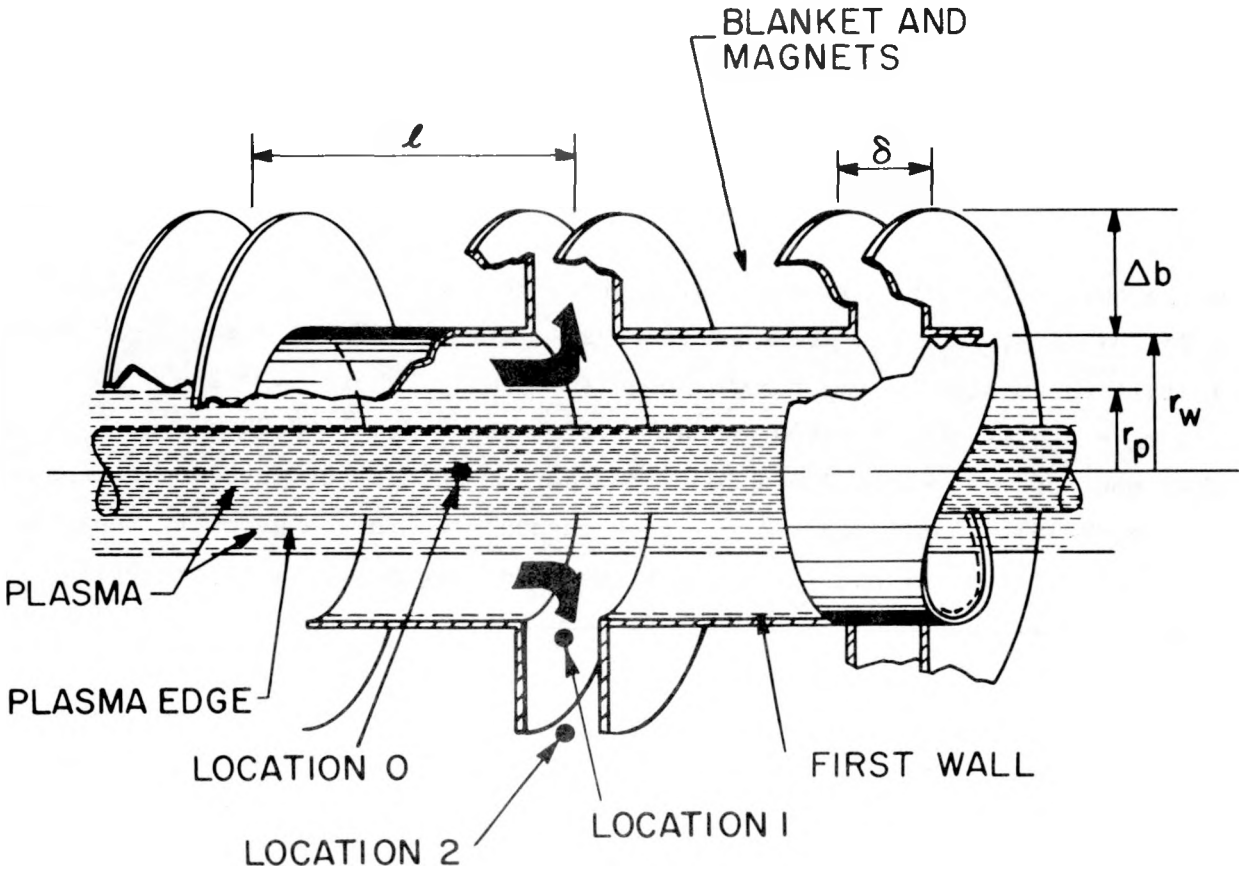

Fig. V-35. Schematic illustration of plasma chamber evacuation model.

$$\eta(\text{kg/s m}) = 0.491\ m\ v_A/(\sqrt{2}\pi d^2)$$

$$= 2.69(10)^{-8}\ v_A \qquad \text{(V-9E)}$$

$$F_{12}(m^3/s) = \pi\delta^3(P_1 + P_2)/[12\eta\ \ell n\ (1 + \Delta b/r_w)] \quad , \qquad \text{(V-10)}$$

where the viscosity η has been evaluated for DT, and $v_A = (8kT/\pi m)^{1/2}$ is average molecular speed. The conductance F_{01} applies to the viscous-molecular flow transition, and F_{12} applies only for viscous flow ($\lambda <$ system dimensions). Defining the time constants $\tau_{01} = V_{01}/2F_{10}$ and $\tau_{12} = V_{12}/2F_{12}$, the following point equations can be formulated to describe the pressure-time response.

$$dP_0/dt = -(P_0 - P_1)/\tau_{01} - dP_1/dt \qquad \text{(V-11)}$$

$$dP_1/dt = -(P_1 - P_2)/\tau_{12} + (P_0 - P_1)(V_{01}/V_{12})/\tau_{01} \quad . \qquad \text{(V-12)}$$

For the RFPR geometry adopted by this study (ℓ = 2.0 m, r_w = 1.5 m, Δb = 2.0 m, $\delta << r_w, \ell, \Delta b$), $\tau_{01} << \tau_{02}$ and consequently $P_1 \to P_0$. In this approximation, Eqs. (V-11) and (V-12) reduce to

$$dP_1/dt = -(P_1 - P_2)/\tau_{12} \qquad \text{(V-13)}$$

$$= -(P_1^2 - P_2^2)/\tau P_2 \quad ,$$

where

$$\tau \equiv (V_{10} + V_{12}/2)\left[12\eta\ \ell n\ (1 + \Delta b/r_w)\right]/\pi\delta^2 P_2 \quad . \qquad \text{(V-14)}$$

Defining $\rho = P_1/P_2 = P_0/P_2$ as the plasma chamber pressure relative to the (constant) tunnel pressure, Eq. (V-13) is readily solved.

$$\rho(t) = \frac{(\rho_0+1) + (\rho_0-1)e^{-t/\tau}}{(\rho_0+1) - (\rho_0-1)e^{-t/\tau}} \qquad \text{(V-15)}$$

Equation (V-15) gives the recovery of the plasma chamber pressure relative to the vacuum tunnel pressure after a pulse injection of purge gas. The recovery time is determined by the characteristic time τ [Eq. (V-14)]. It is noted that within the approximation of viscous flow, the radial extent of the intermodule gap, Δb, has only a weak influence on τ, but τ is strongly dependent on the intermediate gap separation δ.

Equation (V-14) is evaluated as a function of intermodule gap size, δ, on Table V-XV for the fixed parameters shown. In order to achieve the desired vacuum time constant (1-4 s), intermodule spacing in the range 0.05-0.10 m would be required. Give the approximate, but probably optimistic, nature of this viscous flow model and given that transitional or fully molecular flow and absorption/outgassing phenomena will increase τ for a given δ above those cited in Table V-XV, intermodule evacuation alone may not be sufficient to maintain the desirable duty factor ($\gtrsim$ 80%) adopted for this study. Vacuum downcommers may have to be provided at the center of each module to assist in the evacuation of the plasma chamber on a 1-5 s timescale.

2. Vacuum Pumps. Roots blowers and cryopumps have been considered as potential candidates for the primary vacuum system. Two-stage Roots pumps from Leybold-Heraeus, Inc. (Seco Road, Monroeville, PA 15146) have high-pumping speed down to ~ 10^{-5}-torr pressures with significant reduction in speed below that level. These robust rotary-pumps are well suited to maintaining 10^{-3} torr in large systems over long periods of time with little

TABLE V-XV

PARAMETRIC EVALUATION OF VACUUM TIME CONSTANT AS A FUNCTION OF INTERMODULE GAP SIZE FOR TYPICAL RFPR MODULE DIMENSIONS

FIXED PARAMETERS	VALUE
Module length, ℓ(m)	2.0
First-wall radius, r_w(m)	1.5
Blanket/shield thickness, Δb(m)	2.0
Volume of plasma chamber, $V_{01}(m^3) = \pi r_w^2 \ell$	14.1
Volume of intermodule gap, $V_{12}(m^3) = \pi r_w \delta \Delta b(2+\Delta b/r_w)$	31.4 δ
Exhaust gas temperature, T(K)	600.
Average molecular velocity, v_A(m/s)	2248
Gas viscosity, η(kg/s m)	$6.05(10)^{-5}$
Vacuum tunnel pressure, P_2(Pa)	0.26(2 mtorr)

Intermodule gap size, δ(m)	Vacuum time constant, τ(s)
0.025	16.4
0.050	4.2
0.100	1.1

attention. Scaling these pumps to large sizes, a 25,000 ℓ/s pump would be ~ 2.2-m diameter × 3.8-m long and consume ~ 150 kWe. Using one pump per module (total of 40) gives a pumping capacity of 10^6 ℓ/s with a total power consumption of 6 MWe.

The outgassing rate from degreased steel[66] is 10^{-3}-10^{-4} ℓ torr/s m^2, which for a total tunnel surface area of ~ 10^4 m^2 gives 1-10 ℓ torr/s and a minimum base pressure of 10^{-5}-10^{-6} torr for a total pump speed of 10^6 ℓ/s. Between burn pulses (25-s long) the plasma chamber (560 m^3) is filled with DT to ~ 10 mtorr, requiring a throughput of ~ 200 ℓ torr/s from which a minimum base pressure during reactor operation is $2(10)^{-4}$ torr.

Difficulties encountered when using a Roots type system are the relatively high base pressures and the presence of a background magnetic field that could interfere with a rotating machine. An estimate of the maximum allowable magnetic field at the pump gives ~ 0.1 T, requiring the pump to be magnetically shielded, if in the vicinity of the reactor, or to be moved a sufficient distance from the reactor. This requirement does not appear overly stringent, noting that outside of the torus the fields diminish as the inverse cube of the distance. The low base-pressure requirement may present a problem during the initial reactor startup, if a high vacuum purging is required. Generally, however, the normal operating pressure within the tunnel would be a few millitorr, which is ideally suited to the Roots blower.

Use of cryopumps should alleviate both the base-pressure and magnetic-fields problems encountered with the Roots system. A cryogenic system would be similar to that used for the UWMAK-III tokamak design.[67] This pump is similar to a system manufactured by Excalibur Corporation (Waltham Mass.) and consists of a 5 K molecular sieve bonded to a metal substrate with two sets (20 and 80 K) of chevron-shaped metal baffle surfaces placed in front. The total pumping area of this system[67] would be 1,600 m^2, which amounts to 15% of the RFPR tunnel area. One-half of this capacity would be used at any given time, allowing for pump regeneration without interruption of the vacuum system. Using a cryogenic pumping speed for DT of $1.3(10)^5$ liters/s m^2, the pumping capacity of the 1,600-m^2 system is 10^8 ℓ/s, which is 100 times that required for ideal RFPR operation. The pumping speed for helium is approximately 75% that of hydrogen, whereas air is pumped at a rate that is ~ 5% that of hydrogen. Approximately 6.2 MWe of refrigeration power is needed to power this 10^8 ℓ/s cryogenic system.

Using an outgassing rate from the stainless-steel-lined vacuum tunnel of 1-10 ℓ torr/s, the base pressure would be 10^{-7}-10^{-8} torr using the cryopump system. During the burn phase a base pressure of $1(10)^{-6}$ torr can be achieved with a throughput of 200 ℓ torr/s.

Saturation of the molecular sieve with DT is expected when $\sim 5.6(10)^{5}$ ℓ torr/m^2 has been absorbed at 77 K. Dividing this value by the expected throughput of ~ 200 ℓ torr/s predicts that ~ 7 days of operation would drive the cryopump to 30% saturation. As noted above, two identical sets of pumps would be incorporated in the vacuum system. To regenerate one set of cryopumps the saturated system is valved off and warmed to ~ 20 K, and the chevron panels are warmed to 40 K and 100 K. The gas is then pumped out at a pressure of 70-100 torr and sent to the distillation column at atmospheric pressure, where isotope separations are performed. Pumpout occurs in only ~ 1 hour,[67] using a compressor of only ~ 100 ℓ/s capacity at one atmosphere.

In summary, both Roots blowers and cryopumps will require approximately the same electrical power (6.0 MWe versus 6.2 MWe). The advantages of proven robust operation for the Roots system must be balanced with potential voltage problems associated with rotating machinery operating in stray magnetic fields. Additionally, the base pressure for the Roots system is limited to ~ 10^{-5} torr, which would be undesirable only if lower pressures are required during vacuum cleanup. The cryopumps, on the other hand, can achieve a lower base pressure, but alternate, regenerative operation of two systems would be required. Both systems will require roughing vacuum pumps.

F. Electrical System

This section describes the three major coil systems:

- the transformer coil (TC) induces the plasma current, I_ϕ, during the startup phase, sustains the plasma current throughout the burn and runs down the current at quench.
- the vertical field coil (VFC) produces the vertical magnetic field required for plasma equilibrium and provides a portion of the flux change required to induce the plasma current.
- the toroidal field coil (TFC) produces the initial toroidal bias field, B_ϕ, and reversed-field, $-B_R$, necessary for plasma stability.

Coil sets TC and VFC are topologically identical and, therefore, are collectively referred to as the poloidal field coil (PFC) system.

An evident criteria imposed on the magnet coil design is the minimization of the conductor volume and stored energy required for the plasma burn. Reliability and maintenance must also be of prime concern because of the massive magnet coils and the recognized need to allow relatively easy access to a blanket and first-wall structure undergoing high neutron irradiation. The difficulties associated with the movement of large superconducting coils has led to a design in which no coils are disturbed during normal maintenance procedures (Sec. V.G). As shown in Fig. V-36, the poloidal field coils are located in two discrete coil galleries located inside and outside the torus.

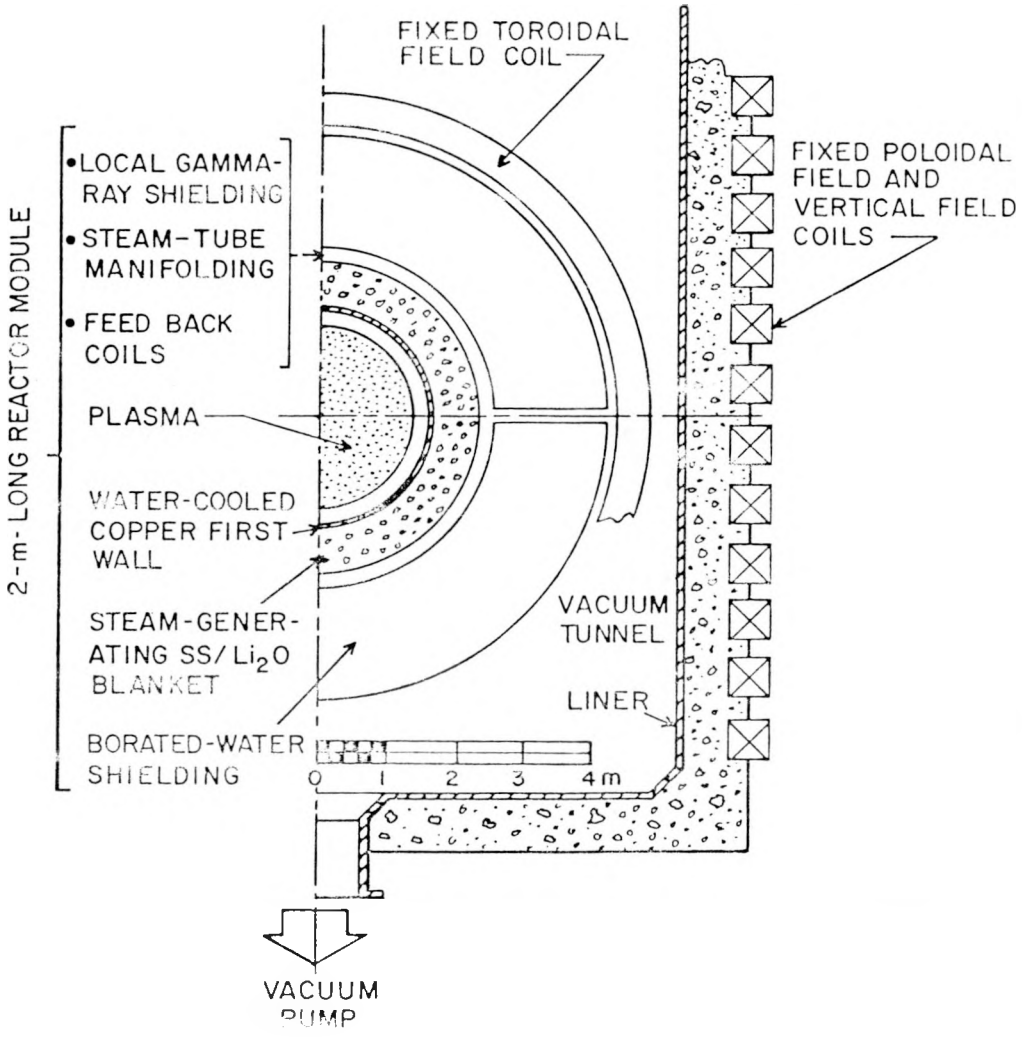

Fig. V-36. Schematic cross-sectional view of RFPR module, vacuum tunnel, and magnet systems showing relative positions and sizes of major core components.

This arrangement greatly increases the reactor accessability at a modest and acceptable cost of increased poloidal field energy; this increased energy amounts to ~ 50% when compared to a coil set that completely encloses the torus. The advantages associated with an open coil set allow relatively straightforward maintenance procedures and are considered to outweigh the disadvantages associated with moderately increasing the size of the electrical supply. Similarily, the toroidal field coils are positioned such that large sections of first-wall/blanket/shield may be removed without disturbing the superconducting TFC windings. The magnetic field ripple arising from gaps between the toroidal-field coils is the major constraint governing the allowable distance between coils.

1. Poloidal Field Coil System.

a. Transformer Coil. A portion of the flux change needed to drive the plasma current is provided by the vertical field coils, as discussed is Sec. V.F.1.b, with the bulk of the flux change provided by the transformer (TC) winding. The transformer coil must produce a field distribution in which magnetic field is excluded from the plasma region. Large currents flowing in these windings must not produce fields which disturb the plasma equilibrium. In order to minimize the required stored energy and coil size, the coil current is varied from $-I_{\phi c}$ to $I_{\phi c}$ during the startup phase; an inverse current program is followed during the rundown of the plasma current. This bipolar operation gives twice the flux change from a given conductor set.

To determine the necessary coil position, the coil current distribution is represented by two separate Fourier series[68] that are evaluated along each coil gallery on the inside and outside of the torus. The Fourier coefficients are then determined by a least-squares minimization of the field produced by the transformer coil inside the plasma. The resultant continuous current distribution is used to determine the required position of conductors carrying equal current. These coil positions are shown in Fig. V-37, where the inside set of 40 equal current windings require 0.717 MA/conductor, and the outer set of 10 conductors carry 0.333 MA/conductor; the total current in the TC set is 32 MA, as determined in Sec. V.F.1.c. Equally spaced flux surfaces produced by this coil are also shown in Fig. V-37, where the exclusion of magnetic field from the plasma gives essentially a constant flux in and near the plasma region. The stray field produced by the TC when carrying 32 MA is found to be only ~ 0.004 T for the continuous current distribution or ~ 0.1% of the field

produced by the plasma. Stray field produced by the discrete coil set shown in Fig. V-37 is ~ 0.01 T or ~ 0.3% of the field produced by the plasma during the burn.

b. Vertical Field System. The vertical field (VFC) system provides plasma equilibrium and a portion of the flux change required to drive the plasma current. Equilibrium of the plasma column requires the addition to the plasma of a nearly uniform vertical field, B_V. An expression for the required quasiuniform vertical field is[69-71]

$$B_V = (\mu_o I_\phi/4\pi R)[\ell n(8R/r_p) + 2\pi\ell_i/\mu_o + \beta_\theta - 1.5], \qquad (V\text{-}16)$$

where ℓ_i is the inductance per unit length of plasma. For the RFPR with Bessel function profiles $2\pi\ell_i/\mu_o = 0.25$. The vertical field roughly must vary directly with the plasma current I_ϕ. This approximation is modified by a correction term which varies only ~ 10% over the entire RFPR startup and shutdown cycle. Using RFPR parameters during the burn ($I_\phi = 20(10)^6$A, $\beta_\theta = 0.3$, $r_p = 1.4$ m and $R = 12.7$ m), a vertical field of $B_V = 0.53$ T is required. In principle, the magnitude and distribution of the plasma current along with β_θ must be known at each point in time with a corresponding vertical field consistently calculated. A feedback system will probably be required, but the design of such a system has not been made. The necessary magnetic field energies along with a first-order determination of the time-dependent currents and voltages are calculated in Sec. V.F.1.c for a system which achieves the desired $B_V = 0.53$ T during the burn.

To provide plasma equilibrium in both the horizontal and vertical directions requires the field to have a curvature that is characterized by the decay index[71]

$$n = -\partial\ell nB_V/\partial\ell nr = \left(\frac{R}{r_p}\right)\frac{B(R-r_p) - B(R+r_p)}{B(R-r_p) + B(R+r_p)} \quad . \qquad (V\text{-}17)$$

The decay index, n, should lie between 0 and 1.5. Constraining the plasma to have a circular cross section further specifies $0 < n \lesssim 0.65$;[71] this criteria is used here.

An infinite number of solutions predict the desired coil positions needed to produce the correct vertical field direction, magnitude and decay index. The desire to minimize magnetic field energies and the volume of required superconductor is of prime consideration. Placement of the vertical fields is restricted to two distinct coil galleries on the inside and/or outside of the torus, as shown in Figs. V-5 and V-36. These physical constraints considerably reduce the number of possible solutions to the coil positioning problem. Locating the vertical field coils inside the torus requires currents that oppose the transformer coils and the flux produced by these coils. Large currents are also required to effect the vertical field at the plasma because of the rapid decay of the magnetic field in the direction outward along the major toroidal radius (analogous to the decay outside of a short solenoid). Positioning the VFC system outside the torus allows coil currents that add to the currents flowing in the transformer coil and thereby to produce flux which serves to induce the plasma current. A minimum vertical field is obtained as a result of the plasma being inside a "short solenoidal coil" in which a quasi-uniform vertical field exists. All requirements of the vertical field coil system are satisfied by coils located at a vertical height of $\pm$ 4.5 m on the outside poloidal field gallery, as shown in Fig. V-38. Equally spaced flux surfaces also exhibit the required concave shape of the vertical field in the plasma (toward the inside of torus). A decay index of $n = 0.51$ results, assuring a circular plasma in equilibrium. A VFC current of 13.5 MA produces the required $B_V = 0.53$ T during the burn phase.

c. Poloidal Field Coil Circuit. With the coil distributions known for the vertical field and transformer coils, the self and mutual inductances of the coils and plasma can be calculated. The magnitude of the transformer current can then be determined, and the overall electrical circuit is used to determine required voltages, currents, and energies. A numerical code[72] is used to calculate all inductances with a distributed current in the plasma having a profile consistent with the Bessel function model used throughout this report (Appendix A). Results of the inductance calculation are given in Fig. V-39 for the self-inductances of the plasma, L_p, vertical-field coil, L_V, and transformer coils, L_T, along with the corresponding mutual inductances. The transformer coil is connected as a two-turn ($N_T = 2$) coil, and the vertical-field coil is connected as a fractional-turn ($N_V = 1.34$) coil to provide the proper impedance match in the circuit shown in Fig. V-39. The

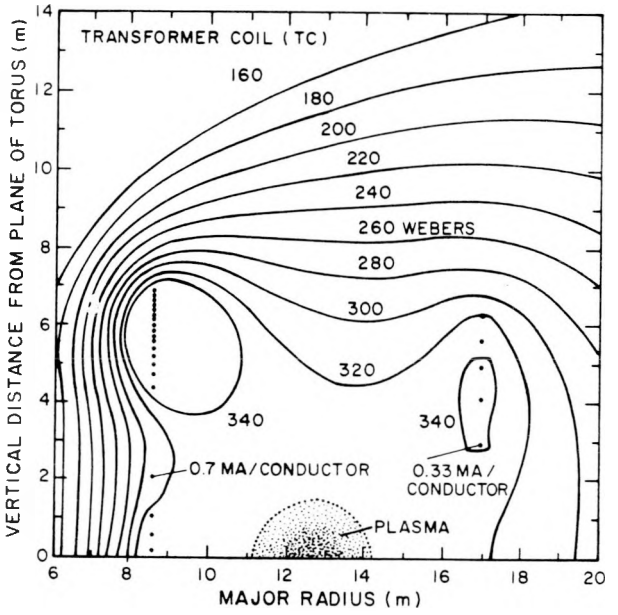

Fig. V-37. Coil positions and currents required by the transformer coil. Equally spaced flux surfaces are also shown.

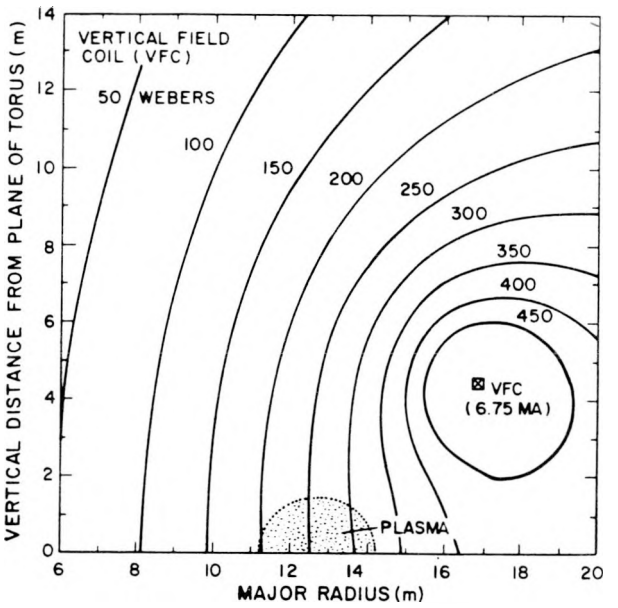

Fig. V-38. Coil location and equally spaces flux surfaces for the vertical field coil system needed to provide equilibrium. Equally spaced flux surfaces are shown.

total current carried by the leads of the vertical field system must then be I_V = 13.5 MA/N_V = 10.1 MA, where 13.5 MA flows in the vertical field coils encircling the torus (Sec. V.F.1.b). A plasma current of I_ϕ = 20 MA requires a flux change of $L_p I_\phi$ = 915 Wb, part of which ($M_{PV} I_V$ = 259 Wb) is provided by the vertical field system with the remainder ($M_{PT} \Delta I_T$ = 656 W) generated by the transformer coils. Consequently, the total current change in the TC is ΔI_T = 32 MA, or a maximum transformer lead current of $\Delta I_T/2$ = 16 MA results. Equally spaced flux surfaces resulting from the poloidal coil and plasma system during the plasma burn are shown in Fig. V-40.

The time response of voltages and currents in the poloidal field circuit are also shown in Fig. V-39. The transformer leads initially carry I_T = - 16 MA (switches S_T closed, S_H and S_V open) with the open-circuited homopolar motor/generator set charged to 17,000 V. Switch S_H is a reversing switch which will allow the homopolar to operate always with a positive charge. Switch S_T is opened while switches S_H^+ and S_V are simultaneously closed, causing the plasma current to be initiated. The plasma and vertical field coil currents increase to the desired values while the transformer lead

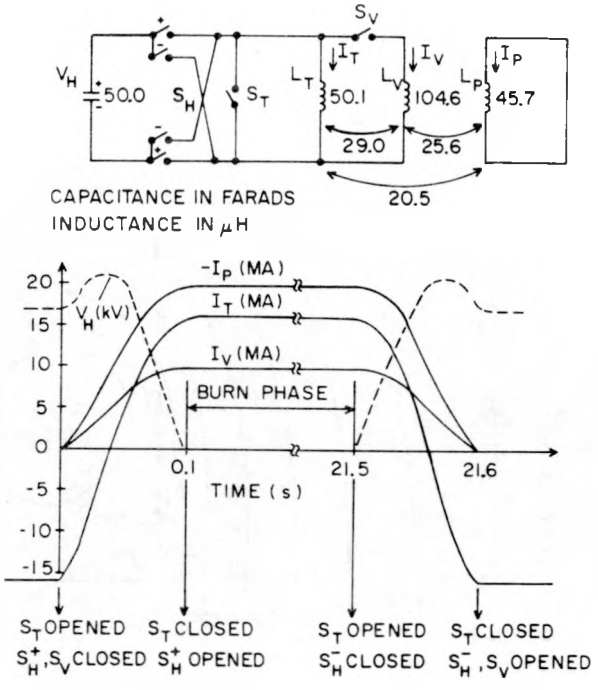

Fig. V-39. Equivalent circuit of the poloidal field coil and plasma system. The switching sequence and resultant time response of currents and voltages are shown.

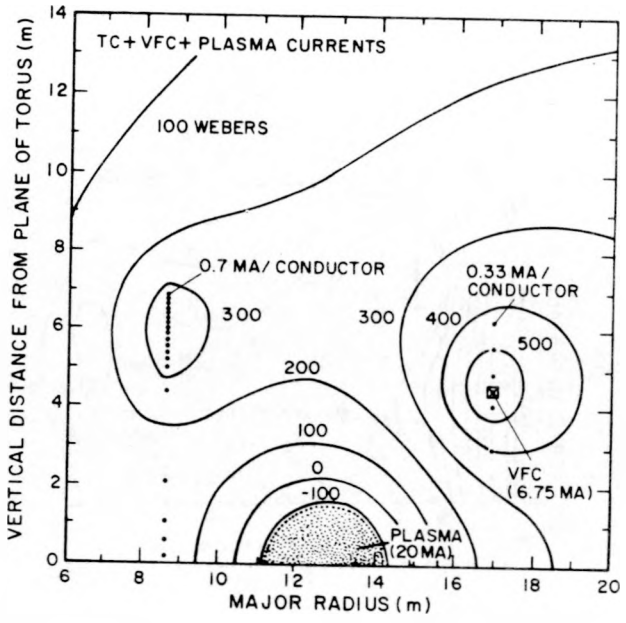

Fig. V-40. Equally spaced flux surfaces for the poloidal field and plasma system during the plasma burn phase.

current changes from -16 to +16 MA and the homopolar voltage goes to zero. Closing switch S_T, after which S_H^+ is opened, maintains constant currents during the plasma burn cycle. Opening switch S_T while closing S_H^- reverses the above procedure and ultimately restores the initial condition, less approximately 10%, dissipated field energy, with switch S_T closed and switches S_H and S_V opened. The maximum voltage achieved by the 50 F homopolar motor/generator is 21 kV, requiring a total energy of 11 GJ.

The time response of the vertical field coil and plasma are nearly identical as shown in Fig. V-39. To first-order this procedure would lead to the desired response of the vertical field circuit, where trim coils could account for higher-order effects (Sec. V.F.1.b).

2. Toroidal Field Coil System. The toroidal field coils (TFC) shown in Fig. V-36, must provide the initial bias field $B_{\phi o}$, that is trapped inside the plasma upon initiation of the toroidal current, and the reversed-field $-B_R$ during the plasma burn phase. Every other 2-m long module is encircled by a toroidal field coil having an inside radius of $r_{c\phi}$ = 3.6 m. Adequate space for first-wall/blanket/shield maintenance without disturbing the TFC is thereby provided. The maximum distance between coils is determined by the maximum tolerable level of magnetic field ripple at the plasma surface. The FINTOR[73] and RFPR designs have maximum spacings of ~ 3 m between the toroidal field coils (measured at $r_{c\phi}$) near the outer edge of the plasma ($R + r_p$), where the magnetic field ripple would be most severe. In the FINTOR design a distance of 3 m between the inside edge of the coil to the plasma yields a ripple of less than 0.2%. Applying these results to the RFPR with a distance of ~ 2.2 m between the coil and plasma edge leads to a field ripple of ~ 0.5%. This ripple is considered to be sufficiently small, although permissible limits within the RFP context are unknown.

Connecting all 10-turn toroidal field coils in parallel results in the

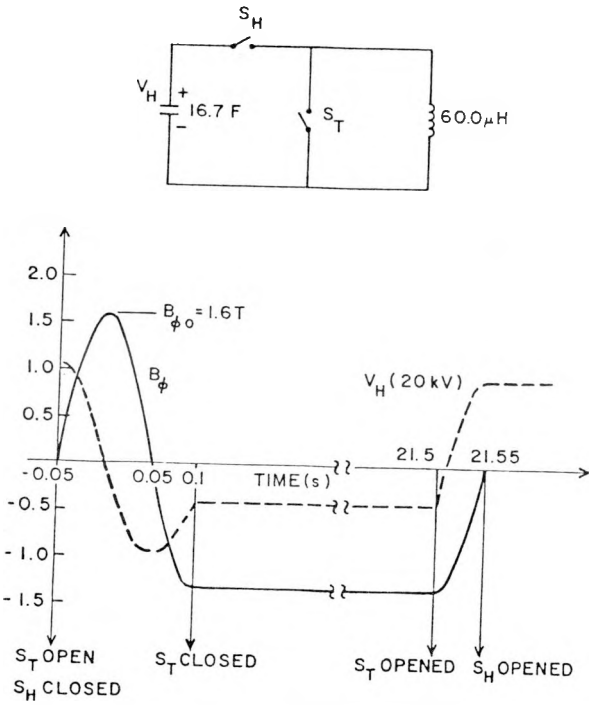

Fig. V-41. Equivalent circuit of the toroidal field coil system. The switching sequence and resultant time response of magnetic fields and voltages are also given.

circuit shown in Fig. V-41. This circuit is driven by a homopolar motor/generator operating at a voltage (21 kV) that is equal to that used for the PFC system. The time response of voltages and magnetic fields is also shown in Fig. V-41. The homopolar generator is charged to 21 kV with switch S_H and S_T open. Closing switch S_H allows current to flow in the TFC, and the toroidal bias field $B_{\phi o}$ is induced. When $B_{\phi o}$ equals 1.6 T the toroidal field circuit is energized, and the toroidal plasma current I_ϕ is induced. The toroidal field circuit continues to "ring" inductively until the required reversed field $-B_R$ is reached. At this point the switch S_T is closed, maintaining the field, $-B_R$, throughout the burn. At the termination of the burn, switch S_H is closed while switch S_T is opened, thereby extracting the toroidal field energy that remains between the quenched plasma and the TFC windings. Opening switch S_H returns the system to its original state. Prior to the next pulse the TFC and TC/VFC energy stores are replenished to makeup for all losses. A homopolar motor/generator store of 3.7 GJ is required to energize the TFC system. A total of 11.1 MA flows in the toroidal field system, with 0.56 MA being carried by each TFC.

3. Magnet Design. The pulsed superconductors needed in this design require a maximum field at the coil of ~ 2 T and a maximum field rate-of-change of ~ 30 T/s. A 20-MJ prototype tokamak ohmic-heating coil, with a field variation of -7 to +7 T in 2 s (or ~ 15 T/s), has been designed.[72] A bid received from commercial vendors of ~ $\$4(10)^5$ for the 750-m-long superconducting (NbTi) cable with a current carrying capability of 50 kA is used to estimate costs of the RFPR coils. The low magnetic fields required for the RFPR, along with a modest increase in the field rate-of-change, implies that the coils required for the poloidal and toroidal field systems are near state-of-the-art. The size of these coils, however, is considerably larger than any system fabricated to date, and the implication of pulsed operation of these large coils will require additional study.

The prototype tokamak design[72] uses a matrix ratio of Cu-10% Ni/Cu/NbTi = 1:2:1 in the superconducting strand. These superconducting strands are co-wound with copper wire to give an overall Cu/NbTi ratio of 15:1. An average current density of ~ 15 MA/m^2 flows in the coil winding which consists[67] of 45 v/o Cu/NbTi, 45 v/o stainless-steel structure, and 10 v/o voidage for He-coolant channels. This structure must then be surrounded by an ~ 0.1-m vacuum space partially filled with

superinsulation. Active coil thicknesses of 0.3 m are used with an outside coil thickness of ~ 0.5 m. The toroidal field coils have a 3.6-m inside radius and are 1.2-m wide by 0.5-m thick. All the coils in the poloidal field system are taken to be ~ 0.5-m thick with the required circumference and length dimensions determined by the required current distribution given in Sec. V.F.1.

4. Homopolar Motor/Generator. Homopolar machines are proposed for the energy-storage element in the poloidal and toroidal field circuits. The homopolar motor/generator behaves as a capacitor, which is ideal for transferring energy at high efficiency when coupled to the inductive loads presented by the RFPR. Unlike ac generators, which require solid-state switching equipment to convert alternating to direct current, the homopolar operates dc with much simpler stator and rotor construction. The rugged homopolar construction allows high power rating and energy storage with a large potential cost savings.

The major components of a drum-type homopolar motor/generator are shown in Fig. V-42. A bias field is produced by superconducting coils imbedded in

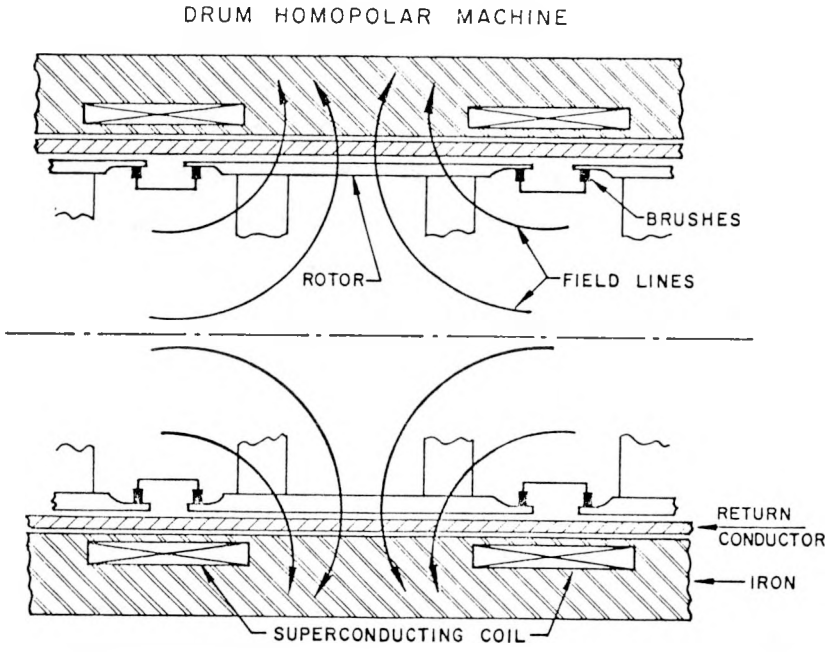

Fig. V-42. Schematic diagram of a drum-type homopolar motor/generator proposed for use as an energy storage and transfer system in the RFPR.

an iron structure. The motion of a conducting rotor through this magnetic field induces a voltage given by

$$V = v\bar{B}L \quad , \tag{V-18}$$

where v is the peripheral rotor velocity, L is the active length and $\bar{B}$ is the average field encountered by the rotor. Adding brushes at the edge of the rotors allows current to be extracted, thereby slowing the rotor speed inversely, imposing an external voltage "charges" the device by increasing the rotor velocity. The energy stored in a cylindrical rotor machine is given by

$$W = \frac{\pi}{4} \rho L r_o^2 v^2 f_i \quad , \tag{V-19}$$

where ρ is the rotor density, f_i is the fraction of flux intercepted by the rotor and r_o is the rotor radius.

Machines using low-inertia rotors constructed of hollow, radially-thin cylinders allow increases in radius, r_o, speed, v, and magnetic field, $\bar{B}$, using superconducting windings. These properties yield low energy costs and high efficiency and are invoked in a comprehensive conceptual engineering design[74] of a 1.3-GJ homopolar machine having a discharge time (0.03 s) that is three times more rapid than that required by the RFPR. The rotor is constructed of lightweight, fiber-reinforced aluminum, allowing high peripheral velocity and long fatigue life. The magnetic field is produced by Nb_3Sn magnets having a peak field of 8 T at the conductor with a flux return provided by the iron yoke attached outside the coils. Copper/graphite brushes connect the external circuit to the rotors with a current return provided by a conductor between the rotor and coils.

The final design parameters chosen in the 1.3-GJ homopolar design[74] are listed in Table V-XVI along with modified parameters used for the toroidal and poloidal field systems of the RFPR. Two series connected machines yield the desired 22-kV voltage necessary to drive the TFC system. Three sets of two series-connected machines energize the PFC system. The slower discharge times required by the RFPR (0.1 s <u>versus</u> 0.03 s) will significantly lower the

TABLE V-XVI

HOMOPOLAR SPECIFICATIONS

PARAMETER	REF. 74 PARAMETERS	TOROIDAL FIELD SYSTEM	POLOIDAL FIELD SYSTEM
Energy rating, W(GJ)	1.29	1.85	1.85
Discharge time, τ_R(s)	0.03	0.05	0.10
Maximum current, I(MA)	12.25	10.6	5.3
Rotor diameter, $2r_o$(m)	2.17	2.60	2.60
Maximum voltage, V(kV)		11	
Number of rotors, N		8	
Rotor density, ρ(kg/m^3)		2300	
Total active length, L(m)		13	
Rotor peripheral velocity, v(m/s)		277	
Average magnetic field, $\bar{B}$(T)		3	
Fraction of flux intercepted by rotor, f_i		0.61	
Transfer efficiency, η_{ETS}		0.95	
Machine cost, c_{ETS}($/J), 1976		$5.1(10)^{-3}$	

stresses applied to the machine when compared to the device reported in Ref. 74.

5. Switches. Both opening (current interrupting) and closing switches are required by the RFPR. Interruption of a current can be performed by a number of conventional devices such as mechanically-actuated oil, gas, or vacuum breakers and solid-state silicon-controlled rectifiers along with many developmental types of switches.[75] The large tokamaks under construction will use an air-blast mechanical interrupter (JET) and vacuum interrupters (TFTR and JT-60). Tests have been performed[76] on special vacuum interrupters that can be used in TFTR. These current interrupters use long-life electrodes and an axial magnetic field to increase reliability. An extrapolated lifetime in excess of 10^4 cycles is expected, although straightforward design changes are expected to increase greatly this lifetime.

Spark-gaps, ignitrons, mechanically-actuated switches and silicon-controlled rectifiers can serve as conventional closing switches. A combination used very successfully at LASL[76] is an ignitron placed in parallel with a mechanical bypass switch. The fast-closing ignitron initially closes

the circuit, although this switch is unable to carry large current for long periods of time. Closing the mechanical bypass switch soon after the ignitron, diverts current to the bypass device and allows continuous current operation. A simple pneumatically operated device submerged in an oil bath represents a mechanical switch[76] that is rugged and inexpensive. Extrapolated lifetimes in excess of 10^4 cycles are found, and a modest developmental effort is expected to increase greatly this estimated lifetime.

A list of switch parameters is given in Table V-XVII for the proposed RFPR. The vacuum interrupter can carry 25 kA for ~ 3 s ($2(10^9)$ A^2 s) before overheating forces the parallel connection of a mechanical bypass switch with higher I^2t ratings. A summary of the switching requirements for the poloidal and toroidal magnetic field systems is given in Table V-XVIII.

G. Operations and Maintenance

The design choices made and optimization procedures used throughout this report reflect a single guiding philosophy: the development of a fusion power system that within the constraints imposed by present understanding of RFP physics can be realistically and economically operated and maintained. The characteristics of the RFP that impact directly on the credible execution of this philosophy are:

TABLE V-XVII

A SUMMARY OF SWITCH CHARACTERISTICS

	VACUUM INTERRUPTER	MECHANICAL BYPASS	D IGNITRON
Maximum current (kA)	25	25	100
Maximum voltage (kV)	50	90	20
Maximum I^2t (A^2 s)	$2(10)^9$	∞	-
Extrapolated lifetime[a]	$> 10^4$	$> 10^4$	∞
Maximum coulombs	-	-	$\sim 10^2$
Cost ($), 1978	$3(10)^3$	10^3	$3(10)^3$

[a]These switches generally have not been designed for longevity, and a modest development program could considerably extend the lifetime of the vacuum-interrupter and the mechanical-bypass switches.

TABLE V-XVIII

SUMMARY OF RFPR SWITCHING REQUIREMENTS[a]

	POLOIDAL FIELD CIRCUIT			TOROIDAL FIELD CIRCUIT	
Switch	S_H	S_V	S_T	S_H	S_T
Type	Closing	Closing	Opening	Closing	Opening
Maximum current (kA)	25	16.7	25	25	25
Maximum voltage (kV)	21	21	21	21	21
Number Required	600	600	600	450	450
Cost (M$)	2.4	1.6	2.4	1.8	1.8

[a]Refer to Figs V-39 and V-41 for switch positions. Each closing switch consists of a parallel connected ignitron and mechanical bypass switch, and each opening switch uses a vacuum interrupter in parallel with a mechanical bypass switch.

- high aspect ratio leading to simple cylindrical blanket/shield modules
- plasma confinement and heating systems that can be combined into a single function
- batch-burn operation with an acceptable overall engineering energy balance and steady-state power plant operation
- a fixed magnet coil system that can be designed to yield an open and accessible system.

The RFPR design presented herein reflects these potential advantages. Even with these advantages, however, operation and maintenance of this ~ 3 GWt toroidal power system will not be easy, and considerable technological development will be required. Additionally, the level of this design does not permit a detailed assessment of subsystem reliability, lifetimes, and replacement times. Given an adequate resolution of these unknowns, the central issue revolves around the remote handling procedures that will be required to maintain and operate this system. Although this study has been strongly guided by these concerns, they remain largely unresolved. Nevertheless, the following points can be made concerning the operation and maintenance of the RFPR.

- Each of the 40, 60-tonne blanket/first-wall module, and 50-tonne shield modules can be removed without disturbing the superconducting coil structures.

- Removal of a shield module will require disconnection of two electrical leads that energize the attached slow-feedback coils.
- Removal of a first-wall/shield module will require the disconnection of two (first-wall) water coolant lines, two (blanket) steam/water lines, and a low-pressure helium purge line.
- Nonscheduled replacement of modules will probably occur under vacuum, using a "vacuum leech" system depicted in Fig. II-6.
- Replacement of a large number of modules will probably occur with the vacuum tunnel uncovered and the reactor hall above this tunnel brought to atmospheric, but inerted, pressure.
- Repair and replacement operations on the torus will probably be made by personnel brought close to the repair site in mobile hot-cell/life-support systems.
- The copper first-wall probably represents the least reliable, shortest-lived component, and a means must be found to allow its replacement and repair by a procedure that is less integral to that for the blanket.

Generally, the remote procuring, attaching, rigging, lifting, movement, and replacement of torus components should present no insurmountable problems. The reliable and expeditious making and breaking of a total of nearly 500 local fluid and electrical connections under remote conditions, however, will require considerable development.

REFERENCES

1. T. R. Hill, "ONETRAN: A Discrete-Ordinate Finite-Element Code for the Solution of a One-Dimensional Multi-Group Transport Equation," Los Alamos Scientific Laboratory report LA-5996-MS (1975).

2. B. Badger, G. L. Kulcinski, R. W. Conn, C. W. Maynard, K. Audenaerde, and H. Avci, "Tokamak Engineering Test Reactor," University of Wisconsin report UWFDM-191 (1977).

3. W. H. Rohsenow, "Boiling," in Handbook of Heat Transfer, W. H. Rohsenow and J. P. Hartnett, Eds. (McGraw-Hill Book Company, New York, 1973) Section 13, pp. 13.34-13.63.

4. P. W. Taubenblat, W. R. Opie, and Y. T. Hsu, "A New Copper Alloy with High Strength and Conductivity," Metals Engineering Quarterly, November 1972, p. 39.

5. R. G. Lawton, "The AYER Heat Conduction Computer Program," Los Alamos Scientific Laboratory report LA-5613-MS, May 1974.

6. R. T. Lahey, Jr., and F. J. Moody, The Thermal-Hydraulics of a Boiling Water Nuclear Reactor (American Nucl. Soc., Monograph Series, Am. Nucl. Soc., 1977).

7. K. Roko, K. Takitani, A. Yoshizaki, and M. Shiraha, "Dryout Characteristics at Low Mass Velocities in a Vertical Straight Tube of a Steam Generator," Proceedings of 6th International Heat Transfer Conf., Toronto, Canada, August 7-11, 1978, Vol. 1, p. 429.

8. A. C. Mueller, "Heat Exchangers," in Handbook of Heat Transfer, W. H. Rohsenow and J. P. Hartnett, Eds. (McGraw-Hill Book Company, New York, 1973) Section 18, p. 18-60.

9. H. W. Godbee and W. T. Ziegler, "Thermal Conductivities of MgO, Al_2O_3, and ZrO_2 Powders to 850°C, I. Experimental," J. of Appl. Phys. 37,40-55 (January 1966).

10. ASME Boiler and Pressure Vessel Code, (An American National Standard - ACI Standard 359-74), Section III, "Rules for Construction of Nuclear Power Plant Components, 1975 Edition, The Am. Soc. of Mechanical Engineers, New York.

11. M. K. Booker, T. L. Hebble, D. O. Hobson, and C. R. Brinkman, "Mechanical Property Correlations for 2/4 Cr-1 Mo Steel in Support of Nuclear Reactor Systems Design," Transaction of the 3rd International Conference on Structural Mechanics in Reactor Technology, Commission of the European Communities, Luxenburg, 1975, Vol. 2, Part F, paper F8/9.

12. M. T. Simned, Fuel Element Experience in Nuclear Power Reactors (An AEC Monograph published by Gordon and Breach Science Publishers, New York 1971).

13. P. Cohen, Water Coolant Technology of Power Reactors (An AEC Monograph published by Gordon and Breach Science Publishers, New York, 1969), p. 334.

14. Ph. Berge and J. R. Donat, "An Evaluation of PWR Steam Generator Tubing Alloys," Nuclear Energy 17, 4, 291-299 (1978).

15. Babcock and Wilcox, Steam/its generation and use, 38th Edition, (Published by Babcock and Wilcox Company, New York, 1972).

16. J. A. Horak and T. H. Blewitt, "Fast Neutron Irradiation Induced Resistivity in Metals," Phys. Stat. Sol. (A) 9, 721-730 (1972).

17. N. F. Mott and H. Jones, The Theory of the Properties of Metals and Alloys (Dover, NY, 1936), pp. 269 and 287.

18. W. A. Harrison, "Resistivity Due to Dislocations in Copper," J. Phys. Chem. Solids 5, 44-46 (1958).

19. Personal communications from R. R. Coltman, Oak Ridge National Laboratory and F. R. Fickett, National Bureau of Standards.

20. R. M. Brick, A. W. Pense, and R. B. Gordon, Structure and Properties of Engineering Materials (McGraw-Hill, NY, 1977), p. 66.

21. T. H. Blewitt and T. J. Koppenaal, in Radiation Effects, W. F. Sheely, Ed. (Gordon and Breach, NY, 1967), p. 585.

22. L. D. Glowinski, J. M. Lanore, C. Fiche, and Y. Adda, "Etude de la Formation des Cavites D'irradiation Dans le Cuivre IV-Etude des Mecanismes," J. Nucl. Mater. 61, 41-52 (1976).

23. W. J. Duffin and F. A. Nichols, "The Effect of Irradiation on Diffusion-Controlled Creep Processes," J. Nucl. Mater. 45, 302-316 (1972/73).

24. N. Amherd (ed.), "Balance-of-Plant Study of Alternative Fusion Reactor Concepts," Electric Power Research Institute report, to be published (1979).

25. J. W. H. Chi, D. L. Chapin, T. Prevenslik, and J. L. Kelly, "An Evaluation of Steam and Boiling-Water-Cooled DTHR Blanket Concepts," Transactions of ANS, 30, 52-53 (1978).

26. R. W. Conn, G. L. Kulcinski, and C. W. Maynard, "NUWMAK, An Attractive Medium Field, Medium Size, Conceptual Tokamak Reactor," Am. Nucl. Soc. Third Topical Meeting on the Tech. of Cont. Nucl. Fusion, Santa Fe, NM, 1978, Vol. 2, pp. 1049-1059.

27. J. S. K. Tsang, O. W. Lazareth, and J. R. Powell, "One- and Two-Dimensional Heating Analyses of Fusion Synfuel Blankets," Transactions of the American Nuclear Society 32, 46-48 (1979).

28. D. L. Smith, R. Clemmer, S. Harkness, J. Jung, H. Stevens, and C. Youngdahl, "Analysis of a Water-Cooled Blanket for a Commercial Tokamak Reactor," Transactions of the American Nuclear Society 32, 58-59 (1979).

29. H. C. Stevens, B. Misra, and C. K. Youngdahl, "Evaluation of Steam as a Potential Coolant for Non-Breeding Blanket Designs," American Nucl. Soc. Third Top. Meeting on the Technology of Controlled Nucl. Fus., Santa Fe, NM, 1978, Vol. 1, pp. 376-384.

30. B. Sternlicht, "Low-Level Heat Recovery Takes on Added Meaning as Fuel Costs Justify Investment," Power, April 1975, pp 84-87.

31. S. L. Milora and J. W. Tester, "Geothermal Energy as a Source of Electric Power, Thermodynamic and Economic Design Criteria," The MIT Press, Cambridge, Mass. (1976).

32. D. W. Brown, M. C. Smith, and R. M. Potter, "A New Method for Extracting Energy from "Dry" Geothermal Reservoirs," Proc. Twentieth Annual Southwestern Petroleum Short Course, Texas Tech. Univ., Lubbock, Texas April 26-27, 1973, pp. 249-255.

33. LASL Project Staff, "Hot Dry Rock Geothermal Energy Development Project," Los Alamos Scientific Laboratory report LA-7109-PR (1978).

34. J. L. Anderson, "The Tritium Systems Test Assembly at the Los Alamos Scientific Laboratory," Am. Nucl. Soc. Third Topical Meeting on the Tech. of Cont. Nucl. Fusion, Santa Fe, NM, 1978, Vol. 2, pp. 674-679.

35. C. W. Schoenfelder and L. A. West, "Tritium Removal: A Preliminary Evaluation of Several Getters," Proc. Int. Conf. on Radiation Effects and Tritium Technology for Fusion Reactors, CONF-750989, 1975, Published by the Energy Res. and Dev. Adm. (1976), Vol. III, pp. 482-506.

36. V. A. Maroni, "Tritium Processing and Containment Technology for Fusion Reactors: Perspective and Status," Proc. of the Second Topical Meeting on the Technology of Controlled Nuclear Fusion, Richland, Washington, 1976, CONF-760935-P3, Vol. III, pp. 799-818.

37. D. K. Sze, I. N. Sviatoslavsky, E. T. Cheng, and H. I. Avci, "Thermal, Mechanical and Neutronic Design Considerations for a Graphite Structure Li_2O Cooled Blanket," University of Wisconsin report UWFDM-223 (1977).

38. K. Sako, M. Ohta, Y. Seki, H. Yamato, T. Hiraoka, K. Tanaka, N. Asami, and S. Mori, "Conceptual Design of a Gas-Cooled Tokamak Reactor," presented at the IAEA Workshop on Fusion Reactor Design, Culham, United Kingdom, 1974, (Nuclear Fusion Supplement, 1974), pp. 27-49.

39. K. Tanaka, H. Kudo, and H. Amano, "Tritium Recovery of the Fusion Reactor of Lithium Oxide Blanket," Proc. Int. Conf. on Radiation Effects and Tritium Technology for Fusion Reactors, CONF-750989, 1975, Published by U.S. Energy Res. and Dev. Adm. (1976), Vol. III, pp. 253-269.

40. Y. Seki, "Gas Production Rates in Lithium Oxide of Fusion Reactor Blankets," Nucl. Sci. Techn. 12, 769-772, (1975).

41. D. Guggi, H. R. Ihle, and U. Kurz, "Tritium Release from Neutron Irradiated Lithium-Aluminum Oxides," Proc. 9th Symp. on Fusion Technology, pp. 337-344 (1976), Published by Commission of European Communities (1976).

42. "Lithium Monoxide," Lithium Corporation of America product bulletin (not dated).

43. J. N. Anno, personal communication, Research Dynamics Inc., (Dec. 1978).

44. H. Kudo and K. Tanaka, "Removal of Tritium from Neutron-Irradiated Lithium Oxide," Radiochem. Radioanal. Letters 23, 57-62 (1975).

45. Handbook of Chemistry and Physics, 57th Ed., (1976-1977).

46. P. A. Akishin and N. G. Rambidi, "Electronographic Investigation of the Structure of the Molecule of Lithium Oxide," Doklady, Physical Chemistry Section, English Translation 118, 83-86 (1957).

47. D. T. Vier, "Thermal and Other Properties of Refractories," Los Alamos Scientific Laboratory report LA-5937-MS (1975).

48. O. K. Sokolov, "Calculation of Viscosity in Molten Salts (Oxides)," Eng. translation, National Aer. Space Adm. report NASA-TTF-416 (1962).

49. JANAF Thermochemical Tables, The Dow Chemical Co., Midland, Mich. (1955).

50. C. H. Shomate and A. J. Cohen, "High Temperature Heat Content and Entropy of Lithium Oxide and Lithium Hydroxide," J. Am. Chem. Soc. 77, 285-286 (1955).

51. H. L. Johnston and T. W. Bauer, "Heat Capacity and Thermodynamic Functions of Li_2O. Thermodynamics of Li_2O-H_2O System," J. Am. Chem. Soc. 73, 1119-1122 (1951).

52. P. A. G. O'Hare, M. Ader, W. N. Hubbard, G. K. Johnson, and J. L. Settle, "Calorimetric Studies on Actinide Compounds and Materials of Interest in Reactor Technology," Proc. Thermodyn. Nucl. Mat. 4th Symp. 2, 439 (1975).

53. M. G. Barker and J. Bentham, "The Influence of Dissolved Non-Metals on the Reaction of Liquid Lithium with the Oxides of Niobium and Tantalum," J. Less Common Metals 40, 1-7 (1975).

54. S. Nasu, H. Kudo, K. Shiozawa, T. Takahashi, T. Kurasawa, M. Tachiki, and K. Tanaka, "Tritium Release from Neutron-Irradiated Li_2O Pellets," J. Nucl. Mat. 68, 261-264 (1977).

55. R. Wiswall and E. Wirsing, "The Removal of Tritium from Fusion Reactor Blankets," Brookhaven National Laboratory report BNL-50748 (1977).

56. T. S. Elleman, L. R. Zumwalt, and K. Verghese, "Hydrogen Transport and Solubility in Non-Metallic Solids," Am. Nuc. Soc. Third Topical Meeting on the Technology of Controlled Nucl. Fusion, Santa Fe, NM, 1978, Vol. 2, pp. 763-770.

57. J. M. Mintz, T. S. Elleman, and K. Verghese, "Tritium Diffusion in Fusion Reactor Blankets," Nucl. Technol. 31, 172 (1976).

58. T. B. Rhinehammer and L. J. Wittenberg, "An Evaluation of Fuel Resources and Requirements for the Magnetic Fusion Energy Program," Monsanto Research Corp. report MLM-2419 (1978).

59. R. W. Webb, "Permeation of Hydrogen through Metals," Atomics International report NAA-SR-10461 (1965).

60. W. G. Perkins and O. R. Begeal, "Permeation and Diffusion of Hydrogen in Ceramuar, Copper, and Ceramuar-Copper Laminates," Sandia (Albuquerque) Laboratory report SC-DC-714493 (1972).

61. W. G. Perkins, and O. R. Beagel, "Permeation and Diffusion of Hydrogen in Ceramuar, Copper and Ceramuar-Copper Laminates," Ber. Bunsenges. Phys. Chem. 76, 863 (1972).

62. W. G. Perkins, "Permeation and Outgassing of Vacuum Materials," J. Vac. Sci. Technol. 10, 543 (1973).

63. W. Jost, "Diffusion in Solids, Liquids, Gases," Academic Press Inc., 1960.

64. L. Katz, M. Guinan, and R. J. Borg, "Diffusion of M_2, D_2, and T_2 in Single-Crystal Ni and Cu," Phys. Rev. B4, 330 (1971).

65. S. Dushman and J. M. Lafferty (ed.), Scientific Foundations of Vacuum Technique, 2nd Edition (John Wiley and Sons, NY, 1962).

66. A. Roth, Vacuum Technology (North Holland Publishing Company, New York 1976).

67. B. Badger, R. W. Conn, G. L. Kulcinski, C. W. Maynard, R. Aronstein, and H. I. Avci, "UWMAK-III, A Noncircular Tokamak Power Reactor Design," University of Wisconsin report UWFDM-150 (1976).

68. R. W. Moses, Jr., and J. K. Ballou, "Inductive Shielding for Pulsed Energy Storage Magnets," IEEE Trans. on Magnetics, MAG-11, 493-496 (March 1975).

69. V. D. Shafranov, Review of Plasma Physics, Vol. 2 (Consultants Bureau, New York, 1966), p. 103.

70. J. M. Greene, J. L. Johnson, and K. E. Weiner, "Tokamak Equilibrium," Phys. of Fluids 14, 671 (1971).

71. V. S. Mukhavatov and V. D. Shafranov, "Plasma Equilibrium in a Tokamak," Nucl. Fusion 11, 605 (1971).

72. D. Weldon, personal communication, Los Alamos Scientific Laboratory (1978).

73. The FINTOR GROUP "FINTOR 1: A Minimum Size Tokamak DT Experimental Reactor," edited by Flaviano Farfaletti Casali, J. R. C. EURATOM - ISPRA (1976).

74. K. I. Thomassen (ed.), "Conceptual Engineering Design of a One-GJ Fast Discharging Homopolar Machine for the Reference Theta-Pinch Reactor," Electric Power Research Institute report EPRI-ER-246, Project 469 (1976).

75. M. Kristiansen (coordinator), "Proceedings of the Workshop on Switching Requirements and R&D for Fusion Reactors," EPRI ER-376-SR, Special Report (1977).

76. Staff of the CTR Division (Compiled by H. Dreicer), "The Reversed Field Pinch Concept and a Preliminary Conceptual Design for a Proof-of-Principle Experiment," Los Alamos Scientific Laboratory report LA-7527-MS (1978).

VI. PHYSICS AND TECHNOLOGY ASSESSMENT

Throughout this report the design bases, uncertainties, unknowns and assumptions have been clearly stated. This section briefly summarizes these items in the form of an assessment.

A. Physics Assessment

1. Equilibrium and Stability. The plasma is assumed to be stable to gross MHD modes with at most the existence of controlled turbulence producing enhanced particle transport and thermal conduction. Varying degrees of gross MHD stability have prevailed in the experiments listed in Table III-I and VI-I. The experiments generally indicate the existence of a stable reversed-field configuration which is eventually lost upon violation of various stability criteria: the maximum allowed beta ($\beta_\theta \simeq 0.5$) is exceeded; the plasma is overly compressed ($\Theta = B_\theta(r_w)/\langle B_\phi \rangle \sim 2$ for operation near minimum energy); or classical processes produce high losses which terminate confinement. The promising results from the generally small experiments outlined in Table VI-I have led to the proposal of a number of new experiments:[14] a 0.24-m bore experiment (ETA BETA II, University of Padua, Italy); a 0.40-m bore device (ZT-40, Los Alamos Scientific Laboratory, Los Alamos, New Mexico); and 0.40-m bore (HBTX-1A), 120-cm bore (RFX) experiments both in the Culham Laboratory, United Kingdom.

The large ZETA experiment provides the best evidence that the RFP configuration will produce stable discharges at significant temperatures and confinement times. Results from this experiment indicates the existence of a stable energy state, as predicted by Taylor[15-17], which lends considerable credibility to this approach. This sinusoidal startup (Figs. III-4 and IV-6) closely follows this minimum-energy state and ultimately settles at $\Theta = 2.0$ and $F = -1.0$ during the constant-current burn. The degree to which the burn trajectory must follow those predicted by minimum-energy calculations is presently unknown.

Equilibrium in the RFPR is provided by the conducting first wall during a ~ 0.1-s timescale and subsequently by feedback coils for longer times. Vertical field coils effectively cancel the outward toroidal drift, as in a tokamak. Stabilization of gross plasma modes is provided by feedback coils located immediately inside the superconducting coil shield. Considering the long feedback times (~ 0.1 s) and the small number of unstable modes expected

TABLE VI-I

SUMMARY OF REVERSED-FIELD PINCH EXPERIMENTS

EXPERIMENT DESIGNATION	REFERENCE	FIRST-WALL RADIUS r_w(cm)	MAJOR RADIUS R(cm)	PLASMA CURRENT I_ϕ(kA)	FILLING PRESSURE P_A(mTorr)	POLOIDAL BETA β_θ	MAXIMUM TEMPERATURE (eV)	ENERGY CONTAINMENT TIME τ_E(ms)
RFP1	1	3.5	25	20	90-100	0.5	130	0.015
ZETA	2-6	50	150	100-900	0.25-2.0	0.10	200	10
HBTX	7	6.5	100	40-110	40	0.4-0.6	110	0.015
ETA-BETA	8-9	5	40	30-150	20-80	0.2-0.3	10	0.01
ETL-TPE-1	10-11	5	40	80-120	30-50	0.6	10	0.02
STP	12	4	12	50	20-30			
ZT-I	13	5	37	30-200	10-100	0.5	10	0.015
ZT-S	13	7.7	40	30-140	10-100	0.5	10	0.03

(primarily m = 1), this approach appears to be technically feasible.[18] As for most magnetic confinement schemes, it is recognized that a large amount of uncertainty exists with respect to the rate of energy loss incurred in a reactor-grade plasma that has achieved some semblance of gross stability. For the RFP, specifically, these uncertainties may be embodied in the "relaxation" processes that are related to the local instabilities that sustain the reversed-field state.

2. Transport. Theoretical predictions of transport in a toroidal device have proven to be generally inaccurate, leading to the development of empirical formulae[19,20] based upon experimental results. Reverse-field pinch experiments have not been of sufficient size to produce reactor-grade plasmas ($T > 1$ keV, $n\tau > 10^{19}$ s/m^3). This absence of relevent experimental information has led to the use of empirical relationships derived from tokamak experiments. A dominant electron thermal-conduction loss[19,20] is approximately described by a confinement time that is a factor of 200 greater than that given by the Bohm loss (Sec. IV. C. 1, Appendix A.). This anomalous electron thermal conduction is expected in a high-temperature plasma in which field inhomogeneities and local turbulence will have a pronounced effect on the predominantly collisionless electrons. Considerable theoretical and experimental uncertainties are associated with this "rationalized" assumption that $\tau_E = 200\ \tau_{Bohm}$ (Appendix A.). The RFPR performance will not be affected seriously by variations in this assumed value of τ_E/τ_{Bohm} that are less than a factor of ~ 2. Within these constraints this Bohm-like scaling is desirable from the viewpoint of the thermal stability of a beta-limited burn. If τ_E/τ_{Bohm} falls much below 100, the thermal loading at the first wall will become a problem, and the $\sim$ 1.5-m-radius plasma would not ignite.

3. Startup. The initially constant toroidal field, $B_{\phi o}$, and increasing toroidal current will result in a field configuration similar to that found in a tokamak. This q-stabilized system must then be transformed into a $dq/dr \neq 0$ RFP configuration by proper programming of the magnetic fields and neutral-gas puffing. The achieving of stability during this period seems unlikely, and turbulence similar to or in excess of that exhibited by tokamaks may result. Pressure balance is assumed during the startup as the plasma current ionizes the DT gas and ultimately drives the plasma to ignition. As for other fusion reactor designs, including tokamaks, the startup models tend to be somewhat heuristic and incomplete. Mathematical modeling of the complex startup

phenomena is difficult and is generally unsubstantiated by experimental results in the reactor regime. This transition from the q-stabilized state to a RFP state and the associated energy and magnetic flux losses is a crucial issue for the RFPR; if these losses are too great, ignition by ohmic heating may not be possible within a reasonable volt-second (flux) constraint.

4. Rundown (Quench). At the end of the burn the plasma current is driven to zero in a half-cycle fall time of $\tau_R \simeq 0.1$ s, and the plasma relaxes to the wall. The quenched plasma is assumed to be wall confined, where energy loss is controlled by energy conduction across the magnetic field trapped inside the plasma and bremsstrahlung radiation loss. For typical post-burn parameters (T_e = 4 keV, β_θ = 0.1, B_θ = 2 T, and Z_{eff} = 3) the bremsstrahlung and conduction loss times are 2.4 s and 3.6 s, respectively, implying the plasma energy would be extracted in ~ 2 s. A highly conservative assumption has been used throughout this model that all of the magnetic field trapped inside the plasma at quench is postulated to be dissipated at the first wall. Using classical resistivity, approximately 20 s is required to ohmically dissipate the magnetic field energy which represents 90% of the total energy in the bore at quench. Since ~ 40% of the total recirculating electric power is required to replace this dissipated field energy, significant increase in the engineering Q-value will occur if a portion of this quench field can be recovered as indicated by numerical calculations.[21] The addition of a neutral gas between the plasma and the vacuum wall would prevent damage to the first wall before the cool buffer layer is established and will enhance considerably the seemingly slow classical loss rate,[21] quenching the plasma within the desired 2-4 s. The proposal of wall confinement at the end of the burn is preliminary and will require more study. Of primary importance to the long-pulsed operation are transient effects which may determine the heat transport and surface damage to the first wall during the set-up phase of the postburn wall-confined plasma. With the advent of large tokamak experiments (TFTR, JET, JT-60, T-15) a concern has developed about the methods of plasma cooling that will be required to assure non-destructive, controlled extraction of appreciable energy densities from the postburn plasma. Like the startup problem, the question of plasma rundown is difficult to resolve by realistic analysis but remains as a crucial issue for any long-pulsed machine.

B. Technology Assessment

The engineering computations made in conjunction with this study should not be considered as a detailed design study. Instead, these computations have focused only on those systems that are perceived to be crucial to the economics and operation of a conceptual power plant. This section briefly assesses the technology associated with key engineering systems.

1. First Wall. The 20-mm-thick copper first wall serves only a passive electrical function in providing short-term eddy currents needed to stabilize gross MHD modes on a ~ 0.1-s timescale. From a thermohydraulic viewpoint alone, no serious problems are anticipated during normal operation; the thermal constraints placed on the first wall, however, impact directly on the overall plant thermal-cycle efficiency (Sec. V. C). Increased electrical resistivity caused by radiation effects, including the buildup of transmutation-induced Ni and Zn impurities, should not significantly affect the electrical function of the first wall (Sec. V. B.4.b). Although hydrogen embrittlement should not pose a problem at the operating temperature, the formation of interstitial gases through the interaction of hydrogen atoms with oxides used for solution hardening may present a problem. Neutron-induced swelling of the copper will be serious, and either alloying and/or mechanical-design techniques may be required to achieve a desirable (~ 5-y) first-wall life. The need and performance criteria for this conducting shell have been established on the basis of present physics understanding; these criteria should be re-evaluated in considerably more detail. Additionally, a more thorough engineering design effort should be applied to this crucial RFPR sub-system.

2. Blanket. The primary objective of the blanket design effort is the utilization of conventional technology to satisfy the requirements of tritium breeding/containment and thermal energy removal. The copper first wall, high-pressure steam tubes, and Li_2O packed around the steam tubes presents no extraordinary constructional difficulties. Thermohydraulic calculations indicate a near steady-state heat flux to the coolant tubes, which minimizes thermal fatigue. The removal of tritium from the blanket by a helium purge stream containing trace amounts of oxygen is considered feasible and adequate. Although leakage of tritium to the high-pressure steam tubes can probably be kept to acceptable levels, tritium barriers may be required for the water-cooled copper first wall. The release rate, tritium blanket inventory,

and the time required to achieve fuel self-sufficiency depend sensitively on the effective tritium diffusivity in Li_2O; diffusivity data for this system is insufficient to quantify the seriousness of this problem, but indications are presented that point to realistic solutions (Sec. V. D). The use of water/steam cooling and the generation of slightly superheated steam for direct cycle to a turbine appear feasible and near to the state-of-the-art. The resulting cycle efficiency of 28% is lower than that optimally predicted for other saturated steam cycles, and improvement is expected by small increases in first-wall and exit-steam temperature (Sec. V.C). These improvements can be obtained by modestly increased materials requirements. The question of physical and morphological stability of the Li_2O packed-bed was not addressed, but could present a problem.

3. Energy Transfer, Storage and Switching. Homopolar motor/generators were proposed to drive the toroidal and poloidal magnet coils. A detailed conceptual engineering design of a 1-GJ homopolar machine with a 30-ms discharge time has been performed.[22] This machine has an active rotor length of ~ 13-m, 2-m-diameter rotors and spins at 277 m/s. The magnetic field is produced by Nb_3Sn magnets with a peak field of 8 T. This 95% efficient machine pushes state-of-the-art in many ways. The combination of surface speed and brush current density has not been achieved in solid brushes. Aluminum rotors are proposed for the first time, and this design would be the first pulsed homopolar to use superconductors. These problems arise only because of the lack of development effort rather than because of fundamental difficulties. A modest program should lead to a homopolar having good efficiency (> 90%) and economics ($\lesssim$ 1¢/J). Parametric studies show that the RFPR performance is not seriously degraded until this efficiency falls below ~ 80%. (Fig. IV-11).

Conventional switching is considered for use in the RFPR with each closing switch consisting of a parallel-connected ignitron and a mechanical bypass switch and with each opening switch constructed of a vacuum interrupter in parallel with a mechanical bypass switch.[14] The reliable operation of ~ 2700 switches, each carrying 25 kA, is of primary concern, providing an impetus to develop larger switching elements (> 100 kA) with high energy transfer efficiency and reliability as design criteria. The technology needed for these switches appears straightforward, although a development effort is

required. Solid-state switches may always be invoked, although economic considerations warrant the development of efficient mechanical breakers.

4. Magnets. Superconducting coils are used for both the poloidal and toroidal systems. A maximum field at the coils of ~ 2.0 T gives a maximum field rate of change of 20-40 T/s for the 0.1-s startup. This rate-of-change and absolute magnitude of magnetic field represent near-term technology for NbTi superconductors. A detailed design of a 20 T/s coil with a maximum field of 7 T has been performed.[23] Potential problems are encountered with the coupling of the toroidal coil to the poloidal system. The enhanced eddy-current losses induced in the toroidal coil can be greatly reduced by alternating the twist direction of the filaments as the coil is wound.

The arrangement of magnets in this design is unique and generally reflect the advantage of pressure confinement primarily by energy-efficient poloidal fields. Consequently, the poloidal field and vertical field coils are removed from the reactor torus per se. The resulting increase in blanket and shield accessibility leads to operational and maintenance advantages that far outweigh the ~ 50% increase in stored magnetic energy. The bipolar operation of the poloidal coil system results in the homopolar motor/generator serving only as a capacitive transfer element, rather than the primary energy store. Homopolar motor/generators serve as an energy store for the toroidal field coils, which are adequately spaced within a 0.5% field-ripple criterion to allow blanket/shield replacement without disturbing these permanently-fixed magnets.

Small, normal feedback coils must be affixed to the inner radius of the shield sub-module. The slow (~ 10 Hz) feedback requirements, coil design, power supplies, and instrumentation/control systems have not been specified. Although preliminary estimates[18] indicate acceptable energy consumption and technical feasibility, this important issue must be addressed in considerably more detail.

5. Vacuum and Tritium Recovery. Using a vacuum tunnel immediately outside the toroidal field coil maintains a relatively small vacuum volume while allowing good access. Serious leaks inside the vacuum tunnel will inevitably force the reactor system to shutdown, although the ease of removing the blanket and shield segments without disturbing superconducting coils and the general accessibility to the reactor components should minimize the reactor downtime. Little design effort has been devoted to this issue,

however. A similar statement must be made about the tritium recovery system, which proposes the use of relatively conventional gas-phase separations. Generally, both vacuum and tritium-recovery systems represents an extention of state-of-the-art techniques to physical scales of size that have yet to be demonstrated, but the required technological innovation should be minimal.

The plasma chamber per se would be pumped through intermodule conductances by the vacuum tunnel, which in turn would be evacuated either by Roots blowers or cryopanels. The vacuum time constant required for the plasma chamber ($\sim$ 4 s) may not be achievable with an intermodule gap that is limited to a few tens of millimeters and in the presence of surface outgasing; vacuum downcommers may have to be added to each 2-m-long module to attain the required evacuation time.

C. Summary Assessment

As for most fusion reactor studies of this nature, the credibility and feasibility of most engineering systems is determined in large part by the physics assumed to generate the reactor plasma model. Energy loss from the plasma incurred during initiation and sustenance of the field-reversed configuration represents the major uncertainty. The plasma/field/first-wall response during the rundown (quench) phase of the long-pulsed operation presents a second important uncertainty. Within the constraints of the assumptions made for both energy confinement and quench processes, feasible technical designs for all engineering systems have been identified. Furthermore, sensitivity studies of the influence of key physics (i.e., beta) and engineering parameters (i.e., ETS efficiency) indicate that a relatively safe margin for error exists before a serious degradation in system performance and cost is incurred.

In many ways the RFPR presents an optimum system on which to examine the technical and economic feasibility of magnetic fusion power, given a favorable resolution of the above mentioned physics issues. This study has shown that an efficient power plant may emerge from the relatively low technology requirements of batch-burn operation. Specifically, the elimination of exotic heating, fueling, and ash-removal systems from the first-generation power plant, while simultaneously operating with a strong promise of high efficiency and low cost, could lead to a relatively low-risk approach to fusion power. Once the still significant uncertainties of batch-burn operation are resolved,

the improvement of system performance can be attacked by incorporating advanced fueling and ash-removal systems. Such improvements would be achieved from the stronger technology base that would be built from economic, batch-burn operation.

REFERENCES

1. T. Ohkawa, H. K. Forsen, A. A. Schupp, Jr., and D. W. Kerst, "Toroidal Discharge Experiments with Rapid Programming," Phys. Fluids 6, 846-857 (1963).

2. E. P. Butt, R. Carruthers, J. T. D. Mitchell, R. S. Pease, P. C. Thonemann, and M. A. Bird, "The Design and Performance of ZETA," Second United Nations International Conf. on the Peaceful Uses of Atomic Energy, Geneva, Switzerland, 1958, Vol. 32, pp. 42-64.

3. W. M. Burton, E. P. Butt, H. C. Cole, A. Gibson, D. W. Mason, and R. S. Pease, "Plasma Loss in ZETA," Nucl. Fus., Suppl. 3, 903-919 (1962).

4. E. P. Butt, H. C. Cole, A. N. Dellis, A. Gibson, M. Rusbridge, and D. Wort, "Conditions for Improved Stability in ZETA," Conf. on Plasma Physics and Controlled Nuclear Fusion Research, Culham, United Kingdom, 1965, pp. 751-764.

5. D. C. Robinson and K. E. King, "Factors Influencing the Improved Stability of ZETA, "Third International Conf. on Plasma Physics and Controlled Nuclear Fusion Research, Novosibirsk, USSR, 1968, Vol. 1, pp. 263-276.

6. E. P. Butt and A. Newton, " New Results from ZETA," Third Topical Conf. on Pulsed High-β Plasmas, Culham, United Kingdom, 1975, pp. 437-441.

7. C. A. Bunting, A. A. Newton, and M. R. C. Watts, "Studies of the Ion Temperature and Total Radiated Energy from Pinches in HBTXI," Third Topical Conference on Pulsed High-β Plasmas, Culham, United Kingdom, 1975, pp. 437-441.

8. A. Buffa, S. Costa, G. F. Nalesso, and G. Malesani, "Experiments on Programmed and Natural Relaxing RFP Configurations," Third Topical Conf. on Pulsed High-β Plasma, Culham, United Kingdom, 1975, pp. 261-265.

9. A. Buffa, S. Costa, R. Giannella, G. Malesani, G. F. Nalesso, and S. Ortolani, "Heating, Diffusion, and Stability of Reverse-Field Pinch Configurations," Sixth International Conf. on Plasma Physics and Controlled Nuclear Fusion Research, Berchtesgaden, West Germany, 1976, (Nuclear Fusion, Supplement 1977), Vol. I. pp. 447-461.

10. K. Ogawa, T. Shimada, S. Kiyama, V. Hirano, Y. Maejima, and I. Hirota, "High-Beta Plasma Confinement in Reversed Field Pinch (ETL TPE-1)," Third

Topical Conference on Pulsed High β Plasmas, Culham, United Kingdom, 1975, pp. 255-259.

11. T. Shimada, Y. Hirano, Y. Maejima, and K. Ogawa, "Toroidal Pinch Experiments in ETL," Sixth International Conference on Plasma Physics and Controlled Nuclear Fusion Research, Berchtesgaden, West Germany, 1976, (Nuclear Fusion, Supplement 1977), Vol. I, pp. 463-469.

12. K. Hirano, S. Kitagawa, M. Wakatani, Y. Kita, S. Yamada, and S. Yamaguchi, "Plasma Confinement of Nagoya High β Toroidal Pinch Experiments," Sixth International Conference on Plasma Physics and Controlled Nuclear Fusion Research, Berchtesgaden, West Germany, 1976, (Nuclear Fusion, Supplement 1977), Vol. I, pp. 503-510.

13. D. A. Baker and J. N. DiMarco, "The LASL Reversed-Field Pinch Program," Los Alamos Scientific Laboratory report LA-6177-MS (1975).

14. Staff of CTR Division (Compiled by H. Dreicer), "The Reversed-Field Pinch Concept and a Preliminary Conceptual Design for a Proof-of-Principle Experiment" Los Alamos Scientific Laboratory report LA-7527-MS (1978).

15. J. B. Taylor, "Relaxation of Toroidal Plasma and Generation of Reverse Magnetic Fields," Phys. Rev. Lett. 33 (19), 1139-1141 (1974).

16. J. B. Taylor, "Relaxation of Toroidal Discharges to Stable States and the Generation of Reverse Magnetic Fields," Fifth IAEA Conf. on Plasma Phys. and Controlled Fusion, Tokyo, Japan, 1974, Vol. 1, pp. 161-167.

17. J. B. Taylor, "Relaxation of Toroidal Discharges," Third Topical Conf. on Pulsed High Beta Plasmas, Culham, United Kingdom, 1975, p. 59.

18. G. Miller, "Wall Resistivity Effects in a Toroidal Pinch, Feedback Stabilization," Los Alamos Scientific Laboratory report LA-7661-MS (1979).

19. A. B. Berlizov, G. A. Bobrovskij, A. A. Bagdasarov, N. L. Vasin, A. N. Vertiporokh, and V. P. Vinogradov, "First Results from the T-10 Tokamak," Sixth Conf. on Plasma Physics and Controlled Nuclear Fusion Research, Berchtesgaden, 1976, Vol. 1, pp. 3-18.

20. E. Apgar, B. Coppi, A. Gondhalekar, H. Helava, D. Komm, and F. Martin, "High-Density and Collisional Plasma Regimes in the Alcator Programme," Sixth Conference on Plasma Physics and Controlled Nuclear Fusion Research, Berchtesgaden, 1976, Vol. 1, pp. 247-266.

21. T. A. Oliphant, G. E. Gryczkowski, and T. Kammash, "Transient Charge-Exchange in a Neutral-Gas Layer," Nucl. Fus. 16, 263-268 (1976).

22. K. I. Thomassen (ed.), "Conceptual Engineering Design of a One-GJ Fast Discharging Homopolar Machine for the Reference Theta-Pinch Reactor," Electric Power Research Institute report EPRI-ER-246, Project 469 (1976).

23. D. Weldon and J. Wollen, personal communication, Los Alamos Scientific Laboratory (1978).

APPENDIX A

RFPR BURN MODEL AND REACTOR CODE

The systems code used to model the RFPR is based on a zero-dimensional, three-particle, time-dependent burn computation. The physics basis for this code is described in this Appendix. Additionally, the RFPR code, provides the following information for each time-dependent plasma simulation:

- Complete time history of all plasma properties, including parameters that are constrained to satisfy stability requirements (particularly β_θ, F, and Θ).
- Complete reactor energy balance and a listing of all system energy requirements that culminates in a final expression for the engineering Q-value, Q_E, or recirculating power fraction, $\varepsilon = 1/Q_E$.
- A simultaneous, time-dependent thermal response of the first wall during the burn phase.
- A simultaneous, time-dependent mechanical/structural response of the first wall during the burn phase
- The creation of a file for an interactive usage of a standardized reactor costing code (Appendix B).

1. Plasma and Magnetic Field Models. MKS units are used throughout, although plasma temperature is expressed in keV units, kT (J) = T (keV) x 10^3e, where e = 1.602(10)$^{-19}$J/eV. The radial dependence of both poloidal B_θ and toroidal B_ϕ fields are described by

$$B_\theta(r) = \begin{cases} A_\theta J_1(\alpha r), & r < r_p \\ \dfrac{\mu_o I_\phi}{2\pi r}, & r > r_p \end{cases} \qquad (A\text{-}1)$$

$$B_\phi(r) = \begin{cases} A_\phi J_o(\alpha r), & r < r_p \\ B_R, & r > r_p \end{cases},$$

where $J_o(\alpha r)$ and $J_1(\alpha r)$ are Bessel functions of the first kind, A_θ and A_ϕ are constants to be determined, $\mu_o = 4\pi(10)^{-7}$ h/m, I_ϕ is the toroidal plasma current, and B_R is the uniform toroidal field outside the plasma. The good agreement between the Bessel function fields model and actual MHD stable field

profiles[1] is shown in Fig. A-1, which gives the radial dependence of B_θ and B_ϕ. These profiles are used to compute appropriate radial averages of plasma properties for use in the zero-dimensional, three-particle burn code.

Toroidal flux conservation is assumed inside the plasma, which implies that initial toroidal flux ($\pi r_w^2 B_{\phi o}$) must equal $B_\phi(r)$ integrated over the plasma area. Performing this integration gives

$$A_\phi = \alpha r_p B_{\phi o}/2x^2 J_1(\alpha r_p), \tag{A-2}$$

where x is the plasma radius r_p divided by the wall radius r_w, and $B_{\phi o}$ is the initial (i.e. prior to preionization) toroidal field. The radius of the plasma is taken as the point of zero B_ϕ field for $x < 1$ ($\alpha r_p = 2.405$), and α must be determined for $x = 1$.

From the Maxwell equations, assuming a static electric field,

$$\mu_o \vec{j} = \vec{\nabla} x \vec{B} \ . \tag{A-3}$$

The plasma current densities are given by

$$j_\phi(r) = \alpha A_\theta J_o(\alpha r)/\mu_o \tag{A-4}$$

$$j_\theta(r) = \alpha A_\phi J_1(\alpha r)/\mu_o . \tag{A-5}$$

The toroidal plasma current I_ϕ must equal the integral of j_ϕ over the plasma cross section, which leads to

$$A_\theta = \mu_o I_\phi/2\pi r_p J_1(\alpha r_p) \ . \tag{A-6}$$

From the Maxwell equations, assuming a static electric field, the pressure balance is given by

$$(\vec{\nabla} x \vec{B}) x \vec{B} = \mu_o \vec{\nabla} p(r) \ . \tag{A-7}$$

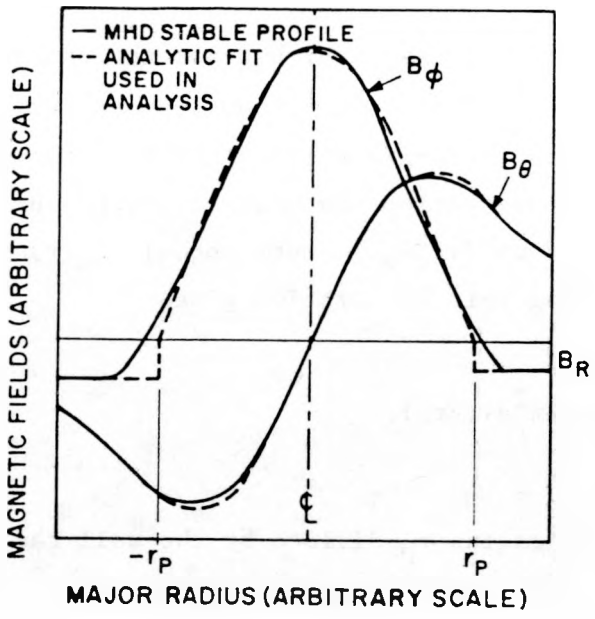

Fig. A-1 Comparison of Bessel function model with numerically computed field profiles.

Substituting the magnetic fields into Eq. (A-7) and integrating over the plasma radius gives the plasma pressure as a function of radius

$$2\mu_o p(r) = (A_\theta^2 - A_\phi^2) \left[J_o^2(\alpha r) - J_o^2(\alpha r_p) \right] . \qquad \text{(A-8)}$$

Within the constraints of this zero-dimensional plasma model use of the average integrated plasma pressure is desirable. Integrating Eq. (A-8) over the plasma area gives

$$\langle p \rangle = p(r) J_1^2(\alpha r_p) / \left[J_o^2(\alpha r) - J_o^2(\alpha r_p) \right] . \qquad \text{(A-9)}$$

The average plasma pressure $\langle p \rangle$ equals the summation of nkT over all plasma species, where an isothermal plasma is generally assumed. Substituting Eq. (A-8) into Eq. (A-9) and utilizing Eqs. (A-2) and (A-6) for A_θ and A_ϕ gives

$$\langle p \rangle = \mu_o I_\phi^2/8(\pi r_p)^2 - (\alpha r_p)^2 B_{\phi o}^2/8\mu_o x^4 \quad . \tag{A-10}$$

For x = 1 Eq. (A-10) is solved for α, which defines the field and pressure profiles during the initial I_ϕ current rise.

A poloidal beta, β_θ is defined as the average plasma pressure divided by the poloidal field pressure at the plasma radius r_p

$$\beta_\theta = \langle p \rangle/(B_\theta^2/2\mu_o) = 1-(A_\phi/A_\theta)^2 \quad . \tag{A-11}$$

This expression is used in the numerical code to monitor stability criteria during the thermonuclear burn.

2. Plasma Energy Balance. The time-rate-of-change of plasma energy is given by

$$d(3p\pi r_p^2/2)/dt = P_\alpha + P_{OHM} - P_{RAD} - P_{COND} - p\ d(\pi r_p^2)/dt \ , \tag{A-12}$$

where the various powers are expressed per meter of toroidal length, and correspond to, respectively, alpha-particle, ohmic, radiation, and thermal conduction. The last term in Eq. (A-12) represents direct conversion work done by high-beta plasma expansion against confining magnetic fields; this term is negligible for the RFPR operating mode considered here. Substituting Eq. (A-10) into Eq. (A-12) and solving for dx/dt gives

$$\frac{d\ell nx}{dt} = \frac{(P_\alpha + P_{OHM} - P_{RAD} - P_{COND})/\pi r_p^2 - 3(B_\theta^2/2\mu_o)d\ell nI_\phi/dt}{3(\alpha r_p)^2(B_{\phi o}^2/2\mu_o)/4x^4 + 2\langle p \rangle} \ , \tag{A-13}$$

where B_θ is defined at the plasma radius r_p.

The spatially dependent alpha-particle-heating power is proportional to n^2 and is numerically integrated over the plasma cross-sectional area using Eq. (A-9) and assuming an isothermal plasma. The result is

$$P_\alpha = 5.64 \times 10^{-13}\ n_D n_T \langle\sigma v\rangle\ A\ , \qquad \text{(A-14)}$$

where n_D and n_T are the spatially averaged deuterium and tritium number densities and A is approximated by an analytic function that within 1% accuracy is given by

$$A = \begin{cases} \left[1.333 + 0.039\ \alpha r_p (1 + 0.21\ (\alpha r_p)^4)\right]\ \pi r_p^2\ , & x = 1 \\ 2.098 \pi r_p^2\ , & x < 1 \end{cases} . \qquad \text{(A-15)}$$

Bremsstrahlung, line, and cyclotron radiation contribute to the radiation power, P_{RAD}. Impurity radiation is incorporated for oxygen and utilizes fitted analytic functions.[2] The average bremsstrahlung power is[3]

$$P_{BR} = 5.35(10)^{-37}\ n_e^2 Z_{eff}\ T_e^{1/2}\ A, \qquad \text{(A-16)}$$

where Z_{eff} is the sum of $n_k Z_k^2$ divided by the sum of $n_k Z_k$ over all ion species k, and the function A is given by Eq. (A-15). The cyclotron radiation leaving a nonabsorbing plasma[3] is numerically integrated over the plasma cross section for $\alpha r_p = 2.405$ to give

$$P_{cy}^T = 6.20(10)^{-17}\ n_e\ (\bar{B})^2\ T_e(1 + T_e/204)\ \pi r_p^2\ , \qquad \text{(A-17)}$$

where an effective magnetic field $\bar{B}$ has been defined as

$$(\bar{B})^2 = 0.6993\ \left[B_\theta^2 + 3(2.405)^2\ B_{\phi o}^2/4x^4\ \right] . \qquad \text{(A-18)}$$

The poloidal field, B_θ, is evaluated at the plasma radius. Accounting for absorption and assuming nonreflecting walls,[3] the actual fraction of cyclotron radiation leaving the plasma is given by

$$k_L = 2.1(10)^{-3} T_e^{7/4} [c\bar{B}\epsilon_o / 2 r_p n_e e]^{1/2} \quad . \tag{A-19}$$

The fraction of P_{CY}^T leaving the plasma for an absorbing plasma and a reflecting cylindrical first wall is given by k_C in Ref. 4. For a first wall with a fraction f formed by holes, therefore, the cyclotron radiation power leaving the plasma and escaping through these holes is $P_{CY}^H = P_{CY}^T k_L f$. The power leaving the plasma and absorbed by the first wall is $P_{CY}^W = P_{CY}^T k_C (1-f)$ for a reflecting metallic wall, and $P_{CY}^W = P_{CY}^T k_L (1-f)$ for a nonreflecting wall. The total power leaving the plasma is $P_{CY} = P_{CY}^H + P_{CY}^W$.

The ohmic heating power P_{OHM} is calculated for $\alpha r_p = 2.405$. From Eqs. (A-3) and (A-7), the perpendicular current must support the plasma pressure. Hence,

$$j_\perp(r) B(r) = \partial p(r) / \partial r \quad . \tag{A-20}$$

The remaining current is directed parallel to field lines

$$j_\parallel(r) = (j_\phi^2 + j_\theta^2 - j_\perp^2)^{1/2} \quad . \tag{A-21}$$

Numerically integrating the ohmic heating power density, $\eta_\parallel j_\parallel^2(r) + \eta_\perp j_\perp^2(r)$, over the plasma cross section, and fitting the result to an analytic function (within 1% accuracy) gives

$$\begin{aligned} P_{OHM} = {} & [(I_\phi \alpha r_p)^2 / 4\pi r_p^2] \\ & \{\eta_\parallel (2-\beta_\theta) + (\eta_\perp - \eta_\parallel)\beta_\theta^2 \\ & [1 - 1.13(1-\beta_\theta)^{1/2} + 0.43(1-\beta_\theta)]\} \quad , \end{aligned} \tag{A-22}$$

where the classical plasma resistivities are assumed[5] and are given below.

$$\eta_{\parallel}(\Omega\ m) = 9.62(10)^{-10} Z_{eff} \ell n\Lambda / \gamma_E T_e^{3/2} \qquad \text{(A-23)}$$

$$\eta_{\perp} = \eta_{\parallel}/0.51$$

where,

$$\gamma_E = 0.582 + 0.418\ [(Z_{eff}-1)/Z_{eff}]^2 \qquad \text{(A-24A)}$$

$$\Lambda = 4.907(10)^{17} T_e^{3/2}/Z_{eff} n_e^{1/2} \quad , \ T_e < 0.0362\ keV \qquad \text{(A-24B)}$$

$$\Lambda = (0.0362/T_e)^{1/2} \quad , \ T_e > 0.0362\ keV \qquad \text{(A-24C)}$$

During the early startup phase ($\alpha r_p < 2.405$) the relatively cool plasma yields $\beta_\theta \sim 0$, and only the parallel resistivity need be considered. The integrated ohmic heating power is then given by

$$P_{OHM} = [\eta_{\parallel}(I_\phi \alpha r_w)^2/2\pi r_w^2][1 + (J_o/J_1)^2(1 - J_1/\alpha r_w J_o)] \ , \qquad \text{(A-25)}$$

where r_w is the first-wall radius and the Bessel functions are evaluated at αr_w.

Conductive losses from the plasma can be properly treated as a function of time only by a one-dimensional MHD code. This level of calculation is beyond the scope of this study, and an approximate expression is used to describe the dominant ion thermal conduction losses. A one-dimensional MHD burn code for the RFPR, however, is presently under development.[6] The conductive power loss in the point-model approximation is taken as

$$P_{COND} = k_{\perp}(\partial T/\partial r)2\pi r_w = 4\pi T_i k_{\perp} \ , \qquad \text{(A-26)}$$

where T(r) is approximated as $(1-r^2/r_w^2)T(r = o)$, which corresponds to the

steady-state solution for an infinite circular cylinder with uniform properties.[7] The thermal conductivity, $k_\perp$(W/m keV), is given by[5]

$$k_\perp(\text{W/m keV}) = 5.07(10)^{-39} A_i^{1/2} n_i^2 \ell n\Lambda / T_i^{1/2} B^2 \quad , \tag{A-27}$$

where $A_i = 2.5$ for DT fuel.

As expected, the conduction power loss given by this classical formalism is small and has little impact on the overall plasma energy balance. Consequently, the ignited plasma would tend to overheat and achieve undesirably high beta values. Early RFPR designs[8] used this expression for classical conduction losses, and were forced to impose on the burn an external means of beta control, such as premature plasma expansion/quench or operating with an off-optimum DT fuel mixture to control the plasma dynamics and beta by fuel burnup.[8] Reactor operation within the constraints of classical transport with a superposed beta restriction would lead to a very restricted and nonoptimal RFPR design. Fortunately, radial particle/energy transport will occur at a level that is far from classical predictions. The RFPR design does not use Eqs. (A-26) and (A-27) for radial transport; rather, an energy transport time τ_E is taken as 200 times the anomalous Bohm time, where $\tau_{BOHM} \sim r_p^2 B_\theta / 63 T_e$. The basis of this assumption is addressed in the following section.

Lastly, alpha-particle heating is treated by a Fokker-Planck calculation,[9] which allows for the possible non-Maxwellian phase-space distributions for both electron and fuel ion species. The addition of particles to the alpha-particle distribution function as a result of the fusion yield is given by

$$\Delta f_\alpha(n/v^3) = (\Delta n_\alpha / \sqrt{\pi}\Delta_d 4\pi v_\alpha^2) e^{-\left[(v - v_\alpha)/\Delta_d\right]^2} \quad , \tag{A-28}$$

where v_α is the velocity corresponding to the 3.52-MeV α-particle, Δn_α is the number density of alpha particles added at each time step Δt, and the Doppler broadening caused by the background ion species is $\Delta_d = (kT_i/2m_i)^{1/2}$.

During each time step the electron temperature is adjusted according to the varying plasma volume, alpha-particle heating, classical electron-ion equipartition[5] and plasma powers P_{OHM} and P_{RAD}. Similarily, the ion temperatures reflect the volume change, ion-electron equipartition, alpha-particle heating, and power loss P_{COND}. At the end of each time step the alpha-particle-velocity distribution is modified to account for plasma expansion, and the energy equipartition between plasma species is followed by the Fokker-Planck calculation.

3. Anomalous Radial Transport. Theoretical understanding of radial transport processes in most toroidal devices is poor. In order to achieve a stable, high-yield burn, the Culham RFP reactor design[10] has postulated the existence of a limiting beta, $\beta_{\theta L}$. When $\beta_\theta < \beta_{\theta L}$, radial transport is taken as classical, whereas for $\beta_\theta > \beta_{\theta L}$ instabilities would grow and saturate, numerically appearing as a rapid loss proportional to $e^{k(\beta_\theta - \beta_{\theta L})}$. The value of the constant k is chosen sufficiently large to assure $\beta_{\theta L}$ is not exceeded by more than a few percent any time during the RFP burn. A physical explanation[11] leads to a basis for this $\beta_{\theta L}$ assumption. Basically, low field shear near the plasma centerline is expected to produce a region that does not satisfy the Suydam criterion,[12] and a turbulent core may result. For this situation confinement would be determined by a stable outer annulus in which the net loss process would be characterized by anomalous electron transport. Anomalous transport within this relatively stable annulus is poorly resolved, but may be explained by microturbulence.

The approximation used to model turbulent transport in the RFPR study differs from the limiting beta model,[10] but the predicted results are nearly identical. The present level of understanding of these processes allows at best a guess at the global energy confinement time, τ_E, in terms of a Bohm diffusion time, $\tau_{Bohm} = r_p^2 B_\theta / 63 T_e$. An energy confinement time for many tokamaks, including T-10[13] at $T_e \sim 1$ keV, scales as $\tau_E \simeq 3.6 r_p^2 B_\theta$; this scaling predicts $\tau_E \simeq 225 \tau_{Bohm}$. On the other hand, empirical "Alcator" scaling[14] predicts $\tau_E \simeq 5.0 (r_p B_\theta)^2 / T_e$, which at $\tau_E \sim 1$ keV gives $\tau_E \simeq 310 \tau_{Bohm}$. It is acknowledged that neither of these empirical scaling laws are applicable to the relatively collisional experimental plasmas from which they originate, and extension or extrapolation of the collisionless reactor plasmas has little basis. Nevertheless, τ_E / τ_{Bohm} is taken to be 200 for the purposes of the RFPR study in the absence of a better approach. The results presented herein are

not significantly altered by changes of ~ 2 in this factor of 200. Generally, this Bohm-like scaling is expected to apply to a toroidal reactor plasma in which field inhomogeneities have a pronounced effect on the collisionless, high-temperature electrons. From the viewpoint of a stable, beta-limited and ignited RFPR burn, Bohm-like scaling is highly desirable.

APPENDIX B

COSTING MODEL

Economic guidelines developed by the Battelle Pacific Northwest Laboratory[15] are used for the costing framework. The costing guidelines describe uniform accounting categories and procedures that have been used in the fission power industry.[16] Unfortunately, a uniform costing data base, presently under development,[17] has yet to be made available for fusion applications. A cost data base, therefore, has been assimilated and generated by LASL to provide a complete, but interim, optimization tool. It is emphasized that absolute cost values are intended only for intercomparisons with other systems that have been costed by the same procedure. This Appendix presents the costing code output and includes the cost accounting summary and cost data base for the RFPR.

FUSION REACTOR ECONOMIC EVALUATION (VER. 1.3)

DESIGNATION: RFPR - 50/50%DT,S.C. COILS,R=12.7M,RW=1.5M,IZ=20 MA,Q=2.0,F=-1.0,P=2.25 MTORR DATE: 79/04/17.

ACC. NO.	ACCOUNT TITLE			MILLION DOLLARS
20. 1.	LAND & PRIVILEGE ACQUISITION			
20. 2.	RELOCATION OF BUILDINGS, UTILITIES, HIGHWAYS, ETC.			
20.	LAND & LAND RIGHTS			2.500
21. 1. 1.	GENERAL YARD IMPROVEMENTS			
21. 1. 2.	WATERFRONT IMPROVEMENTS			
21. 1. 3.	TRANSPORTATION ACCESS (OFF PLOT)			
21. 1.	SITE IMPROVEMENTS & FACILITIES		11.000	
21. 2. 1.	BASIC BUILDING STRUCTURES	46.601		
21. 2. 2.	BUILDING SERVICES	4.546		
21. 2. 3.	CONTAINMENT STRUCTURES			
21. 2.	REACTOR BUILDING		51.147	
21. 3. 1.	BASIC BUILDING STRUCTURES	16.160		
21. 3. 2.	BUILDING SERVICES	1.440		
21. 3.	TURBINE BUILDING		17.600	
21. 4. 1.	INTAKE STRUCTURES			
21. 4. 2.	DISCHARGE STRUCTURES			
21. 4. 3.	UNPRESSURIZED INTAKE & DISCHARGE CONDUITS			
21. 4. 4.	RECIRCULATING STRUCTURES			
21. 4. 5.	COOLING TOWER SYSTEMS			
21. 4.	COOLING SYSTEM STRUCTURES		10.500	
21. 5. 1.	BASIC BUILDING STRUCTURES	9.000		
21. 5. 2.	BUILDING SERVICES	1.000		
21. 5.	POWER SUPPLY & ENERGY STORAGE BUILDING		10.000	
21. 6. 1.	REACTOR AUXILIARIES BUILDING(INCL. SWITCHGEAR BAY)	62.500		
21. 6. 2.	RADIOACTIVE WASTE BUILDING	7.500		
21. 6. 3.	FUEL STORAGE BUILDING			
21. 6. 4.	CONTROL ROOM BUILDING	3.188		
21. 6. 5.	DIESEL GENERATOR BUILDING	1.425		
21. 6. 6.	ADMINISTRATION BUILDING	2.125		
21. 6. 7.	SERVICE BUILDING	2.500		
21. 6. 8.	HELIUM STORAGE BUILDING	.440		
21. 6. 9.	MISCELLANEOUS STRUCTURES & BUILDING WORK	7.500		
21. 6.	MISCELLANEOUS BUILDINGS		87.178	
21. 7.	VENTILATION STACK		.800	
21.98.	SPARE PARTS ALLOWANCE			
21.99.	CONTINGENCY ALLOWANCE		28.234	
21.	STRUCTURES & SITE FACILITIES			216.458
22. 1. 1. 1	BREEDING MATERIAL(INCL. TRITIUM BREEDING)	3.299		
22. 1. 1. 2	FIRST WALL & STRUCTURAL MATERIAL	22.127		
22. 1. 1. 3.	ATTENUATORS, REFLECTORS, & MULTIPLIERS			
22. 1. 1. 4	WALL MODIFIERS(COATINGS, LINERS, LIMITERS, ETC.)	0.000		
22. 1. 1. 5.	OTHERS			
22. 1. 1.	BLANKET & FIRST WALL		25.426	
22. 1. 2. 1.	PRIMARY			
22. 1. 2. 2	SECONDARY	16.592		
22. 1. 2.	SHIELD		16.592	
22. 1. 3. 1	PRINCIPAL FIELD MAGNET	38.838		
22. 1. 3. 2	SECONDARY FIELD MAGNET	28.037		
22. 1. 3.	MAGNETS		66.875	
22. 1. 4. 1.	BEAM HEATING(NEUTRAL, ION OR ELECTRON)			
22. 1. 4. 2.	RF HEATING			
22. 1. 4. 3.	LASER HEATING			
22. 1. 4. 4.	OTHER HEATING SYSTEMS			
22. 1. 4.	SUPPLEMENTAL HEATING SYSTEMS		0.000	
22. 1. 5. 1.	REACTOR STRUCTURE			
22. 1. 5. 2.	EQUIPMENT SUPPORT STRUCTURE			
22. 1. 5.	PRIMARY STRUCTURE & SUPPORT		12.830	
22. 1. 6. 1.	PLASMA CHAMBER VACUUM(INCL. PUMPS/COMP./PIPE)			
22. 1. 6. 2.	MAGNET DEWAR VACUUM(INCL. PUMPS/COMP./PIPE)			
22. 1. 6. 3.	SUPPLEMENTAL HEATING VACUUM(INCL. PUMPS/COMP./PIPE)			
22. 1. 6. 4.	DIRECT CONVERTOR VACUUM(INCL. PUMPS/COMP./PIPE)			
22. 1. 6. 5.	REACTOR VACUUM SYSTEM(LOW GRADE)			
22. 1. 6. 6.	REACTOR VACUUM WALL			
22. 1. 6.	REACTOR VACUUM SYSTEMS(UNLESS INTEGRAL ELSEWHERE)		18.665	
22. 1. 7. 1	HEATING	0.000		
22. 1. 7. 2	CONFINEMENT	117.600		
22. 1. 7. 3	CONTROL SYSTEM	0.000		
22. 1. 7. 4	CENTRAL ENERGY STORAGE	0.000		
22. 1. 7. 5	OTHER	0.000		
22. 1. 7.	POWER SUPPLY, SWITCHING & ENERGY STORAGE		117.600	
22. 1. 8.	IMPURITY CONTROL			
22. 1. 9. 1.	VACUUM TANK			
22. 1. 9. 2.	DIRECT CONVERTOR MODULES			
22. 1. 9. 3.	THERMAL PANELS			
22. 1. 9. 4.	POWER CONDITIONING EQUIPMENT			
22. 1. 9.	DIRECT ENERGY CONVERSION SYSTEM		0.000	
22. 1.	REACTOR EQUIPMENT			257.988

22. 2. 1. 1.	PUMPS & MOTOR DRIVES(MODULAR & NONMODULAR)			
22. 2. 1. 2.	PIPING			
22. 2. 1. 3.	HEAT EXCHANGERS			
22. 2. 1. 4.	TANKS(INCL. DUMP,MAKE-UP,CLEAN-UP,TRIT.,HOT STORAGE)			
22. 2. 1. 5.	CLEAN-UP SYSTEM			
22. 2. 1. 6.	THERMAL INSULATION, PIPING & EQUIPMENT			
22. 2. 1. 7.	TRITIUM EXTRACTION			
22. 2. 1.	PRIMARY COOLANT SYSTEM			
22. 2. 2. 1	PUMPS & MOTOR DRIVES(MODULAR & NONMODULAR)	0.000		
22. 2. 2. 2	PIPING	0.000		
22. 2. 2. 3	HEAT EXCHANGERS	0.000		
22. 2. 2. 4	TANKS(INCL. DUMP,MAKE-UP,CLEAN-UP,TRIT.,HOT STORAGE)	0.000		
22. 2. 2. 5	CLEAN-UP SYSTEM	0.000		
22. 2. 2. 6	THERMAL INSULATION, PIPING & EQUIPMENT	0.000		
22. 2. 2. 7	TRITIUM EXTRACTION	0.000		
22. 2. 2.	INTERMEDIATE COOLANT SYSTEM		0.000	
22. 2.	MAIN HEAT TRANSFER & TRANSPORT SYSTEMS			
22. 3. 1. 1.	REFRIGERATION			
22. 3. 1. 2.	PIPING			
22. 3. 1. 3.	FLUID CIRCULATION DRIVING SYSTEM			
22. 3. 1. 4.	TANKS			
22. 3. 1. 5.	PURIFICATION			
22. 3. 1.	MAGNET COOLING SYSTEM		36.000	
22. 3. 2. 1.	REFRIGERATION			
22. 3. 2. 2.	PIPING			
22. 3. 2. 3.	FLUID CIRCULATION DRIVING SYSTEM			
22. 3. 2. 4.	TANKS			
22. 3. 2. 5.	PURIFICATION			
22. 3. 2.	SHIELD & STRUCTURE COOLING SYSTEM		2.010	
22. 3. 3. 1.	REFRIGERATION			
22. 3. 3. 2.	PIPING			
22. 3. 3. 3.	FLUID CIRCULATION DRIVING SYSTEM			
22. 3. 3. 4.	TANKS			
22. 3. 3. 5.	PURIFICATION			
22. 3. 3.	SUPPLEMENTAL HEATING SYSTEM COOLING SYSTEM			
22. 3. 4. 1.	REFRIGERATION			
22. 3. 4. 2.	PIPING			
22. 3. 4. 3.	FLUID CIRCULATION DRIVING SYSTEM			
22. 3. 4. 4.	TANKS			
22. 3. 4. 5.	PURIFICATION			
22. 3. 4.	POWER SUPPLY COOLING SYSTEM			
22. 3. 5.	OTHER COOLING SYSTEMS			
22. 3.	AUXILIARY COOLING SYSTEMS			38.010
22. 4. 1.	LIQUID WASTE PROCESSING & EQUIPMENT			
22. 4. 2.	GASEOUS WASTES & OFF-GAS PROCESSING SYSTEM			
22. 4. 3.	SOLID WASTE PROCESSING EQUIPMENT			
22. 4.	RADIOACTIVE WASTE TREATMENT & DISPOSAL			6.900
22. 5. 1.	FUEL PURIFICATION SYSTEMS			
22. 5. 2.	LIQUEFACTION			
22. 5. 3.	FUEL PREPARATION			
22. 5. 4.	FUEL INJECTION			
22. 5. 5.	FUEL STORAGE			
22. 5. 6.	TRITIUM RECOVERY			
22. 5. 7.	EMERGENGY AIR DETRITIATION			
22. 5.	FUEL HANDLING & STORAGE SYSTEMS(FUEL INJECTION)			1.080
22. 6. 1. 1.	BLANKET & COIL MAINTENANCE EQUIPMENT			
22. 6. 1. 2.	COMPONENTS ROTATED INTO SERVICE TO ALLOW MAINT.			
22. 6. 1. 3.	OTHER MAINTENANCE EQUIPMENT			
22. 6. 1.	MAINTENANCE EQUIPMENT			
22. 6. 2.	SPECIAL HEATING SYSTEMS(START-UP,TRACE, ETC.)			
22. 6. 3.	COOLANT RECEIVING, STORAGE & MAKE-UP SYSTEMS			
22. 6. 4.	GAS SYSTEMS			
22. 6. 5.	BUILDING VACUUM SYSTEMS			
22. 6.	OTHER REACTOR PLANT EQUIPMENT			10.950
22. 7. 1.	REACTOR I&C EQUIPMENT(BURN CONTROL, DIAGNOSTICS, ETC.)			
22. 7. 2.	RADIATION MONITORING SYSTEMS			
22. 7. 3.	ISOLATED INDICATING & RECORDING GAUGES, ETC.			
22. 7.	INSTRUMENTATION & CONTROL(I&C)			16.000
22.98.	SPARE PARTS ALLOWANCE			18.546
22.99.	CONTINGENCY ALLOWANCE			49.639
22.	REACTOR PLANT EQUIPMENT			397.114

23. 1. 1.	TURBINE-GENERATORS & ACCESSORIES		
23. 1. 2.	FOUNDATIONS		
23. 1. 3.	STANDBY EXCITERS		
23. 1. 4.	LUBRICATING SYSTEM		
23. 1. 5.	GAS SYSTEMS		
23. 1. 6.	REHEATERS		
23. 1. 7.	SHIELDING		
23. 1. 8.	WEATHER-PROOF HOUSING		
23. 1.	TURBINE-GENERATORS	53.700	
23. 2. 1.	WATER INTAKE COMMON FACILITIES		
23. 2. 2.	CIRCULATING WATER SYSTEMS		
23. 2. 3.	COOLING TOWERS		
23. 2. 4.	OTHER SYSTEMS WHICH REJECT HEAT TO THE ATMOSPHERE		
23. 2.	HEAT REJECTION SYSTEMS	11.190	
23. 3. 1.	CONDENSERS		
23. 3. 2.	CONDENSATE SYSTEM		
23. 3. 3.	GAS REMOVAL SYSTEM		
23. 3. 4.	TURBINE BY-PASS SYSTEMS(EXCL. PIPING)		
23. 3.	CONDENSING SYSTEMS	6.180	
23. 4. 1.	REGENERATORS & RECUPORATORS		
23. 4. 2.	PUMPS		
23. 4. 3.	TANKS		
23. 4.	FEED HEATING SYSTEM	9.180	
23. 5. 1.	TURBINE AUXILIARIES		
23. 5. 2.	AUXILIARIES COOLING SYSTEM(EXCL. PIPING)		
23. 5. 3.	MAKE-UP TREATMENT SYSTEM(EXCL. PIPING)		
23. 5. 4.	CHEMICAL TREATMENT & CONDENSATE PURIFICATION SYSTEMS		
23. 5. 5.	CENTRAL LUBRICATION SERVICE SYSTEM(EXCL. PIPING)		
23. 5. 6.	MAIN STEAM(OR OTHER FLUID) SYSTEM		
23. 5.	OTHER TURBINE PLANT EQUIPMENT	56.400	
23. 6.	INSTRUMENTATION & CONTROL(I&C) EQUIPMENT	1.740	
23.98.	SPARE PARTS ALLOWANCE	.138	
23.99.	CONTINGENCY ALLOWANCE		
23.	TURBINE PLANT EQUIPMENT		138.528
24. 1. 1.	GENERATOR CIRCUITS		
24. 1. 2.	STATION SERVICE		
24. 1.	SWITCHGEAR	3.168	
24. 2. 1.	STATION SERVICE & STARTUP TRANSFORMERS		
24. 2. 2.	LOW VOLTAGE UNIT SUBSTATION & LIGHTING TRANSFORMERS		
24. 2. 3.	BATTERY SYSTEM		
24. 2. 4.	DIESEL ENGINE GENERATORS		
24. 2. 5.	GAS TURBINE GENERATORS		
24. 2. 6.	MOTOR GENERATOR SETS		
24. 2.	STATION SERVICE EQUIPMENT	6.245	
24. 3. 1.	MAIN CONTROL BOARD FOR ELECTRIC SYSTEM		
24. 3. 2.	AUXILIARY POWER & SIGNAL BOARDS		
24. 3.	SWITCHBOARDS (INCL. HEAT TRACING)	2.082	
24. 4. 1.	GEN. STATION GROUNDING SYSTEM & CATHODIC PROTECTION		
24. 4.	PROTECTIVE EQUIPMENT	.072	
24. 5. 1.	CONCRETE CABLE TUNNELS, TRENCHES & ENVELOPES		
24. 5. 2.	CABLE TRAYS & SUPPORT		
24. 5. 3.	CONDUIT		
24. 5. 4.	OTHER STRUCTURES		
24. 5.	ELECTRICAL STRUCTURES & WIRING CONTAINERS	.842	
24. 6. 1.	GENERATOR CIRCUITS WIRING		
24. 6. 2.	STATION SERVICE POWER WIRING		
24. 6. 3.	CONTROL WIRING		
24. 6. 4.	INSTRUMENT WIRING		
24. 6. 5.	CONTAINMENT PENETRATIONS		
24. 6.	POWER & CONTROL WIRING	6.299	
24. 7. 1.	REACTOR BUILDING LIGHTING		
24. 7. 2.	TURBINE BUILDING LIGHTING		
24. 7. 3.	COOLING SYSTEMS STRUCTURES LIGHTING		
24. 7. 4.	POWER SUPPLY & ENERGY STORAGE BUILDING LIGHTING		
24. 7. 5.	MISCELLANEOUS BUILDINGS LIGHTING		
24. 7. 6.	YARD LIGHTING		
24. 7.	ELECTRICAL LIGHTING	38.010	
24.98.	SPARE PARTS ALLOWANCE		
24.99.	CONTINGENCY ALLOWANCE		
24.	ELECTRIC PLANT EQUIPMENT		56.716

25. 1. 1.	CRANES, HOISTS, MONORAILS, & CONVEYORS		
25. 1. 2.	RAILWAY		
25. 1. 3.	ROADWAY EQUIPMENT		
25. 1. 4.	WATERCRAFT		
25. 1. 5.	VEHICLE MAINTENANCE EQUIPMENT		
25. 1.	TRANSPORTATION & LIFTING EQUIPMENT	4.150	
25. 2. 1.	AIR SYSTEMS(EXCL. PIPING)		
25. 2. 2.	WATER SYSTEMS(EXCL. PIPING)		
25. 2. 3.	AUXILIARY HEATING BOILERS(EXCL. PIPING)		
25. 2.	AIR & WATER SERVICE SYSTEMS	7.700	
25. 3. 1.	LOCAL COMMUNICATIONS SYSTEMS		
25. 3. 2.	SIGNAL SYSTEMS		
25. 3.	COMMUNICATIONS EQUIPMENT	.300	
25. 4. 1.	SAFETY EQUIPMENT		
25. 4. 2.	SHOP, LABORATORY, & TEST EQUIPMENT		
25. 4. 3.	OFFICE EQUIPMENT & FURNISHINGS		
25. 4. 4.	CHANGE ROOM EQUIPMENT		
25. 4. 5.	ENVIRONMENTAL MONITORING EQUIPMENT		
25. 4. 6.	DINING FACILITIES		
25. 4.	FURNISHINGS & FIXTURES	.653	
25.98.	SPARE PARTS ALLOWANCE	.640	
25.99.	CONTINGENCY ALLOWANCE	1.920	
25.	MISCELLANEOUS PLANT EQUIPMENT		15.364
26. 1.	REACTOR COOLANT		
26. 2.	INTERMEDIATE COOLANT	0.000	
26. 3.	TURBINE CYCLE WORKING FLUIDS		
26. 4.	OTHER MATERIALS	1.299	
26.98.	SPARE PARTS ALLOWANCE		
26.99.	CONTINGENCY ALLOWANCE		
26.	SPECIAL MATERIALS		1.299

FUSION REACTOR ECONOMIC EVALUATION (VER. 1.3)

DESIGNATION: RFPR - 50/50%DT,S.C. COILS,R=12.7M,RW=1.5M,IZ=20 MA,Q=2.0,F=-1.9,P=2.25 MTORR DATE: 79/04/17.

ACC. NO.	ACCOUNT TITLE	MILLION DOLLARS	
20.	LAND & LAND RIGHTS	2.500	
21.	STRUCTURES & SITE FACILITIES	216.458	
22.	REACTOR PLANT EQUIPMENT	397.114	
23.	TURBINE PLANT EQUIPMENT	138.528	
24.	ELECTRIC PLANT EQUIPMENT	56.716	
25.	MISCELLANEOUS PLANT EQUIPMENT	15.364	
26.	SPECIAL MATERIALS	1.299	
90.	TOTAL REACTOR DIRECT CAPITAL COST		827.979
91. 1.	TEMPORARY FACILITIES		
91. 2.	CONSTRUCTION EQUIPMENT		
91. 3.	CONSTRUCTION SERVICES		
91.	CONSTRUCTION FACILITIES, EQUIPMENT & SERVICES (15%)		124.197
92.	ENGINEERING & CONSTRUCTION MANAGEMENT SERVICES (15%)		124.197
93. 1.	TAXES & INSURANCE		
93. 2.	STAFF TRAINING & PLANT STARTUP		
93. 3.	OWNER'S G&A		
93.	OTHER COSTS (5%)		41.399
94.	INTEREST DURING 10 YEAR CONSTRUCTION (10%/YR. = 84.4%)		719.845
95.	ESCALATION DURING 10 YEAR CONSTRUCTION (5%/YR. = 33.8%)		377.807
99.	TOTAL REACTOR CAPITAL COST		2215.424

THERMAL POWER (MWTH)	= 3000.00	DIRECT INVESTMENT COST ($/KWE)	= 1103.97
GROSS ELECTRIC POWER (MWE)	= 905.00	TOTAL INVESTMENT COST ($/KWE)	= 2953.90
NET ELECTRIC POWER (MWE)	= 750.00	CAPITAL RETURN 15% (MILLS/KWEH)	= 59.75
1/RECIRCULATING POWER FRACTION	= 5.84	OPERATING 2% (MILLS/KWEH)	= 6.55
PLANT FACTOR	= .85	POWER COST (MILLS/KWEH)	= 66.29

COST DATA BASE

DESIGNATION: RFPR - 50/50%DT,S.C. COILS,R=12.7M,RW=1.5M,IZ=20 MA,O=2.0,F=-1.0,P=2.25 MTORR DATE: 79/04/17.

ACC. NO.	ACCOUNT TITLE	UNIT COST		NO. OF UNITS	REFERENCE
20. 1. 0. 0	LAND & PRIVILEGE ACQUISITION	0.		.1000E+01	
20. 2. 0. 0	RELOCATION OF BUILDINGS, UTILITIES, HIGHWAYS, ETC.	0.		.1000E+01	
20. 0. 0. 0	LAND & LAND RIGHTS	.2500E+04	$/ACRE	.1000E+04	1
21. 1. 1. 0	GENERAL YARD IMPROVEMENTS	0.		.1000E+01	
21. 1. 2. 0	WATERFRONT IMPROVEMENTS	0.		.1000E+01	
21. 1. 3. 0	TRANSPORTATION ACCESS (OFF PLOT)	0.		.1000E+01	
21. 1. 0. 0	SITE IMPROVEMENTS & FACILITIES	.1100E+08	$	.1000E+01	2
21. 2. 1. 0	BASIC BUILDING STRUCTURES	.8200E+03	$/M3	.5683E+05	3,4,5
21. 2. 2. 0	BUILDING SERVICES	.8000E+02	$/M3	.5683E+05	3,4,5
21. 2. 3. 0	CONTAINMENT STRUCTURES	0.		.1000E+01	
21. 2. 0. 0	REACTOR BUILDING	0.		.1000E+01	
21. 3. 1. 0	BASIC BUILDING STRUCTURES	.1010E+03	$/M3	.1600E+06	6,7
21. 3. 2. 0	BUILDING SERVICES	.9000E+01	$/M3	.1600E+06	6,7
21. 3. 0. 0	TURBINE BUILDING	0.		.1000E+01	
21. 4. 1. 0	INTAKE STRUCTURES	0.		.1000E+01	
21. 4. 2. 0	DISCHARGE STRUCTURES	0.		.1000E+01	
21. 4. 3. 0	UNPRESSURIZED INTAKE & DISCHARGE CONDUITS	0.		.1000E+01	
21. 4. 4. 0	RECIRCULATING STRUCTURES	0.		.1000E+01	
21. 4. 5. 0	COOLING TOWER SYSTEMS	0.		.1000E+01	
21. 4. 0. 0	COOLING SYSTEM STRUCTURES	.3500E+04	$/MWTH	.3000E+04	2
21. 5. 1. 0	BASIC BUILDING STRUCTURES	.4500E+03	$/M3	.2000E+05	3
21. 5. 2. 0	BUILDING SERVICES	.5000E+02	$/M3	.2000E+05	3
21. 5. 0. 0	POWER SUPPLY & ENERGY STORAGE BUILDING	0.		.1000E+01	
21. 6. 1. 0	REACTOR AUXILIARIES BUILDING(INCL. SWITCHGEAR BAY)	.5000E+03	$/M3	.1250E+06	3
21. 6. 2. 0	RADIOACTIVE WASTE BUILDING	.5000E+03	$/M3	.1500E+05	3
21. 6. 3. 0	FUEL STORAGE BUILDING	0.		.1000E+01	
21. 6. 4. 0	CONTROL ROOM BUILDING	.3750E+03	$/M3	.8500E+04	7
21. 6. 5. 0	DIESEL GENERATOR BUILDING	.3750E+03	$/M3	.3800E+04	7
21. 6. 6. 0	ADMINISTRATION BUILDING	.2500E+03	$/M3	.8500E+04	7
21. 6. 7. 0	SERVICE BUILDING	.2500E+03	$/M3	.1000E+05	7
21. 6. 8. 0	HELIUM STORAGE BUILDING	.1100E+03	$/M3	.4000E+04	3
21. 6. 9. 0	MISCELLANEOUS STRUCTURES & BUILDING WORK	.7500E+07	$	.1000E+01	3
21. 6. 0. 0	MISCELLANEOUS BUILDINGS	0.		.1000E+01	
21. 7. 0. 0	VENTILATION STACK	.8000E+06	$	.1000E+01	3
21.98. 0. 0	SPARE PARTS ALLOWANCE	0.	FRACTION	-.1000E+01	
21.99. 0. 0	CONTINGENCY ALLOWANCE	.1500E+00	FRACTION	-.1000E+01	
21. 0. 0. 0	STRUCTURES & SITE FACILITIES	0.		.1000E+01	
22. 1. 1. 1	BREEDING MATERIAL(INCL. TRITIUM BREEDING)	.7500E+04	$/M3	.4399E+03	8
22. 1. 1. 2	FIRST WALL & STRUCTURAL MATERIAL	.5030E+05	$/M3	.4399E+03	9
22. 1. 1. 3	ATTENUATORS, REFLECTORS, & MULTIPLIERS	0.		.1000E+01	
22. 1. 1. 4	WALL MODIFIERS(COATINGS, LINERS, LIMITERS, ETC.)	0.		0.	
22. 1. 1. 5	OTHERS	0.		.1000E+01	
22. 1. 1. 0	BLANKET & FIRST WALL	0.		.1000E+01	
22. 1. 2. 1	PRIMARY	0.		.1000E+01	
22. 1. 2. 2	SECONDARY	.8000E+04	$/M3	.2074E+04	8
22. 1. 2. 0	SHIELD	0.		.1000E+01	
22. 1. 3. 1	PRINCIPAL FIELD MAGNET	.5300E+03	$/M-50KA	.7328E+05	
22. 1. 3. 2	SECONDARY FIELD MAGNET	.5300E+03	$/M-50KA	.5290E+05	
22. 1. 3. 0	MAGNETS	0.		.1000E+01	
22. 1. 4. 1	BEAM HEATING(NEUTRAL, ION OR ELECTRON)	0.		.1000E+01	
22. 1. 4. 2	RF HEATING	0.		.1000E+01	
22. 1. 4. 3	LASER HEATING	0.		.1000E+01	
22. 1. 4. 4	OTHER HEATING SYSTEMS	0.		.1000E+01	
22. 1. 4. 0	SUPPLEMENTAL HEATING SYSTEMS	0.		0.	
22. 1. 5. 1	REACTOR STRUCTURE	0.		.1000E+01	
22. 1. 5. 2	EQUIPMENT SUPPORT STRUCTURE	0.		.1000E+01	
22. 1. 5. 0	PRIMARY STRUCTURE & SUPPORT	.7900E+05	$/M3	.1624E+03	8
22. 1. 6. 1	PLASMA CHAMBER VACUUM(INCL. PUMPS/COMP./PIPE)	0.		.1000E+01	
22. 1. 6. 2	MAGNET DEWAR VACUUM(INCL. PUMPS/COMP./PIPE)	0.		.1000E+01	
22. 1. 6. 3	SUPPLEMENTAL HEATING VACUUM(INCL. PUMPS/COMP./PIPE)	0.		.1000E+01	
22. 1. 6. 4	DIRECT CONVERTOR VACUUM(INCL. PUMPS/COMP./PIPE)	0.		.1000E+01	
22. 1. 6. 5	REACTOR VACUUM SYSTEM(LOW GRADE)	0.		.1000E+01	
22. 1. 6. 6	REACTOR VACUUM WALL	0.		.1000E+01	
22. 1. 6. 0	REACTOR VACUUM SYSTEMS(UNLESS INTEGRAL ELSEWHERE)	.3300E+05	$/M3	.5656E+03	8
22. 1. 7. 1	HEATING	0.		0.	
22. 1. 7. 2	CONFINEMENT	.8000E-02	$/J	.1470E+11	4,10,11
22. 1. 7. 3	CONTROL SYSTEM	0.		0.	
22. 1. 7. 4	CENTRAL ENERGY STORAGE	0.		0.	
22. 1. 7. 5	OTHER	0.		0.	
22. 1. 7. 0	POWER SUPPLY, SWITCHING & ENERGY STORAGE	0.		.1000E+01	
22. 1. 8. 0	IMPURITY CONTROL	0.		.1000E+01	
22. 1. 9. 1	VACUUM TANK	0.		.1000E+01	
22. 1. 9. 2	DIRECT CONVERTOR MODULES	0.		.1000E+01	
22. 1. 9. 3	THERMAL PANELS	0.		.1000E+01	
22. 1. 9. 4	POWER CONDITIONING EQUIPMENT	0.		.1000E+01	
22. 1. 9. 0	DIRECT ENERGY CONVERSION SYSTEM	0.		0.	
22. 1. 0. 0	REACTOR EQUIPMENT	0.		.1000E+01	
22. 2. 1. 1	PUMPS & MOTOR DRIVES(MODULAR & NONMODULAR)	0.		.1000E+01	
22. 2. 1. 2	PIPING	0.		.1000E+01	
22. 2. 1. 3	HEAT EXCHANGERS	0.		.1000E+01	
22. 2. 1. 4	TANKS(INCL. DUMP,MAKE-UP,CLEAN-UP,TRIT.,HOT STORAGE)	0.		.1000E+01	
22. 2. 1. 5	CLEAN-UP SYSTEM	0.		.1000E+01	
22. 2. 1. 6	THERMAL INSULATION, PIPING & EQUIPMENT	0.		.1000E+01	
22. 2. 1. 7	TRITIUM EXTRACTION	0.		.1000E+01	
22. 2. 1. 0	PRIMARY COOLANT SYSTEM	0.		.1000E+01	
22. 2. 2. 1	PUMPS & MOTOR DRIVES(MODULAR & NONMODULAR)	0.		0.	
22. 2. 2. 2	PIPING	0.		0.	
22. 2. 2. 3	HEAT EXCHANGERS	0.		0.	
22. 2. 2. 4	TANKS(INCL. DUMP,MAKE-UP,CLEAN-UP,TRIT.,HOT STORAGE)	0.		0.	
22. 2. 2. 5	CLEAN-UP SYSTEM	0.		0.	

22. 2. 2. 6	THERMAL INSULATION, PIPING & EQUIPMENT	0.		0.	
22. 2. 2. 7	TRITIUM EXTRACTION	0.		0.	
22. 2. 2. 0	INTERMEDIATE COOLANT SYSTEM	0.		0.	
22. 2. 0. 0	MAIN HEAT TRANSFER & TRANSPORT SYSTEMS	0.		.1000E+01	
22. 3. 1. 1	REFRIGERATION	0.		.1000E+01	
22. 3. 1. 2	PIPING	0.		.1000E+01	
22. 3. 1. 3	FLUID CIRCULATION DRIVING SYSTEM	0.		.1000E+01	
22. 3. 1. 4	TANKS	0.		.1000E+01	
22. 3. 1. 5	PURIFICATION	0.		.1000E+01	
22. 3. 1. 0	MAGNET COOLING SYSTEM	.3600E+08		.1000E+01	3
22. 3. 2. 1	REFRIGERATION	0.		.1000E+01	
22. 3. 2. 2	PIPING	0.		.1000E+01	
22. 3. 2. 3	FLUID CIRCULATION DRIVING SYSTEM	0.		.1000E+01	
22. 3. 2. 4	TANKS	0.		.1000E+01	
22. 3. 2. 5	PURIFICATION	0.		.1000E+01	
22. 3. 2. 0	SHIELD & STRUCTURE COOLING SYSTEM	.6700E+03 $/MWTH		.3000E+04	2
22. 3. 3. 1	REFRIGERATION	0.		.1000E+01	
22. 3. 3. 2	PIPING	0.		.1000E+01	
22. 3. 3. 3	FLUID CIRCULATION DRIVING SYSTEM	0.		.1000E+01	
22. 3. 3. 4	TANKS	0.		.1000E+01	
22. 3. 3. 5	PURIFICATION	0.		.1000E+01	
22. 3. 3. 0	SUPPLEMENTAL HEATING SYSTEM COOLING SYSTEM	0.		.1000E+01	
22. 3. 4. 1	REFRIGERATION	0.		.1000E+01	
22. 3. 4. 2	PIPING	0.		.1000E+01	
22. 3. 4. 3	FLUID CIRCULATION DRIVING SYSTEM	0.		.1000E+01	
22. 3. 4. 4	TANKS	0.		.1000E+01	
22. 3. 4. 5	PURIFICATION	0.		.1000E+01	
22. 3. 4. 0	POWER SUPPLY COOLING SYSTEM	0.		.1000E+01	
22. 3. 5. 0	OTHER COOLING SYSTEMS	0.		.1000E+01	
22. 3. 0. 0	AUXILIARY COOLING SYSTEMS	0.		.1000E+01	
22. 4. 1. 0	LIQUID WASTE PROCESSING & EQUIPMENT	0.		.1000E+01	
22. 4. 2. 0	GASEOUS WASTES & OFF-GAS PROCESSING SYSTEM	0.		.1000E+01	
22. 4. 3. 0	SOLID WASTE PROCESSING EQUIPMENT	0.		.1000E+01	
22. 4. 0. 0	RADIOACTIVE WASTE TREATMENT & DISPOSAL	.2300E+04 $/MWTH		.3000E+04	3
22. 5. 1. 0	FUEL PURIFICATION SYSTEMS	0.		.1000E+01	
22. 5. 2. 0	LIQUEFACTION	0.		.1000E+01	
22. 5. 3. 0	FUEL PREPARATION	0.		.1000E+01	
22. 5. 4. 0	FUEL INJECTION	0.		.1000E+01	
22. 5. 5. 0	FUEL STORAGE	0.		.1000E+01	
22. 5. 6. 0	TRITIUM RECOVERY	0.		.1000E+01	
22. 5. 7. 0	EMERGENCY AIR DETRITIATION	0.		.1000E+01	
22. 5. 0. 0	FUEL HANDLING & STORAGE SYSTEMS(FUEL INJECTION)	.3800E+03 $/MWTH		.3000E+04	3
22. 6. 1. 1	BLANKET & COIL MAINTENANCE EQUIPMENT	0.		.1000E+01	
22. 6. 1. 2	COMPONENTS ROTATED INTO SERVICE TO ALLOW MAINT.	0.		.1000E+01	
22. 6. 1. 3	OTHER MAINTENANCE EQUIPMENT	0.		.1000E+01	
22. 6. 1. 0	MAINTENANCE EQUIPMENT	0.		.1000E+01	
22. 6. 2. 0	SPECIAL HEATING SYSTEMS(START-UP,TRACE, ETC.)	0.		.1000E+01	
22. 6. 3. 0	COOLANT RECEIVING, STORAGE & MAKE-UP SYSTEMS	0.		.1000E+01	
22. 6. 4. 0	GAS SYSTEMS	0.		.1000E+01	
22. 6. 5. 0	BUILDING VACUUM SYSTEMS	0.		.1000E+01	
22. 6. 0. 0	OTHER REACTOR PLANT EQUIPMENT	.3650E+04 $/MWTH		.3000E+04	2
22. 7. 1. 0	REACTOR I&C EQUIPMENT(BURN CONTROL, DIAGNOSTICS, ETC.)	0.		.1000E+01	
22. 7. 2. 0	RADIATION MONITORING SYSTEMS	0.		.1000E+01	
22. 7. 3. 0	ISOLATED INDICATING & RECORDING GAUGES, ETC.	0.		.1000E+01	
22. 7. 0. 0	INSTRUMENTATION & CONTROL(I&C)	.1600E+08 $		.1000E+01	2
22.98. 0. 0	SPARE PARTS ALLOWANCE	.5000E-01 FRACTION		-.1000E+01	
22.99. 0. 0	CONTINGENCY ALLOWANCE	.1500E+00 FRACTION		-.1000E+01	
22. 0. 0. 0	REACTOR PLANT EQUIPMENT	0.		.1000E+01	
23. 1. 1. 0	TURBINE-GENERATORS & ACCESSORIES	0.		.1000E+01	
23. 1. 2. 0	FOUNDATIONS	0.		.1000E+01	
23. 1. 3. 0	STANDBY EXCITERS	0.		.1000E+01	
23. 1. 4. 0	LUBRICATING SYSTEM	0.		.1000E+01	
23. 1. 5. 0	GAS SYSTEMS	0.		.1000E+01	
23. 1. 6. 0	REHEATERS	0.		.1000E+01	
23. 1. 7. 0	SHIELDING	0.		.1000E+01	
23. 1. 8. 0	WEATHER-PROOF HOUSING	0.		.1000E+01	
23. 1. 0. 0	TURBINE-GENERATORS	.1790E+05 $/MWTH		.3000E+04	2
23. 2. 1. 0	WATER INTAKE COMMON FACILITIES	0.		.1000E+01	
23. 2. 2. 0	CIRCULATING WATER SYSTEMS	0.		.1000E+01	
23. 2. 3. 0	COOLING TOWERS	0.		.1000E+01	
23. 2. 4. 0	OTHER SYSTEMS WHICH REJECT HEAT TO THE ATMOSPHERE	0.		.1000E+01	
23. 2. 0. 0	HEAT REJECTION SYSTEMS	.3730E+04 $/MWTH		.3000E+04	2
23. 3. 1. 0	CONDENSERS	0.		.1000E+01	
23. 3. 2. 0	CONDENSATE SYSTEM	0.		.1000E+01	
23. 3. 3. 0	GAS REMOVAL SYSTEM	0.		.1000E+01	
23. 3. 4. 0	TURBINE BY-PASS SYSTEMS(EXCL. PIPING)	0.		.1000E+01	
23. 3. 0. 0	CONDENSING SYSTEMS	.2060E+04 $/MWTH		.3000E+04	2
23. 4. 1. 0	REGENERATORS & RECUPORATORS	0.		.1000E+01	
23. 4. 2. 0	PUMPS	0.		.1000E+01	
23. 4. 3. 0	TANKS	0.		.1000E+01	
23. 4. 0. 0	FEED HEATING SYSTEM	.3060E+04 $/MWTH		.3000E+04	2
23. 5. 1. 0	TURBINE AUXILIARIES	0.		.1000E+01	
23. 5. 2. 0	AUXILIARIES COOLING SYSTEM(EXCL. PIPING)	0.		.1000E+01	

23. 5. 3. 0	MAKE-UP TREATMENT SYSTEM(EXCL. PIPING)	0.		.1000E+01	
23. 5. 4. 0	CHEMICAL TREATMENT & CONDENSATE PURIFICATION SYSTEMS	0.		.1000E+01	
23. 5. 5. 0	CENTRAL LUBRICATION SERVICE SYSTEM(EXCL. PIPING)	0.		.1000E+01	
23. 5. 6. 0	MAIN STEAM(OR OTHER FLUID) SYSTEM	0.		.1000E+01	
23. 5. 0. 0	OTHER TURBINE PLANT EQUIPMENT	.1880E+05	$/MWTH	.3000E+04	2
23. 6. 0. 0	INSTRUMENTATION & CONTROL(I&C) EQUIPMENT	.5800E+03	$/MWTH	.3000E+04	2
23.98. 0. 0	SPARE PARTS ALLOWANCE	.1000E-02	FRACTION	-.1000E+01	2
23.99. 0. 0	CONTINGENCY ALLOWANCE	0.	FRACTION	-.1000E+01	2
23. 0. 0. 0	TURBINE PLANT EQUIPMENT	0.		.1000E+01	
24. 1. 1. 0	GENERATOR CIRCUITS	0.		.1000E+01	
24. 1. 2. 0	STATION SERVICE	0.		.1000E+01	
24. 1. 0. 0	SWITCHGEAR	.3500E+04	$/MWEG	.9050E+03	2
24. 2. 1. 0	STATION SERVICE & STARTUP TRANSFORMERS	0.		.1000E+01	
24. 2. 2. 0	LOW VOLTAGE UNIT SUBSTATION & LIGHTING TRANSFORMERS	0.		.1000E+01	
24. 2. 3. 0	BATTERY SYSTEM	0.		.1000E+01	
24. 2. 4. 0	DIESEL ENGINE GENERATORS	0.		.1000E+01	
24. 2. 5. 0	GAS TURBINE GENERATORS	0.		.1000E+01	
24. 2. 6. 0	MOTOR GENERATOR SETS	0.		.1000E+01	
24. 2. 0. 0	STATION SERVICE EQUIPMENT	.6900E+04	$/MWEG	.9050E+03	2
24. 3. 1. 0	MAIN CONTROL BOARD FOR ELECTRIC SYSTEM	0.		.1000E+01	
24. 3. 2. 0	AUXILIARY POWER & SIGNAL BOARDS	0.		.1000E+01	
24. 3. 0. 0	SWITCHBOARDS (INCL. HEAT TRACING)	.2300E+04	$/MWEG	.9050E+03	2
24. 4. 1. 0	GEN. STATION GROUNDING SYSTEM & CATHODIC PROTECTION	0.		.1000E+01	
24. 4. 0. 0	PROTECTIVE EQUIPMENT	.8000E+02	$/MWEG	.9050E+03	2
24. 5. 1. 0	CONCRETE CABLE TUNNELS, TRENCHES & ENVELOPES	0.		.1000E+01	
24. 5. 2. 0	CABLE TRAYS & SUPPORT	0.		.1000E+01	
24. 5. 3. 0	CONDUIT	0.		.1000E+01	
24. 5. 4. 0	OTHER STRUCTURES	0.		.1000E+01	
24. 5. 0. 0	ELECTRICAL STRUCTURES & WIRING CONTAINERS	.9300E+03	$/MWEG	.9050E+03	2
24. 6. 1. 0	GENERATOR CIRCUITS WIRING	0.		.1000E+01	
24. 6. 2. 0	STATION SERVICE POWER WIRING	0.		.1000E+01	
24. 6. 3. 0	CONTROL WIRING	0.		.1000E+01	
24. 6. 4. 0	INSTRUMENT WIRING	0.		.1000E+01	
24. 6. 5. 0	CONTAINMENT PENETRATIONS	0.		.1000E+01	
24. 6. 0. 0	POWER & CONTROL WIRING	.6960E+04	$/MWEG	.9050E+03	2
24. 7. 1. 0	REACTOR BUILDING LIGHTING	0.		.1000E+01	
24. 7. 2. 0	TURBINE BUILDING LIGHTING	0.		.1000E+01	
24. 7. 3. 0	COOLING SYSTEMS STRUCTURES LIGHTING	0.		.1000E+01	
24. 7. 4. 0	POWER SUPPLY & ENERGY STORAGE BUILDING LIGHTING	0.		.1000E+01	
24. 7. 5. 0	MISCELLANEOUS BUILDINGS LIGHTING	0.		.1000E+01	
24. 7. 6. 0	YARD LIGHTING	0.		.1000E+01	
24. 7. 0. 0	ELECTRICAL LIGHTING	.4200E+05	$/MWEG	.9050E+03	2
24.98. 0. 0	SPARE PARTS ALLOWANCE	0.	FRACTION	-.1000E+01	2
24.99. 0. 0	CONTINGENCY ALLOWANCE	0.	FRACTION	-.1000E+01	2
24. 0. 0. 0	ELECTRIC PLANT EQUIPMENT	0.		.1000E+01	
25. 1. 1. 0	CRANES, HOISTS, MONORAILS, & CONVEYORS	0.		.1000E+01	
25. 1. 2. 0	RAILWAY	0.		.1000E+01	
25. 1. 3. 0	ROADWAY EQUIPMENT	0.		.1000E+01	
25. 1. 4. 0	WATERCRAFT	0.		.1000E+01	
25. 1. 5. 0	VEHICLE MAINTENANCE EQUIPMENT	0.		.1000E+01	
25. 1. 0. 0	TRANSPORTATION & LIFTING EQUIPMENT	.4150E+07	$	.1000E+01	2
25. 2. 1. 0	AIR SYSTEMS(EXCL. PIPING)	0.		.1000E+01	
25. 2. 2. 0	WATER SYSTEMS(EXCL. PIPING)	0.		.1000E+01	
25. 2. 3. 0	AUXILIARY HEATING BOILERS(EXCL. PIPING)	0.		.1000E+01	
25. 2. 0. 0	AIR & WATER SERVICE SYSTEMS	.7700E+07	$	.1000E+01	2
25. 3. 1. 0	LOCAL COMMUNICATIONS SYSTEMS	0.		.1000E+01	
25. 3. 2. 0	SIGNAL SYSTEMS	0.		.1000E+01	
25. 3. 0. 0	COMMUNICATIONS EQUIPMENT	.3000E+06	$	.1000E+01	2
25. 4. 1. 0	SAFETY EQUIPMENT	0.		.1000E+01	
25. 4. 2. 0	SHOP, LABORATORY, & TEST EQUIPMENT	0.		.1000E+01	
25. 4. 3. 0	OFFICE EQUIPMENT & FURNISHINGS	0.		.1000E+01	
25. 4. 4. 0	CHANGE ROOM EQUIPMENT	0.		.1000E+01	
25. 4. 5. 0	ENVIRONMENTAL MONITORING EQUIPMENT	0.		.1000E+01	
25. 4. 6. 0	DINING FACILITIES	0.		.1000E+01	
25. 4. 0. 0	FURNISHINGS & FIXTURES	.6530E+06	$	.1000E+01	2
25.98. 0. 0	SPARE PARTS ALLOWANCE	.5000E-01	FRACTION	-.1000E+01	
25.99. 0. 0	CONTINGENCY ALLOWANCE	.1500E+00	FRACTION	-.1000E+01	
25. 0. 0. 0	MISCELLANEOUS PLANT EQUIPMENT	0.		.1000E+01	
26. 1. 0. 0	REACTOR COOLANT	0.		.1000E+01	
26. 2. 0. 0	INTERMEDIATE COOLANT	0.		0.	
26. 3. 0. 0	TURBINE CYCLE WORKING FLUIDS	0.		.1000E+01	
26. 4. 0. 0	OTHER MATERIALS	.4330E+03	$/MWTH	.3000E+04	2
26.98. 0. 0	SPARE PARTS ALLOWANCE	0.	FRACTION	-.1000E+01	
26.99. 0. 0	CONTINGENCY ALLOWANCE	0.	FRACTION	-.1000E+01	
26. 0. 0. 0	SPECIAL MATERIALS	0.		.1000E+01	
90. 0. 0. 0	TOTAL REACTOR DIRECT CAPITAL COST	0.		.1000E+01	1
91. 1. 0. 0	TEMPORARY FACILITIES	0.	FRACTION	-.1000E+01	1
91. 2. 0. 0	CONSTRUCTION EQUIPMENT	0.	FRACTION	-.1000E+01	1
91. 3. 0. 0	CONSTRUCTION SERVICES	0.	FRACTION	-.1000E+01	1
91. 0. 0. 0	CONSTRUCTION FACILITIES, EQUIPMENT & SERVICES (15%)	.1500E+00	FRACTION	-.1000E+01	1
92. 0. 0. 0	ENGINEERING & CONSTRUCTION MANAGEMENT SERVICES (15%)	.1500E+00	FRACTION	-.1000E+01	1
93. 1. 0. 0	TAXES & INSURANCE	0.	FRACTION	-.1000E+01	1
93. 2. 0. 0	STAFF TRAINING & PLANT STARTUP	0.	FRACTION	-.1000E+01	1
93. 3. 0. 0	OWNER'S G&A	0.	FRACTION	-.1000E+01	1
93. 0. 0. 0	OTHER COSTS (5%)	.5000E-01	FRACTION	-.1000E+01	1
94. 0. 0. 0	INTEREST DURING 10 YEAR CONSTRUCTION (10%/YR. = 64.4%)	.6440E+00	FRACTION	-.1000E+01	1
95. 0. 0. 0	ESCALATION DURING 10 YEAR CONSTRUCTION (5%/YR. = 33.8%)	.3380E+00	FRACTION	-.1000E+01	1
99. 0. 0. 0	TOTAL REACTOR CAPITAL COST	0.		.7500E+03	1

Reference List for 1978 Cost Data Base[a]

1. (15.) S. C. Schulte, T. L. Willke, and J. R. Young, "Fusion Reactor Design Studies-Economic Evaluation Guidelines," Battelle Pacific Northwest Laboratories report PNL-SA-2648 (1977).

2. (18.) B. Badger, M. A. Abdou, R. W. Boom, R. G. Brown, T. E. Cheng, and R. W. Conn, "UWMAK-I, A Toroidal Fusion Reactor Design," University of Wisconsin report UWFDM-68 (1975).

3. (19.) B. Badger, R. W. Conn, G. L. Kulcinski, C. W. Maynard, R. Aronstein, and H. I. Avci, "UWMAK-III, A Noncircular Tokamak Power Reactor Design," University of Wisconsin report UWFDM-150 (1976).

4. (20.) R. Hancox, personal communication, Culham, United Kingdom, (1977).

5. (21.) D. J. Bender and G. A. Carlson, "System Model for Analysis of the Mirror Fusion-Fission Reactor," Lawrence Livermore Laboratory report UCRL-52293 (October 1977).

6. (22.) J. C. Scarborough, "Comparative Capital Costs for the Prototype Large Breeder Reactor," NUS Corporation, 4 Research Place, Rockville, Maryland (also presented at the ANS Winter meeting, San Francisco, CA, December 1977).

7. (23.) United Engineers and Constructors, Inc., "Pressurized Water Reactor Plant," WASH-1230, Vol. 1 (June 1972).

8. (24.) B. Badger, G. L. Kulcinski, R. W. Conn, C. W. Maynard, K. Audenaerde, and H. Avci, "Tokamak Engineering Test Reactor," University of Wisconsin report UWFDM-191 (1978).

9. (25.) D. L. Kummer (Principal Investigator), "Alloys for the Fusion Reactor Environment," Prepared by McDonnell Douglas Astronautics Company for Division of Magnetic Fusion Energy, ERDA (April 1977). (Draft)

10. (26.) K. I. Thomassen (Principal Investigator), "Conceptual Engineering Design of a One-GJ Fast Discharging Homopolar Machine for the Reference Theta-Pinch Fusion Reactor," EPRI ER-246, Project 469 (August 1976).

11. (27.) R. E. Stillwagon, "Design Studies of Reversible Energy Storage and Transfer Systems for the Reference Theta-Pinch Reactor," Westinghouse report E.M. 4620 (September 1974).

[a]The numbers in parentheses refer to reference positions with the appendices.

APPENDIX C

STANDARD FUSION REACTOR DESIGN TABLE

This Appendix contains the comprehensive and uniform design table for the RFPR. The format of this table follows exactly the DOE/OFE guidelines.[28]

TABLE OF REACTOR DESIGN PARAMETERS

	PARAMETER	UNIT	VALUE	FOOTNOTE
1.	Characteristic Machine Dimensions			
1.1	Reactor Envelope (vacuum tunnel)			a
1.1.1	Height	m	9.0	
1.1.2	Width	m	9.0	
1.1.3	Length	m	80	
1.2	Plasma Chamber			
1.2.1	Major Radius	m	12.7	
1.2.2	Minor Radius	m	1.5	
1.2.3	Volume	m^3	564	
1.2.4	Inner Surface Area	m^2	752	
2.	Plasma Parameters			
2.1	Plasma Dimensions			a
2.1.1	R, Major Radius	m	12.7	
2.1.2	r_p, Minor Radius	m	1.3	
2.1.3	Plasma Elongation		none	
2.2	n_o, Centerline Density	m^{-3}	$7.4(10)^{20}$	b
2.3	$\bar{n}$, Average Density	m^{-3}	$2.0(10)^{20}$	
2.4	τ_E, Energy Confinement Time	s	1.1	
2.5	τ_e, Electron Confinement Time	s	long	c
2.6	τ_i, Ion Confinement Time	s	long	c
2.7	$n\tau_E$ (Averaged Through Plasma)	s/m^3	$2.2(10)^{20}$	
2.8	$\beta_{\phi o}$, Centerline Toroidal Beta		0.65	d
2.9	$<\beta_\phi>$, Average Toroidal Beta		0.65	e
2.10	$\beta_{\Theta o}$, Centerline Poloidal Beta		1.1	f
2.11	$<\beta_\Theta>$, Average Poloidal Beta		0.30	g
2.12	I_ϕ, Plasma Current	MA	20	
2.13	T_{io}, Centerline Ion Temperature	keV	15	h

	PARAMETER	UNIT	VALUE	FOOTNOTE
2.14	$\bar{T}_i$, Average Ion Temperature	keV	15	
2.15	T_{eo}, Centerline Electron Temperature	keV	16	h
2.16	$\bar{T}_e$, Average Electron Temperature	keV	16	
2.17	Z_{eff}, Effective Plasma Ion Charge		1.0-3.3	i
2.18	q, Plasma Safety Factor		NA	
2.19	Volt-Seconds Requirement	V-s	915	
2.20	Reactor Cycle	Steady-State/Pulsed		j
2.20.1	Burn Pulse Length	s	21.6	
2.20.2	Total Pulse Length	s	26.6	
2.21	Fuel Cycle		50%D-50%T	
2.22	Plasma Heating Method		Ohmic Heating	
2.23	Plasma Heating Power	MW	100-400	k
2.24	Plasma Heating Energy or Frequency	keV or Hz	NA (not applicable)	
2.25	Q_p, Plasma Energy Gain		120	l
3.	Power Output			
3.1	Plasma Power (Peak)	MWt	4700	a
3.2	Plasma Power (Total Cycle Time Average)	MWt	2670	a
3.3	Power to Blanket (Peak)	MWt	4700	
3.4	Power to Blanket (Total Cycle Time Average)	MWt	2670	
3.5	Blanket Power Amplification Factor		1.12	b
3.6	Power to Direct Convertor (Peak)	MWt	NA	
3.7	Power to Direct Convertor (Total Cycle Time Average)	MWt	NA	
3.8	Power to Divertor (Peak)	MWt	NA	
3.9	Power to Divertor (Total Cycle Time Average)	MWt	NA	
3.10	Plasma Chamber Power Density (Total Cycle Time Average)	MW/m^3	5.3	c
3.11	Nuclear Island Power Density (Total Cycle Time Average)	MW/m^3	0.02	c,d
3.12	Plant Gross Electrical Output	MWe	905	

	PARAMETER	UNIT	VALUE	FOOTNOTE
3.13	Plant Net Electrical Output	MWe	750	
3.14	Thermal Cycle Efficiency	%	30	
3.15	Direct Convertor Efficiency	%	NA	
3.16	Net Plant Efficiency	%	25	
4.	Reactor Coolant System			
4.1	Blanket Coolant Type		H_2O	a
4.2	Blanket Outlet Temperature (Hot Leg)-Peak/Average	°C	280/278	
4.3	Blanket Inlet Temperature (Cold Leg)-Peak/Average	°C	110/110	
4.4	Blanket Outlet Pressure-Peak/Average	MPa	5.51	
4.5	Blanket Inlet Pressure-Peak/Average	MPa	5.52	
4.6	Blanket Coolant Flow Rate	kg/s	788	
4.7	Blanket Coolant Pipe Material		Steel	
4.8	First-Wall Coolant Type		H_2O	b
4.9	First-Wall Outlet Temperature-Peak/Average	°C	257/257	
4.10	First-Wall Inlet Temperature-Peak/Average	°C	87/87	
4.11	First-Wall Outlet Pressure-Peak/Average	MPa	5.50/5.50	
4.12	First-Wall Inlet Pressure-Peak/Average	MPa	5.52/5.52	
4.13	First-Wall Coolant Flow Rate	kg/s	1584	
4.14	Total Number of Blanket Coolant Loops		1(40 Modules)	
4.15	Type of Blanket Coolant Circulator		Feedwater Pump	c
4.16	Power Input to Each Circulator	MWe	3	d
4.17	Peak First-Wall/Blanket Temperature in Case of Loss-of-Coolant Flow	°C	NIL INCREASE	e
4.18	Energy Storage	J	$8(10)^9$	f

	PARAMETER	UNIT	VALUE	FOOTNOTE
5.	Intermediate Coolant System		NA	a
5.1	Coolant Type			
5.2	IHX Outlet Temperature (Hot Leg)	°C	NA	
5.3	IHX Inlet Temperature (Cold Leg)	°C	NA	
5.4	IHX Outlet Pressure	MPa	NA	
5.5	IHX Inlet Pressure	MPa	NA	
5.6	Coolant Flow Rate	kg/s	NA	
5.7	Coolant Pipe Material		NA	
5.8	Total Number of Coolant Loops		NA	
5.9	Type of Coolant Circulator		NA	
5.10	Power Input to Each Circulator	MWe	NA	
5.11	Number of IHX Per Loop		NA	
5.12	IHX Material-Shell/Tube		NA	
5.13	Energy Storage	J	NA	
6.	Steam Generation (SG) System			
6.1	Steam Outlet Temperature	°C	Refer to	a
6.2	Steam Outlet Pressure	MPa	Section 4	
6.3	Steam Flow Rate	kg/s	of the table	
6.4	Feedwater Temperature	°C		
6.5	Number of Steam Generators per Loop		NA	
6.6	Number of Modules per SG		NA	
6.7	SG Materials, Shell/Tube		NA	
7.	Shield Coolant System			
7.1	Total Energy Deposited in the Shield	MWt	21	a
7.2	Shield Coolant Type		H_2O/H_2BO_4	
7.3	Shield Outlet Temperature-Peak/ Average	°C	90/90	
7.4	Shield Inlet Temperature-Peak/ Average	°C	30/30	
7.5	Coolant Outlet Pressure-Peak/ Average	MPa	0.1/0.1	

	PARAMETER	UNIT	VALUE	FOOTNOTE
7.6	Coolant Inlet Pressure-Peak/ Average	MPa	0.1/0.1	
7.7	Coolant Flow Rate	kg/s	85	
8.	Reactor Auxiliary Systems			
8.1	Vacuum Pumping System			
8.1.1	Plasma Chamber Pressure	torr	$2.25(10)^{-3}$	
8.1.2	Plasma Chamber Volume	m^3	564	
8.1.3	Number of Pumps		40	a
8.1.4	Capacity of Each Pump	torr-litre/s	56	a
8.2	Magnet Cooling System Cooling Load	Wt	$3(10)^4$	b
8.3	Plasma Heating System Cooling Load	Wt	NA	c
8.4	Plasma Fueling System			
8.4.1	Type		Gas Puff	
8.4.2	Fuel Composition		50%D-50%T	
8.4.3	Fueling Rate	kg/s	$1.5(10)^{-5}$	
8.4.4	Pellet Size (if used)	m	NA	
8.4.5	Pellet Injection Frequency (if used)	s^{-1}	NA	
8.5	Tritium Processing and Recovery System			
8.5.1	Total Tritium Inventory	kg	12	d
8.6	Impurity Control System			
8.6.1	Type		Batch Burn	
9.	Reactor Components			
9.1	Blanket/First Wall	First Wall:AMAX Cu		a
9.1.1	Structural Material	Blanket: Stainless Steel		a
9.1.2	Breeding Material		Li_2O	
9.1.3	Breeding Ratio		1.11	
9.1.4	Number of Modules		40	
9.1.5	Weight of Module	Tonne	60	b
9.1.6	Weight of Largest Single Component	Tonne	4.1	c
9.1.7	Dimensions of Largest Component	m x m x m	3-m diam x 2-m long	c

	PARAMETER	UNIT	VALUE		FOOTNOTE
9.1.8	First-Wall Loading (Peak/ Average				
9.1.8.1	14.1-MeV Neutrons	MW/m^2	5.0/2.8		
9.1.8.2	Alpha Particle Flux	MW/m^2	1.24/0.68		
9.1.8.3	Electromagnetic Radiation	MW/m^2	0.19/0.12		
9.1.8.4	Plasma Thermal Conduction	MW/m^2	1.2/0.59		
9.1.8.5	First-Wall Life	$MW-y/m^2$	15		
9.2	Shielding				
9.2.1	Material	0.1-m Pb/1.5-m	H_2O/H_2BO_4		d
9.2.2	Number of Modules		80		
9.2.3	Weight of each Module	Tonne	75 w H_2O		
9.2.4	Weight of Largest Single Component	Tonne	50 w/o H_2O		
9.2.5	Dimensions of Largest Component	m x m x m	Hemi-cylindrical shield tank: 7-m o.d. x 4-m i.d. x 2-m long		
9.3	Magnets				
			Poloidal	Toroidal	
9.3.1	Superconducting	yes/no	yes		
9.3.2	Conductor Material		15:1/Cu:NbTi		
9.3.3	Structural Material		Stainless Steel		
9.3.4	Operating Temperature	K	4		
9.3.5	Coolant		Helium		
9.3.6	Maximum Stress in Coil	N/m^2	$2.8(10)^8$	$1.3(10)^8$	e
9.3.7	Maximum Force Transmitted to Building	N/m^2	$1.6(10)^6$	$1.6(10)^6$	e
9.3.8	Maximum Field	T	2	2	
9.3.9	Field on Axis	T	0	3.8	f
9.3.10	Number of Magnets		52	20	g
9.3.11	Field Ripple-Plasma Edge	%	0.3	0.5	
9.3.12	Stored Energy	J	$1.1(10)^{10}$	$3.7(10)^9$	
9.4	Energy Transfer and Storage				
9.4.1	Plasma Preparation		NA		h
9.4.1.1	Type		NA		
9.4.1.2	Energy Per Unit	MJ	NA		
9.4.1.3	Total Energy	MJ	NA		

	PARAMETER	UNIT	VALUE		FOOTNOTE
9.4.1.4	Peak Power Transfer Rate	W	NA		
9.4.1.5	Transfer Time	s	NA		
9.4.1.6	Depth of Discharge	%	NA		
9.4.1.7	Recharge Time	s	NA		
9.4.1.8	Pulse Frequency	s^{-1}	NA		
9.4.1.9	Switching Requirements		NA		
9.4.1.9.1	Current	A	NA		
9.4.1.9.1	Volts	V	NA		
9.4.1.9.3	Number		NA		
9.4.2	Primary Power Supply		Poloidal	Toroidal	
9.4.2.1	Type				
9.4.2.2	Energy Per Unit	GJ	1.85	1.85	
9.4.2.3	Total Energy	GJ	3.7	11.1	
9.4.2.4	Transfer Time	s	0.1	0.1	
9.4.2.5	Recharge Time	s	26.6	26.6	i
9.4.2.6	Pulse Frequency	s^{-1}	0.075	0.075	j
9.4.2.7	Switching Requirements				k
9.4.2.7.1	Current	A	$25(10)^3$	$25(10)^3$	
9.4.2.7.2	Volts	V	$21(10)^3$	$21(10)^3$	
9.4.2.7.3	Number	Opening	600	450	
		Closing	1200	450	

10.	Electrical Power Requirements			
10.1	Cold Start Power from Grid	MWe vs s	200 vs 75	
10.2	Auxiliary Power Requirements (Normal Operation)	MWe	155	
10.2.1	Electrical Energy Storage	MWe	See 10.2.2	
10.2.2	Magnet Power Supply (Other than Energy Storage)	MWe	112	a
10.2.3	Blanket Circulators	MWe	NA	
10.2.4	First Wall Coolant Circulators	MWe	NA	
10.2.5	Shield Coolant Circulators	MWe	nil	
10.2.6	Refrigeration System	MWe	9	
10.2.7	Vacuum System	MWe	6	
10.2.8	Plasma Heating System	MWe	NA	

	PARAMETER	UNIT	VALUE	FOOTNOTE
10.2.9	Miscellaneous Reactor Plant Auxiliaries	MWe	4	
10.2.10	Feed Pump System	MWe	3	
10.2.11	Condensing System	MWe	2	
10.2.12	Heat Rejection System	MWe	9	
10.2.13	Misc. BOP Auxiliaries	MWe	10	
11.	Buildings			
11.1	Reactor Building		23-m radius	
11.1.1	Characteristic Dimensions	m x m x m	x 35-m high	
11.1.2	Enclosed Volume	m^3	$5.7(10)^4$	
11.1.3	Minimum Wall Thickness for Shielding	m	2	
11.1.4	Internal Pressure, Normal/ Accident	MPa	0.1/0.2	a
11.1.5	Containment Atmosphere		Argon	
11.2	Electrical Energy Storage Building			
11.2.1	Characteristics Dimensions	m x m x m	10-m high x 16-m x 120-m	
11.2.2	Wall Thickness for Shielding	m	1	
11.2.3	Internal Pressure, Normal/ Accident	MPa	0.1/0.1	
11.2.4	Safety Related or Not (e.g., Is it a containment building?)	Yes/No	No	
11.3	Reactor Service Building			
11.3.1	Characteristic Dimensions	m x m x m	16-m high x 16-m x 340-m	b
11.3.2	Special Functions (i.e., hot cells, blanket processing equipment, etc.)	Tritium handling, radwaste, hot cells, cryogenics and helium storage, maintenance and storage		
12.	Reactor Maintenance			
12.1	Blanket/First Wall Replacement	% Surface Area/y Tonne/y	15 360	a
12.2	Radioactive Material Storage Requirement, Years/Volume	y/m^3	10/4000	

Footnotes for Reactor Design Table

1. Characteristic Machine Dimensions

[a]The vacuum tunnel encloses the toroidal field coils and has the dimensions given with an average length of 80 m (at the major toroidal radius of 12.7 m.

2. Plasma Parameters

[a]All quoted plasma parameters are time averaged over the 21.6-s plasma burn period.

[b]Bessel function model used assuming an isothermal plasma.

[c]Classical particle confinement times during the burn are $\sim 10^3$ s. Trapped-particle effects should be small, and the particle confinement time is assumed long with essentially no particles lost during the burn.

[d]Uses time-averaged particle densities and toroidal field pressures on axis for the Bessel function model.

[e]The plasma energy divided by the toroidal field energy (both time averaged) trapped inside the plasma.

[f]The centerline particle pressure divided by the poloidal field pressure (both time averaged) at the plasma edge using the Bessel function model.

[g]The average particle pressure divided by the poloidal field pressure (both time averaged) at the plasma edge.

[h]The plasma has been assumed isothermal in the radial direction.

[i]The buildup of alpha particles during the 21.6-s batch burn increases Z_{eff} from 1 to 3.3, assuming complete confinement.

[j]Only the plasma and first wall operate in a pulsed mode (21.6-s burn and 26.6 s cycle). All thermal systems outside the first wall operate steady state.

[k]Ohmic heating is inherent to the confinement scheme with no auxiliary sources required. As the plasma heats from 1 to 4 keV and ignites, the total ohmic power to the plasma varies from 400 to 100 MW.

[l]Integrated alpha-particle plus 14.1-MeV neutron output divided by the time-averaged ohmic heating input.

3. Power Output

[a]Blanket amplification not included.

[b]Neutron worth computed to be 16.3 MeV/neutron for the water-cooled Li_2O blanket.

[c]Uses the total thermal output of 3000 MWt.

[d]The "Nuclear Island" is defined as everything covered by Account No. 22 in the cost accounting summary (See Appendix B).

4. Reactor Coolant System

[a]Granular Li_2O is packed around an array of high pressure steam tubes which extract the thermal energy from blanket. This is a superheated steam cycle with dry steam generated in the blanket being fed directly to the turbine, and is analogous to a coal-fired power plant.

[b]The first wall is cooled by an H_2O coolant stream that is separate from the blanket.

[c]No intermediate loops are used and the first wall and blanket coolant flow is provided directly by the feedwater pumps.

[d]Total for first wall and blanket loops.

[e]The heat loss through the insulating annulus (0.01 m) between the high-temperature blanket and the shield (90 C) is ~ 0.01 of the total thermal power which exceeds the radiation produced blanket afterheat. The blanket temperature should not increase above the normal operating temperature during a loss-of-coolant flow if the reactor is immediately shutdown.

[f]The total thermal energy stored in both first wall and blanket coolant loops.

5. Intermediate Coolant System

[a]None required in this single-loop direct-cycle system.

6. Steam Generation System

[a]Steam is generated directly by the RFPR blanket.

7. Shield Coolant System

[a]An annular tank of 7-m o.d. × 4-m i.d. x 2-m long filled with borated water acts as the shield for the superconducting coils. The pumping power required to cool this large pool of water is insignificant.

8. Reactor Auxiliary Systems

[a]Roots blowers with a pumping speed of 25,000 l/s have a capacity of 56 torr-litre/s when pumping on the $2.25(10)^{-3}$ torr vacuum. One roots blower is required for each 2-m module. The possible use of cryopumps is also discussed in the text. (Sec. V.E.2).

[b]Taking a refrigeration efficiency of $3.3(10)^{-3}$ gives a total required electric power of 9 MW to drive the magnet cryogenic system.

[c]The current flowing in the plasma induced by the magnet coils heats the plasma to ignition.

[d]This estimate is based upon a one month supply of tritium. Considerable uncertainty exists in the estimated tritium inventory retained in the Li_2O blanket (Sec. V.D.2).

9. Reactor Components

[a]The first wall is a 2-cm thick × 3-m diam. × 2-m long structure consisting of AMAX (0.06% Mg, 0.15% Zr, 0.4% Cr, balance Cu) copper. The granular Li_2O blanket (0.5-m thick), which is cooled by high-pressure water tubes, is located immediately outside the first wall.

[b]The copper first wall and blanket (2-m long × 3-m i.d. × 4-m o.d.) is constructed as a single 60-tonne unit.

[c]After removing the first-wall/blanket module from the reactor and subsequent dismantling, the largest single component is expected to be the first wall.

[d]Two borated water shield tanks are required for each 2-m long first wall/blanket module requiring a total of 80 hemi-cylindrical shield tanks. After draining the hemi-cylindrical shield tanks and lifting the 50-tonne components from the reactor, the first-wall/blanket modules may be removed.

[e]The coil structures are self-supporting against forces directed radially outward or inward from the coil center. Lateral support must be provided by the surrounding building structure with the magnitude estimated by the maximum magnetic field present.

[f]The toroidal field peaks on axis (Bessel function model) and is much less near the coil.

[g]Fifty transformer coils (40 windings carrying 0.72 MA/conductor and 10 carrying 0.33 MA conductor) and two vertical field coils (each carrying 6.75 MA) comprise the poloidal field coil system. Twenty 9-turn toroidal field coils carry 5 MA each (0.56 MA in the lead).

[h]No pre-ionization of the plasma is considered necessary with randomly scattered free electrons sufficient for breakdown. At the starting density of $2(10)^{20}/m^3$ a minimum electric field of 10 V/m is required for breakdown[29] with ~ 100 V/m actually present.

[i]See footnote(a) of the next section (10).

[j]Two cycles during the 26.6 s burn period.

[k]Present day switching elements are used.

10. Electrical Power Requirements

[a]This recirculating power would be supplied continuously from the electric generator. The homopolar motor/generators would be charged by 112 MWe of recirculated power during most (> 98%) of the 26.6-s cycle. Only during the two energy transfer periods of 0.2-s each would the charging process be interrupted. This 0.2-s interruption corresponds to $\lesssim$ 20 MJ (0.17% of the total 12-GJ energy store) of energy which must be shunted elsewhere. This energy could simply be resistively dissipated, however, the inductance of the charging circuit should "absorb" small perturbation with a minimal amount of variation in the electric power being recirculated from the power plant generator.

11. Buildings

[a]Normal operating pressure is slightly less than atmospheric as in the present-day nuclear power plants. The accident condition is assumed to be the loss of primary coolant into the containment building.

[b]The building length of 340 m reflects the total required length and not the actual building dimension.

12. Reactor Maintenance

[a]A material lifetime of 15 MW-yr./m^2 is used for the first wall/blanket module. Taking the reactor wall loading of 2.75 MW/m^2 and a plant availability of 0.85 gives a replacement rate of ~ 360 tonne/yr. This requires a storage volume of ~ 400 m^3 for ~ 10 years (primarily for the radioactive decay of iron) for a total required volume of ~ 4000 m^3.

APPENDIX D

BLANKET TRITIUM TRANSPORT MODEL

Several issues concerning tritium may influence the blanket design and operation. A blanket design that attains tritium self-sufficiency in a reasonable time represents one such issue. Additionally, the time and spatial dependence of the tritium inventory within the Li_2O blanket is related to the issue of tritium release rate. A time-dependent, one-dimensional tritium release model has been developed to address this issue, and this Appendix describes the tritium model and results that have evolved.

1. Development of Model. Figure D-1 illustrates a portion of the

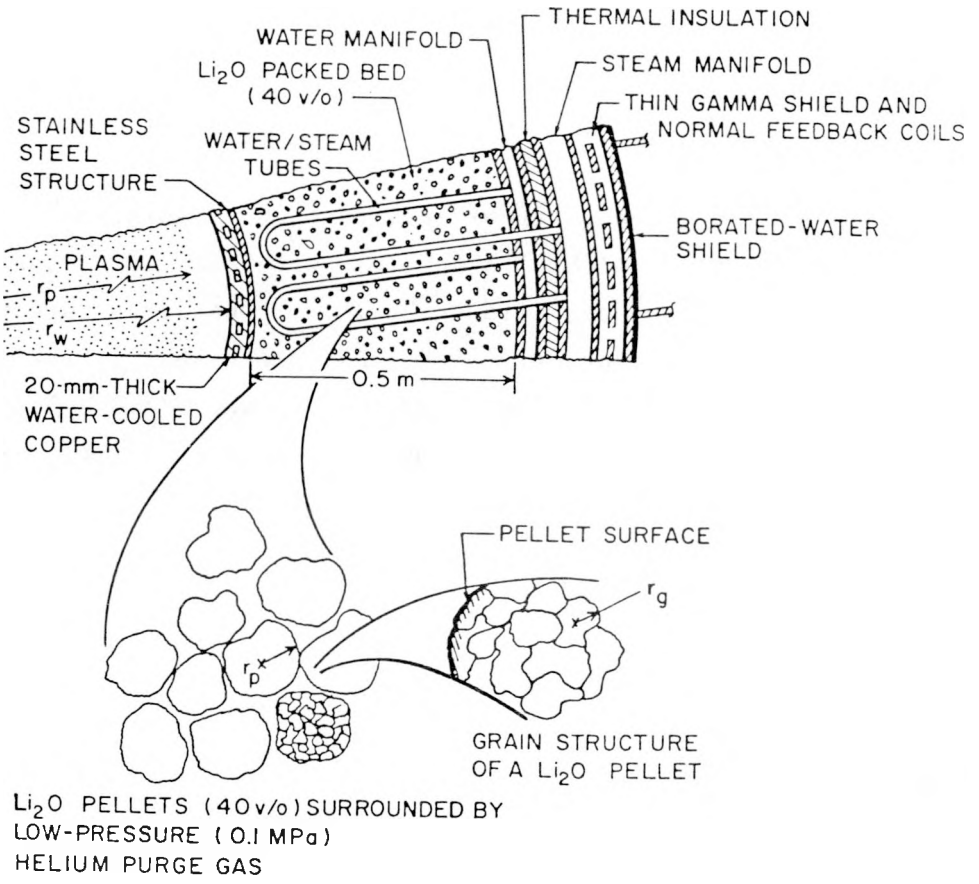

Figure D-1. Lithium-oxide packed-bed blanket illustrating tritium diffusion model used to evaluate release rates and blanket inventories.

blanket/first-wall layout and a magnified view of the Li_2O packed bed in which tritium is bred. The Li_2O pellet is idealized as a sphere of radius r_p that is composed of grains of radius r_g. Tritium being bred within a given grain is released to the ambient He purge gas after a complex sequence of physical chemical processes involving bulk diffusion within a grain, diffusion from a given grain along grain boundary surfaces, surface reaction to form T_2 and T_2O, de-adsorption from Li_2O surfaces, and finally bulk transport in the slowly-drifting He purge gas. This model assumes that bulk diffusion within the grain is the rate-limiting process, grain boundary and other surface processes are rapid, and the helium purge rate is sufficiently rapid to permit the assumption of a zero gas-phase chemical activity. Furthermore, the grains themselves are assumed to be idealized spheres of radius $r_g << r_p$. Consequently, within a grain, the tritium concentration, $C(r,t)$, is given by the solution to

$$\partial C(r,t)/\partial t = (D/r^2)\partial\left[r^2 \partial C(r,t)/\partial r\right]/\partial r + S \quad , \qquad (D\text{-}1)$$

where D is a spatially-independent diffusivity, r is the spatial dimension within a grain that is situated within a pellet with its own spatial coordinate within the blanket, and S is the tritium generation rate that depends on blanket location but not on r. Physical processes of tritium decay, lithium burnup, and nondiffusive tritium release (i.e., lithium recoil) are not included in this model. Imposing the conditions that $C(r,t = 0) = C(r = r_g, t) = 0$, and invoking symmetry, Eq. (D-1) is readily solved[7] to yield the concentration profile, $C(r,t)$, within a grain.

$$C(r,t)\ (kg/m^3) =$$

$$(r_g^2 - r^2)S/6D + (2r_g^3 S/\pi^3 Dr) \sum_{n=1}^{\infty} \left[(-1)^n/n^3\right] \sin(n\pi r/r_g) e^{-Dt(n\pi/r_g)^2} \qquad (D\text{-}2)$$

Integration of Eq. (D-2) over the grain volume gives the tritium inventory within a given grain

$$I_g/(4\pi r_g^3/3) \quad (kg/m^3) = (Sr_g^2/15D)\left[1 - (90/\pi^4)\sum_{n=1}^{\infty} e^{-Dt(n\pi/r_g)^2}/n^4\right]. \quad (D\text{-}3)$$

Conservation of tritium requires $L_g = 4\pi r_g^3 S/3 - dI_g/dt$, wherein the tritium leakage rate from a given grain, L_g(kg/s) can be computed.

$$L_g/(4\pi r_g^3/3) \quad (kg/s\ m^3) = S\left[1 - (6/\pi^2)\sum_{n=1}^{\infty} e^{-Dt(n\pi/r_g)^2}/n^2\right] \quad (D\text{-}4)$$

These expressions for the grain inventories and leakage rates are based on the assumption of an isothermal grain. While this assumption is valid for distances on the order of r_g, a given pellet located at a specific blanket position clearly could support significant thermal gradients. Furthermore, the temperature distribution within a pellet of radius r_p will depend upon the local heating rate and boundary conditions. In order to reduce this problem to a tractable form, the following approximation is made. First, if the spherical pellet of radius r_p is subjected to a uniform thermal power density $G(W/m^3)$, the temperature within the pellet at radius $r' < r_p$ is given by

$$T(r') = (G/6k)(r_p^2 - r'^2) + T(r_p) \quad , \quad (D\text{-}5)$$

where k is the spatially-independent thermal conductivity and a steady-state temperature is used. Using Eq. (D-5), an average pellet temperature <T> can be computed to replace the pellet surface temperature, $T(r_p)$ in Eq. (D-5)

$$T(r') = \langle T\rangle + (G/k)\ (r_p^2/10 - r'^2/6) \quad . \quad (D\text{-}6)$$

The "macrodistribution" of blanket temperature given in Sec. V.B.2 is used along with the dependence of nuclear heating on blanket position (Sec. V.B.1) to evaluate <T> and G in Eq. (D-6). The tritium inventory within a given pellet, I_p, and the associated leakage rate, L_p, can now be computed by integration over all grains, using the temperature distribution [Eq. (D-6)] that is appropriate for a given blanket position, (i.e., <T> and

G). Expressed in terms of integrals, the local pellet tritium inventory and leakage rates are given by

$$I_p = \int_o^{r_p} \left[I_g(r)/(4\pi r_g^3/3) \right] 4\pi r^2 dr \qquad \text{(D-7)}$$

$$L_p = \int_o^{r_p} \left[L_g(r)/(4\pi r_g^3/3) \right] 4\pi r^2 dr \ . \qquad \text{(D-8)}$$

These integrations are performed numerically in conjunction with Eqs. (D-3), (D-4), and (D-6). The problem of determining an appropriate, temperature-dependent, diffusivity for Li_2O is addressed in Sec. V.D.2. The resulting integral quantities represent "local" variables which must be subjected to an additional summation over the blanket thickness, incorporating the appropriate variation of <T> and G with blanket position. Table D-I summarizes the macrodistribution of G and S for the five-zone Li_2O blanket model described in Sec. V.B.1, and Fig. D-2 gives the temperature distributions that have been folded into the integration prescription described above.

2. Evaluation of Model. The temperature profiles depicted in Fig. D-2 reflect the design criterion that the Li_2O not exceed its melting point of ~ 1700 K. As noted in Sec. V.B.2, a certain degree of flexibility is

TABLE D-I

MACRODISTRIBUTIONS OF BLANKET (Li_2O) TEMPERATURE, POWER DENSITY, AND TRITIUM BREEDING RATE USED TO DETERMINE TRITIUM INVENTORY AND RELEASE RATES

RADIAL POSITION (m)	AVERAGE CELL TEMPERATURE (K)	POWER DENSITY MW/m	POWER DENSITY MW/m^3	TRITIUM BREEDING RATE T/n	TRITIUM BREEDING RATE kg/m^3s
1.63	1242	9.36	9.43	0.4715	$2.48(10)^{-8}$
1.73	1013	5.43	5.14	0.3157	$1.56(10)^{-8}$
1.83	820	2.93	2.63	0.1761	$8.23(10)^{-9}$
1.93	782	1.54	1.30	0.0940	$4.16(10)^{-9}$
2.03	658	0.87	0.70	0.0552	$2.32(10)^{-9}$

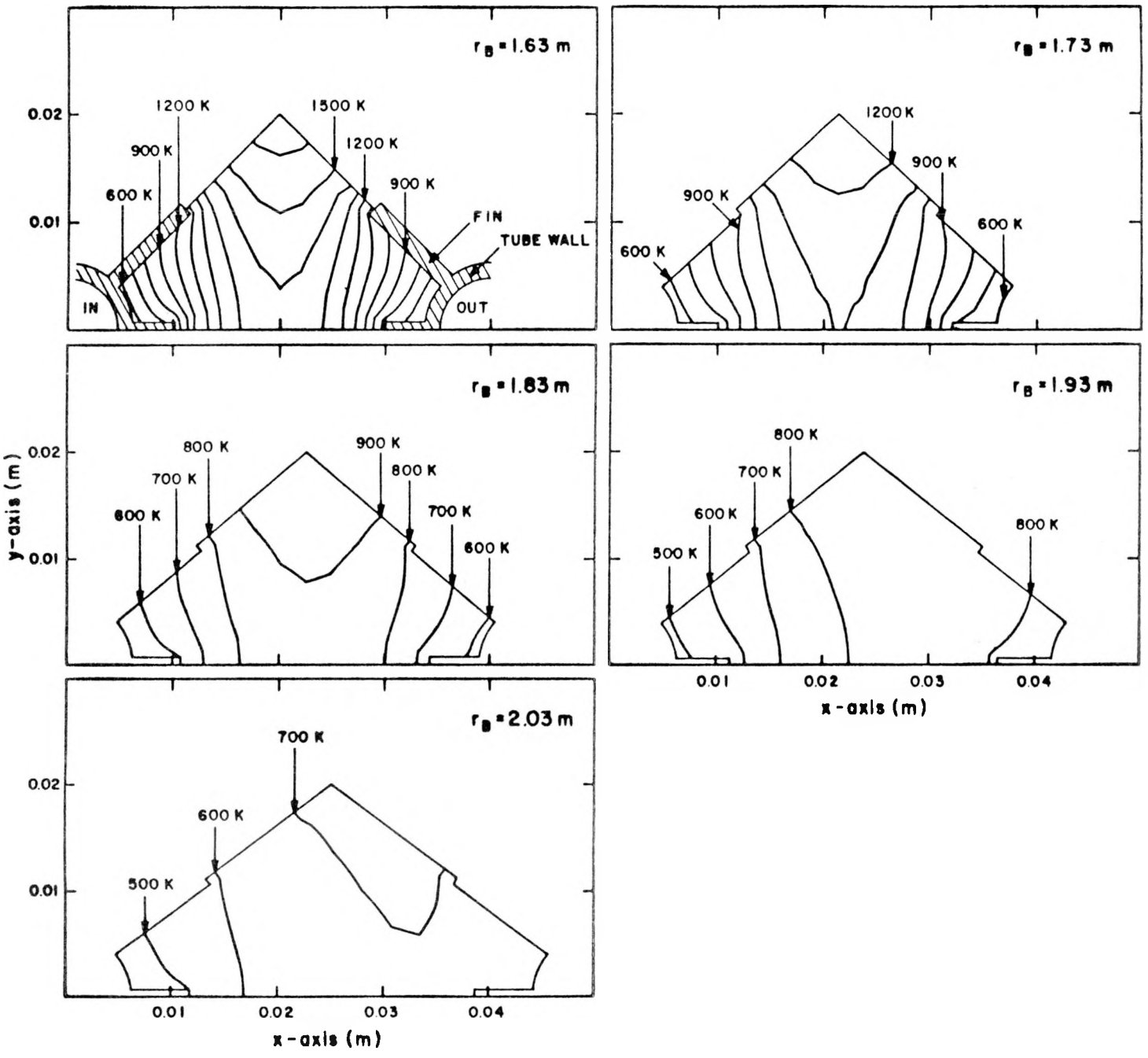

Fig. D-2. Temperature distribution within the Li_2O unit cell (Fig. V-15) at various radial positions in the packed-bed blanket. The variation of these isotherms with time during the long-pulsed burn is insignificant.

afforded by incorporation of external fins on the steam/water coolant U-tubes. The wide variation in the blanket temperature results in a correspondingly wide variation in local tritium leakage rate and inventory. The temporal evolution of $I(kg/m^3)$ and $L(kg/s\ m^3)$ for the calculational unit cell located nearest the first wall is depicted in Figs. D-3 and D-4, respectively. For the reasons discussed in Sec. V.D.2, the temperature dependence of tritium diffusivity chosen to model Li_2O was that for BeO. The time evolution of the total tritium inventory and release rate has been evaluated parametrically as a function of r_g and r_p in Sec. V.D.2 (Figs. V-30 and V-31) for both the radial temperature profile given in Table D-I, as well as the more favorable case where the first-wall unit cell (Fig. D-2) is repeated throughout the blanket by proper tailoring of the fin structure on the coolant tubes. Additionally, the radial profile of tritium inventory is shown as a function of time in Fig. V-32 (Sec. V.D.2). Finally, Fig. V-34 illustrates the strong influence of the tritium diffusivity selected to model the tritium release rate and inventory.

3. Tritium Inventory Question. Simply guaranteeing that the tritium breeding ratio BR exceeds unity by an acceptable margin does not assure tritium self-sufficiency. A blanket design that requires retention of the tritium within the breeding material for times on the order of the blanket life (~ 5 y) will force the reactor plant to rely on external tritium sources for that period of time. This section briefly addresses this issue. The environmental issue associated with large blanket inventories is not considered here.

Within the context of the above discussion, tritium self-sufficiency is taken as a point in the reactor operation where tritium leakage from the blanket becomes equal to or greater than the burnup rate (0.048 kg/MWt y). If $R(kg/m\ s)$ is the linear usage rate, this condition can be written as

$$L \geq R/BR \quad , \tag{D-9}$$

where now $L(kg/m\ s)$ is the linear leakage rate of tritium from the blanket.

The time for self-sufficiency, τ^*, occurs when $L/R = 1/BR$, and is shown graphically in Figs. V-30 and V-31 as a function of r_p and r_g; τ^* depends most sensitively on the grain radius, r_g, for the diffusivity used.

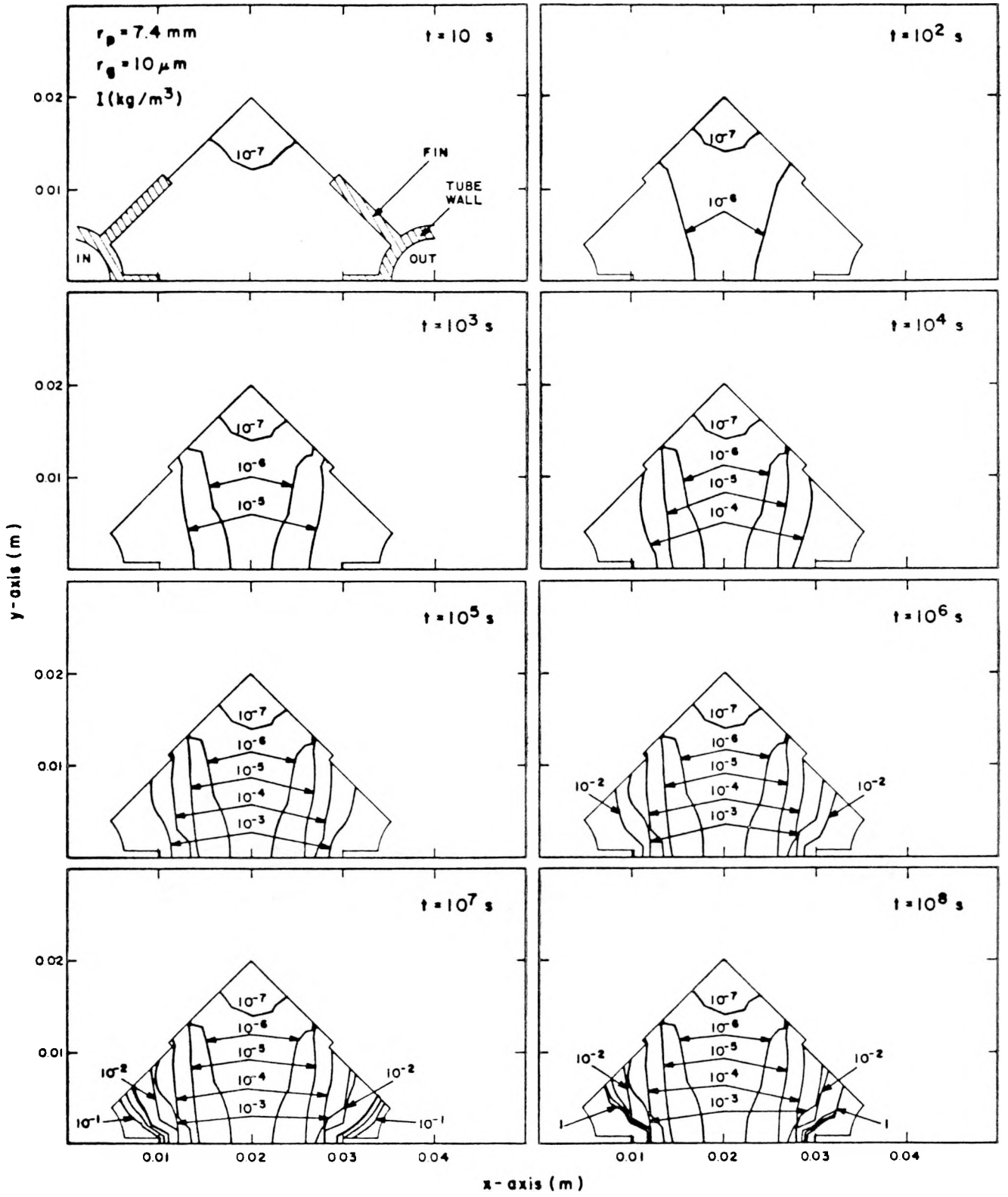

Fig. D-3. Distribution of tritium within the r_B = 1.63-m unit cell (Fig. D-2) as a function of time.

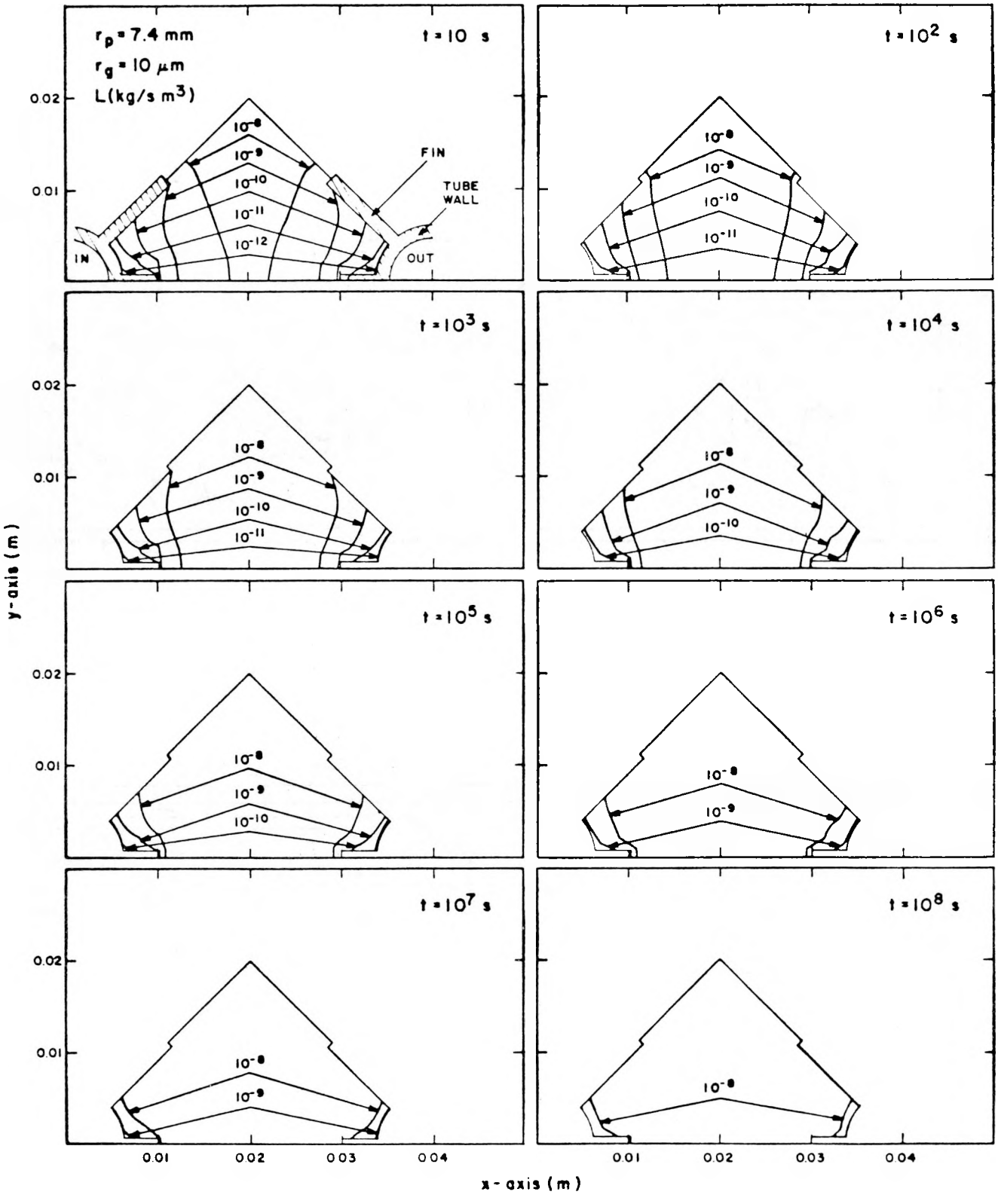

Fig. D-4. Distribution of tritium leakage rates within the r_B = 1.63-m unit cell (Fig. D-2) as a function of time.

Generally, the temperature profiles used in Table D-I leads to untenably large values of τ^* for any realistic value of r_p and r_g. Increasing the temperature in the outer blanket regions (Fig. V-31) decreases τ^* to more acceptable levels from the viewpoint of reduced tritium inventories and shortened times to self-sufficiency. Finally, use of an ad hoc Li_2O/T_2 diffusivity derived from tritium release data (Fig. V-28) leads to extremely rapid tritium release rates and negligible blanket inventories.

Another quantity of interest is the amount of tritium, I^*, necessary to sustain the reactor until self-sufficiency is achieved. Integration of the simple balance, $R/BR = dI^*/dt + L$, leads to

$$R\tau^*/BR = I^* + \int_o^{\tau^*} L dt, \qquad (D\text{-}10)$$

which, recalling that $L = R - dI/dt$, gives the following expression for I^*, the total amount of tritium that must be "borrowed" before the reactor becomes self-sufficient.

$$I^* = R\tau^*(1 - BR)/BR + I(\tau^*) \qquad (D\text{-}11)$$

Table V-XIV summarizes τ^* and I^* for a range of r_p and r_g values, using the BeO diffusivity data.

While the results presented in this Appendix and Sec. V.D.2 depend sensitively on the assumed tritium diffusivity, it can be concluded that the ideal Li_2O system will have to operate at a higher temperature, and alternative temperature profiles should be considered. Furthermore, smaller grain sizes, r_g, and large pellet sizes, r_p, would be more desirable. The magnitude of r_p, however, is limited by center melting, a limit that has been indicated on Figs. D-30 and D-31. Lastly, these conclusions must be tempered with the assumptions intrinsically made in formulating and evaluating this model: bulk grain diffusion is rate limiting, rapid grain boundary diffusion, rapid surface reactions, no tritium chemical activity within the helium purge gas, no radiation effects, applicability of BeO diffusivities to the description of Li_2O, and constant pellet morphology (grain size).

APPENDIX E

SUMMARY REVIEW OF DESIGN POINT EVOLUTION

Previous conceptual designs (RFPR-I)[8] were based on normal-conducting coils and an iron-cored poloidal field transformer. One design (RFPR-IA) used a 50-50% DT fuel mixture (2.0 mtorr) that was ohmically heated to ignition by a 40-MA toroidal plasma current. Using a maximum plasma compression of $1/x = 2.5$ (at $\beta_\Theta \sim 0$) in a 2-m minor radius device yields an experimentally achievable[1] current density of 20 MA/m^2. The plasma temperature increases by alpha-particle heating to ~ 30 keV in 1.2 s at which time $\beta_\Theta \sim 0.35$; the plasma is subsequently expanded to the wall by reducing the plasma current to avoid stability-related β limits ($\beta_\Theta < 0.5$ at the wall radius). A total plasma burnup of 11% produces a 2 MW/m^2 wall loading with a cycle time of 8.7 s. Power costs, c_p(mills/kWeh), direct costs, c_D($/kWe), and Q_E versus the sum of toroidal and poloidal coil thicknesses are shown in Fig. E-1 for the RFPR-IA (50-50% DT, normal coils) design. In all cases the toroidal coil thickness is 20% of the total coil thickness, giving comparable current densities in each room-temperature coil with a conductor filling fraction of 0.7. A short, vigorous burn is characteristic of this operating mode and results in the ohmic losses incurred within the room-temperature magnets being a relatively small contribution to the recirculating power fraction; a total coil thickness of 0.4-0.6 m for the iron-core system is adequate. The RFPR-IA air-core system, using a bipolar current change incurs ohmic losses during the dwell time between burn pulses and optimizes at a much larger coil thickness of 1.5 m. The power costs for the bipolar, air-core system shown in Fig. E-1 are reduced from 110 mills/kWeh to 89 mills/kWeh, however, when the massive iron core is eliminated in conjunction with a 50% reduction in the required energy transfer and storage (ETS) system.

Further reduction in the system costs can be realized by increasing Q_E, which minimizes the balance-of-plant costs. A large fraction (~ 50%) of the recirculating power in the RFPR-IA (50-50% DT) case is attributable to the resistive loss of field energy trapped inside the plasma during the quench. A larger fusion energy release (i.e., prolonged plasma burns) for a given investment of field energy is necessary to increase Q_E. An earlier conceptual design[8] (RFPR-IB) used a 90-10% DT fuel mixture (1.25 mtorr) in

which burnup of the fuel provides an inherent temperature limiting mechanism and β_Θ control. The prolonged RFPR-IB burn (6.9 s) requires a smaller (30 MA) current to achieve a 1.54 MW/m^2 wall loading for a cycle time of 11.9 s in a 2 m radius device using a maximum plasma compression of $1/x = 2.5$ (at $\beta_\Theta \sim 0$). The plasma temperature rises to ~ 50 keV in 3 s and remains relatively constant during the burn as a result of fuel burnup.

Costing results for the RFPR-IB (90-10% DT, normal coils) are given in

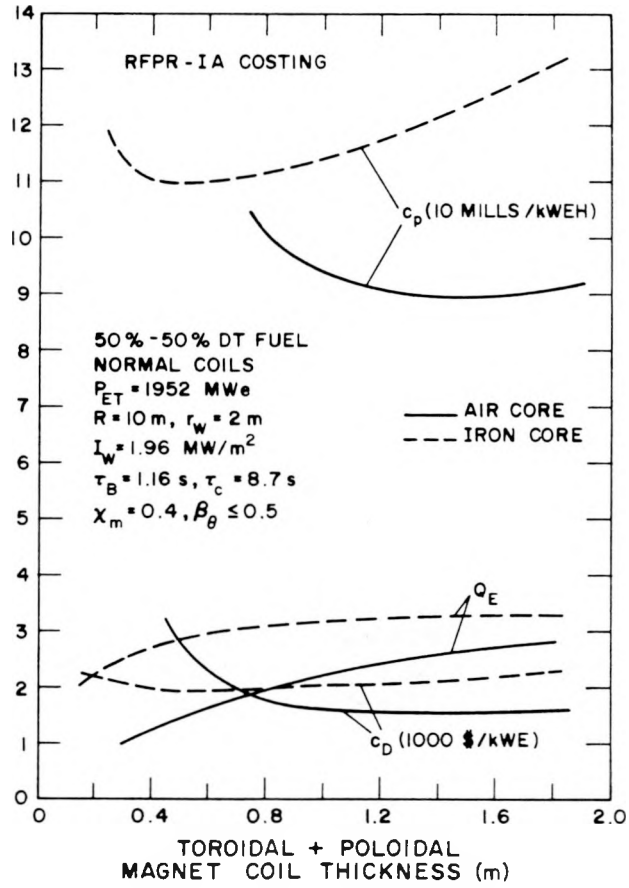

Fig. E-1. RFPR-IA costs for a 50-50% DT fuel mixture for which β_Θ control is provided by premature quench, resulting in a burnup of 11%. Ideal MHD stability criteria allow a maximum compression of $1/x \simeq 2.5(\Theta = 8, F = -2)$. Air- and iron-core poloidal systems with normal conducting coils are compared on a cost basis.

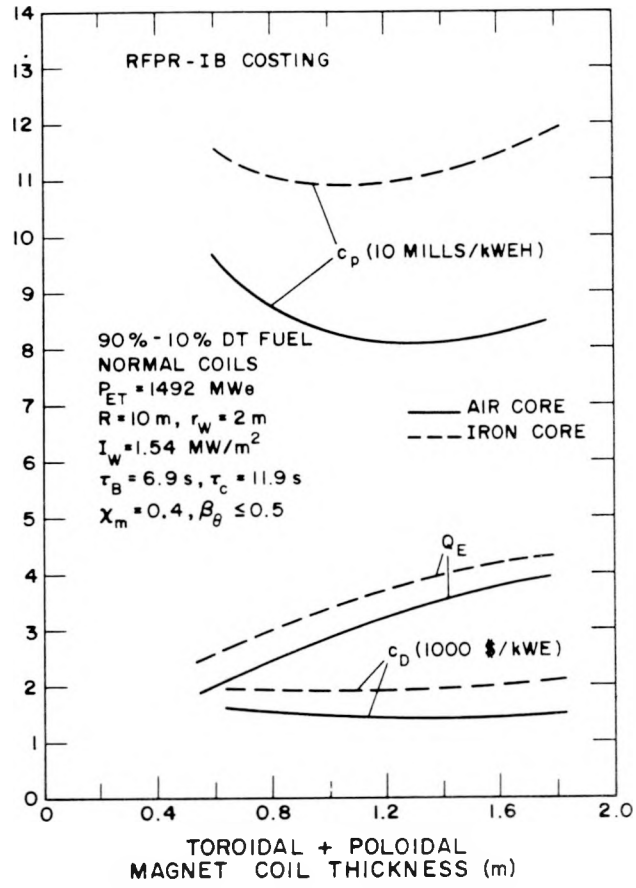

Fig. E-2. RFPR-IB costing for a 90-10% DT fuel mixture for which β_Θ control is provided by fuel burnup. Ideal MHD stability criteria allow a maximum compression of $1/x \simeq 2.5(\Theta = 8, F = -2)$. Air- and iron-core poloidal systems with normal conducting coils are compared on a cost basis.

Fig. E-2 along with Q_E curves. The large cost advantage in using a bipolar air-core rather than iron-core transformer again results. A cost reduction from 89 to 81 mills/kWeh (at the cost optimum) from the 50-50% (RFPR-IA) to the 90-10% (RFPR-IB) DT case is caused primarily by the ~ 40% reduction in required energy storage (40 MA to 30 MA) and the increase in Q_E from 2.7 to 3.4. The relatively small increase in Q_E results from the large ohmic losses incurred during the longer RFPR-1B burn cycle. As a consequence the use of pulsed-superconducting coils has been given impetus. The superconducting mode of operation is designated as RFPR-II.

The state-of-the-art superconducting cable[30] proposed for RFPR-II (94% copper and 6% NbTi) operates at an average current density of 17 MA/m^2. Use of superconductors requires the addition of ~ 1-m-thick radiation shield. Optimized costs and Q_E for the designs with superconducting coils and normal-conducting coils are summarized in Table E-I. Significant increases in Q_E and reductions in cost result for all RFPR-II designs, except for the iron-core 50-50% DT fuel system in which ohmic losses made an insignificant

TABLE E-I

OPTIMIZED COST SUMMARY FOR A RANGE OF RFPR CONCEPTUAL DESIGNS[a]

	IRON CORE		AIR CORE	
	NORMAL COILS RFPR-I	SUPER-CONDUCTING RFPR-II	NORMAL COILS RFPR-I	SUPER-CONDUCTING RFPR-II
50-50% DT:				
Q_E	2.80	3.33	2.65	4.31
C_D($/kWe)	1950	2290	1550	1300
c_p(mills/kWeh)	110	130	89	73.6
90-10% DT:				
Q_E	3.60	6.05	3.40	7.83
c_D($/kWe)	1930	1811	1420	1150
c_p(mills/kWeh)	109	103	81	65.5

[a]It is emphasized that the costing procedure adopted here is intended only for the intercomparison of RFPR design options and should not be used to make economic comparisons with existing energy systems on the basis of present cost.[15]

contribution to the energy balance. Using an air-core poloidal field system and superconducting poloidal/toroidal field coils projects to a minimum-cost RFPR system. These results of early attempts to define an RFPR design, point to the desirability of a long-pulse system using superconducting coils. Simultaneously, the minimum-energy-state criterion for RFP stability (F-Θ criteria, Sec. III.B) was adopted for these long-pulse operating modes, leading to the physics design basis used in the present design.

The present RFPR design proposes long pulsed operation, but the possibility of a refueled, steady-state operation remains. Other RFP reactor designs have assumed the possibility of a refueled steady state, however, the LASL design conservatively assumes a batch-burn operation. Although refueling may be technologically feasible, loss of confinement may depend on the resistive dissipation of the trapped B_ϕ flux,[11] which has a time constant given as $\tau_\eta \sim 100\ r_w^2 T_e^{3/2}/\ell n\Lambda$ using the classical value of resistivity. Taking $r_w = 1.5$ m, $T_e = 20$ keV, and $\ell n\Lambda = 20$ gives $\tau_\eta = 1000$ s; requiring the energy dissipation to be less than 10% gives an allowable burn time of 100 s. The characteristic time for fuel burnup f_B in a batch-burn of constant temperature and initial density, n_o, is $\tau_B = 2f_B/\left[n_o\langle\sigma v\rangle(1-f_B)\right]$. Substituting representative reactor parameters of $n_o = 2(10)^{20}/m^3$, $f_B = 0.5$, and $\langle\sigma v\rangle = 4.3(10)^{-22} m^3/s$ at 20 keV gives $\tau_B = 23$ s, which is comparable to the field dissipation time. The field configuration, therefore, may not be maintained sufficiently long to make refueling possible. Wesson and Sykes[31] have shown on the basis of MHD calculations that the B_ϕ flux contained within the plasma may be replenished by turbulence, although, the resultant plasma loss is unknown. Until better quantified, these questions have led LASL to postulate a batch burn, recognizing that a refueled steady state would improve the already good RFPR energy balance.

REFERENCES

1. D. A. Baker and J. N. DiMarco, "The LASL Reversed-Field Pinch Program," Los Alamos Scientific Laboratory report LA-6177-MS (1975).

2. K. I. Thomassen (ed.), "Ohmic Heating Systems Study for a Tokamak EPR," Los Alamos Scientific report (CTR Division) submitted to the Division of Fusion Energy in the Department of Energy (1977).

3. D. J. Rose and M. Clark, Jr., Plasma and Controlled Fusion, 2nd Ed., (The M.I.T. Press, Massachusetts Institute of Technology, Cambridge, Massachusetts, 1965), 493 pp.

4. R. A. Krajcik, "The Effect of a Metallic Reflector Upon Cyclotron Radiation," Nucl. Fus. 13, 7 (1973).

5. S. I. Braginskii, "Transport Processes in a Plasma," in Reviews of Plasma Physics, M. A. Leontovich, Ed., (Consultants Bureau, New York, 1965), Vol. 1.

6. R. W. Moses, Los Alamos Scientific Laboratory and R. Nebel, University of Illinois, unpublished Reversed-Field Pinch Code Development (1979).

7. H. S. Carslaw and J. C. Jaeger, Conduction of Heat in Solids (Oxford on the Clarendon Press, London, 1959), 510 pp.

8. R. L. Hagenson, R. A. Krakowski, and K. I. Thomassen, "A Toroidal Fusion Reactor Based on the Reversed-Field Pinch (RFP)," in Fusion Reactor Design Concepts (IAEA Workshop on Fusion Reactor Design, Madison, Wisconsin, 1977), IAEA, Vienna (1978), pp. 337-355.

9. T. A. Oliphant, "Fuel Burnup and Direct Conversion of Energy in a DT Plasma," Los Alamos Scientific Laboratory report LA-DC-10528 (1969).

10. R. Hancox and W. R. Spears, "Reversed-Field Pinch Reactor Study II. Choice of Parameters," UKAEA report CLM-R-172, Culham Laboratory (1977).

11. J. P. Christiansen and K. V. Roberts, "Evolution of the Reversed-Field Pinch," Nucl. Fus. 18, 181 (1978).

12. B. R. Suydam, "Stability of a Linear Pinch," Proc. 2nd UN International Conf. on the Peaceful Uses of Atomic Energy, 31, 157-159 (1958).

13. A. B. Berlizov, G. A. Bobrovskij, A. A. Bagdasarov, N. L. Vasin, A. N. Vertiporokh, and V. P. Vinogradov, "First Results from the T-10 Tokamak," Sixth Conf. on Plasma Physics and Controlled Nuclear Fusion Research, Berchtesgaden, 1976, Vol. 1, pp. 3-18.

14. E. Apgar, B. Coppi, A. Gondhalekar, H. Helava, D. Komm, and F. Martin, "High-Density and Collisional Plasma Regimes in the Alcator Programme," Sixth Conf. on Plasma Physics and Controlled Nuclear Fusion Research, Berchtesgaden, 1976, Vol. 1, pp. 247-266.

15. S. C. Schulte, T. L. Willke, and J. R. Young, "Fusion Reactor Design Studies-Economic Evaluation Guidelines," Battelle Pacific Northwest Laboratories report PNL-SA-2648 (1977).

16. NUS Corporation, "Guide for Economic Evaluation of Nuclear Reactor Plant Designs, NUS-531 (January 1969).

17. S.Schulte, personal communication, Battelle, Pacific Northwest Laboratories (1979).

18. B. Badger, M. A. Abdou, R. W. Boom, R. G. Brown, T. E. Cheng, and R. W. Conn, "UWMAK-I, A Toroidal Fusion Reactor Design," University of Wisconsin report UWFDM-68 (1975).

19. B. Badger, R. W. Conn, G. L. Kulcinski, C. W. Maynard, R. Aronstein, and H. I. Avci, "UWMAK-III, A Noncircular Tokamak Power Reactor Design," University of Wisconsin report UWFDM-150 (1976).

20. R. Hancox, personal communication, Culham, United Kingdom, (1977).

21. D. J. Bender and G. A. Carlson, "System Model for Analysis of the Mirror Fusion-Fission Reactor," Lawrence Livermore Laboratory report UCRL-52293 (October 1977).

22. J. C. Scarborough, "Comparative Capital Costs for the Prototype Large Breeder Reactor," NUS Corporation, 4 Research Place, Rockville, Maryland (also presented at the ANS Winter meeting, San Francisco, CA, December 1977).

23. United Engineers and Constructors, Inc., "Pressurized Water Reactor Plant," WASH-1230, Vol. 1 (June 1972).

24. B. Badger, G. L. Kulcinski, R. W. Conn, C. W. Maynard, K. Audenaerde, and H. Avci, "Tokamak Engineering Test Reactor," University of Wisconsin report UWFDM-191 (1978).

25. D. L. Kummer (Principal Investigator), "Alloys for the Fusion Reactor Environment," Prepared by McDonnell Douglas Astronautics Company for Division of Magnetic Fusion Energy, ERDA (April 1977). (Draft)

26. K. I. Thomassen (Principal Investigator), "Conceptual Engineering Design of a One-GJ Fast Discharging Homopolar Machine for the Reference Theta-Pinch Fusion Reactor," EPRI ER-246, Project 469 (August 1976).

27. R. E. Stillwagon, "Design Studies of Reversible Energy Storage and Transfer Systems for the Reference Theta-Pinch Reactor," Westinghouse report E.M. 4620 (September 1974).

28. C. R. Head, "Standard Fusion Reactor Design Contents," USDOE/OFE memo CRH-478 (March 7, 1979).

29. C. C. Baker (Principal Investigator), "Experimental Fusion Power Reactor Conceptual Design Study," Electric Power Research Institute report EPRI ER-289 (1976).

30. D. Weldon and J. Wollen, personal communication, Los Alamos Scientific Laboratory (1978).

31. A. Sykes and J. A. Wesson, "Field Reversal in Pinches," Phys. Rev. Letts. 37, 140 (1976).

Printed in the United States of America. Available from
National Technical Information Service
US Department of Commerce
5285 Port Royal Road
Springfield, VA 22161

Microfiche $3.00

001-025	4.00	126-150	7.25	251-275	10.75	376-400	13.00	501-525	15.25
026-050	4.50	151-175	8.00	276-300	11.00	401-425	13.25	526-550	15.50
051-075	5.25	176-200	9.00	301-325	11.75	426-450	14.00	551-575	16.25
076-100	6.00	201-225	9.25	326-350	12.00	451-475	14.50	576-600	16.50
101-125	6.50	226-250	9.50	351-375	12.50	476-500	15.00	601-up	

Note: Add $2.50 for each additional 100-page increment from 601 pages up.